Coupling the Thermodynamics, Kinetics and Geodynamics of Multiphase Reactive Transport in Earth's Interior

Lucy E. L. Tweed

Submitted in partial fulfillment of the
requirements for the degree of
Doctor of Philosophy
under the Executive Committee
of the Graduate School of Arts and Sciences

COLUMBIA UNIVERSITY

2021

Abstract

Coupling the Thermodynamics, Kinetics and Geodynamics of Multiphase Reactive Transport in Earth's Interior

Lucy E. L. Tweed

Multiscale multiphase reactive transport is a central phenomenon governing geologic processes in Earth's interior. In the upper mantle, melts, produced by partial melting of the peridotitic mantle, and volatile-rich fluids, derived from dehydration of subducting plates, buoyantly ascend through the mantle's porous network. Reaction between these melts and fluids and the surrounding solid matrix control the composition of magmas that reach Earth's crust. Melt-rock reaction is strongly coupled to the dynamics of melt transport: not only do the transport pathways modulate the extent of chemical interaction between melts and the solid matrix, but the melt-rock reactions also feedback into the transport dynamics through reactive changes to bulk physical properties including permeability, density, and viscosity. These feedbacks can result in the emergence of self-organized transport networks, such as the network of high-porosity dunite channels beneath mid-ocean ridges. Understanding the various feedbacks between reaction and melt transport requires consistent coupling of multicomponent multiphase thermodynamics and geodynamics. However, the high-dimensionality of such coupled problems presents a major theoretical and computational challenge. Existing models of reactive multiphase flow have therefore tended to focus separately on the geochemistry of melt-rock interaction, or on the dynamics of melt transport, with simplified thermo-chemical couplings.

In this dissertation I present a new thermodynamically consistent and tractable framework for integrating multicomponent thermodynamics and multiphase geodynamics. I use a non-equilibrium thermodynamic formulation to describe reaction as a

time-dependent irreversible process alongside heat and mass transport. This theory is implemented using new thermodynamics software developed through the ENKI project. The main benefits of this approach are two-fold. Firstly, it extends the reach of existing multiphase computational thermodynamics to model macroscopic disequilibrium reaction paths — this is the first step towards being able to model a host of metastable reaction phenomena in igneous and metamorphic systems. I model disequilibrium batch reaction for a simple system in chapter 2. Secondly, it allows self-consistent integration of multiphase thermodynamics in two-phase flow models, to better explore coupling between reaction and transport. This is demonstrated in chapter 5.

Chapter 1 gives a broad introduction to multiphase reactive flow and further discusses the motivation for this work. I outline past work and discuss the scope of problems in which coupling between reaction and transport plays a critical role in geodynamic and geochemical evolution.

In chapter 2 I present a general theory for integrating computational thermodynamics and geodynamics. This approach is based on the standard conservation equations for porous melt transport within a deformable solid matrix, but extends the governing equations to include multiple solid phases. The multiphase reactive coupling is described using a kinetic framework that includes explicit stoichiometric reactions between minerals, melts, and fluids. Using the theory of non-equilibrium thermodynamics, the macroscopic reaction rates are controlled by the reaction affinities — providing closed-form expressions for the net reactive mass transfers. This formulation of disequilibrium reaction is the principle contribution of this dissertation. Coupled with the conservation equations it can describe both equilibrium and disequilibrium reaction paths and is applicable to a range of geological conditions. I outline approaches for modeling melt-mediated, fluid-mediated, and subsolidus grain-boundary-mediated reaction. In extension to previous theories of two-phase flow, this framework permits modeling of more realistic melting and

crystallization reactions, including eutectic and peritectic melting. The theoretical framework is supported by software developed as part of the ENKI project. I briefly summarize the software infrastructure in this chapter.

In the remaining chapters I step through the workflow for implementing this approach for a series of model problems in the Mg_2SiO_4–SiO_2 binary system. The Mg_2SiO_4–SiO_2 subsystem is an important bounding binary for understanding mantle melting and represents the simplest subsystem for exploring coupled reactive transport dynamics. Widely used thermodynamic models of silicate melting (i.e. MELTS) do not extend to the binary, and existing binary melting models involve complex treatments of melt speciation to account for significant non-ideality at high silica contents. Here, I am concerned mostly with reaction for mafic compositions relevant to mantle magmatism. Therefore, in chapter 3 I present a simple thermodynamic model for melting in the Mg_2SiO_4–SiO_2 system. I use a numerically efficient asymmetric binary mixing model to describe solution in the melt, which is calibrated using a compilation of phase equilibrium experimental data. This chapter is not a self-contained study in and of itself, but rather sets up the thermodynamic model that I will use in the remaining chapters.

Chapter 4 applies the theoretical framework to a series of simple model problems for disequilibrium reaction and reactive melt transport in the Mg_2SiO_4–SiO_2 system. Disequilibrium reaction paths can be non-intuitive, and I start by modeling reaction in uniform batch systems. All of the calculations are consistent with the phase diagram in the equilibrium limit. More general conservation equations for disequilibrium reaction in open-system batch reactors are derived in Appendix C. I then integrate irreversible reaction with the dynamics of diffusion and advection of heat and mass to model the formation of reactive fronts around fusible heterogeneities, and a eutectic/peritectic disequilibrium steady-state melting column. This is the first self-consistent inclusion of eutectic/peritectic melting into magma dynamics.

Finally, in chapter 5 I apply this framework to explore the formation of dunite channels by incongruent open-system melting. I develop a series of 1-D and 2-D models to investigate the formation of dunite channels in a harzburgitic mantle within the Mg_2SiO_4–SiO_2 binary system. The models predict that influx of deep silica-poor melts promotes a reactive channeling instability that organizes melt into high-porosity dunite channels. During decompression melting in the absence of a basal melt flux, no channelization is observed. This implies that an additional flux of melt is required, either from melting of deep fusible heterogeneities, or from large-scale melt focusing toward the ridge axis at depth. Alternatively, flux melting of additional melt components could help drive reactive channelization in natural peridotite systems.

Table of Contents

List of Figures xii

List of Tables xiii

Acknowledgments xvi

Chapter 1: The Need for an Integrated modeling Approach to Fluid and Magma Transport 1

1.1 Introduction 1

1.2 Open questions on Open systems 9

1.3 Previous approaches to coupling reaction and transport 12

1.4 The role of disequilibrium in the dynamics of Earth's interior 15

1.5 Dissertation overview 18

Chapter 2: A Tractable Kinetic Framework for Coupling Computational Thermodynamics and Geodynamics 21

2.1 Introduction 21

2.2 General system description 24

2.3 Conservation Equations 26

2.3.1 Conservation of mass 26

2.3.2 Conservation of momentum 29

2.3.3 Conservation of energy 30
2.3.4 Closures 33
2.4 Thermodynamics 34
2.5 Reactive system 37
2.5.1 Rate laws 39
2.5.2 Choice of reactions 42
2.5.3 Linearly independent reactions 43
2.5.4 Equilibrium and kinetic considerations 45
2.5.5 Melt-mediated reactions 47
2.5.6 Fluid-mediated reactions 48
2.5.7 Grain boundary-mediated reactions 49
2.5.8 Dependent reactions 51
2.6 Supporting software 52
2.7 Conclusions and future directions 54

Chapter 3: A Simple Analogue Model for Mantle Melting: The Mg_2SiO_4–SiO_2 Binary System 57
3.1 Introduction 57
3.2 Thermodynamic model for the Mg_2SiO_4–SiO_2 binary system 59
3.2.1 Subsolidus phase assemblage 59
3.2.2 Melt solution model 60
3.2.3 Calibration 61
3.3 Comparison to the melting systematics of natural peridotites 64
3.4 Summary 66

Chapter 4: Model Examples of Disequilibrium Reaction and Reactive Transport in the Mg_2SiO_4-SiO_2 System 68

4.1 Introduction 68

4.2 Mg_2SiO_4-SiO_2 system description 69

4.2.1 Thermodynamics 69

4.2.2 Reactions 70

4.2.3 Kinetics 73

4.2.4 Implementation 74

4.3 0-D batch reactors 75

4.3.1 Adiabatic reaction paths 77

4.3.2 Heated reaction paths 82

4.3.3 Adiabatic decompression reaction paths 84

4.4 Reaction-diffusion dynamics 88

4.4.1 Decompression melting of an eclogite inclusion 90

4.5 1-D reactive porous flow 93

4.5.1 Batch melting column 96

4.6 Discussion 102

4.7 Summary 106

Chapter 5: Formation of High-Porosity Dunite Channels by Reactive Melt Transport . 108

5.1 Introduction 108

5.2 Thermodynamic and reactive system 110

5.3 Governing equations 114

5.3.1 Scaling 116

5.4 Model setup . . . 118
5.4.1 Initial and boundary conditions . . . 118
5.4.2 Parameters . . . 120
5.4.3 Numerical implementation . . . 121
5.5 Results . . . 122
5.5.1 1-D models . . . 122
5.5.2 2-D models . . . 129
5.6 Discussion . . . 133
5.6.1 Channel geometry and evolution . . . 133
5.6.2 Melt inflow as a driver of channelization . . . 136
5.6.3 Model limitations . . . 137
5.6.4 Future work . . . 138
5.7 Conclusions . . . 139

References . . . 160

Appendix A: Thermodynamic relations . . . 161

Appendix B: Deriving independent reaction sets . . . 163

Appendix C: Evolution equations for an open system batch reactor . . . 164
C.0.1 Conservation of composition . . . 165
C.0.2 Conservation of phase mass . . . 166
C.0.3 Conservation of energy . . . 167

Appendix D: Pressure-split formulation 170

Appendix E: Numerical solution using finite elements 172

List of Figures

1.1 Schematic figure illustrating the components of the coupled model. The grey shaded boxes show the inputs of each model component, and the boxes below give examples of useful outputs. The arrows illustrate how variables are passed from one model component to another. 5

2.1 Schematic figure illustrating the components of the coupled model. The grey shaded boxes show the inputs of each model component, and the boxes below give examples of useful outputs. The arrows illustrate how variables are passed from one model component to another. 52

3.1 Calculated Mg_2SiO_4–SiO_2 binary phase diagram at 1 bar (left) and 1 GPa (right). Phase abbreviations as in text. Colored markers include both experimental brackets and interpolated data from Bowen and Anderson (1914) and Hudon et al. (2005). 63

3.2 Pressure dependence of fo-en cotectic. The solid lines show the phase boundaries for the 1 bar and 2 GPa phase diagrams. The dashed line shows the variation in the cotectic melt composition with increasing pressure. In this calibration the melting reaction transitions from eutectic to peritectic around 0.2 GPa 64

3.3 a) Experimental olivine- and orthopyroxene-saturated partial melts from the LEPR database plotted in wt concentration where MO accounts for all oxides other than MgO and SiO_2. Note that all natural melts are more silicic than the binary melts. The fractional harzburgite melt composition is from Wasylenki et al. (2003) b) forsterite-enstatite cotectic boundary plotted on a similar ternary but in molar concentration and reproduced from Kushiro (1975). The concentrations of the oxides have been scaled by the number of cations per formula unit. Note the deflection of the cotectic boundary with the addition of monovalent and divalent cations. 65

3.4 a) Experimental liquidus constraints with phase boundaries reproduced from the quasichemical model of Kim et al. (2017). b) Approximate thermodynamic fit at 1bar using a regular asymmetric solution model. The dashed lines show the liquidus temperature contours. c) Approximate thermodynamic fit at 1 GPa 66

4.1 $Mg_2SiO_4-SiO_2$ binary at 1bar contoured for the three different melting reactions 72

4.2 Cartoon illustration of reactive system in the Mg_2SiO_4–SiO_2 system, showing the phase assemblage and the three reactions. R_j and A_j refer to the reaction rate and affinity of reaction j. 73

4.3 Isobaric adiabatic reaction paths for a system initially comprising a disequilibrium assemblage of ol and qz. Three different kinetic rate laws are shown: crystallization rate equal to melting rate (solid line); crystallization rate $5\times$ faster than melting (dashed line); crystallization $20\times$ faster than melting (dotted line). (a) Melt composition versus temperature compared to equilibrium phase diagram. (b) Phase volume fraction evolution. (c) Temperature evolution. (d) Chemical affinities of the three reactions. (e) Reaction rates of the three reactions: The rates converge to zero at equilibrium. 79

4.4 Isobaric adiabatic reaction paths for three different initial temperatures. (a) Melt composition versus temperature compared to the equilibrium phase diagram. The metastable extensions of the the saturation surfaces of ol, opx and qz are shown in dashed lines. The dark purple shaded region indicates the region in which melt is more stable than ol and qz. The light purple shading shows the temperature range over which subsolidus melt-mediated reactions are possible. (b) Phase volume fraction evolution. Note that no reaction occurs for $T_0 = 1350°C$ (c) Temperature evolution. 81

4.5 Isobaric heated reaction paths for $Da_Q = 10^5$ (solid), $Da_Q = 10^3$ (dashed), $Da_Q = 10^2$ (dotted). $Da_Q = 10^6$ approximates equilibrium batch melting. (a) Melt composition versus temperature compared to the equilibrium phase diagram. Circle shows the initial melt composition (at the ol-opx peritectic), and the cross shows the final condition. (b) Temperature evolution, and (c) normalized phase fraction evolution plotted versus relative reaction time. Note that for $Da_Q = 10^2$ the fraction of ol decreases slightly during initial melting contrary to what would be expected for the equilibrium peritectic melting reaction. 83

4.6 Internal entropy production σ for reaction paths shown in Fig 6: $Da_Q = 10^5$ (solid), $Da_Q = 10^3$ (dashed), $Da_Q = 10^2$ (dotted). 84

4.7 Calculated 0-D adiabatic decompression reaction paths for a 'harzburgite' (ol + opx) and 'eclogite' (opx + qz) assemblage. The reaction paths follow equilibrium batch melting trends. The discontinuity in the eclogite melting path is due to the qz-crs transition. 85

4.8 Olivine reactive mass transfer rate Γ_{ol} for 0-D adiabatic decompression with a range in upwelling rates. W_0 is in m yr^{-1}. $\Gamma_{ol} < 0$=eutectic melting, and $\Gamma_{ol} > 0$=peritectic melting. The blue line shows the transition to peritectic melting in the equilibrium phase diagram. 87

4.9 Isothermal decompression melting of a fusible eclogite (opx + qz) inclusion in a harzburgitic (ol + opx) matrix for a system that is open to diffusion of both heat and SiO_2. On the left is the P-T path of the system. The eclogite solidus (dotted line) and harzburgite solidus (dashed line) are shown. On the right are numbered snapshots of the system at different pressures. The phase assemblage is shown as a cumulative phase volume fraction and the melt composition in wt fraction SiO_2 is shown in red. 91

4.10 Calculated steady-state 1-D melting profiles in the Mg_2SiO_4-SiO_2 system. This is a near-equilibrium model with $Da \approx 10^4$. The solid phase fractions in plot (h) are normalized to 100% for the solid assemblage. The transition from eutectic to peritectic melting can be seen in subplot (i) in which Γ_{ol} becomes positive at 0.5 GPa, resulting in melting reaction opx=ol +f. 99

4.11 Thermodynamic phase properties for the steady-state profiles shown in Figure 4.10 from the solidus to the surface. (a) Phase densities; (b) $\Delta\rho = \rho_s - \rho_f$ is the density difference between the aggregate solid and melt. The observed variation in the ρ_f and $\Delta\rho$ is due to the variation in melt composition with pressure. (c) Phase entropies; (d) Latent heat of melting. The entropies of all phases are temperature-dependent, but s_f varies more extensively due to variation in melt composition. 100

4.12 Calculated 1-D steady state melting columns for a range of Da compared to the calculated profile for equilibrium ($Da = \infty$) batch and fractional melting. All other model parameters in the disequilibrium melting columns are set to the reference values. F and T are the same for fractional and batch melting and are represented by the red dashed line. The fractional melt composition is the accumulated fractional melt composition that we would expect for melt transported in chemically-isolated channels. 101

4.13 Surface melt compositions and temperatures from steady state melting columns shown in Fig. 4.12 for different Da, plotted on the 1 bar phase diagram. For low Da the melts are silica-deficient as they have not maintained equilibrium with the solid during ascent. The ol-opx cotectic for different pressures in GPa are plotted for comparison. 103

5.1 Calculated equilibrium phase diagrams for mafic compositions in the Mg_2SiO_4-SiO_2 binary system at (a) 1 bar, and (b) 1 GPa. (c) Variation fo-en cotectic melt composition as a function of pressure 111

5.2 Model setup for 2-D upwelling column models. On the right is the setup for the decompression melting models with no melt flux across the lower boundary ($\phi_f = 0$). On the left is the setup for decompression melting with an influx of melt across the lower boundary ($\phi_=0.01$). For these models we apply 'masks' to ζ and Γ_i to impose a rigid unreactive buffer zone below the solidus. These are given by $\zeta_{mask} = 1000 + \frac{1-1000}{2}\left(\tanh\left(\frac{P_{sol}-P}{\lambda}\right) + 1.\right)$ and $\Gamma_{mask} = \frac{1}{2}\left(\tanh\left(\frac{P_{sol}-P}{\lambda}\right) + 1\right)$. The boundary conditions are the same for the 1-D models. 119

5.3 The initial fields for the modal proportions of olivine and opx in the solid residue ($\frac{\phi_{ol}}{1-\phi_f}$ and $\frac{\phi_{opx}}{1-\phi_f}$) used in the 2-D models. These are obtained from the steady state 1-D decompression melting profiles, with uniform random noise imposed over the top. The maximum amplitude of the random fluctuations is $\varepsilon_\phi = 0.05$. 121

5.4 1-D column models shown for $t = 10$ in model time. (a)-(e) show results for decompression melt models. The dashed lines correspond to 'closed-system' batch melting where we have set $K = 0$. (f)-(j) show results for the fluxed inflow models. These do not reach steady state due to the sustained flux of melt on the bottom boundary. Profiles at $t = 2, 4, 6, 7, 8, 9, 10$. 123

5.5 Schematic illustration of the additional component of flux melting driven by transport of melt relative to the solid matrix (i.e. open-system melting). Pressure decreases vertically on the y-axis and the x-axis is the concentration of a component k in the melt. The black lines show two examples of the equilibrium concentration of component k in the melt. Melt must react with the surrounding solid to maintain equilibrium as it ascends, with the additional component of flux melting given by Γ_f^{open}. The degree of flux melting therefore increases with solubility gradient and melt velocity. 125

5.6 Analysis of reaction rates for 1-D melting columns. Plots (a) and (c) show the net reactive mass transfer into/out of each phase Γ_i and the reactive mass transfer of silica into/out o the melt Γ_f^q for melting columns with an upwelling rate of 4 cm yr^{-1}. Peritectic reaction corresponds to $\Gamma_{ol} > 0$. The dashed lines are for closed system batch melting ($K = 0$) and the solid lines are for open system melting. (b) and (d) show the relative contribution of flux melting to the total melting rate for different W_0. For decompression melting this is independent of W_0, but for the fluxed inflow models it increases as W_0 decreases. 126

5.7 Time evolution of static ($W_0 = 0$) fluxed inflow model. The orthopyroxene field is the modal opx in the solid residue. Channels emerge pervasively through the melting region. Melt influx produces a thick dunite layer at the top of the domain. 128

5.8 Cross section of the 2-D fluxed inflow model at $P = 0.4$ GPa and for $t = 593$ kyr. Plotted are ϕ_{opx}, ϕ_f, c_f^q and nondimensional melt flux magnitude $\boldsymbol{q}$ and melting rate Γ_f. 130

5.9 (a) Porosity field and (b) cross section of 2-D decompression melting model for $W_0 = 4$ cm yr^{-1}. For the reference parameters no channelization is observed. 131

5.10 (a) Porosity field, (b) modal opx, and (c) cross section with renormalized fields for the fluxed inflow model with $W_0 = 1$ cm yr^{-1}. The position of the cross section is shown by the dashed line in (a). 132

5.11 Dimensionless compaction pressure $\mathcal{P}$ field for the static fluxed inflow model at $t = 512$ kyr. blue and beige colors show compacting regions and dark red colors show decompacting regions. Porosity contours are plotted over the top. 134

5.12 Snapshots of melt flux at (a) 512 kyr and (b) 638 kyr for the 2-D static fluxed infow model showing evolution in channel morphology over time. (c) Modal proportion of olivine in the solid residue at 638 kyr preserves a time-integrated record of melt transport. 135

C.1 Schematic sketch of the open batch reactor. Heterogeneous reaction R_j and heat production Q^I occur within the system, while boundary heat flux Q^E and the advective mass fluxes Ψ_i^{in} and Ψ_i^{out}, into and out of the system respectively, allow it to exchange heat and mass with the surroundings. As the system expands it does work on the environment at a rate W 165

List of Tables

3.1 Data Sources for Mg_2SiO_4–SiO_2 melt calibration 61

4.1 Parameters, definitions, and reference values for batch reactor models 76

4.2 Parameters, definitions, and reference values for reaction-diffusion models . . 89

4.3 Dimensional parameters, definitions, and reference values 95

4.4 Scaling parameters and non-dimensional numbers, definitions, and values . . 95

5.1 Parameters, definitions, and reference values 122

Acknowledgements

Doing a PhD is a very hard thing. Much harder than I expected in fact, and in very different ways. It goes without saying that it would not have been possible without the support and guidance of many wonderful people.

My first thanks goes to my advisor Marc Spiegelman. Marc has been instrumental in all of the work presented here. He has taught me a lot during my time at Lamont about melt transport and numerical modeling, but most importantly about the philosophy of modeling: "All models are wrong, but some are more useful than others". Thank you for always being game to talk Science and for your remarkable willingness in helping me work through the myriad computational issues. Most of all though, thank you for being patient with me through the ups and downs, and for tolerating the many many rabbit holes (I maintain that they were mostly interesting, if sometimes irrelevant). I would also like to thank the rest of the Committee-men: Peter Kelemen and Ben Holtzman. Thanks to Peter for the amazing field experiences in Oman, Trinity and the Josephine. And thanks to both Peter and Ben for the many meandering discussions from the thermodynamics of grain boundaries to pyroxenites-the-size-of-Manhattan, and back again.

I cannot imagine my time in New York without the wonderful friends I've made there. My love and thanks go, in particular, to Maayan Yehudai – who's been my rock – and to the rest of the Miami gang: Bar Oryan, Carly Peltier and Leah Werier. New York will always be tinted with our shakshuka brunches and living room pyjama discos. To Shailee Shah, my roommate, who made home feel like home. To Anna Barth and Henry Towbin, my comrades in high-T geochemistry; its been a blast. Henry I will never forget the elephant seals. And to the many others with whom I've shared such wonderful memories.

Lamont has been a stellar place to do a PhD. I've been inspired by the outstanding

breadth of research being done here, and the constant exposure to new ideas. More than anything though my time has been influenced by the community at Lamont. I cannot overstate the role that the Gender and Diversity coffee hour, and the organic community of students and postdocs that developed around it, has had on my experience. Thank you for your dedication in chipping away at some of those systemic barriers. A huge thank you to Kuheli Dutt and Maayan for all their work and leadership in this. I am also grateful to Terry Plank and Einat Lev for their encouragement and guidance, and the rest of the magma reading group for creating that lab-group vibe that I craved. My experience of Lamont would not have been the same without the friendly and steady presence of my wonderful office mates Juan Carlos De Obeso and Laura Haynes. The DEES administration have also provided fantastic support and I'm particularly thankful to Goran Ekstrom, Kaleigh Matthews and Carol Mountain for providing empathetic ears through some of the rough spots.

Much of my research has been tied to the ENKI project and I feel very lucky to have got to know the fun and dynamic group of people who have been part of this. For this I am particularly thankful to Mark Ghiorso and Aaron Wolf, for making it all happen and for the many insightful conversations. The ENKI workshops and the numerous mini-meetings were some of the most intellectually stimulating parts of my PhD experience. I am also thankful to Cian Wilson, who was involved in these meetings and who helped me with TerraFERMA on numerous occasions, and Owen Evans who sunk a significant amount of his time into developing the codegeneration tools that I have used in a lot of the models in this thesis.

This last year has been a bizarre one with the pandemic sweeping me back to the UK. I would never have imagined I'd be writing this from my childhood bedroom and I am so unbelievably grateful to have had the support of my family and my lovely friends over here. You will all be thrilled that you no longer have to ask me that daunting question "... so how is the PhD going?", or to pretend you have any interest, at all, in rocks. Thanks also to Team Rainbow who've been with me since we were all just embryonic geologists, and who's consistent mocking and good humour have reminded me to never take this job too seriously.

Entropy is the price of structure.

ILYA PRIGOGINE

Chapter 1

The Need for an Integrated modeling Approach to Fluid and Magma Transport

1.1 Introduction

The cycling of energy and chemical components between Earth's interior and the surface is driven by large scale mantle convection. Tectonic motions drive subducting plates into the mantle, forming the down-going limbs of large-scale convection cells (e.g. Forsyth and Uyeda, 1975; Hager and O'Connell, 1981) with a return upward flow in hot buoyancy-driven mantle plumes (e.g. Morgan, 1971; Davies and Richards, 1992), and through passive upwelling of the upper mantle beneath mid-ocean ridges. Ascent and descent of rocks in these large-scale flows drive phase transformation and heterogeneous reaction as phase assemblages evolve to maintain chemical equilibrium. Partial melting of peridotitic mantle beneath mid-ocean ridges, subduction zone arcs, and hotspot volcanoes is a primary response to this internal dynamism. Terrestrial magmatism produces new igneous crust and conveys volatile elements between Earth's interior and the atmosphere, constituting a fundamental mode of chemical differentiation on Earth. In tandem with subduction of oceanic lithosphere, it is responsible for maintaining a stable surface environment over geological time (Hirschmann, 2006; Dasgupta and Hirschmann, 2010). Understanding the melting process, including the physical mechanisms by which melts are transported to the surface, is therefore crucial to understanding the geochemical and geodynamic evolution of the Earth system.

Mantle melting is an inherently open-system process. In the convecting mantle incipient melts segregate from their source by concurrent compaction of the solid matrix and buoy-

ant ascent of partial melt through an interconnected porous network (Scott and Stevenson, 1984; McKenzie, 1984; Fowler, 1985). As magma encounters new pressure and temperature conditions, it reacts with the surrounding solid residues in order to maintain chemical equilibrium. The major and trace element compositions of primary basalts are therefore reflective of both the initial melting conditions and the subsequent melt-rock reactions. As the degree to which magma interacts with rocks on ascent is modulated by the transport mechanism (e.g. Spiegelman and Kenyon, 1992; Kelemen et al., 1997) consideration of the physics of melt extraction is integral to mantle melting models. At the same time, reaction feeds back into the transport dynamics by modifying the porosity, permeability and material properties of the rock (Aharonov et al., 1995, 1997; Spiegelman et al., 2001; Schiemenz et al., 2011; Katz and Weatherley, 2012; Weatherley and Katz, 2012; Jordan and Hesse, 2015; Keller and Katz, 2016). The complex interplay between reaction and transport produces a number of non-linearities which play a key role in the emergent behaviour of the system as a whole. A major goal toward understanding mantle melting is therefore to develop integrated models that consistently couple both the petrology and geodynamics of melting and melt extraction.

Coupling between reaction and transport is not restricted to basaltic melts within melting regions. Within most settings of melting, on rising through the hot convecting mantle, magmas encounter the cool thermal boundary layer at the base of the lithosphere. Here, reactive crystallization in response to the conductive geotherm can result in melt ponding or impregnation of the mantle by diffuse porous flow (Dick, 1989; Elthon, 1992; Boudier and Nicolas, 1995; Dijkstra et al., 2003). However, it likely also plays a role in driving hydrofracture and the formation of lithospheric dykes (Kelemen et al., 1995b; Aharonov et al., 1997; Korenaga and Kelemen, 1997). Reactive transport is increasingly recognized as an important mechanism for fractionation in the lower crust (Jackson and Cheadle, 1998; Jackson et al., 2003; Solano et al., 2012, 2014). This is particularly the case beneath magmatic arcs where large regions of the lower arc crust have been suggested to exist, either intermittently or perpetually, in a mush-like state (Annen and Sparks, 2002; Annen et al., 2005; Cashman

et al., 2017). The importance of coupled reactive transport further extends to fluid migration within subduction zones where fluid transport and fluid-rock reaction across the slab mantle interface are both controlled by the intense deformation and chemical disequilibrium in this region (e.g. Davies, 1999; Wilson et al., 2014; Plümper et al., 2016). All of these scenarios describe open system processes where reactive fluids mediate the exchange of chemical components between major Earth reservoirs including the convecting mantle, lithospheric mantle, lower crust, and surface environment. Moreover, in each scenario reactive fluid flow strongly influences the chemical, thermal, and mechanical state of the system. While the processes mentioned here span a significant range in thermal and mechanical regimes, and involve a variety of fluids, from high temperature aqueous fluids to silicate melts, they can all be considered within a consistent conceptual framework of reactive fluid flow in a deformable multiphase solid matrix. Coupled reactive flow also extends to low temperature hydrothermal and metamorphic fluid flow. The geochemical consequences of aqueous reactive transport in these settings has been extensively studied (Lichtner, 1985; Steefel and Lasaga, 1994; Ferry and Gerdes, 1998). In this thesis I therefore focus on high-temperature reactive transport phenomena associated with igneous processes with particular emphasis on feedbacks between reaction and transport.

Partial melting and fluid dehydration proceed at the grain-scale with fluids segregating from their source by concurrent buoyant porous flow of the fluid phase and compaction of the solid residue. A continuum formulation describing coupled multiphase flow was laid out by several workers in what are often referred to as the compaction equations (McKenzie, 1984; Scott and Stevenson, 1984; Fowler, 1985). Much of the debate around melt and fluid transport in the upper mantle and lithosphere has focused on whether transport occurs by diffuse porous flow or by rapid transport in localized channels. These endmember modes of transport entail very different degrees of chemical interaction between the fluid and surrounding rock. Diffuse grain-scale porous flow allows for extensive reaction and equilibration between melts and the surrounding solid matrix. Rapid channelized flow, on the other hand, permits

less extensive interaction and, depending on the scale of the channels and the rate of melt transport within them, can preserve disequilibrium between the melt and matrix (Spiegelman and Kenyon, 1992; Hart, 1993). Channels can take the form of melt-filled fractures or high-permeability porous channels. Within the high-temperature asthenosphere viscous deformation dominates, and channelization is thought to primarily occur in the form of porous channels (Kohlstedt and Holtzman, 2009). This is supported by the occurrence of replacive dunites in the mantle sections of ophiolites (Kelemen et al., 1995a). However hydrofracture within high-flux regions of the asthenosphere cannot be ruled out based on field evidence (Sleep, 1988; Kelemen et al., 1997). In the conductive boundary layer in the lithosphere, cooler temperatures allow hydrofracture and melt tranport in melt-filled fractures (Spence and Turcotte, 1985; Keller et al., 2013). There is abundant evidence for this in ophiolites and orogenic peridotites through the occurrence of pyroxenite and gabbro dikes and veins (e.g. Boudier and Coleman, 1981; Quick, 1981; Shervais and Mukasa, 1991). Hydrofracture is also an important mechanism within subducting slabs, and may additionally play a role in transporting fluids within the mantle wedge (Davies, 1999; Pirard and Hermann, 2015; Plümper et al., 2016).

Reaction and transport are nonlinearly coupled through physical rock properties. This includes thermodynamic properties—including density, heat capacity, entropy and expansivity—which depend on the mineral and melt assemblage; and bulk material properties—including permeability, bulk and shear viscosity, and diffusivity—which depend on both the phase assemblage and geometric factors such as the rock microstructure. Melt has a weakening effect on partially molten regions with experimental studies indicating that viscosity decreases exponentially with melt fraction (Kohlstedt and Zimmerman, 1996; Kohlstedt et al., 2000; Zimmerman and Kohlstedt, 2004). The rheological feedback can produce meso-scale high-porosity shear bands in response to local stresses (Stevenson, 1989; Holtzman et al., 2003; Spiegelman, 2003; Katz et al., 2006). The rheological effect of melts and fluids has also been considered in the large-scale context of plate boundary dynamics (e.g. Gerya and

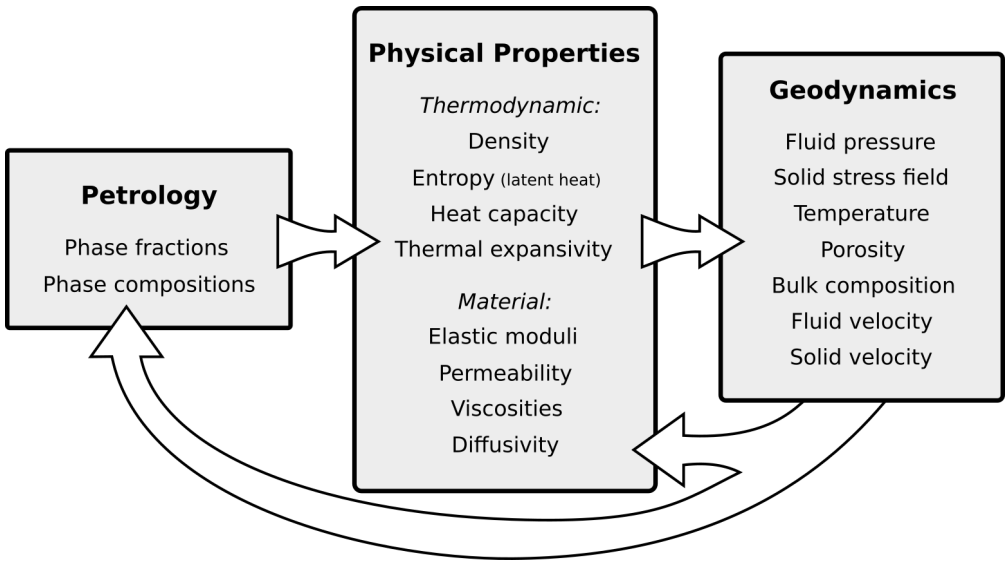

Figure 1.1: Schematic figure illustrating the components of the coupled model. The grey shaded boxes show the inputs of each model component, and the boxes below give examples of useful outputs. The arrows illustrate how variables are passed from one model component to another.

Meilick, 2011; Wilson et al., 2014). Over and above the presence of melts, further feedbacks arise from reaction between melts and their host rocks. It has frequently been suggested that reaction plays a role in driving melt channelization, either through coupling with the permeability structure (e.g. Aharonov et al., 1995, 1997; Spiegelman et al., 2001; Plümper et al., 2016), or via hydrofracture in response to reaction-induced density changes (Miller et al., 2003; Malvoisin et al., 2015; Evans et al., 2018, 2020). Understanding the different transport mechanisms above therefore requires consideration of melt-rock reaction. Feedbacks between multiphase reaction and transport are chiefly associated with the following properties:

1. **Density:** Melting and dehydration are associated with a decrease in bulk density. The resulting bouyancy force drives melts towards the surface, and if retained within pore spaces can result in diapirism (Jha et al., 1994). Reactive density changes also produce local pressure variations (increasing during melting/dehydration and decreasing during crystallization/hydration). Depending on the rheology of the matrix this may have the potential to drive hydrofracture.

2. **Viscosity:** Melts and fluids have dramatically lower viscosity than the solid residue. Increases in porosity therefore result in decreases in the bulk and shear viscosity of the multiphase aggregate. Local reductions in pressure due to the rheological weakening can further promote a reactive feedback as more melt is drawn in to the region. Volatile components, which preferentially enter melts and fluids, also have a profound impact on solid rheology. Hydration reduces solid viscosity, promoting deformation and potentially providing a conduit for further fluid and melt transport, for example in the hydrated subduction channel above subducting plates (Hebert et al., 2009; Gerya and Meilick, 2011). Whereas dehydration can result in embrittlement of the solid residue (Murrell and Ismail, 1976; Raleigh and Paterson, 1965; Green and Houston, 1995; Jung et al., 2004).

3. **Entropy:** The release and absorption of latent heat modulates temperature which can influence transport dynamics through the solid rheology. For example heat released during crystallization at the lithosphere-asthenosphere boundary has been suggested to cause thermal erosion and drive focusing of melt beneath continental rifts (Accardo et al., 2020; Hopper et al., 2020) and subduction zone arcs (England and Katz, 2010).

4. **Permeability:** All else being equal, we expect that permeability increases with porosity. If the resultant increase in melt flux enhances dissolution, then a positive feedback can ensue producing a reaction-infiltration instability. If melt or fluid flow is accompanied by crystallization, the feedback becomes negative: melt flux closes off porosity and so promotes diffuse porous flow or the formation of an impermeable reactive front.

The reaction-permeability feedback has been a particular focus of attention in studies of magma dynamics. Reactive dissolution of pyroxene and crystallization of olivine during adiabatic ascent of melt beneath mid-ocean ridges increases porosity and permeability (Kelemen, 1990). The resulting local increase in melt flux drives further reaction, and it has been suggested that this could lead to a reaction infiltration instability that focuses melt into the

high permeability channels. These are thought to be represented by dunite channels observed in ophiolites (Aharonov et al., 1995; Kelemen et al., 1995a). Reactive channelization has been the subject of numerous modeling and experimental efforts (Aharonov et al., 1997; Spiegelman et al., 2001; Hewitt, 2010; Liang et al., 2010; Schiemenz et al., 2011; Weatherley and Katz, 2012; Keller and Katz, 2016). While studies often focus on individual feedback mechanisms, in natural petrological systems all of the above feedbacks operate simultaneously, and interact with one another. Consistent coupling of reaction and transport that accounts for reactively induced changes in physical properties is therefore important.

Such feedbacks can be put in the broader context of coupling between petrology and geodynamics. Similar coupling between phase change and dynamics also operates in subsolidus regions and can have significant consequences on mantle dynamics both at the large- and small-scale. The relative change in density of a subducting slab and the surrounding peridotitic mantle with increasing pressure, for example, determines whether a subducting slab will stagnate at the transition zone or penetrate through to the lower mantle (King et al., 2015; Goes et al., 2017). Likewise, the long-term stability of large low-shear velocity provinces at the core-mantle boundary requires a fine balance between the thermal expansivity and the compressibility of the accumulated material (Burke et al., 2008). Feedbacks are particularly strong within partially molten and fluid-saturated regions as melting and dehydration are accompanied by dramatic changes in physical properties.

Thermodynamics provides a consistent unifying framework linking petrological phase assemblages with their thermochemical and physical properties. Inclusion of thermodynamics in geodynamics therefore presents a powerful tool for coupling petrology with descriptions of multiphase reactive transport. Self-consistent thermodynamic databases of minerals, melts, and fluids, parameterized from relevant thermochemical data and phase equilibrium experiments, are now available for a range of pressure-temperature-composition (P-T-X) conditions (Berman, 1988; Holland and Powell, 1998, 2011; Stixrude and Lithgow-Bertelloni, 2005; Stixrude et al., 2011). In addition to self-consistently describing thermodynamic properties

of a given phase assemblage, including the equation of state and the heat capacity, equilibrium assemblages can be calculated from these thermodynamic databases using appropriate energy minimization algorithms (e.g. Connolly, 2005; Ghiorso, 2013). Computational thermodynamics has the benefit over other parameterizations of melting or crystallization (e.g. McKenzie and Bickle, 1988; Katz et al., 2003) in that they allow for more reliable interpolation and extrapolation between experimental constraints.

Until recently, computational thermodynamics has largely evolved in isolation from computational geodynamics. This historic divide has emerged from two separate communities within the geosciences. It can also be viewed as a pragmatic move to reduce what is a very complex system down into numerically tractable sub-problems, and has permitted a lot of progress to be made on both sides. Petrological models are based on considerations of uniform batch systems. Forward models and interpretations of observed phase assemblages often assume endmember dynamic behaviour such as batch or fractional melting and crystallization. Some approximation of open-system processes can made using variable fluid-rock ratios or with models including assimilation fractional crystallization (e.g. Kelemen, 1990; Lambart et al., 2012). However there is no description of the actual space- and time-dependent system dynamics. Conversely, geodynamic models of mantle melting have focused on the physics of melt segregation and transport. The continuum formulation of multiphase flow is based on the conservation of mass, momentum, and energy. The governing equations include closures to describe melt-rock reaction. However, when included, reaction is generally only considered in a parameterized and ad-hoc way. Furthermore, reactive transport models do not tend to self-consistently couple phase assemblages and other thermodynamic properties.

Without considering nonlinear couplings between reaction and transport, such approaches fail to capture emergent system behaviour. A mechanistic understanding of reactive transport processes in Earth's interior therefore requires a holistic modeling approach that consistently couples geodynamics and petrology. Furthermore, coupled approaches would aid better interpretation of field observations in places where open system reaction has played a

role. Inclusion of petrological models into space and time dependent dynamic models provides a framework for interpreting structural petrological features, such as reaction zones, where spatial relationships between rock assemblages are key to understanding system behaviour.

1.2 Open questions on Open systems

Integrated modeling approaches are key to a host of open questions in petrology and geodynamics. Mid-ocean ridges are the best understood geodynamic settings of mantle melting. Here, the solid mantle upwells adiabatically and undergoes pressure-release melting. Polybaric partial melts segregate from their source and bouyantly ascend to the surface where they are emplaced at the surface over a narrow zone of crustal accretion. Various lines of evidence indicate that mid-ocean ridge basalts (MORBs) are not in equilibrium with the uppermost residual mantle (Stolper, 1980; Elthon and Scarfe, 1984; Johnson et al., 1990); most notably, MORB is undersaturated in orthopyroxene. This observation is often accounted for in geochemical models as fractional melting (e.g. McKenzie and Bickle, 1988). Maintaining this disequilibrium in practice requires efficient segregation at small melt fractions and rapid channelized melt transport (Spiegelman and Kenyon, 1992). It is thought that this occurs through macroscale high-porosity channels corresponding to dunite bodies observed in ophiolites, which are in chemical equilibrium with MORB (Kelemen et al., 1995a, 1997). However, there remain significant questions concerning the relative role of reactive and rheological feedbacks in channel formation, the controls on channel morphology, locations of channel initiation, and the effect of the energetics of melting, among other things. Further questions also remain on the role of enriched pyroxenitic domains within mantle melting regions. Geochemical data from primitive basalts from mid-ocean ridges and subduction zones are often interpreted in terms of linear mixing between deep silica-rich pyroxenitic melts and peridotitic melts (e.g. Sobolev et al., 2007; Shorttle et al., 2014). However, such interpretations do not account for reaction and re-equilibration of pyroxenite-derived melts

with the enclosing peridotite during ascent (Yaxley and Green, 1998; Yaxley, 2000; Lambart et al., 2012).

Other geodynamic settings of mantle melting involve more complex lithospheric and crustal processing, and elucidating the melting regime and transport processes is more difficult. Beneath hotspot volcanoes including Hawaii and the Basin and Range Province, melting and transport in the convecting mantle may be similar to that beneath mid-ocean ridges. However Mg-Si thermobarometry records equilibration depths corresponding to the lithosphere-asthenosphere boundary (Ferguson et al., 2013; Plank and Forsyth, 2016), suggesting that melts either ponded at this depth or were transported by diffuse porous flow up to this level, before being rapidly transported to the surface in lithospheric dykes (e.g. Havlin et al., 2013). The transition from porous flow to dyking is difficult to model within a continuum framework (Keller et al., 2013) and is currently an active area of research. The role of reactive crystallization in modulating the pressure field (Aharonov et al., 1997; Korenaga and Kelemen, 1997) and the rheological response within this region remain open questions.

In subduction zones melting occurs through a combination of decompression and flux melting due to the introduction of volatile slab components. There remains substantial debate regarding the specific mechanism of material transport from the slab to the hot corner of the mantle wedge. The leading model involves fluid-mediated mass-transfer from dehydration of altered oceanic crust and sediment melting (Tatsumi et al., 1986; Plank and Langmuir, 1993; Manning, 2004). The fluids are thought to transmit the characteristic trace element signature of arc magmas including enrichment in light rare earth elements and large ion lithophile elements (Kay, 1984; McCulloch and Gamble, 1991). However, the slab-mantle interface represents a major geochemical gradient, and it is unclear how fluids are effectively transferred from the slab to the locus of melting within the mantle wedge without being heavily modified or assimilated by their interaction with the surrounding peridotite. One explanation of this is that fluids extensively metasomatize the overlying mantle wedge such

that residual fluids can flow through without further modification (Tatsumi et al., 1986; Malaspina et al., 2006). Another explanation is that fluids are transported by focused flow through hydrofractures (Davies, 1999; Pirard and Hermann, 2015; Plümper et al., 2016). Alternatively, recent measurements of the hydrous peridotite solidus suggest melting may begin directly above the subducting slab (Grove et al., 2006; Till et al., 2011). As flux melting is an open-system process, the subsequent melting and reactive melt transport within the hot mantle wedge also require coupled approaches to modeling reaction and transport.

While theories of multiphase flow initially emerged within the mantle dynamics community, reactive porous flow is increasingly being considered as an important feature in crustal magmatic systems. In volcanic arcs it has been suggested that the majority of crustal differentiation occurs in lower crustal "hot zones" (Annen and Sparks, 2002; Annen et al., 2005; Cashman et al., 2017). Here, intermediate and silicic magmas are generated by crystallization of mantle derived melts coupled with partial melting of the crust (e.g. Hildreth and Moorbath, 1988). Chemical differentiation of arc magmas is therefore an open-system process that is strongly modulated by factors that regulate melt-solid interaction including melt flux, intrusion geometry and the mode of magma migration. Arc crust is compositionally, thermally and rheologically heterogeneous on a range of scales. The upper crust is dominated by brittle processes, whereas high temperature regions in the lower crust below established magmatic systems are likely dominated by viscous processes. In these regions porous flow could have a major control on magmatic architecture (Solano et al., 2012; Jackson et al., 2018). Crustal magmatic systems are complicated by displaying significant temporal and spatial variations in porosity. While the idea of cold-storage, in which much of the lower crust is postulated to exist in a mush-like state (e.g. Cashman et al., 2017), is increasingly recognised as important, there are intervals of time when pockets of high melt fraction must exist (e.g. Cooper and Kent, 2014). As these melt pockets exceed the disaggregation threshold for a two-phase system, continuum models that span the transition from porous flow to a melt suspension are required (Keller and Suckale, 2019). Calls for integrated modeling

approaches for arc magmatism therefore need to be tempered with the requirement for general theories that can account for this rheological diversity. The upshot of this complexity is that any particular modeling approach is likely to be restricted to a particular region of the crustal magmatic system. Significant advances in theoretical approaches are required before trans-crustal multiphase dynamic models become a reality.

1.3 Previous approaches to coupling reaction and transport

The principle barrier to coupled approaches is the sheer complexity of non-isothermal multiphase multicomponent reaction within a deformable matrix. A typical upper mantle lherzolite comprises twelve major chemical components and up to five phases, the relative abundances and compositions of which change continuously as a function of pressure, temperature and bulk composition. Tracking these changes within space- and time-dependent geodynamic models is challenging, particularly in open systems in which the bulk composition changes continuously.

One approach for managing the complexity of coupled models has been to use simple parameterized models of mantle melting. Early studies investigating melt segregation from the convecting mantle modeled reactive dissolution and precipitation by imposing fixed solubility gradients in one component isothermal systems (Aharonov et al., 1995, 1997; Spiegelman et al., 2001; Spiegelman and Kelemen, 2003). This was extended by later studies that included a proper treatment of the energetics of reaction by assuming chemical equilibrium, and using parameterized phase diagrams, involving a melt and a homogeneous solid, to approximate mantle melt productivity (Šrámek et al., 2007; Katz, 2008; Hewitt, 2010; Katz and Weatherley, 2012; Weatherley and Katz, 2012). More recently, this parameterized approach has been generalized to allow for disequilibrium between the melt and solid residue (Rudge et al., 2011; Keller and Katz, 2016; Keller et al., 2017). Unlike models of magma dynamics in the mantle, which have been simulated in multiple dimensions, reactive transport in the lower crust has only recently been explored through numerical models. Existing parameter-

ized models of crustal reactive transport are limited to one dimension (Jackson and Cheadle, 1998; Jackson et al., 2003; Solano et al., 2012, 2014).

Parameterized melting relations can provide a reasonable approximation for the degree of melting and latent heat of fusion, and their inclusion in magma dynamics simulations has yielded important insights into the reaction-permeability-flux feedbacks that are responsible for melt channelization (Aharonov et al., 1995; Kelemen et al., 1995a). However, the melting parameterizations do not include a description of the mineralogical evolution of the residual mantle, or an accurate representation of the mineral-melt reactions. Melting of typical mantle lherzolite transitions from a pseudo-eutectic melting reaction at depth, to incongruent melting at lower pressure, in which olivine crystallization and melting occur concurrently (Walter, 1998). Exhaustion of residual phases, such as clinopyroxene and plagioclase, can also produce discontinuous changes in the melt productivity (Asimow et al., 1995; Hirschmann et al., 1999). Without accounting for such complexities, it is not possible to directly compare model outputs to assemblages observed in peridotite massifs, or to accurately forward model primary basalt composition; together these constitute our only direct observations of mantle melting preserved in the geological record. The sensitivity of the dynamics to details of the thermodynamics, such as the compositional gradient of the melt saturation surface and the latent heat, means that it is also not clear whether features, such as channels, observed in existing models would be reproducible if more realistic multiphase thermodynamics were included.

Another approach has been to directly solve for the equilibrium assemblages using equilibrium thermodynamic models (Hebert et al., 2009; Tirone et al., 2009; Tirone and Sessing, 2017; Tirone, 2018; Oliveira et al., 2018; Tirone, 2019; Oliveira et al., 2020). This is generally approached using a multi-step iterative process. First the equations describing the dynamics are solved; the equilibrium assemblage for the resulting pressure, temperature and bulk composition conditions is then calculated at every grid point and time-step by free-energy minimization, and the relevant variables, including the change in melt fraction, and

the updated densities, heat capacities, and entropies, are passed back to the dynamics code; and so forth. The difficulty with this approach is that multiphase free-energy minimization is computationally expensive. Minimization algorithms are also often based on the Newton method, meaning that convergence is not guaranteed (e.g. Ghiorso, 1985; Ghiorso and Sack, 1995), and additional measures must be put in place to ensure convergence (Tirone et al., 2009; Oliveira et al., 2018).

One way around this has been to use precalculated look-up tables (Dufek and Bachmann, 2010; Karakas and Dufek, 2015; Malvoisin et al., 2015). These have been widely used in convection simulations with constant bulk composition (Afonso et al., 2008; Babeykoa and Sobolev, 2008; Chen and Gerya, 2016). For closed system models such as these, where chemical equilibrium can be assumed, look-up tables likely present the most practical way forward. However this approach becomes intractable in open systems for which the dimension of the look-up table must increase to include the dimension of the compositional space. For this reason existing studies on open systems have been restricted to modeling transport of a single component.

The complexity of these problems therefore presents both a theoretical and computational challenge. Any general theory should self-consistently describe the phase assemblage, the thermodynamic properties and the dynamics, while also being general enough to be applied to a variety of thermodynamic systems and solid rheologies. In addition to a general tractable theory, a major roadblock has been the availability of appropriate interoperable software and robust numerical solvers that can deal with the various timescales of transport, reaction, and thermal and chemical diffusion. Computational tools in petrological thermodynamics and geodynamics have been developed separately with the purpose of serving very different scientific communities, mirroring the conceptual division between dynamics and petrology. To explore coupled thermodynamic-geodynamic problems going forwards there is a need for flexible and reproducible computational tools that allow integration of thermodynamic models into multiphysics problems.

1.4 The role of disequilibrium in the dynamics of Earth's interior

There is increasing recognition of the role of chemical disequilibrium in igneous and metamorphic processes. Magmas erupted at the surface commonly display a range of disequilibrium features including crystal zonation, resorption and mantling textures, metastable mineral assemblages, and trace element and isotopic disequilibrium (e.g. Davidson et al., 2007; Ganne et al., 2018). These features are generally attributed to open-system dynamic processes in the cool upper crust (Bachmann and Huber, 2016). Metastable mineral assemblages are also increasingly recognised during prograde metamorphism due to sluggish reaction kinetics (e.g. Carlson et al., 2015). Faster reaction can be expected at the high temperatures of the convecting mantle making the assumption of local equilibrium (Thompson, 1959; Hofmann and Hart, 1978) more applicable. However, the role of metastability has been increasingly acknowledged during geodynamic processes in Earth's interior. Metastability during olivine-group phase transformations (Iidaka and Suetsugu, 1992; Tetzlaff and Schmeling, 2000; Mosenfelder et al., 2001) in the low temperatures of slab interiors is one well-recorded example.

Consideration of equilibrium also requires a consideration of scale. The lengthscale over which equilibrium is maintained is controlled by the relative rates of reaction, mass transport and diffusion. Melt localization, in the form of veins, dykes, and porous channels, permits disequilibrium between melt and adjacent solid residue. There is abundant evidence for such features in mantle exposures. Indeed MORB composition requires macroscale disequilibrium between ascending melts and the mantle residue (e.g. Kelemen et al., 1997). As continuum approximations, geodynamic models are applied at much larger scales than those of small-scale melt localizations; with grid-sizes typically on the order of 10-1000 m. Reaction at this scale is therefore best approximated as a disequilibrium process, with the kinetics constrained from appropriate upscaling analysis.

Equilibrium thermodynamics has played a pivotal role in petrology: phase diagrams,

constrained from phase equilibrium experiments, have long provided a framework for understanding the petrogenesis of igneous and metamorphic rocks; equations of state have allowed us to project the properties of geologic materials to high pressures and temperatures in Earth's interior; and partitioning relations of trace elements have provided a tool for understanding fractionation processes and isotope systematics allowing us to explore these processes back in time. More recently, computational thermodynamics has opened up the possibility to forward model equilibrium phase assemblages and reaction paths. However, equilibrium thermodynamics is restricted to idealized reversible processes whereby the system evolves via a sequence of equilibrium states. The time-dependence of processes involved are not accounted for.

Non-equilibrium thermodynamics, which was developed over the course of the mid 20th century by workers including Onsager and Prigogine, extends the second law of thermodynamics to include irreversible processes (Onsager, 1931a; Prigogine, 1961, 1967). In allowing for irreversibility and time-dependence, non-equilibrium thermodynamics shifts thermodynamics from a theory describing the state of systems to one describing system evolution. The basic premise of classical irreversible thermodynamics is that thermodynamic fluxes are related to driving forces through linear phenomenological relations: for example Fick's law of diffusion relating chemical diffusion to chemical gradients. Irreversible entropy production is then related to the product of forces and fluxes. Empirical evidence demonstrates that thermodynamic forces and fluxes, such as thermal and compositional diffusion, are coupled. In the linear limit this coupling is described by the Onsager reciprocal relations (Onsager, 1931a). Non-equilibrium thermodynamics has lead to a plethora of studies across fields from biology to chemical engineering. There has been particular interest in how dissipative processes in open systems lead to self-organization (Prigogine and Nicolis, 1967; Prigogine and Lefever, 1968; Prigogine and Glansdorff, 1973). Such emergent structures are widespread in the geological sciences (Fowler, 1985), being responsible for river networks, mountain belts, fracture networks, crystal zonation and layered reaction zones. In petrology non-equilibrium

thermodynamics has been applied to the study of small-scale coupled phenomena such as Soret diffusion in silicate melts (e.g. Walker and DeLong, 1982), crystal zonation (e.g. Allègre et al., 1981) and diffusive reaction zone growth (e.g. Fisher, 1973; Joesten, 1977). However, a systematic theoretical framework and computational infrastructure for modeling irreversible heterogeneous reaction in igneous and metamorphic systems has yet to be developed. Existing computational thermodynamic tools have instead largely been geared towards equilibrium calculations.

Following de Groot and Mazur (1984) and Prigogine (1967), extension of computational thermodynamics to non-equilibrium processes can be made by treating chemical reaction as an irreversible process in which reaction rates are a function of the chemical affinities. Irreversible entropy production is then self-consistently expressed as the product of reaction rates and chemical affinities. This approach has the benefit of implicitly accounting for the time-dependence of reaction. Furthermore, as the extent of disequilibrium depends on the relative timescales of reaction, diffusion and mass transport it can be applied to both disequilibrium and equilibrium systems. Given an appropriate set of reactions, linear rate laws would also naturally drive the system to equilibrium, given sufficient time, thus removing the need for on-the-fly free-energy minimization. Non-equilibrium thermodynamics therefore presents a promising, and arguably more natural, way of including multiphase reaction into time- and space-dependent dynamic models. However, application of non-equilibrium thermodynamics to disequilibrium reaction has limitations. Firstly, it only describes phenomena on a macroscopic phenomenological level. Geochemical kinetics is a highly complex field, with heterogeneous reaction proceeding via a complex interplay of diffusion, mass transport, and surface reaction at the grain scale. Any macroscopic description unavoidably fails to capture the details of such small scale phenomena. However the kinetics in igneous and metamorphic systems are poorly understood and a detailed mechanistic description is rarely feasible. Secondly, classical irreversible thermodynamics is restricted to linear phenomenological relations. While this is applicable to kinetic rate laws close to equilibrium, further

from equilibrium reaction is characterized by non-linear rate laws. Description of multiphase reaction within a non-equilibrium thermodynamic framework does however tractably capture the macroscopic evolution of the system—including phase abundances, compositions and physical properties of the multiphase assemblage—close to equilibrium in a way that allows us to couple bulk petrological evolution with other dynamic processes.

1.5 Dissertation overview

In this dissertation I will present a thermodynamically consistent framework for integrating multiphase multicomponent thermodynamics and geodynamics. This work builds on previous formulations of magma dynamics, establishing the set of conservation equations for mass, momentum, and energy describing melt transport within a deformable porous medium. As my focus here is on the thermodynamic and reactive coupling, we describe the mechanics on a sufficiently general level that it can be applied to a range of rheological conditions. We refer to the significant body of work exploring multiphase transport for various mechanical regimes (Connolly and Podladchikov, 1998; Bercovici et al., 2001; Bercovici and Ricard, 2003; Rozhko et al., 2007; Keller et al., 2013; Evans et al., 2018, 2020). The most significant modification to the conservation equations is the extension to multiple thermodynamic solid phases, which together behave as a single mechanical phase. The thermodynamic and reactive coupling is based on the theory of non-equilibrium thermodynamics (Prigogine, 1967; de Groot and Mazur, 1984), whereby the reactive system is rephrased in terms of an independent set of stoichiometric reactions. This permits modeling of both quasi-equilibrium and disequilibrium reaction within a multiphase assemblage while avoiding the need for pre-calculated look-up tables or on-the-fly energy minimization. I will present reactive formulations for modeling melt-mediated, fluid-mediated and subsolidus reaction to extend applicability to a range of geological processes. This general theory is presented in chapter 2.

Implementation of any physical model requires suitable computational infrastructure. In parallel with the theory and application described here is an ongoing software development

as part of the ENKI project (http://enki-portal.org/). A principal aim of this project is the development of flexible and modular themodynamics and kinetic modeling software targeted at integrating thermodynamics into geodynamics models. The work in this dissertation has both informed and been supported by this effort. A very brief outline of the software components used in this work is included in chapter 2.

A further goal of this dissertation is to map out a workflow demonstrating how this theoretical framework is applied to a problem of geological interest. Here I focus on reactive melt transport beneath mid-ocean ridges. The various stages of this workflow are presented in chapters 3 to 5. Firstly, in chapter 3 I describe the calibration of the Mg_2SiO_4-SiO_2 binary system. This simple system served as a good first-order analogue for eutectic and peritectic mantle melting. In particular it captures the gradient in silica content of basaltic melts with decreasing pressure, which has a significant impact on reactive behaviour of ascending melts. As our goal is to demonstrate the coupling between eutectic and peritectic melting and melt transport, rather than to accurately capture all details of the phase diagram, we calibrate the melt solution using a simple asymmetric regular solution model. In chapter 4 I test the model by applying it to a range of simple problems exploring disequilibrium reaction and open-system melting. These problems are divided into those looking at non-isothermal disequilibrium batch reaction path models, and dynamic models coupling reaction with mass diffusion and poro-viscous transport. Disequilibrium reaction paths are often non-intuitive and this hierarchy of models permits exploration of the various assumptions and model parameters used. This exploration is a prerequisite for any complex multiphysics problem. Finally, in chapter 5 I apply this framework to 2D models of reactive channelization and the formation of dunite channels in the Mg_2SiO_4-SiO_2 binary system. This is the first model of reactive transport in a eutectic or peritectic reactive system and allows us to more accurately describe the melt-rock reactions during melt ascent. Our findings corroborate previous models using simpler parameterized melting relations, that channel initiation likely requires some additional flux of melt. This could be from focusing of melt towards the ridge

axis, or from deep hydrous melting or melting of enriched heterogeneities at depth.

The kinetic and thermodynamic coupling is described here on a general level and therefore could be applicable to a range of multiphase systems with arbitrarily complex multiphysics coupling. Our emphasis while setting up the theory and in the model examples has been on poro-viscous dynamics relevant to magma dynamics in the the asthenosphere. Application to other rheological conditions and reactive systems will likely entail many different theoretical and numerical challenges. As it is difficult to predict what these will be, the basic theory presented here is far from complete and should rather be viewed as a skeleton on which later adaptations and extensions can grow.

Chapter 2

A Tractable Kinetic Framework for Coupling Computational Thermodynamics and Geodynamics

2.1 Introduction

Many important problems in Earth sciences can be described by multiphase, multicomponent reactive porous transport in a deformable, permeable solid matrix. This includes melt transport within the asthenosphere and lithosphere beneath mid-ocean ridges, subduction zones, continental rifts and interplate volcanoes; as well as transport of aqueous fluids within subducting slabs and in the overlying mantle wedge. These phenomena have proven extremely difficult to model due to the complexity of both the mechanical and thermochemical processes involved. Partial melting and crystallization are strongly coupled to the both the thermal structure and mechanical behaviour of these regions. Furthermore, chemical reactions between melts and fluids and the surrounding rocks modify the permeability structure of the solid matrix resulting in feedbacks between transport and reaction. Despite these various couplings, the thermodynamics and dynamics of multiphase flow are often treated in isolation. This has largely been a pragmatic move to reduce what are very complex systems down into numerically tractable sub-problems, and has permitted a lot of progress to be made on both sides. However, furthering our understanding of terrestrial magmatism and geodynamics increasingly calls for a more holistic approach.

Dynamic modeling approaches are based on the continuum formulation of two-phase flow describing the coupled porous flow of the melt within a viscously compacting solid matrix (McKenzie, 1984; Scott and Stevenson, 1984; Fowler, 1985). These equations are derived via

conservation of mass, momentum, and energy, along with a set of appropriate constitutive relations. The original formulations assumed viscous deformation of the host rock, however these have since been extended to include elastic (Evans et al., 2018, 2020), visco-elastic (Connolly and Podladchikov, 1998; Omlin et al., 2018), and visco-elasto-plastic (Keller et al., 2013) rheologies, as well as the effects of surface tension and damage (Bercovici et al., 2001; Bercovici and Ricard, 2003). The two-phase flow equations are strongly non-linear and produce diverse behaviour. Early solutions focused on the formation of magmatic solitary waves (e.g. Scott and Stevenson, 1984; Spiegelman, 1993a; Wiggins and Spiegelman, 1995; Jordan et al., 2018), and the focusing of melt at mid-ocean ridges and subduction zones in response to solid flow fields (Spiegelman and McKenzie, 1987). Additional non-linearities are introduced by mechanical feedbacks which have been shown to focus melts into high-porosity shear bands (Stevenson, 1989; Holtzman et al., 2003; Spiegelman and Kelemen, 2003; Katz et al., 2006). As mechanical phenomena, much of this behavior can be examined purely from conservation of mass and momentum. Modelling the actual melting process, however, also requires conservation of energy (Hewitt and Fowler, 2008; Hewitt, 2010; Katz, 2008). This describes the thermal structure by accounting for the transport of heat by the melt and solid, the latent heat of melting and crystallization, as well as adiabatic terms due to decompression. Given an expression for melt productivity as a function of pressure and temperature (e.g. Katz et al., 2003), conservation of porosity, momentum and energy together provide a first-order description of adiabatic decompression melting. Such thermo-mechanical models have proven useful for exploring the large-scale geodynamics of plate boundaries (e.g. Katz, 2008; Wilson et al., 2014; Sim et al., 2020). However, these models generally neglect the compositional dependence of melting which has an important bearing on both the dynamics of melt extraction and the melting process itself. Variation in equilibrium melt composition with pressure causes partial melts to react with surrounding rocks during ascent. As melts reactively dissolve peridotite minerals, this results in an additional component of flux melting. Feedbacks between permeability and dissolution can also focus melts into high porosity

reactive channels (Aharonov et al., 1995). In subduction zones, flux melting from influx of hydrous slab components is the principal melting mechanism. Consistent treatment of melting across geodynamic settings therefore requires inclusion of both the thermodynamics and chemistry of melting.

Previous models exploring coupled reactive melt transport in the mantle have largely been motivated by the observation that mid-ocean ridge basalts (MORBs) are not in equilibrium with the shallow orthopyroxene-bearing mantle (Stolper, 1980; Elthon and Scarfe, 1984; Johnson et al., 1990). This has lead to the view that melt transport predominantly occurs by focused flow in high-porosity channels (Spiegelman and Kenyon, 1992). This is supported by the occurence of dunite bodies, which are in equilibrium with MORB, but surrounded by strongly trace-element depleted harzburgite, in the mantle section of ophiolites (Kelemen et al., 1995a, 1997). A suite of numerical studies and linear stability analysis have demonstrated that melt channelisation could be driven by a reaction infiltration instability arising from the reactive dissolution of pyroxene during melt ascent (Aharonov et al., 1995, 1997; Spiegelman et al., 2001; Spiegelman and Kelemen, 2003; Hewitt, 2010; Liang et al., 2010; Schiemenz et al., 2011; Katz and Weatherley, 2012; Jordan and Hesse, 2015; Keller and Katz, 2016; Rees Jones and Katz, 2018). However existing models have so far been restricted to simple parameterized phase diagrams involving a single solid and melt phase, which vary smoothly in composition between fictive endmembers. It has not been possible to include the eutectic and peritectc melting reactions within the current framework, and there are still questions as to whether reactive channelization can be initiated within a relatively uniform peridotitic mantle. Furthermore, by not dealing with multiple mineral phases it is not possible to capture the discontinuous changes in melting and crystallization rates that occur due to phase exhaustion (e.g. exhaustion of clinopyroxene during adiabatic decompression melting), phase saturation (e.g. crystallization of plagioclase during melt infiltration in the lithosphere), and solid phase transitions (e.g. the spinel-plagioclase transition). Inclusion of more complex thermodynamic systems, while also consistently coupling the dynamics to

the thermodynamic properties of the phase assemblage, would permit further exploration of other open system reactive processes including fluid transport and flux melting in subduction zones.

Multicomponent multiphase thermodynamics provides a consistent framework for coupling reaction and transport dynamics (Stixrude and Lithgow-Bertelloni, 2005; Poulet et al., 2010). In this work we develop a tractable theoretical framework for integrating computational thermodynamics and multiphase fluid dynamics. Our approach is based on the concepts of non-equilibrium thermodynamics in which reaction occurs via a set of explicit stoichiometric reactions. This allows us to model thermodynamic systems of arbitrary complexity, involving multiple mineral phases. We will describe reactive formulations that are suitable for modeling melt-mediated, fluid-mediated, and subsolidus reaction. As reaction is treated as an irreversible process alongside heat and mass transport it can be applied to systems both close to and far from chemical equilibrium as the extent of local disequilibrium depends on the relative timescales of reaction and mass transport. The reactive formulation is integrated with conservation equations for two-phase flow which are generalized to allow for multiple solid phases. This chapter is organized as follows: Section 2.2 gives an overview of the modelling approach. Section 2.3 derives the general conservation equations. Section 2.4 describes coupling to thermodynamic models and 2.5 describes the reactive framework. Section 2.6 briefly describes the supporting software. Finally, section 2.7 discusses potential applications and limitations of this modelling approach.

2.2 General system description

Here we will lay out a general formulation for describing advection, thermal and compositional diffusion, and reaction within a compacting multiphase medium. Like previous formulations we consider a system comprising up to two mechanical phases with distinct velocity fields — that is a multiphase solid and a melt or fluid. As a continuum approximation these equations apply to systems that adhere to the assumptions of generalized porous

flow in which the system size is much larger than the pore spacing within the permeability network. In the limit of zero porosity they reduce to the equations for a reactive single phase continuum.

We do not consider scenarios where both a melt and a fluid or vapor phase are present. Such a scenario may occur within subduction zones and is expected in upper crustal magmatic systems. A continuum approach to modelling magmatic systems of more than two phases has been formulated by Keller and Suckale (2019) and can be viewed as an extension of the dynamic model used here. As an extension to previous magma dynamics however, we incorporate a multimineralic solid. Individual minerals constitute thermodynamic phases which are defined by distinct free-energy functions, contrary to mechanical phases which are defined on the basis of their velocity field.

The chemistry is described by considering a general C-component system comprising N thermodynamic phases, including the melt or fluid and all minerals in the solid assemblage. Each phase i has a composition described by K_i phase endmembers which reflect the stoichiometry of that phase. The endmembers may represent linearly independent phase components, or non-independent solution species. Summing over all phases, there is a total of $K_{tot} = \sum_{i=1}^{N} K_i$ phase endmembers in the system. The endmembers are generally distinct from the system components, and in a reactive system we have the condition $K_{tot} > C$.

The average assemblage evolves via a set of J stoichiometric reactions each reacting at a rate R_j. Our reactive formulation is based on that of de Groot and Mazur (1984) who describe irreversible reaction between species in a homogeneous system. Here we extend this to reaction between phase endmembers in a multiphase heterogeneous system. Reactions may be either homogeneous (involving endmembers of a single phase) or heterogeneous (involving endmembers in different phases). In high temperature magmatic systems it is reasonable to assume that individual phases are in homogeneous equilibrium whereby species within a given solution phase are in chemical equilibrium. In this case only heterogeneous reactions need to be considered. However the framework we describe here is generic and does not

require this assumption.

Both the geodynamic and thermochemical models are based on mixture theory (Drew, 1971) in which the mechanical and thermodynamic phases are treated as interpenetrating continua. As such, all variables — including pressure, stess, temperature, phase velocity, phase volume fraction, and phase composition — are average macroscopic properties of the system. All processes are therefore described on a phenomenological level. Spatial averaging at the macroscale means that these processes cannot generally be directly compared to the microscopic processes from which they are derived. Rather phenomenological relations, such as those describing permeability and bulk rheology, are obtained empirically or from appropriate upscaling analysis. Despite the inherent loss of information involved in this approach, it has the benefit of maintaining tractability, while still providing important insight at the system scale.

2.3 Conservation Equations

2.3.1 Conservation of mass

Given N phases each with K_i endmembers, conservation of mass for each endmember is given by

$$\frac{\partial}{\partial t}\rho_i\phi_i c_i^k + \boldsymbol{\nabla}\cdot\rho_i\phi_i c_i^k\boldsymbol{v}_i = -\boldsymbol{\nabla}\cdot\boldsymbol{J}_i^k + \Gamma_i^k \quad (i=1,2,...,N; k=1,2,...,K_i-1). \tag{2.1}$$

Where ρ_i and ϕ_i are the density and volume fraction of phase i respectively, and c_i^k is the mass concentration of endmember k in phase i. $\boldsymbol{v}_i$ is the velocity field of phase i, which is $\boldsymbol{v}_s$ for the solid phases, and $\boldsymbol{v}_f$ for the melt. $\boldsymbol{J}_i^k$ is the sum of the diffusive and dispersive fluxes of endmember k *within* phase i. To ensure conservation of mass within each phase,

the diffusive fluxes of its endmembers must cancel

$$\sum_{k=1}^{K_i} \boldsymbol{\nabla} \cdot \boldsymbol{J}_i^k = \mathbf{0} \tag{2.2}$$

Γ_i^k is the net reactive mass transfer per unit volume of endmember k in phase i. If all reactions are heterogeneous, this corresponds to the interphase mass transfer into or out of phase i, but if the phase is not in homogeneous equilibrium Γ_i^k may also include the formation/destruction of endmember k in speciation reactions.

$$\Gamma_i^k = \sum_{j=1}^{J} \nu_{ij}^k R_j, \tag{2.3}$$

where R_j is the reaction rate of the j^{th} chemical reaction in units of density per unit time. $R_j > 0$ for the forward reaction, and $R_j < 0$ for the reverse reaction. ν_{ij}^k is the dimensionless mass-weighted stoichiometric coefficient of endmember k in reaction j. By convention $\nu_{ij}^k < 0$ for reactants, and $\nu_{ij}^k > 0$ for products. They are related to the molar stoichiometric coefficients $\tilde{\nu}_{ij}^k$ by

$$\nu_{ij}^k = \frac{\tilde{\nu}_{ij}^k M_i^k}{M_j} \tag{2.4}$$

where M_i^k is the molar mass of endmember k. We have normalized by the mass of reaction M_j which is calculated by summing the masses of all the products of the reaction

$$M_j = \sum_{i}^{N} \sum_{k}^{K_i} \tilde{\nu}_{ij}^k M_i^k \quad \text{for } \tilde{\nu}_{ij}^k > 0 \tag{2.5}$$

This leads to

$$\sum_{i=1}^{N} \sum_{k=1}^{K_i} \nu_{ij}^k = 1 \quad \text{for } \nu_{ij}^k > 0. \tag{2.6}$$

For a balanced stoichiometric reaction, in which there are no sources or sinks of mass, we

also have

$$\sum_{i=1}^{N}\sum_{k=1}^{K_i}\nu_{ij}^{k}=0. \tag{2.7}$$

While the stoichiometry of each reaction $\boldsymbol{\nu}_j$ is fixed, the net reaction, described by the Γ_i^k terms, will vary as the rates of the individual reactions change.

Only K_i-1 equations of the form (2.1) are required for each phase, as we can use the closure $\sum_{k=1}^{K_i} c_i^k=1$ to get the final endmember concentration. We therefore require $K_{tot}-N$ conservation of endmember equations in total to track the composition of all the phases in the system.

Summing equation (2.1) over all the endmembers in each phase we get the conservation of mass for phase i

$$\frac{\partial}{\partial t}\rho_i\phi_i+\boldsymbol{\nabla}\cdot\rho_i\phi_i\boldsymbol{v}_i=\Gamma_i \quad (i=1,2,...,N). \tag{2.8}$$

Where we have used the closure $\sum_{k=1}^{K_i} c_i^k=1$, and assumed that the diffusive fluxes $\boldsymbol{J}_i^k$ cancel within each phase. Γ_i gives the net mass transfer rate (over all its endmembers) into/out of the phase i:

$$\Gamma_i=\sum_{k=1}^{K_i}\sum_{j=1}^{J}\nu_{ij}^{k}R_j. \tag{2.9}$$

Given that all reactions are balanced, as stated in equation (2.7), we necessarily have the condition

$$\sum_{i=1}^{N}\Gamma_i=0 \tag{2.10}$$

In a static, closed isothermal system, equations (2.1) and (2.8), along with a description of the reaction rates terms R_j, would be sufficient to describe the reaction paths. However, in a dynamic non-isothermal system in which the fluid and solid can flow, additional closures are required to describe the velocity fields $\boldsymbol{v}_i$, and the temperature T. For these closures we need to conserve momentum and energy respectively.

2.3.2 Conservation of momentum

If we assume that inertia is negligible in both fluid and solid phases and that the fluid phase is sufficiently inviscid that averaged deviatoric stresses in the fluid are negligible, conservation of momentum proceeds exactly as described in Rudge et al. (2011).

The separation flux between the melt and solid is given by the extended form of Darcy's law

$$\phi_f(\boldsymbol{v}_f - \boldsymbol{v}_s) = -\frac{K}{\mu}\left(\boldsymbol{\nabla} P - \rho_f \boldsymbol{g}\right), \tag{2.11}$$

where K is the permeability, which is a function of ϕ_f, μ is the melt viscosity and $\boldsymbol{g}$ is the acceleration due to gravity. The above equation neglects the effects of surface energy which, while being beyond the scope of this paper, is important when modelling damage and shear localization (Bercovici et al., 2001; Bercovici and Ricard, 2003; Parsons et al., 2008; Takei and Holtzman, 2009; Evans et al., 2018).

By conservation of total stress, force balance in the solid is described by

$$\boldsymbol{\nabla} P = \boldsymbol{\nabla} \cdot \boldsymbol{\sigma}'_s + \bar{\rho}\boldsymbol{g}, \tag{2.12}$$

where P is the fluid pressure, and $\bar{\rho} = \sum_i^N \rho_i \phi_i$ is the net density of the multiphase assemblage. $\boldsymbol{\sigma}'_s$ is the effective stress in the solid in excess of the fluid pressure

$$\boldsymbol{\sigma}'_s = \boldsymbol{\sigma}_s + P\boldsymbol{I}. \tag{2.13}$$

Here we use the convention that negative stresses are compressive.

2.3.3 Conservation of energy

The temperature evolution equation is derived from the entropy balance (de Groot and Mazur, 1984; Rudge et al., 2011)

$$\sum_{i=1}^{N}\left[\rho_i\phi_i\frac{\mathrm{D}_i s_i}{\mathrm{D}t}+s_i\Gamma_i\right]=-\boldsymbol{\nabla}\cdot\boldsymbol{j}+\sigma. \tag{2.14}$$

Where s_i is the entropy per unit mass of phase i, $\boldsymbol{j}$ is the entropy flux from the heat and mass fluxes, and σ is the internal entropy production (Tolman and Fine, 1948). Substituting in the standard thermodynamic relations, we get the following temperature evolution equation

$$\sum_{i=1}^{N}\left[\rho_i\phi_i C_{Pi}\frac{\mathrm{D}_i T}{\mathrm{D}t}-\phi_i\alpha_i T\frac{\mathrm{D}_i P}{\mathrm{D}t}+Ts_i\Gamma_i\right]=-\boldsymbol{\nabla}\cdot\boldsymbol{q}+Q+\Psi+\sum_{i=1}^{N}\sum_{k=1}^{K_i}\mu_i^k\left[\boldsymbol{\nabla}\cdot\boldsymbol{J}_i^k-\Gamma_i^k\right] \tag{2.15}$$

where $\frac{\mathrm{D}_i}{\mathrm{D}t}=[\frac{\partial}{\partial t}+\boldsymbol{v}_i\cdot\boldsymbol{\nabla}]$ is the Lagrangian derivative following phase i. C_{Pi} is the specific isobaric heat capacity, and α_i is the thermal expansivity of phase i. The more explicit form for the latent heat of reaction used here can be compared to the latent heat to melting L used in previous magma dynamics formulations (e.g. Hewitt and Fowler, 2008) according to

$$L=-\frac{\sum_{i=1}^{N}s_i\Gamma_i}{\Gamma_{lq}} \tag{2.16}$$

On the RHS of Eq. (2.15), $\boldsymbol{q}$ is the heat flux, Q is the internal heat production, and Ψ represents the sources of heat from relative fluid flow and viscous dissipation. The final terms give the dissipative heat sources from diffusion and disequilibrium reaction. Using the definition of Γ_i^k we can rewrite the final dissipative term as

$$-\sum_{i=1}^{N}\sum_{k=1}^{K_i}\mu_i^k\Gamma_i^k=\sum_{i=1}^{N}\sum_{k=1}^{K_i}\sum_{j=1}^{J}\nu_{ij}^k\mu_i^k R_j=\sum_{j=1}^{J}A_j R_j \tag{2.17}$$

where A_j is the chemical affinity of reaction j, which is a scalar measure of disequilibrium and the thermodynamic driving force for reaction. This is defined as

$$A_j = -\Delta_r G = -\sum_{i=1}^{N}\sum_{k=1}^{K_i} \nu_{ij}^k \mu_i^k(P,T,\boldsymbol{c}). \tag{2.18}$$

$\Delta_r G$ is the Gibbs free energy of reaction, and μ_i^k is the chemical potential of endmember k in phase i.

The entropy flux from Eq. (2.14) is then

$$\boldsymbol{j} = \frac{1}{T}\left(\boldsymbol{q} - \sum_{i=1}^{N}\sum_{k=1}^{K} \mu_i^k \boldsymbol{J}_i^k\right) \tag{2.19}$$

and the internal entropy production is

$$\sigma = \frac{1}{T}\left(Q + \Psi - \frac{\boldsymbol{q}\cdot\boldsymbol{\nabla}T}{T} - \sum_{i=1}^{N}\sum_{k=1}^{K_i} \boldsymbol{J}_i^k \cdot \boldsymbol{\nabla}\left(\frac{\mu_i^k}{T}\right) + \sum_{j=1}^{J} A_j R_j\right) \tag{2.20}$$

The terms in σ relate to irreversible processes including radioactive decay, viscous dissipation, chemical diffusion, and reaction. By the second law of thermodynamics, $\sigma \geq 0$. For a system in mechanical, thermal and chemical equilibrium, all the dissipative terms disappear such that $\sigma = 0$. But in natural dynamic systems there is always a finite degree of irreversibility (otherwise nothing would happen!).

While the second law puts a robust constraint on σ, if all of the terms in Eq.(2.20) can couple, it only puts a weak constraint on the individual terms. In the case that the fluxes (e.g. $\boldsymbol{q}, \boldsymbol{J}_i^k, R_j$) are assumed to be any linear combination of the forces (e.g. $\boldsymbol{\nabla}T, \boldsymbol{\nabla}\left(\frac{\mu_i^k}{T}\right), A_j$), given certain symmetry considerations, this leads to Onsager's reciprocal relations (Onsager, 1931a,b). A stronger constraint is to assume that each term in Eq.(2.20) is independent and positive, which *in the linear case* corresponds to a diagonal Onsager's relationship implying

that

$$\begin{aligned} \boldsymbol{q} &\propto -\boldsymbol{\nabla} T, && \text{Fourier's law} \\ \boldsymbol{J}_i^k &\propto -\boldsymbol{\nabla}\left(\frac{\mu_i^k}{T}\right), && \text{Fick's law} \\ R_j &\propto A_j, && \text{linear reaction rates} \\ Q, & && \text{positive heat production} \\ \Psi, & && \text{positive viscous dissipation} \end{aligned} \tag{2.21}$$

As the relationship between forces and fluxes is empirical, there is actually no obvious requirement for linearity. For example, while Fourier's law and Fick's law are robust for a large range of chemical potential and thermal gradients, studies of reaction kinetics have shown that reaction rates are only linear for very small perturbations from equilibrium (Prigogine, 1967). Non-linear phenomenological relations lie outside the scope of classical irreversible thermodynamics. However, a more general constraint to ensure positive entropy production from the reaction term would be

$$\text{sign}(R_j) = \text{sign}(A_j) \tag{2.22}$$

We discuss the form of the reaction rates R_j further in section 2.5.1.

The assumption of mutually independent sources of entropy ignores coupling between terms in σ. Such coupling is known to arise, for example during Soret diffusion (Walker and DeLong, 1982; Lesher and Walker, 1991), however it is unclear that there is sufficient experimental constraints to write down general coupled terms. Given addition constraints, this assumption could easily be relaxed.

2.3.4 Closures

The full system of equations governing conservation of mass, momentum and energy can now be written

$$\frac{\partial}{\partial t}\rho_i\phi_i c_i^k + \boldsymbol{\nabla}\cdot\rho_i\phi_i c_i^k\boldsymbol{v}_i = -\boldsymbol{\nabla}\cdot\boldsymbol{J}_i^k + \Gamma_i^k \quad (i=1,2,...,N; k=1,2,...,K_i-1) \tag{2.23}$$

$$\frac{\partial}{\partial t}\rho_i\phi_i + \boldsymbol{\nabla}\cdot\rho_i\phi_i\boldsymbol{v}_i = \Gamma_i \quad (i=1,2,...,N) \tag{2.24}$$

$$\phi_f(\boldsymbol{v}_f - \boldsymbol{v}_s) = -\frac{K}{\mu}\left(\boldsymbol{\nabla}P - \rho_f\boldsymbol{g}\right) \tag{2.25}$$

$$\boldsymbol{\nabla}P = \boldsymbol{\nabla}\cdot\boldsymbol{\sigma}_s' + \bar{\rho}\boldsymbol{g} \tag{2.26}$$

$$\sum_{i=1}^{N}\left[\rho_i\phi_i C_{Pi}\frac{\mathrm{D}_i T}{\mathrm{D}t} - \phi_i\alpha_i T\frac{\mathrm{D}_i P}{\mathrm{D}t} + T s_i\Gamma_i\right] = -\boldsymbol{\nabla}\cdot\boldsymbol{q} + Q + \Psi + \sum_{i=1}^{N}\sum_{k=1}^{K_i}\mu_i^k\left[\boldsymbol{\nabla}\cdot\boldsymbol{J}_i^k - \Gamma_i^k\right] \tag{2.27}$$

To complete the description for deformation of the solid phase requires additional constitutive equations to relate the effective stress to the solid deformation. For example, for an isotropic compressible poro-viscous system consistent with viscous creep of mantle rocks at high pressure and temperature:

$$\begin{aligned}\boldsymbol{\sigma}_s' =& 2\eta\dot{\epsilon}_d + \zeta\mathrm{Tr}(\dot{\epsilon})\boldsymbol{I} \\ =& \eta\left(\nabla\boldsymbol{v}_s + \nabla\boldsymbol{v}_s^T - \frac{2}{3}\boldsymbol{\nabla}\cdot\boldsymbol{v}_s\boldsymbol{I}\right) + \zeta\boldsymbol{\nabla}\cdot\boldsymbol{v}_s\boldsymbol{I}\end{aligned} \tag{2.28}$$

where η is the solid shear viscosity, $\dot{\epsilon}_d$ is the deviatoric strain rate, ζ is the solid bulk viscosity, and $\mathrm{Tr}(\dot{\epsilon})$ is the isotropic strain rate.

Alternative solid rheologies could be used. For example, two-phase flow equations have been derived by past workers for a range of rheologies including poro-elastic (Biot, 1941; Evans et al., 2018), viscoelastic (Connolly and Podladchikov, 1998; Omlin et al., 2018), visco-elasto-plastic (Keller et al., 2013) and poro-elastic with phase-field cracking (Evans et al., 2020).

To close the momentum equations, constitutive relations must be specified for permeability K, and the rheological coefficients which, in the case of a poroviscous system, are the solid bulk and shear viscosity ζ, and η. These are emergent properties of the bulk two-phase medium. As they depend on properties of the aggregate at the grain-scale, they are typically the most uncertain part of the model. While they can be derived based on assumptions about the interphase forces and surface energy terms (McKenzie, 1984; Scott and Stevenson, 1984; Bercovici et al., 2001), direct estimates have also been made experimentally (Hirth and Kohlstedt, 1995a,b; Kohlstedt and Zimmerman, 1996; Miller et al., 2014), and using homogenization techniques (Simpson et al., 2010a,b). Widely-used expressions for K, ζ, and η are

$$K = K_0 \phi_f^n, \quad n \approx 3 \tag{2.29}$$

$$\zeta = \zeta_0 (1 - \phi_f) \phi_f^m, \quad m \approx -1 \tag{2.30}$$

$$\eta = \eta_0 (1 - \phi_f) \tag{2.31}$$

Where K_0, ζ_0, and η_0 are constants that depend on the microscale geometry. Alternative rheological models for partially molten mantle rocks have been explored using micro-mechanical models, by Takei and Holtzman (2009) and Rudge (2018); which infer a weaker porosity dependence for ζ.

The final closures are those for the thermodynamic properties ρ_i, C_{Pi}, α_i, s_i, and μ_i^k, and the reactive mass transfer terms Γ_i^k and Γ_i.

2.4 Thermodynamics

Descriptions of the thermodynamic properties of phases are obtained from thermodynamic databases. Widely used examples for igneous and metamorphic phase assemblages include Berman (1988), Holland and Powell (1998), Holland and Powell (2011), Ghiorso and Sack (1995), Stixrude and Lithgow-Bertelloni (2005), and Stixrude et al. (2011). These

databases are calibrated from calorimetric, volumetric, and phase equilibrium experimental data and describe the properties of pure phase endmembers including standard state enthalpies, entropies, volumes, heat capacities, and equations of state. Together these describe the Gibbs free energy of the pure phases which, when expressed as a function of P and T, constitutes a fundamental thermodynamic relation from which all other thermodynamic properties can be derived by taking appropriate derivatives (see Appendix B). Derivation of properties in this way guarantees thermodynamic self-consistency (Stixrude and Lithgow-Bertelloni, 2005). While the underlying calibrations may be based on a different thermodynamic potential such as the Helmholtz energy, they can be transformed to the Gibbs energy by Legendre transformation. Mineral endmembers are determined by the mineral stoichiometry and therefore have mineral-like compositions such as forsterite Mg_2SiO_4. There is greater ambiguity in the choice of melt endmembers as silicate melts do not have long-range order and so are not bound by the same stoichiometric constraints as minerals. For convenience mineral-like endmembers have been used in existing models of natural silicate melts used (Ghiorso and Sack, 1995; Holland and Powell, 1998; Green et al., 2012). Species in aqueous or mixed fluids typically include both ionic and neutral molecular species (e.g. Helgeson, 1970).

Thermodynamic phase models are assembled from the models of the constituent endmembers. In addition to the weighted contributions of the Gibbs free energies of the pure endmembers, there are further contributions to the Gibbs free energy of the solution phase from ideal mixing and the excess energy of mixing. These terms are described in solution models which are fit from phase equilibrium experiments and vary in complexity from purely ideal mixing (e.g. Ghiorso and Sack, 1995) to complex non-ideal mixing with internal ordering on sites (e.g. Sack and Ghiorso, 1994). Calculating the solubility of components in fluids also requires models of aqueous speciation.

Currently, thermodynamic databases are accessible through various software packages, many of which are geared towards the calculation of equilibrium phase assemblages (Ghiorso,

1985; Powell et al., 1998; Connolly, 2005; De Capitani and Petrakakis, 2010). These software packages are not designed to be interoperable with dynamics codes, and the underlying thermodynamic databases are not easily customized for particular model problems. Application of the framework described here leverages a new software infrastructure for thermodynamic modelling as part of the ENKI project which is described further in section 2.6. The ENKI software (enki-portal.org) uses a flexible hierarchical structure to describe the thermodynamic models which separately describes pure endmembers and phases. The phases may contain any number of endmembers and therefore may be pure phases or solution phases, but all share the same interface. Mineral phases such as pyroxenes, and aqueous solutions involve mixing between non-linearly independent species. If these phases are in homogeneous equilibrium, speciation can be calculated within the phase description using an internal solver. The endmembers used in the reactive model would then be the subset of linearly independent endmembers that describe the phase composition. However if homogeneous equilibrium is not assumed, internal speciation reactions can be included in the overall reactive scheme, in which case the endmembers used in the reactive model would be the full set of non-independent species. We discuss this further in section 2.5.8.

In this formulation the same thermodynamic models are used to characterize both the thermodynamic phase properties (including ρ_i, C_{Pi}, α_i, and s_i) and the relative stability of phases in the reactive system through the reaction affinities (see section 2.5.1). The major advantages of this approach are that: (1) it consistently couples the dynamics and the petrology of the system; (2) it is internally thermodynamically consistent; and (3) it is consistent with equilibrium calculations in the limit of fast reaction rates. Previous models have tended to use fixed values for the densities, latent heats, and other thermodynamic properties. Using values directly from the thermodynamic models allows us to test these assumptions. In many cases properties such as C_{Pi} and α_i are likely to vary only slightly over the course of a reaction path. However, others including ρ_i and s_i may vary more substantially and feedback into the dynamics.

2.5 Reactive system

The multiphase assemblage reacts via a set of J irreversible reactions. As an example let us consider partial melting in the CMSH system. At high temperature, the system comprises a four component silicate melt Lq comprising endmembers forsterite (fo(Lq), Mg_2SiO_4), silica (q(Lq), SiO_2), diopside (di(Lq), $CaMgSi_2O_6$), and water (w(Lq), H_2O); pure forsterite olivine Ol (fo(Ol), Mg_2SiO_4); a binary orthopyroxene solid solution comprising endmembers enstatite (en(Opx), $Mg_2Si_2O_6$) and diopside (di(Opx), $CaMgSi_2O_6$); a binary clinopyroxene solid solution, also comprising endmembers enstatite (en(Opx), $Mg_2Si_2O_6$) and diopside (di(Opx), $CaMgSi_2O_6$); and pure water W (w(W), H_2O). In this system we can write down the following reactions

$$R_1: \quad \text{fo(Ol)} \rightleftharpoons \text{fo(Lq)} \tag{2.32}$$

$$R_2: \quad \text{en(Opx)} \rightleftharpoons \text{fo(Lq)} + \text{q(Lq)} \tag{2.33}$$

$$R_3: \quad \text{di(Opx)} \rightleftharpoons \text{di(Lq)} \tag{2.34}$$

$$R_4: \quad \text{en(Cpx)} \rightleftharpoons \text{fo(Lq)} + \text{q(Lq)} \tag{2.35}$$

$$R_5: \quad \text{di(Opx)} \rightleftharpoons \text{di(Lq)} \tag{2.36}$$

$$R_6: \quad \text{w(W)} \rightleftharpoons \text{w(Lq)} \tag{2.37}$$

Where the $\rightleftharpoons$ symbol is used to indicate that, although irreversible, reactions can proceed in either direction depending on their chemical affinities. The stoichiometric coefficients of

these reactions can be assembled into $K_{tot} \times J$ molar stoichiometric matrix $\tilde{\boldsymbol{\nu}}$

$$\tilde{\boldsymbol{\nu}} = \begin{bmatrix} \begin{pmatrix} 0 \\ -1 \\ 0 \\ 0 \end{pmatrix} & \begin{pmatrix} 0 \\ -1 \\ -1 \\ 0 \end{pmatrix} & \begin{pmatrix} -1 \\ 0 \\ 0 \\ 0 \end{pmatrix} & \begin{pmatrix} 0 \\ -1 \\ -1 \\ 0 \end{pmatrix} & \begin{pmatrix} -1 \\ 0 \\ 0 \\ 0 \end{pmatrix} & \begin{pmatrix} 0 \\ 0 \\ 0 \\ -1 \end{pmatrix} \\ \begin{pmatrix} 1 \\ 0 \\ 0 \end{pmatrix} & \begin{pmatrix} 0 \\ 1 \\ 0 \end{pmatrix} & \begin{pmatrix} 0 \\ 0 \\ 1 \end{pmatrix} & \begin{pmatrix} 0 \\ 0 \\ 0 \end{pmatrix} & \begin{pmatrix} 0 \\ 0 \\ 0 \end{pmatrix} & \begin{pmatrix} 0 \\ 0 \\ 0 \end{pmatrix} \\ \begin{pmatrix} 0 \\ 0 \end{pmatrix} & \begin{pmatrix} 0 \\ 0 \end{pmatrix} & \begin{pmatrix} 0 \\ 0 \end{pmatrix} & \begin{pmatrix} 1 \\ 0 \end{pmatrix} & \begin{pmatrix} 0 \\ 1 \end{pmatrix} & \begin{pmatrix} 0 \\ 0 \end{pmatrix} \\ \begin{pmatrix} 0 \end{pmatrix} & \begin{pmatrix} 0 \end{pmatrix} & \begin{pmatrix} 0 \end{pmatrix} & \begin{pmatrix} 0 \end{pmatrix} & \begin{pmatrix} 0 \end{pmatrix} & \begin{pmatrix} 1 \end{pmatrix} \end{bmatrix} \tag{2.38}$$

Which can be transformed to it mass-based equivalent according to Eq. (2.4). The columns of $\tilde{\boldsymbol{\nu}}$ correspond to the reactions above, and the internal parentheses are used to separate phases such that $\nu_{i,j}^k$ refers to endmember k in phase i. Each reaction is assumed to proceed at an independent rate R_j such that the reactive mass transfers for endmembers and phases can be given in closed form as

$$\Gamma_i^k = \sum_{j=1}^{J} \nu_{ij}^k R_j, \quad \Gamma_i = \sum_{k=1}^{K_i} \sum_{j=1}^{J} \nu_{ij}^k R_j \tag{2.39}$$

As written here there are two components of the reactive closures: the first is the set of reactions and their stoichiometry, as given above; and the second is closed-form expressions for the macroscopic reaction rates R_j.

2.5.1 Rate laws

From consideration of transition state theory (Aagaard and Helgeson, 1982; Lasaga, 1981) a general rate law for reaction at mineral surfaces can be written

$$R_j = r_j S_j \left(\mathbf{\Phi}_j\right) \left(1 - \exp\left(-\frac{M_0}{M_j}\frac{A_j}{RT}\right)\right) \tag{2.40}$$

Where r_j is the effective rate constant (units: kg m^{-2} s^{-1}); S_j is the available reactive surface area (units: m^2 m^{-3}) which is a function of $\mathbf{\Phi}_j$, the phases involved in reaction j; A_j is the chemical affinity of the reaction; R is the gas constant; M_j is the mass of reactants; and M_0 is a reference mass used to normalize the affinity term. Close to equilibrium when affinities are small ($A_j << RT$) this expression can be linearized to give

$$R_j = r_j S_j(\mathbf{\Phi}_j)\frac{M_0}{M_j}\frac{A_j}{RT} \tag{2.41}$$

Far from equilibrium on the other hand, the affinity term becomes negligible and the rate is simply controlled by the reactive surface area

$$R_j = r_j S_j(\mathbf{\Phi}_j) \tag{2.42}$$

However, during igneous and metamorphic reaction at high temperature we can reasonably assume that we are in the linear low affinity regime. This has been confirmed experimentally for melting and crystallization reactions in in silicic magmatic systems (Edwards and Russell, 1996). Linear reaction rates also fit within the framework of classical irreversible thermodynamics (Prigogine, 1967). Despite this, although linear rate laws can be justified from transition state theory, for complex reactions this requires a number of assumptions (Lasaga, 1986). Non-linear dependencies on A_j for other heterogeneous reaction mechanisms, such as Burton–Cabrera–Frank growth and diffusion-controlled growth, are both predicted theoretically and have been demonstrated experimentally (Lasaga, 1998). Linear rates are

therefore far from universal. To account for this and to allow for different rates for the forward and reverse reactions we can write the more general thermodynamic rate law as a piece-wise function

$$R_j = \begin{cases} r_j^+ S_j^+(\mathbf{\Phi}_{rj}^+) f^+(A_j), \ A_j \geq 0 \\ r_j^- S_j^-(\mathbf{\Phi}_{rj}^-) f^-(A_j), \ A_j < 0 \end{cases} \tag{2.43}$$

where the '+' superscript refers to the forward reaction and '-' refers to the reverse reaction. $f(A_j)$ is now the thermodynamic driving function which may or may not be linear.

The functional forms of r_j, S_j and $f(A_j)$ depend on the details of the reaction kinetics and on the rock microstructure. As the kinetics vary significantly depending on factors including proximity to equilibrium, temperature, phase proportion, and local environmental effects, it is not possible to write down one reaction rate law that is globally applicable. Our software allows users to freely specify the functional form of the reaction kinetics symbolically and then auto-generate C++ and python bindings for incorporation into reactive flow codes (see Section 2.6). Close to equilibrium, i.e. for systems in which reaction is fast relative to other processes, the details of the kinetics become less important. However, on a phenomenological level, there are some general requirements that must be considered to ensure positivity of phase mass, and consistency with the second law.

Thermodynamic driving function $f(A_j)$ relates the reaction rate to the thermodynamic stabilities of the reactants and products. As such, it controls the direction that the reaction proceeds: if $A_j > 0$ then it follows that $(f(A_j), R_j) > 0$, and if $A_j < 0$ then $(f(A_j), R_j) < 0$. Similar to the 2nd law constraint described in section 2.3.3, this give us the condition

$$\text{sign}(f(A_j)) = \text{sign}(A_j) \tag{2.44}$$

In equilibrium $A_j = 0$ and reaction ceases: we must therefore also have the condition

$$f(A_j) \to 0 \text{ as } A_j \to 0. \tag{2.45}$$

As the affinities always point in the direction of equilibrium, if $f(A_j)$ is proportional to A_j in some way, the system will react so as to minimize the chemical potential energy. Given an appropriate set of reactions, in a closed system the assemblage is guaranteed to converge to equilibrium. The major advantage of using such a closed-form thermodynamic rate law is that it avoids the need to solve for the equilibrium state of the system directly by free energy minimization. Although we have assumed that reaction rates are independent, in that they are only dependent on their respective chemical affinities, in systems comprising solution phases the reactions will still be strongly coupled through the phase compositions. For example in the system above addition of water to the melt would act to destabilize olivine, orthopyroxene, and clinopyroxene relative to the melt, thus driving further melting via the other reactions.

Rate constant r_j is the scale factor that controls the overall reaction rate. Generally r_j can be described by an Arrhenius form

$$r_j = r_{0j} \exp\left(\frac{E_a}{RT}\right) \tag{2.46}$$

where r_{0j} is the rate constant prefactor, and E_a is the activation energy which may be pressure- and temperature-dependent (Lasaga, 1998). The rate constant may also be influenced by a number of local environmental factors. This includes species that have a catalytic or prohibitory affect on the reaction, or the availability of surfaces for heterogeneous nucleation.

Reactive surface area S_j is required to describe the surface area available for heterogeneous reactions. In the case of homogeneous reactions, reaction does not occur across a phase interface and $S_j = 1$. For heterogeneous reactions S_j is a function of the volume fractions of the reactant phase or phases, which we denote here as $\mathbf{\Phi}_{rj}$. What counts as a reactant depends on the direction the reaction is proceeding: for the forward reaction ($A_j > 0$) the phases on the LHS are the reactants; for the reverse reaction ($A_j < 0$) the reactants are the

phases on the RHS. The functional form of S_j depends on the rock microstructure and on the pore geometry. However, to maintain positivity of phase fractions, S_j must tend to 0 when any reactant phase disappears from the assemblage:

$$S_j \to 0 \quad \text{as} \quad \mathbf{\Phi}_j \to \mathbf{0} \tag{2.47}$$

Given this, S_j will act to switch off reaction when any reactant phases are exhausted, allowing phases to appear and disappear from the mineral assemblage. Considering the CMSH system above as an example, the reactive surface areas for the melting reactions 1-5 could be approximated as linear functions of the phase fractions. The reverse reactions depend on the availabilty of the melt. In partially molten rocks, melt is distributed in tubes along grain boundaries (e.g. Yoshino et al., 2005) implying a reactive surface area that has a square root dependence on melt porosity. As both of these constraints satisfy (2.47), the reactive surface areas may be written

$$S^+_{1-5} = S_0 \theta \Phi_j \quad S^-_{1-5} = S_0 \sqrt{\phi_{lq}} \tag{2.48}$$

Where S_0 is the total mineral surface area, which depends on grain size, and θ is a geometrical constant, which depends on the wetting angle (von Bargen and Waff, 1986).

2.5.2 Choice of reactions

Equally important as the rate law is the choice of reactions themselves. In natural geological phase assemblages, reaction takes place via a complex network of reactions occurring in series and parallel at the grain scale (Zhang, 2008). The reaction mechanisms of geochemical reactions, particularly those at high temperature involving solid solutions, are poorly understood. Here, we are only interested in capturing the average macroscopic evolution of the phase assemblage and are therefore describing reaction on a phenomenological level. Thus, the goal is to find a minimal, or near-minimal, set of reactions that is able to define the equilibrium state of the system, while also providing a tractable approximation of the

natural kinetic pathways in the system. The latter is particularly important when the system is reacting far from equilibrium.

2.5.3 Linearly independent reactions

In any reactive system there is a set of $\mathcal{J} = K_{tot} - C$ linearly independent reactions that represent the minimum number of reactions required to describe the phase assemblage evolution. A suitable linearly independent set can be derived by considering the endmember space of the reactive system. The mathematical formulation for reactive systems has been written down by a number of authors including Smith (1982), Steefel and MacQuarrie (1996), and Lichtner (1985), the latter two of whom focus on aqueous reactions. While descriptions differ in terminology, the underlying linear algebra is the same.

For partial melting in the CMSH system the reactions (2.32)-(2.37) constitute a linearly independent set. This can be recognized by writing out the full endmember space in terms of the system components. The table below shows the phase endemember compositions as a function of their constituent oxides

Phases	Lq				Ol	Opx		Cpx		W
Endmembers	di	fo	q	w	fo	en	di	en	di	w
CaO	1	0	0	0	0	0	1	0	1	0
MgO	1	2	0	0	2	2	1	2	1	0
SiO_2	2	1	1	0	1	2	2	2	2	0
H_2O	0	0	0	1	0	0	0	0	0	1

Where we have grouped together endmembers belonging to each phase. This compositional

table can equivalently be compiled into a $C \times K_{tot}$ formula matrix $\boldsymbol{F}$

$$\boldsymbol{F} = \begin{bmatrix} 1 & 0 & 0 & 0 & 0 & 0 & 1 & 0 & 1 & 0 \\ 1 & 2 & 0 & 0 & 2 & 2 & 1 & 2 & 1 & 0 \\ 2 & 1 & 1 & 0 & 1 & 2 & 2 & 2 & 2 & 0 \\ 0 & 0 & 0 & 1 & 0 & 0 & 0 & 0 & 0 & 1 \end{bmatrix} \tag{2.49}$$

A set of independent reactions can be constructed from the null space of $\boldsymbol{F}$ — as such these reactions sometimes referred to as a set of 'null-space reactions'. In simple systems such a set can often be determined by inspection, but a more general approach to constructing linearly independent reactions is detailed in Appendix D. Writing out the stoichiometric coefficients of the reactions above again, but this time removing the inner parentheses

$$\tilde{\boldsymbol{\nu}} = \begin{bmatrix} 0 & 0 & -1 & 0 & -1 & 0 \\ -1 & -1 & 0 & -1 & 0 & 0 \\ 0 & -1 & 0 & -1 & 0 & 0 \\ 0 & 0 & 0 & 0 & 0 & -1 \\ 1 & 0 & 0 & 0 & 0 & 0 \\ 0 & 1 & 0 & 0 & 0 & 0 \\ 0 & 0 & 1 & 0 & 0 & 0 \\ 0 & 0 & 0 & 1 & 0 & 0 \\ 0 & 0 & 0 & 0 & 1 & 0 \\ 0 & 0 & 0 & 0 & 0 & 1 \end{bmatrix} \tag{2.50}$$

we see that each column $\tilde{\boldsymbol{\nu}}_j$ represents a balanced reaction that satisfies

$$\boldsymbol{F}\tilde{\boldsymbol{\nu}}_j = \boldsymbol{0} \tag{2.51}$$

In most systems the set of independent reactions is non-unique. Reactions (2.32)-(2.37) are

written in what is sometimes referred to as 'canonical form' (Smith, 1982). This is where the phase endmembers are partitioned into secondary species s_j, which appear in only one reaction, and basis species b_κ, which appear in multiple reactions and whose compositions span the column space of $\boldsymbol{F}$. We use the convention whereby basis species fill the top rows of the stoichiometric matrix, and the secondary species fill the remaining rows. Such reactions then have the general form

$$s_j = \sum_{\kappa=1}^{C} \nu_{\kappa,j} b_\kappa \tag{2.52}$$

Note that as we are considering the full set of endmembers within the system as a whole, we have used a different set of endmember indices. The endmember (row) indices here can be transformed into those used for referring to endmembers k in phases i above according to

$$\kappa = \sum_{i=1}^{i-1} K_i + k \tag{2.53}$$

Even when written in form (2.52) the reactions are non-unique as there there are multiple possible choices for the set of basis species. For instance, in the example above an alternative set of reactions could be written in terms of olivine and orthopyroxene endmembers and aqueous water: fo(Ol), en(Opx), di(Opx), w(W). The choice of reactions partly rests on which set best approximates the kinetics of natural systems, but considerations must also be made to guarantee convergence to equilibrium.

2.5.4 Equilibrium and kinetic considerations

In a heterogeneous system the choice of basis species comes down to which phases represent appropriate reaction-mediating phases. There are three important considerations:

1. To be thermodynamically consistent, reactions must be chosen such that the reactive system converges to the global equilibrium under closed-system conditions. If all the reacting phases, and thus all phase endmembers, are known a priori to be saturated in the equilibrium assemblage, convergence is guaranteed for any independent set of

reactions. As all the reactants and products are stable, the equilibrium condition is then simply defined by the fixed point

$$\boldsymbol{A} = \mathbf{0} \tag{2.54}$$

Where $\boldsymbol{A}$ is a vector of the reaction affinities. However, the more general case is that the set of reacting phases represents a super-set of phases including both those that are saturated and those that are undersaturated at equilibrium. To comply with mass conservation constraints, reactions are turned off when reactant phase fractions tend to zero. If all the mediating phases are reacted out of the system, then no further reaction can occur. To guarantee the system converges to the global equilibrium, reactions must be universally applicable and must therefore be mediated by phases that are known, a priori, to be saturated. As these phases are stable throughout the course of the reaction path we therefore refer to them as *omnipresent* phases. The saturation states of the other reacting phases are then effectively tested against these mediating phases through the reaction affinities. The general equilibrium condition is then

$$\begin{cases} A_j = 0 \text{ for } s_j \text{ in saturated phases} \\ A_j > 0 \text{ for } s_j \text{ in undersaturated phases} \end{cases} \tag{2.55}$$

2. Mediating phases must also comprise endmembers that constitute a compositional basis set. Unless there are two mediating phases this is generally restricted to *omnicomponent* phases such as silicate melts and aqueous fluids. These represent excellent choices for mediating phases as they not only comprise a basis set of species, but they are also not bound by the same stoichiometric constraints of mineral phases. If all the reactions occur via the omnicomponent phase all the chemical affinities and therefore reaction rates become coupled through its chemical potentials (Ghiorso, 2013). Many saturation state algorithms used to compute equilibrium phase relations in multicom-

ponent systems rely on such omnicomponent phases (e.g. Ghiorso, 1985; Asimow and Ghiorso, 1998). In subsolidus phase assemblages, which lack both a melt and a fluid, or in which the fluid is assumed to be pure water, an omnicomponent grain boundary phase can be constructed. We discuss the context for melt-, fluid-, and grain boundary mediated reactions below.

3. Finally, for an equilibrium problem, as long as the preceding conditions discussed are met, the choice of reactions does not affect the reaction path. This is also true of systems operating very close to equilibrium. Disequilibrium systems, however, are path-dependent, and the choice of reactions significantly impacts the macroscopic reaction pathway, thereby controlling the time-dependent behaviour of the system. The chosen set of basis species should therefore reasonably approximate the reactive intermediates in order to match the macroscopic kinetics of the system at the scale being considered.

2.5.5 Melt-mediated reactions

In partially molten systems a set of melt-mediated reactions can be written as given above for the CMSH system in 2.32-2.37.

$$s_j = \sum_{k=1}^{C} \nu_{j,k}[\text{melt endmember}]_k \tag{2.56}$$

Where s_j are mineral endmembers or components of a fluid phase if present. In addition to guaranteeing convergence to equilibrium in partially molten and near-solidus systems, melt-mediated reactions also serve as a reasonable approximation of the grain-scale kinetics. In partially molten systems the melt is generally the wetting phase (Holness, 2006), meaning that it provides a physical pathway connecting all the mineral surfaces. Furthermore, due to the high diffusivity of melt compared to solid minerals (Zhang, 2008) melt channels and films serve as a fast kinetic pathway for components to be transported to different reactive surfaces.

Theoretical, numerical and experimental studies looking at grainscale kinetic mechanisms have demonstrated the role of dissolution-reprecipitation during mantle melting (Liang, 2003; Lo Cascio et al., 2004; Morgan and Liang, 2003).

2.5.6 Fluid-mediated reactions

Aqueous or mixed volatile fluids (H_2O-CO_2-H_2S) occur in a huge range of geological environments, from the critical zone to the upper mantle. Transport in the fluid is orders of magnitude faster than through solid minerals, meaning that where fluids are present they serve to transport various species between reactive mineral surfaces (Putnis, 2002). In some cases, such as during metasomatism or hydrothermal alteration, the fluid transport itself is the main driver of disequilibrium. In others, the fluid serves to catalyse reactions within an already metastable mineral assemblage. The solubility of mineral components within fluids is strongly dependent on the thermodynamic conditions. This is also true of the speciation of components within the fluid. However, in general, it is possible to write a set of mineral-fluid reactions of the form

$$s_j = \sum_{k=1}^{C} \nu_{j,k}[\text{fluid species}]_k \tag{2.57}$$

Originating with the seminal work of Helgeson (Helgeson, 1968; Helgeson et al., 1969) there is a vast literature on mineral-fluid interactions. This includes a substantial body of work integrating aqueous reactions into porous transport models (e.g. Lichtner, 1985; Steefel and Lasaga, 1994). We therefore will not seek to review this here. Aqueous reactive transport modeling has been applied across a huge range of geological environments including groundwater and contaminant transport, hydrothermal processes, weathering, and metamorphic reaction. Substantially less work however has focused on the impact of reactive fluid transport at high pressure and temperature. In these settings coupling between the solid and fluid flow by compaction means that the mechanical models required to model fluid transport become more complex. There is also the potential for significant coupling between fluid-rock reaction and the transport dynamics.

2.5.7 Grain boundary-mediated reactions

In systems that lack both a melt or a fluid, there is no obvious omnicomponent phase. While reactions mediated by a set of mineral phases could be written, loss of any one of these mediating phases, across a univariant reaction for example, would render the reaction set inadequate. More importantly, beyond very simple systems in which there are just one or two reactions, such a set is unlikely to accurately represent heterogeneous reaction mechanisms. Reaction via grain-boundaries provides a more realistic description (Fisher, 1973; Joesten, 1977). Diffusion along grain boundaries is several orders of magnitude faster than within minerals (Dohmen and Milke, 2010). Grain boundaries thus provide a short-circuit pathway for transport of components between mineral surfaces. Solid state diffusion, even in the presence of grain boundaries is still several orders of magnitude slower than fluid transport, and therefore we can expect grain boundary-mediated reactions rates to be much slower than fluid-mediated reaction. However there is a suggestion that at high pressures and temperatures, reaction may preferentially occur via an amorphous grain boundary phase due to the limited solubility in aqueous fluids (Konrad-Schmolke et al., 2018).

A solution to subsolidus anhydrous reaction mechanisms is therfore to introduce a hypothetical omnicomponent grain boundary phase. We say *hypothetical* as grain boundaries do not represent a macroscopic phase in the thermodynamic sense. While they can be identified as transitional regions between adjacent crystals from which thermodynamic properties can be defined (Takei, 2019), the nature of grain boundaries varies depending on the orientation and types of adjacent phases. As a result there is no thermodynamic model for a macroscopic grain boundary phase across the entire heterogeneous assemblage.

In general grain boundary reactions may be written

$$s_j = \sum_{k=1}^{C} \nu_{j,k}[\text{grain boundary endmember}]_k \tag{2.58}$$

In the absence of thermodynamic constraints we are free to select any viable set of com-

positional endmembers within the grain boundary. Rather than defining a thermodynamic model a priori, we use mass balance constraints to solve for the grain boundary chemical potentials.

We illustrate this description of grain boundary mediated reactions by considering the dehydration of amphibole in the CMSH system. While this reaction involves a fluid phase, in many applications this may be approximated as pure water. In such a case a grain boundary phase can effectively serve as a substitute for the aqueous solution. The role of the fluid in catalyzing the metamorphic reactions can be accounted for through catalytic terms in the rate constant. If we assume the grain boundary comprises mineral-like endmembers the set of grain boundary-mediated reactions describing dehydration of tremolite is

$$R_1: \quad \text{fo(Ol)} \rightleftharpoons \text{fo(GB)} \tag{2.59}$$

$$R_2: \quad \text{en(Opx)} \rightleftharpoons \text{fo(GB)} + \text{q(GB)} \tag{2.60}$$

$$R_3: \quad \text{di(Opx)} \rightleftharpoons \text{di(GB)} \tag{2.61}$$

$$R_4: \quad \text{en(Cpx)} \rightleftharpoons \text{fo(GB)} + \text{q(GB)} \tag{2.62}$$

$$R_5: \quad \text{di(Opx)} \rightleftharpoons \text{di(GB)} \tag{2.63}$$

$$R_6: \quad \text{w(W)} \rightleftharpoons \text{w(GB)} \tag{2.64}$$

$$R_7: \quad \text{2tr(Act)} \rightleftharpoons \text{4di(GB)} + \text{3fo(GB)} + \text{5q(GB)} + \text{2w(GB)} \tag{2.65}$$

Where tr(Act) is pure tremolite. Assuming that the hypothetical grain boundary phase always occupies a negligible volume fraction $\phi_{gb} = \varepsilon_{gb}$ which cannot grow or shrink, and that it has fixed composition, we can then calculate the reaction affinities using a further set of C mass balance constraints of the form:

$$\Gamma^k_{GB} = 0 \tag{2.66}$$

For the grain boundary phase above we have four constraints

$$\Gamma^{fo}_{GB} = R_1 + R_2 + R_4 + 3R_7 = 0 \tag{2.67}$$

$$\Gamma^{q}_{GB} = R_2 + R_4 + 5R_7 = 0 \tag{2.68}$$

$$\Gamma^{di}_{GB} = R_3 + R_5 + 4R_7 = 0 \tag{2.69}$$

$$\Gamma^{w}_{GB} = R_6 + 2R_7 = 0 \tag{2.70}$$

which can be solved for μ^k_{GB} by unrolling the chemical affinities in the reaction rate expressions. The result of this system of equations is that the chemical potentials of the grain boundary are always intermediate between those of the reacting phases. As it occupies a vanishing volume fraction it does not need to be considered in the conservation equations for the dynamics. Just as melt- and fluid-mediated reactions bear comparison to saturation state algorithms, this grain boundary-mediated approach can be considered as a time-dependent version of the algorithmic extension to MELTS (Asimow and Ghiorso, 1998).

2.5.8 Dependent reactions

While a set of $\mathcal{J}$ independent reactions is the minimum number required to describe the macroscopic phase assemblage evolution, there is no strict requirement that the reactions need to be limited to a linearly independent set. Indeed there may be reactive systems in which it is prudent to include some additional non-independent reactions such that $J > \mathcal{J}$. There are two particularly important scenarios where this is the case. The first is in solution phases in which the species are not in homogeneous equilibrium. This would rarely be expected in high temperature systems, but does occur in low-temperature aqueous fluids, particularly for redox reactions. The second is for polymorphic phase transitions such as the olivine-group phase transitions. As both of these represent homogeneous reactions which occur within a given phase, writing them as heterogeneous melt- or fluid- or grain boundary-

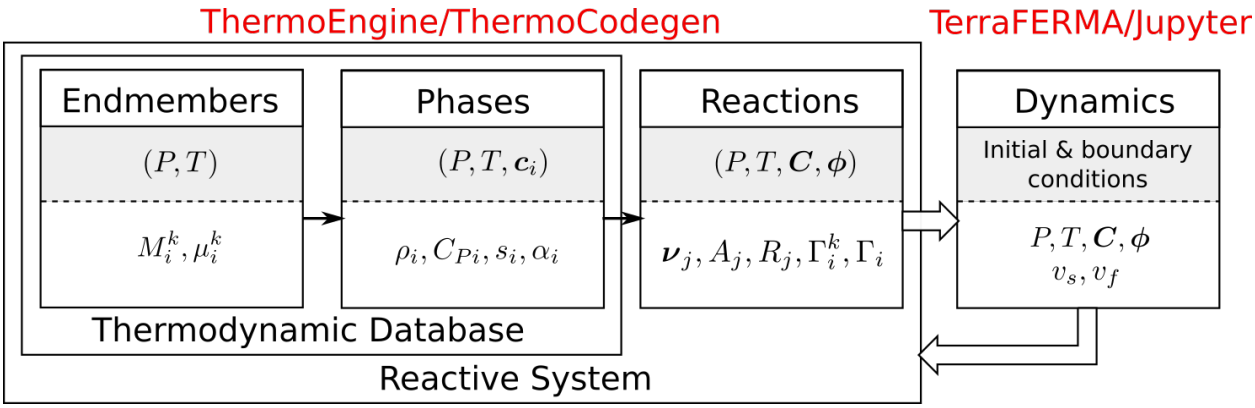

Figure 2.1: Schematic figure illustrating the components of the coupled model. The grey shaded boxes show the inputs of each model component, and the boxes below give examples of useful outputs. The arrows illustrate how variables are passed from one model component to another.

mediated reactions would result in unrealistic reaction paths. Both of these are also restricted to phases which comprise non-independent endmembers (typically referred to in this context as species).

Dependent reactions become more important in systems far from equilibrium as reaction pathways in such systems are strongly dependent on the reaction mechanism. In cases where detailed kinetic information is available, it may be appropriate to model reaction as a complex multistep process, for example in the case of mineral hydrolysis (Murphy and Helgeson, 1987). However, at high temperature, systems tend to operate close to equilibrium and detailed kinetic information is rarely available. It is therefore reasonable to assume an independent reaction set.

2.6 Supporting software

The conservation equations and reactive framework we have described here are very general and could be used to address a range of model problems. To explore the behavior of different systems, we therefore need a supporting software framework that also allows flexibility both in the choice of the reactive system and the phenomenological relations, including the constitutive relations for deformation, fluid flow, and reaction.

A major obstacle in the development of coupled thermochemical-dynamic models has been the lack of interoperability between existing computational thermodynamics software and dynamics codes. Thermodynamics software packages often lack the appropriate bindings, and do not provide the high-level derivatives of thermodynamic properties required for efficient numerical solution to dynamics problems. Most significantly however, is the lack of a standard interface for the widely-used thermodynamic databases, which means that switching to using a different database is a laborious process. Furthermore, the databases themselves are defined for specific composition and phase spaces, and are not readily customizable for a particular assemblage or reduced model system, as is often desirable when coupling to dynamics.

The ENKI project (enki-portal.org) is an open-source web-based software project that addresses these issues through the development of tools for thermodynamic model description, development, and calibration. It provides a standard interface to interact with thermodynamic models of minerals, melts, and fluids, and supports a range of workflows, including calibration of new thermodynamic databases, generalized equilibrium calculations, disequilibrium reaction path modelling, and integration into geodynamics models.

To implement the theory described here, we utilize the two primary software packages in the ENKI project, ThermoEngine and ThermoCodegen. Both rely on a common set of packages (coder.py) for automatic generation of fast C code for custom thermodynamic databases from symbolic descriptions of thermodynamic models using SymPy. ThermoCodegen provides a software framework for description, storage and retrieval of the thermodynamic potential models of endmembers and phases using hierarchical xml (SPuD) files. The Coder module in ThermoEngine is a SymPy-based code-generation tool that uses symbolic differentiation to derive all other thermodynamic variables of the phases, and their derivatives, from the underlying potential model. Given a set of xml description files we can automatically generate fast compiled (C and C++) libraries that implement the thermodynamic models. Once a thermodynamic database of endmembers and phases has been created, a

custom reactions library describing the reactive system, the reaction stoichiometries, and the rate laws for irreversible reaction is built using ThermoCodegen, also using automatic code-generation. The hierarchical nature of the software components is illustrated in Figure 2.1. The reactions library is the principal means of interacting with the reactive system, and returns all the thermochemical variables of interest (ρ_i, μ_i^k, A_j Γ_i^k, Γ_i, C_{Pi}, α_i, s_i, β_i), and their derivatives with respect to P, T, and $\boldsymbol{C}$ (and ϕ_i for Γ_i^k/Γ_i) out to third order. All libraries are wrapped in python so that the system may be explored in a python environment or by directly interfacing with the underlying libraries. A major advantage of this software is that it allows the user to easily manage the complexity of the models so that they are customized for the particular system of interest, and produces reproducible and transparent code. Description of the ENKI software and example workflows for generating custom thermodynamic and reactive models will be the subject of future contributions.

Importantly, the thermodynamics and kinetics libraries have been designed to be interoperable with existing dynamics codes. Here we use the TerraFERMA software package (Wilson et al., 2017, terraferma.github.io) to model the dynamics. TerraFERMA leverages several advanced computational libraries (FEniCS and PETSc) along with a hierarchical options management system, SpuD, to facilitate development of reproducible and transparent Finite Element Models. Phase diagrams and simple reaction paths are calculated in well-documented Jupyter notebooks using the python interface.

2.7 Conclusions and future directions

The aim of this work was to lay out a basic framework that integrates the description of multiphase multicomponent thermodynamics, and geodynamics. We have done this by extending the description of two-phase flow to include a multiphase solid, and formulating reactive closures based on a set of stoichiometric reactions. We assume that reactions proceed irreversibly according to thermodynamic rate laws in which the reaction rates are proportional to the chemical affinities. In high temperature systems this has the primary

benefit of avoiding computationally expensive free-energy minimization. It also provides a more natural description of reaction as a time-dependent irreversible process. As the proximity to equilibrium depends on the rate of reaction relative to other fluxes, we can model both equilibrium and disequilibrium scenarios, removing the need to assume equilibrium a priori.

There are several major classes of problems that can be addressed. The first is the coupling of reaction with melt transport in the mantle. The framework incorporates explicit mineral-melt reactions thus opening up the ability to include peritectic and eutectic-style melting reactions into magma dynamics calculations. Such reactions more closely describe the actual melting reaction and allows us to self-consistently model both the melt chemistry and the mineralogy of the residual solid matrix. Application to the formation of high-porosity dunite channels by reactive melting of ascending melts is a primary target. Other open questions in magma dynamics where reactive feedbacks play a role include the fate of deep silica-rich melts of enriched pyroxenitic heterogeneities, the transition from viscous porous flow to brittle fracture at the base of the thermal boundary layer, flux melting and melt focusing in subduction zones, and the transport of subduction zone fluids across the slab-matle transition. Some of these processes require more complex solid rheologies which are readily included in the equations laid out here.

More generally, when coupled with conservation of energy, the reactive framework extends the reach of computational thermodynamics to irreversible reaction. In the absence of detailed kinetic information, application of irreversible thermodynamics to macroscopic heterogeneous reaction is limited to systems relatively close to equilibrium. However, even small degrees of overstepping may still have important geochemical and dynamic consequences. An example is metastability in subducting slabs which is predicted for both the breakdown of hydrous phases, as well as deep phase transitions involving olivine (Iidaka and Suetsugu, 1992; Mosenfelder et al., 2001) and pyroxene (Hogrefe et al., 1994). These have consequences for the depth range of fluid delivery to the overlying mantle wedge, and the

seismogenic and dynamic behaviour of the subducting slab in the upper mantle (Kirby et al., 1996; Tetzlaff and Schmeling, 2000) respectively. Disequilibrium processes are also pervasive in crustal magmatic systems. In particular, disequilibrium crystallization (La Spina et al., 2016; Arzilli et al., 2019) and volatile exsolution (Mangan and Sisson, 2000) during eruption have also been proposed as a driver of explosive fragmentation. The thermo-kinetic framework presented here would have the benefit over previous attempts to model overstepping in volcanic systems (e.g. Proussevitch and Sahagian, 2005), as it self-consistently couples the relative stability of different phases, the bulk density, and the latent heat of reaction.

Development of the theory and supporting software have been guided by the principles of tractability, self-consistency, flexibility, reproducibilty and extensibility. Any macroscale description is inherently approximate as averaging over processes at a local scale unavoidably results in a loss of information. The goal of coupled thermodynamic-geodynamic models is to understand reaction and the transfer of heat and mass at a large scale. The complexity of these processes requires us to use approaches that have a tractable level of complexity while still capturing key processes at the system scale. The approach described here is based on mixture theory, which describes variables as continuum fields and averages processes locally. Macroscopic behaviour of the system can still be captured, as evidenced by the success of continuum models in developing our understanding of magma dynamics and other porous media reactive transport problems. However, a continuum description for heterogeneous reaction kinetics is particularly challenging as, in contrast to geodynamic processes, chemical disequilibrium operates at the grain scale, in the form of crystal chemical zonation and fine-scale variations in modal abundance. As for other phenomenological processes, effective bridging between scales requires upscaling and averaging methods to inform the appropriate set of reactions and the kinetic rate laws for a given problem. Although such upscaling analysis has done for low temperature aqueous environments (e.g. Li et al., 2006), it is yet to be explored in mantle systems.

Chapter 3

A Simple Analogue Model for Mantle Melting: The Mg_2SiO_4–SiO_2 Binary System

3.1 Introduction

The melting relations and thermodynamic properties of mantle phases are fundamental to our understanding of planetary differentiation. The melt composition and solidus temperature during deep partial melting determines the dynamics of core formation (Siebert et al., 2013; Hirose et al., 2017) and crystallization of the early magma ocean (Labrosse et al., 2007; Monteux et al., 2016). In the modern Earth the systematics of partial melting control the location and extent of partial melting in the upper mantle, and may also account for the presence of melt within ultra-low velocity zones at the core-mantle boundary (Williams and Garnero, 1996; Lay et al., 2004). Much of our understanding of melting systematics has evolved from the study of simple systems comprising a reduced set of thermodynamic components. Inclusion of simple thermodynamic systems into coupled dynamic models therefore presents a tractable first step for understanding thermo-chemical coupling during melt and fluid transport.

MgO and SiO_2 are the most abundant oxides in the mantle making the Mg_2SiO_4–SiO_2 an important bounding binary in the chemical evolution of Earth's interior. It was one of the first systems to be systematically studied in the early days of geochemical thermodynamics (Bowen and Anderson, 1914), and since then has formed a basis for our understanding of silicic magmatic systems. Early experimental studies on liquidus relations showed that enstatite melts incongruently at atmospheric pressure (Bowen and Anderson, 1914; Chen

and Presnall, 1975). The presence of eutectic melting between enstatite and quartz and low pressure liquid immiscibility in high silica melts was also revealed (Ol'shanskii, 1951; Hageman and Oonk, 1986). Subsequent studies demonstrated a systematic shift in the composition of the cotectic between forsterite and enstatite to lower melt silica contents with increasing pressure (Taylor, 1973; Chen and Presnall, 1975; Kato and Kumazawa, 1985; Liu and Presnall, 1990; Herzberg and Zhang, 1998; Presnall et al., 1998), causing a transition from peritectic (en $\rightarrow$ fo + lq) to eutectic (fo + en $\rightarrow$ lq) melting of enstatite around 0.5 GPa (Hudon et al., 2005). The shift in eutectic melt composition to lower silica has a fundamental influence on the melting systematics of basaltic mantle melts (Walter, 1998). During open system melting the gradient in equilibrium silica content drives open-system reaction between the ascending melt and the surrounding residue

$$\mathrm{en} + \mathrm{lq}_1 \rightarrow \mathrm{fo} + \mathrm{lq}_2 \tag{3.1}$$

which is accompanied by an increase in porosity (Kelemen, 1990). Near-fractional partial melting requires transport of melt in chemically isolated channels (Spiegelman and Kenyon, 1992). It has been suggested that open-system incongruent melting itself is responsible for initiating a reactive channeling instability (Aharonov et al., 1995, 1997; Spiegelman et al., 2001). The Mg_2SiO_4–SiO_2 binary therefore provides a rich analog model for exploring reactive transport and related phenomena using our new multiphase reactive formulation. The presence of both forsterite-enstatite and enstatite-quartz melting eutectics also allows us study the interactions between melts of different lithologies. While natural systems permit more direct model-observation intercomparison, inclusion of the Mg_2SiO_4–SiO_2 sub-system provides a means to tractably explore complex couplings between eutectic and peritectic style melting and transport dynamics.

Description of polybaric partial melting requires a model of the Gibbs free energy of the melt as a function of pressure, temperature and composition. The thermodynamic pro-

gram MELTS is widely used for modelling silicic magmatic systems (Ghiorso and Sack, 1995). However, the underlying thermodynamic model for the silicate melt is calibrated from experiments in natural systems for which the free energy surface is relatively flat. This parameterization does not extend to the Mg_2SiO_4–SiO_2 binary in which the melt contains substantial short-range ordering and greater curvature of the free energy surface. It is therefore necessary to construct and calibrate a custom thermodynamic model for melt solution along the binary. The purpose of this chapter is to calibrate a simple melt solution model in the Mg_2SiO_4–SiO_2 binary in order to investigate open-system melt-rock reaction in the mantle. As our goal is not to capture the full complexity of the phase diagram, we will use a simple asymmetric regular formulation that successfully captures the variation of the olivine-orthopyroxene cotectic with pressure.

3.2 Thermodynamic model for the Mg_2SiO_4–SiO_2 binary system

3.2.1 Subsolidus phase assemblage

The subsolidus phase assemblage along the Mg_2SiO_4–SiO_2 binary comprises pure forsterite olivine ($fo(ol)$, Mg_2SiO_4), pure enstatite orthopyroxene ($en(opx)$, $Mg_2Si_2O_6$), and a pure silica quartz ($q(qz)$, SiO_2). As these are all pure phases we simply us the standard state models from the Berman database (Berman, 1988). The molar Gibbs free energy of ol and opx is

$$G_{ol} = \mu^{\circ}_{fo} \tag{3.2}$$

$$G_{opx} = \mu^{\circ}_{en} \tag{3.3}$$

Where μ°_{fo} and μ°_{en} are the standard state chemical potentials of forsterite and orthoenstatite. Quartz undergoes a polymorphic phase transition along the solidus at low pressure, transitioning from β-quartz (bqz) to β-cristobalite ($bcrs$) (Hudon et al., 2002). We include

this polymorphic phase transition within the phase description of qz by setting

$$G_{qz} = \min(\mu^{\circ}_{bqz}, \mu^{\circ}_{bcrs}) \tag{3.4}$$

While enstatite also undergoes a polymorphic transition from protoenstatite to orthoenstatite at around 1.5GPa (Chen and Presnall, 1975), we have omitted this in this simple treatment.

3.2.2 Melt solution model

We use the melt endmember models from the xMELTS calibration (Ghiorso et al., 2007). The melt solution in Mg_2SiO_4–SiO_2 is very non-ideal, with strong interactions between melt species. Certain features of the phase diagram, including the low pressure miscibility gap at high-silica concentrations, are very sensitive to the relative Gibbs free energy of mixing. To accurately capture this non-ideality requires an associated speciation model (Holland and Powell, 2003), or a highly parameterized quasichemical model (Harvey et al., 2015; Kim et al., 2017) to account for ordering of species at intermediate silica contents. Both of these approaches require internal solvers to calculate the melt speciation. For our present purposes, we are more interested in the general topology for low and intermediate silica contents. We therefore model solution in the melt with a numerically efficient binary asymmetric regular solution model (Berman and Brown, 1984).

We take the melt endmembers to be silica liquid ($q(f)$, Si_2O_4) and forsterite liquid ($fo(ol)$, Mg_2SiO_4), where the silica endmember is used on a four oxygen basis to improve the form of the entropy of mixing. The expression for the molar Gibbs free energy of the melt solution is comprised of three components: the standard state Gibbs free energy of the pure endmembers G°_f, the ideal entropy of mixing G^{ideal}_f, and the excess energy due to non-ideal mixing G^{excess}_f.

$$G_f = \underbrace{x^q_f \mu^{q\circ}_f + x^{fo}_f \mu^{fo\circ}_f}_{G^{\circ}_f} + \underbrace{x^q_f RT \ln x^q_f + x^{fo}_f RT \ln x^{fo}_f}_{G^{ideal}_f} + \underbrace{\left(x^q_f W_{q,fo} + x^{fo}_f W_{fo,q}\right) x^q_f x^{fo}_f}_{G^{excess}_f} \tag{3.5}$$

Table 3.1: Data Sources for Mg_2SiO_4–SiO_2 melt calibration

Bowen and Anderson (1914)
Boyd et al. (1964)
Taylor (1973)
Chen and Presnall (1975)
Kato and Kumazawa (1985)
Hageman and Oonk (1986)
Herzberg and Zhang (1998)
Presnall et al. (1998)
Liu and Presnall (1990)
Hudon et al. (2005)

Where x_f^q and $x_f^{fo} = 1 - x_f^q$ are the molar silica (Si_2O_4) and forsterite concentrations respectively. The chemical potentials of the pure endmembers $\mu_f^{q\circ}$ and $\mu_f^{fo\circ}$ are taken from the xMELTS calibration (Ghiorso et al., 2007). $W_{q,fo}$ and $W_{fo,q}$ are binary interaction parameters. We assume that both parameters are first order functions of pressure P such that

$$W_{q,fo} = W_{q,fo}^H - PW_{q,fo}^V \tag{3.6}$$

$$W_{fo,q} = W_{fo,q}^H - PW_{fo,q}^V \tag{3.7}$$

3.2.3 Calibration

The interaction parameters are fit from experimental phase equilibrium constraints on the liquidus surfaces. The liquidus surfaces are defined by the melt-solid equilibria

$$G_{ol} = \mu_f^{fo} \tag{3.8}$$

$$G_{opx} = \mu_f^{fo} + \frac{1}{2}\mu_f^q \tag{3.9}$$

$$G_{qz} = \frac{1}{2}\mu_f^q \tag{3.10}$$

and the surface of the high silica miscibility gap is given by the melt-melt equilibrium

$$\begin{aligned} \mu_f^q(x_1) &= \mu_f^q(x_2) \\ \mu_f^{fo}(x_1) &= \mu_f^{fo}(x_2) \end{aligned} \tag{3.11}$$

where x_1 and x_2 correspond to compositions on either side of the solvus.

Given models of the solid phases, the interaction parameters can be fit from a set of experimental constraints which each constrain a point on the liquidus surface in pressure-temperature-composition (P-T-x) space. This is done by finding the values of the mixing parameters that minimize a set of residuals of the form

$$A_i = G_{ol}(P_i, T_i) - \mu_f^{fo}(P_i, T_i, x_i) \tag{3.12}$$

Where the conditions (P_i, T_i, x_i) represent a single experimental liquidus constraint. To provide a good fit, a large experimental database is required with constraints that are spread widely in P-T-x space.

We compiled experimental constraints from the literature. The list of data sources are given in Table 3.1. Constraining melt compositions for small degrees of melting remains a major challenge in experimental petrology. Experiments therefore typically take the approach of bracketing the liquidus surface with a series of distinct starting compositions. For this kind of data we take the liquidus temperature to be the midpoint of the liquidus bracket. To increase the number of data-points, and to ensure a good fit for the *ol-opx* cotectic, we supplement the experimental brackets with some synthetic data taken from existing interpolated phase diagrams.

We carried out the calibration in Python using scipy.optimize.leastsq. The thermodynamic models of the phases were described using a python package we developed called Pyezthermo which served as a prototype for thermocodegen (see section 2.6 above). The phase models have been tested against models developed using thermocodegen, which is used

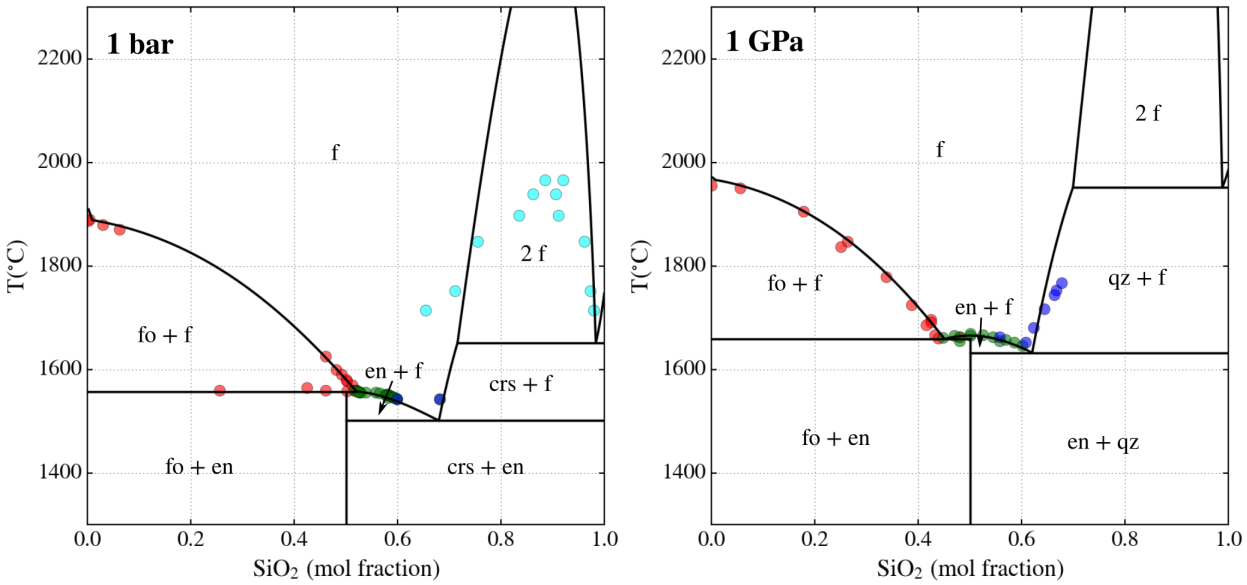

Figure 3.1: Calculated Mg_2SiO_4–SiO_2 binary phase diagram at 1 bar (left) and 1 GPa (right). Phase abbreviations as in text. Colored markers include both experimental brackets and interpolated data from Bowen and Anderson (1914) and Hudon et al. (2005).

in the remaining chapters, and were found to be identical.

The fitted interaction parameters are as follows

$$\begin{aligned} W^H_{q,fo} &= 35168 \text{ J mol}^{-1} \quad W^V_{q,fo} = 0.7959 \text{ J mol}^{-1}\text{bar}^{-1} \\ W^H_{fo,q} &= -56504 \text{ J mol}^{-1} \quad W^V_{fo,q} = -1.8783 \text{ J mol}^{-1}\text{bar}^{-1} \end{aligned} \tag{3.13}$$

Calculated phase diagrams using these values at 1 bar and 1 GPa are shown in Figure 3.1. As expected, the phase diagram provides a poor match at the high silica end where there a fewer experimental constraints. This is particularly evident for the miscibility gap which is very sensitive to the excess energy of mixing. The phase diagram does, however, provide a good description of the variation in the fo-en cotectic with decreasing pressure, as shown in Figure 3.2.

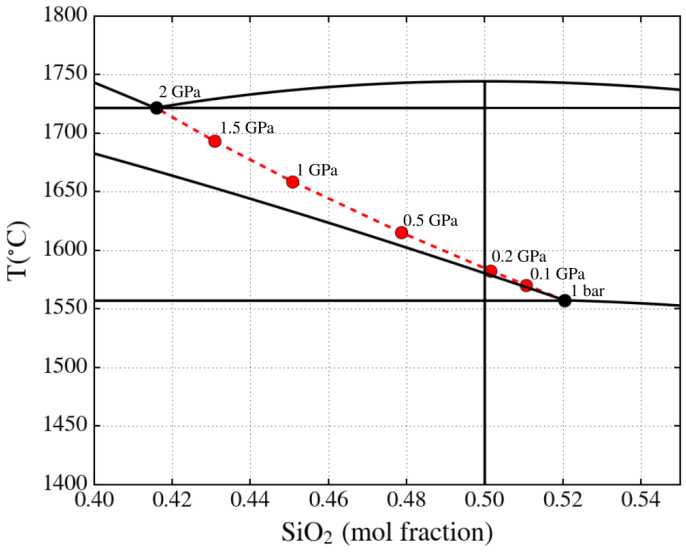

Figure 3.2: Pressure dependence of fo-en cotectic. The solid lines show the phase boundaries for the 1 bar and 2 GPa phase diagrams. The dashed line shows the variation in the cotectic melt composition with increasing pressure. In this calibration the melting reaction transitions from eutectic to peritectic around 0.2 GPa

3.3 Comparison to the melting systematics of natural peridotites

The Mg_2SiO_4–SiO_2 sub-system provides a useful framework for understanding complex phase equilibria in ultramafic and mafic rocks. However, in contrast to melting along the binary, natural peridotites melt incongruently up to pressures of 2 GPa (Figure 3.3). This is reflected in higher silica concentrations in natural peridotite melts. As noted by Kushiro (1975) and others (Ryerson, 1985; Hirschmann et al., 1998), this can be attributed to the presence of monovalent and divalent cations which have a tendency to depolymerize the melt and, in so doing, decrease the silica activity. This enhances the stability of olivine relative to orthopyroxene resulting in an expansion of the olivine phase field. A simple way of approximating the melting behavior of natural peridotites is with the addition of a third component as a 'depolymerising agent' which acts as a proxy for the combined behavior of oxides, other than MgO and SiO_2, in natural systems. This is shown for the Mg_2SiO_4–SiO_2–K_2O ternary phase diagram in Figure 3.4(a), which shows a strong deflection in the fo-en cotectic for small additions of K_2O. Below this in Figures 3.4(b) and (c) we have fit an

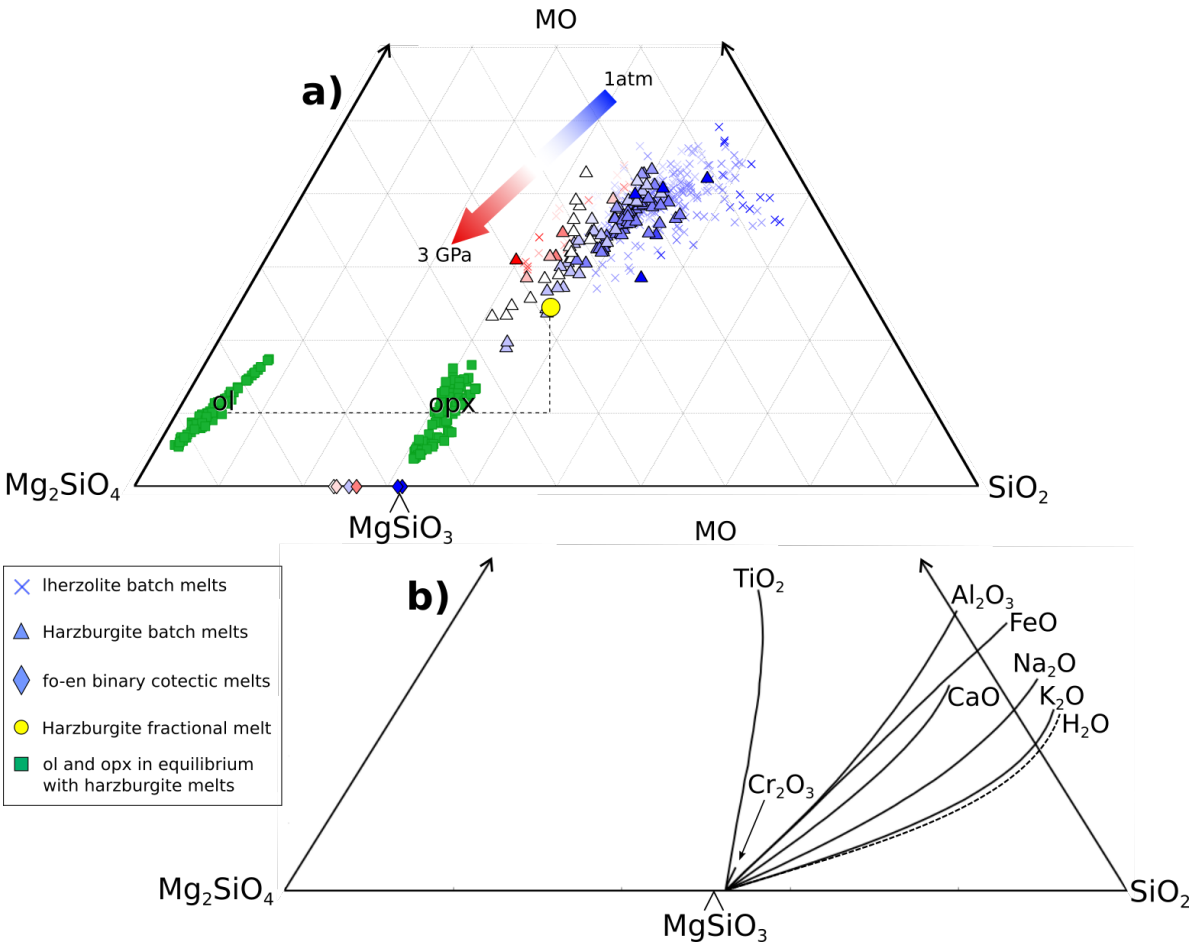

Figure 3.3: a) Experimental olivine- and orthopyroxene-saturated partial melts from the LEPR database plotted in wt concentration where MO accounts for all oxides other than MgO and SiO_2. Note that all natural melts are more silicic than the binary melts. The fractional harzburgite melt composition is from Wasylenki et al. (2003) b) forsterite-enstatite cotectic boundary plotted on a similar ternary but in molar concentration and reproduced from Kushiro (1975). The concentrations of the oxides have been scaled by the number of cations per formula unit. Note the deflection of the cotectic boundary with the addition of monovalent and divalent cations.

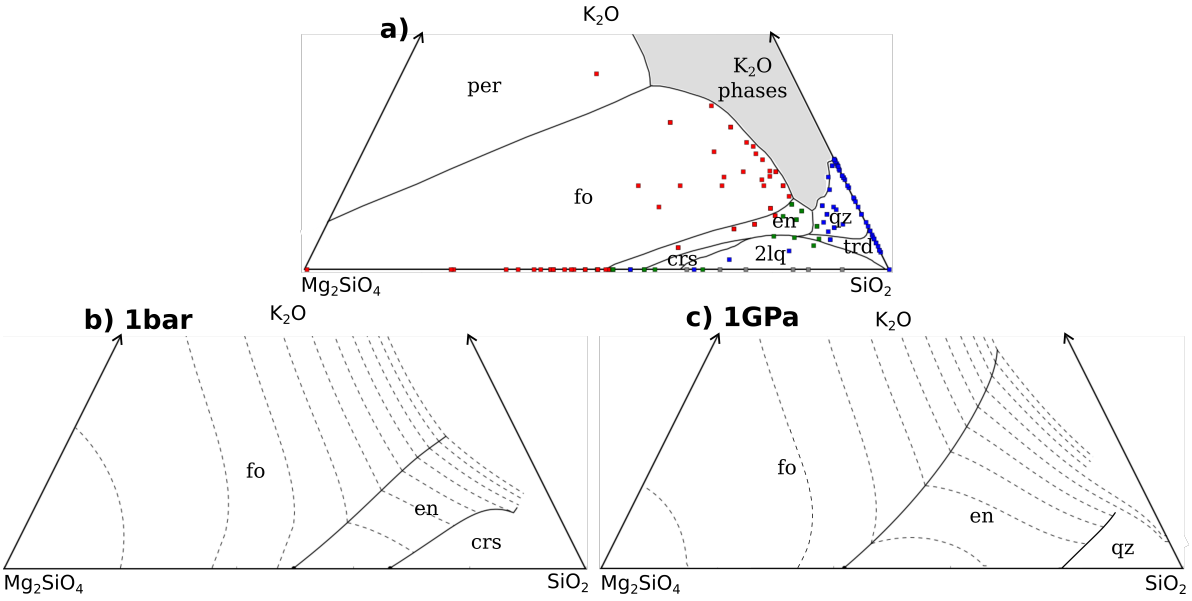

Figure 3.4: a) Experimental liquidus constraints with phase boundaries reproduced from the quasichemical model of Kim et al. (2017). b) Approximate thermodynamic fit at 1bar using a regular asymmetric solution model. The dashed lines show the liquidus temperature contours. c) Approximate thermodynamic fit at 1 GPa
. Concentrations are in mass units in all plots.

approximate ternary liquidus surface, again using a regular asymmetric solution, but with the addition of a K_2O component in the melt to modify the silica activity.

3.4 Summary

In conclusion, we have calibrated a simple model for melting at low pressure in the Mg_2SiO_4–SiO_2 binary system. While an asymmetric binary regular solution model does not accurately capture some details of the phase diagram, including the low-pressure miscibility gap in high-silica melts, it does capture the general liquidus morphology. Moreover we are able to accurately reproduce the variation in silica concentration of the fo-en cotectic with decreasing pressure. This arises from the expansion of the olivine phase field in response to pressure-induced changes in the melt polymerization and is reflected in the systematics of natural peridotite melts.

The Mg_2SiO_4–SiO_2 binary serves as useful model to explore coupling between thermody-

namics and magma dynamics in the mantle. It provides a reasonable first-order approximation of peridotite melting, while also containing sufficient complexity to push the boundaries of what previous reactive transport models have been able to deal with. The workflow for integrating this system into a geodynamics code in described in the following chapter.

Chapter 4

Model Examples of Disequilibrium Reaction and Reactive Transport in the Mg_2SiO_4-SiO_2 System

4.1 Introduction

The goal of this chapter is to demonstrate the application of the general kinetic formulation, described in chapter 2, for integrating thermodynamics and geodynamics. The theory serves two purposes: the first is to extend the reach of computational thermodynamics in petrology to the modeling macroscopic irreversible reaction; the second is to integrate computational thermodynamics and complex phase relations with computational geodynamics. As described in chapter 1, this particularly pertains to open-system reactive flow of melts and fluids. Here we apply the framework to the Mg_2SiO_4-SiO_2 binary system. This is an important bounding binary that has long helped to elucidate phase relations relations in mafic and ultramafic rocks. Despite its relative simplicity compared to natural systems, the Mg_2SiO_4-SiO_2 system contains a variety of reaction morphologies, including divariant liquidus surfaces, eutectic and peritectic melting reactions, and subsolidus polymorphic phase transitions. Inclusion of such a system in magma dynamics marks a significant advance on previous theories, and opens up the potential for modeling more realistic melt-rock reactions.

To gain intuition for disequilibrium reaction in this system we will present a hierarchy of models beginning with the simplest possible 0-D batch reactor models in which there is no advection or diffusion. These models demonstrate the consistency with the equilibrium phase diagram in the equilibrium limit, and also allow us to explore the impact of choices made in the kinetic models. The behaviour of disequilibrium systems can be non-intuitive, and

these simple models provide a framework for understanding the time-dependent behaviour of the system. We then add in diffusion of heat and mass to explore open-system reaction in a dynamically simple system. Finally, we will integrate the thermodynamic and reactive model into the full magma dynamics equations derived in chapter 2.

4.2 Mg_2SiO_4-SiO_2 system description

At low pressures, the mineral phases we must consider are Mg_2SiO_4 olivine, $MgSiO_3$ orthopyroxene, and a polymorphic silica phase. All the minerals are pure stoichiometric phases, but for clarity, and consistency with the nomenclature in the reactive framework described above, we refer to the phases as olivine (ol), orthopyroxene (opx) and quartz (qz), and to their respective endmember compositions as forsterite ($fo(ol)$, Mg_2SiO_4), enstatite ($en(opx)$, Mg_2SiO_6), and silica ($q(qz)$, SiO_2). The silicate melt (f) comprises two endmembers, which we take to be forsterite ($fo(f)$, Mg_2SiO_4) and silica ($q(f)$, Si_2O_4).

There are five phase endmembers in total in the system, as such five variables are required to fully characterize the phase assemblage. These include the proportions of the four phases (ϕ_{ol}, ϕ_{opx}, ϕ_{qz}, ϕ_f) and the melt composition c_f^q. There is only one compositional variable, as the melt is the only solution phase. The vector of phase compositions is then

$$\boldsymbol{C} = \begin{bmatrix} \boldsymbol{c}_f \\ \boldsymbol{c}_{ol} \\ \boldsymbol{c}_{opx} \\ \boldsymbol{c}_{qz} \end{bmatrix} = \begin{bmatrix} \begin{pmatrix} c_f^q \\ c_f^{fo} \end{pmatrix} \\ c_{ol}^{fo} \\ c_{opx}^{en} \\ c_{qz}^{q} \end{bmatrix} = \begin{bmatrix} \begin{pmatrix} c_f^q \\ 1 - c_f^q \end{pmatrix} \\ 1 \\ 1 \\ 1 \end{bmatrix} \tag{4.1}$$

4.2.1 Thermodynamics

We use the same thermodynamic models as described in the previous chapter. As described there, the Gibbs free energy models of pure solid phases are taken from the Berman

database (Berman, 1988). The silica phase undergoes a polymorphic phase transition from quartz to cristobalite along the liquidus at low pressure. We account for this by including both the β-quartz ($\beta - qz$) and β-cristobalite ($\beta - crs$) endmember models within the phase solution of qz, and assume that it always occurs as the stable polymorph. The melt solution is modeled as described above. The melt enedmembers are modeled using the xMELTS calibration (Ghiorso et al., 2007), and the melt solution is modeled using the asymmetric regular solution model with the mixing parameters given above.

4.2.2 Reactions

The full compositional space of the phase endmembers is described by the formula matrix

$$\boldsymbol{F} = \begin{array}{c} \\ \mathrm{SiO_2} \\ \mathrm{MgO} \end{array} \begin{array}{c} \begin{array}{ccccc} q_f & fo_f & fo_{ol} & en_{opx} & q_{qz} \end{array} \\ \begin{bmatrix} 2 & 1 & 1 & 2 & 1 \\ 0 & 2 & 2 & 2 & 0 \end{bmatrix} \end{array} \tag{4.2}$$

There are five phase endmembers in total, and two system components, meaning that there are three independent reactions. As we are considering reaction paths involving a partial melt we will use the set of independent melt-mediated reactions

$$\begin{aligned} &1.\ fo(ol) = fo(f) \\ &2.\ en(opx) = \frac{1}{2}q(f) + fo(f) \\ &3.\ q(qz) = \frac{1}{2}q(f) \end{aligned} \tag{4.3}$$

we use the reaction indexes (1, 2, 3) to refer to the reaction rates and affinities of the respective reactions, as illustrated in Figure 4.2. In this simple system, each of these reactions corresponds to the liquidus surfaces of the different solid phases. As such the liquidus surfaces mark the contours in pressure-temperature-composition space along which $A_j = 0$. The

affinity contours for the reactions are shown in Figure 4.1.

The molar stoichiometric matrix for this reactive system is

$$\tilde{\boldsymbol{\nu}} = \begin{bmatrix} \begin{pmatrix} \tilde{\nu}^{q}_{f,1} \\ \tilde{\nu}^{fo}_{f,1} \end{pmatrix} & \begin{pmatrix} \tilde{\nu}^{q}_{f,2} \\ \tilde{\nu}^{fo}_{f,2} \end{pmatrix} & \begin{pmatrix} \tilde{\nu}^{q}_{f,3} \\ \tilde{\nu}^{fo}_{f,3} \end{pmatrix} \\ \tilde{\nu}^{fo}_{ol,1} & \tilde{\nu}^{fo}_{ol,2} & \tilde{\nu}^{fo}_{ol,3} \\ \tilde{\nu}^{en}_{opx,1} & \tilde{\nu}^{en}_{opx,2} & \tilde{\nu}^{en}_{opx,3} \\ \tilde{\nu}^{q}_{qz,1} & \tilde{\nu}^{q}_{qz,2} & \tilde{\nu}^{q}_{qz,3} \end{bmatrix} = \begin{bmatrix} \begin{pmatrix} 0 \\ 1 \end{pmatrix} & \begin{pmatrix} 1/2 \\ 1 \end{pmatrix} & \begin{pmatrix} 1/2 \\ 0 \end{pmatrix} \\ -1 & 0 & 0 \\ 0 & -1 & 0 \\ 0 & 0 & -1 \end{bmatrix} \tag{4.4}$$

Where we have put parentheses around the melt coefficients for clarity. In mass-weighted units the stoichiometric coefficients become

$$\boldsymbol{\nu} = \begin{bmatrix} \begin{pmatrix} 0 \\ 1 \end{pmatrix} & \begin{pmatrix} \frac{M^{q}_{f}}{2M^{en}_{opx}} \\ \frac{M^{fo}_{f}}{M^{en}_{opx}} \end{pmatrix} & \begin{pmatrix} 1 \\ 0 \end{pmatrix} \\ -1 & 0 & 0 \\ 0 & -1 & 0 \\ 0 & 0 & -1 \end{bmatrix} \tag{4.5}$$

Where M^{k}_{i} is the molar mass of endmember k in phase i. From equation (2.9) the reactive mass transfer rates for each phase are then

$$\begin{aligned} \Gamma_{f} &= \Gamma^{q}_{f} + \Gamma^{fo}_{f} = \left(\frac{M^{q}_{f}}{2M^{en}_{opx}}R_2 + R_3\right) + \left(R_1 + \frac{M^{fo}_{f}}{M^{en}_{opx}}R_2\right) = R1 + R_2 + R_3 \\ \Gamma_{ol} &= \Gamma^{fo}_{ol} = -R_1 \\ \Gamma_{opx} &= \Gamma^{en}_{opx} = -R_2 \\ \Gamma_{qz} &= \Gamma^{q}_{qz} = -R_3 \end{aligned} \tag{4.6}$$

Where R_j is the reaction rate of reaction j, in units of ρs^{-1}. By construction the reactive mass transfer terms sum to zero.

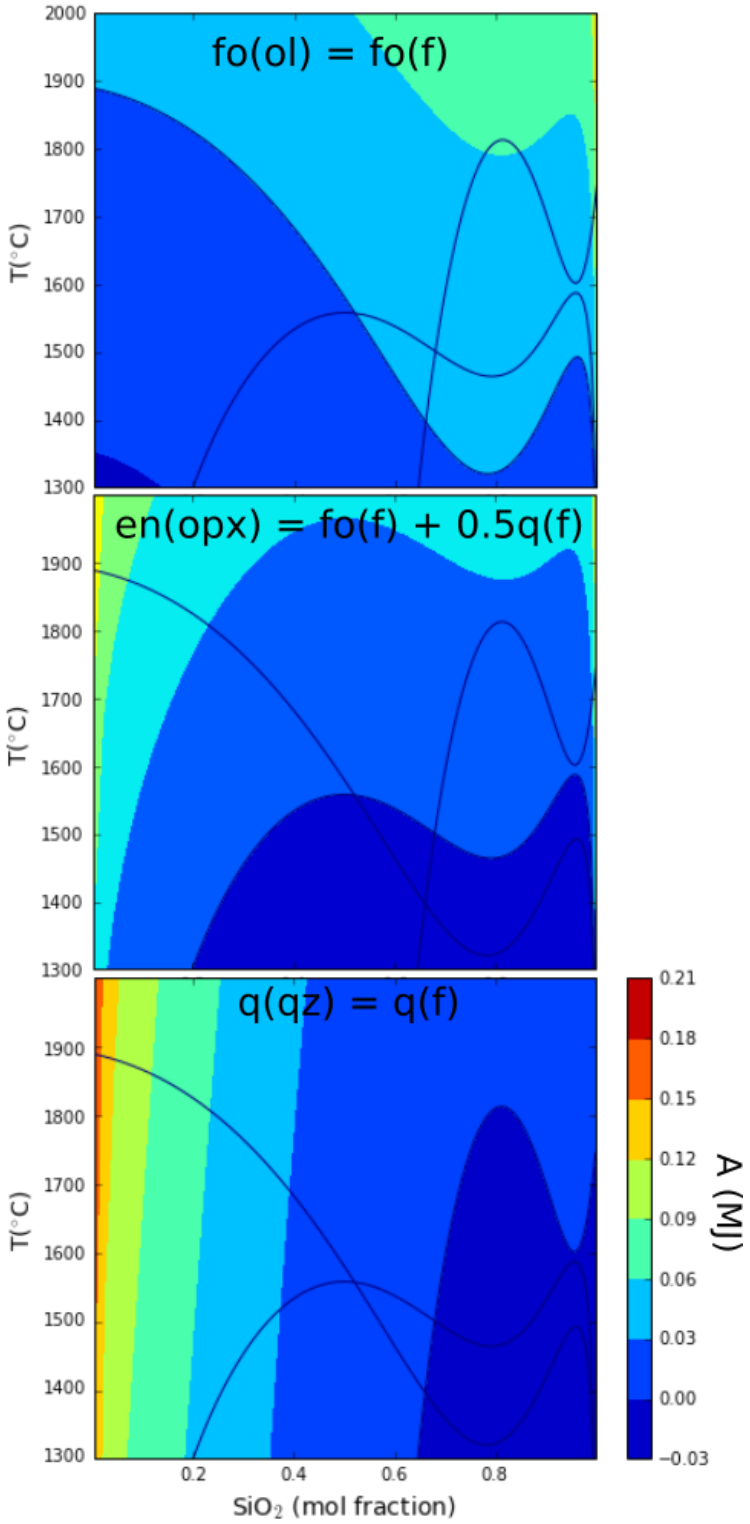

Figure 4.1: $Mg_2SiO_4 - SiO_2$ binary at 1bar contoured for the three different melting reactions

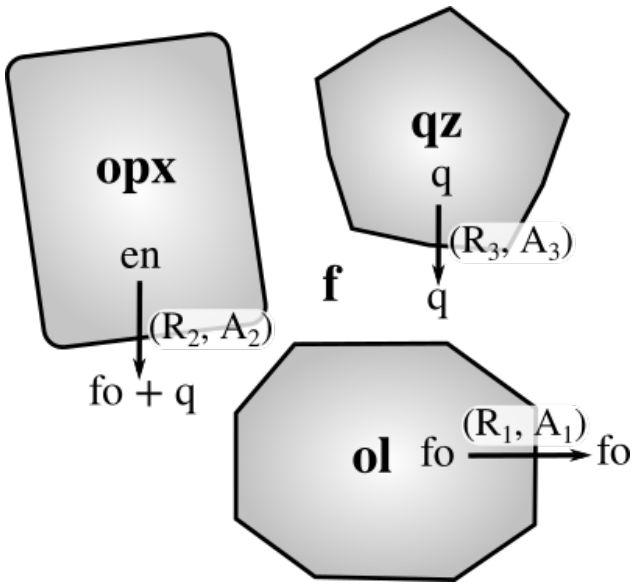

Figure 4.2: Cartoon illustration of reactive system in the Mg_2SiO_4–SiO_2 system, showing the phase assemblage and the three reactions. R_j and A_j refer to the reaction rate and affinity of reaction j.

4.2.3 Kinetics

We assume the reactions proceed at independent rates according to a piecewise rate law as described in chapter 2.

$$R_j = \begin{cases} r_j^+ S_j^+(\mathbf{\Phi}_{rj}) f^+(A_j), \ A_j \geq 0 \\ r_j^- S_j^-(\mathbf{\Phi}_{rj}) f^-(A_j), \ A_j < 0 \end{cases} \tag{4.7}$$

The rate constant is assumed to have an Arrhenius temperature dependence

$$r_j = \begin{cases} r_j^+ \exp\left(-\frac{T}{T_0}\right), \ A_j \geq 0 \\ r_j^- \exp\left(-\frac{T}{T_0}\right), \ A_j < 0 \end{cases} \tag{4.8}$$

As a simplification, we assume that T_0 is the same for all reactions, but we allow the pre-exponential factors to differ for the forward (melting) and reverse (crystallization) reactions. Without evidence to the contrary, we assume that the rate constants are the same for all three reactions. These options may be easily modified if necessary.

In partially molten rocks, melt is distributed in tubes along grain boundaries. Given this geometry, it would be expected that the reactive surface area be proportional to $\sqrt{\phi_f}$. However, since the derivative of $\sqrt{\phi_f}$ becomes singular at $\phi_f = 0$, we use the following, more numerically stable, function for the reactive surface area

$$S_j = \begin{cases} S_0 \frac{\phi_{r,j}}{\phi_{r,j}+\epsilon}, & A_j \geq 0 \\ S_0 \frac{\phi_f}{\phi_f+\epsilon}, & A_j < 0 \end{cases} \tag{4.9}$$

where $\phi_{r,1} = \phi_{ol}, \phi_{r,2} = \phi_{opx}, \phi_{r,3} = \phi_{qz}$, and S_0 is the total surface area per unit volume of the aggregate solid phase. The parameter ϵ controls how rapidly the reactive surface area tends to zero. We use $\epsilon = 0.1$ for all the model examples below.

In high temperature magmatic systems, reaction is fast and affinities of reaction are likely small enough that a linear thermodynamic driving function can be used

$$f(A_j) = \frac{M_0}{M_j}\frac{A_j}{RT}. \tag{4.10}$$

where M_0 is a reference molar mass, and M_j is the mass of reaction defined above. We scale the affinity by M_j to normalize each reaction to one mole of reactant.

4.2.4 Implementation

The thermodynamic and kinetic models are constructed using custom thermodynamics and kinetic modeling tools from the ENKI software project (http://enki-portal.org/). Specifically we use the thermocodegen package and coder module of thermoengine to generate the custom thermodynamics and kinetics libraries. All the choices of functions, variables and parameters described above for the Gibbs free energy models of the endmembers and phases are recorded in hierarchical xml schema using the thermocodegen package. These schema are then used as input to coder which is a SymPy-based code-generation module which generates custom compiled C++ libraries with python bindings. Coder uses auto-

matic symbolic differentiation to derive all of the thermodynamic variables (i.e. μ_i^k, ρ_i, s_i, C_{Pi}, α_i) and their derivatives, from the underlying Gibbs free energy models (G_i). This ensures thermodynamic self-consistency, and avoids the need to hand-code these functions. The software utilizes the natural hierarchical structure of thermodynamic models in which the phase models are dependent on the underlying endmember models.

Given this compiled thermodynamic database, the reactions library is also generated in a similar way: the stoichiometries and reaction rates of the reactive system are described in a hierarchical xml schema which are input into a code generation module within the thermocodegen package. This generates a custom compiled C++ reactions library with Python bindings through which all of the thermodynamic properties of the underlying endmembers and phases can be accessed, as well as the properties of the reactions including the stoichiometries ($\boldsymbol{\nu}_j$), chemical affinities (A_j), reaction rates (R_j), and reactive mass transfer terms (Γ_i and Γ_i^k), as well as their derivatives where appropriate.

4.3 0-D batch reactors

We begin by exploring the disequilibrium behaviour of the system by considering a 0-D batch reactor model. In this case, all spatial dependence of the model is removed and the governing equations reduce to a set of ordinary differential equations describing conservation of mass and energy.

$$\frac{\mathrm{d}}{\mathrm{d}t}\rho_i\phi_i = \Gamma_i \quad i = ol,\ opx,\ qz,\ f \tag{4.11}$$

$$\rho_f\phi_f\frac{\mathrm{d}}{\mathrm{d}t}c_f^q = \Gamma_f^q - c_f^q\Gamma_f \tag{4.12}$$

$$\sum_{i=1}^{N}\left[\rho_i\phi_i C_{Pi}\frac{\mathrm{d}T}{\mathrm{d}t} - \phi_i\alpha_i T\frac{\mathrm{d}P}{\mathrm{d}t} + Ts_i\Gamma_i\right] = Q_{ext} - \sum_{k=1}^{K_i}\sum_{i=1}^{N}\mu_i^k\Gamma_i^k \tag{4.13}$$

where Q_{ext} is the external heating rate in $\mathrm{Jm^{-3}s^{-1}}$. As the equations are written on a mass per volume basis, the total volume of the system may increase or decrease during reaction: this shows up as a change in the total volume fraction of the phases $\sum_i \phi_i$. In

Table 4.1: Parameters, definitions, and reference values for batch reactor models

Temperature	T_0	1925 K
Pressure	P_0	1.2 GPa
Density	ρ_0	3000 $\mathrm{kgm^{-3}}$
Heat capacity	C_{P0}	1 $\mathrm{Jkg^{-1}K^{-1}}$
Expansivity	α_0	5e-5 $\mathrm{K^{-1}}$
Gravity	g	9.81 $\mathrm{ms^{-2}}$
Solid velocity	W_0	(0.1, 0.02) $\mathrm{myr^{-}1}$
Heating rate	Q_{ext}	$\mathrm{Jm^{-3}}s^{-1}$
Rate constant	r_0	1e-8 $\mathrm{kgm^{-2}s^{-1}}$
Reactive surface area	S_0	6000 $\mathrm{m^2m^{-3}}$
Reaction rate	$r^* = \frac{r_0 S_0}{\rho_0}$	2e-8 $\mathrm{s^{-1}}$
Damköhler number	$Da_Q = \frac{\rho_0 C_{P0} T_0 r^*}{Q_{ext}}$	1e2–1e5
Adiabatic parameter	$Ad = \frac{\alpha_0 P_0}{\rho_0 C_{P0}}$	
Decompression rate	$\frac{\mathrm{d}P}{\mathrm{d}t} = -\rho_0 g W_0$	

the full partial differential equations this expansion or contraction would be taken up in the divergence of the solid and melt velocity fields. The 0-D equations could be written in a fully mass-conservative form by writing them on a mass basis and multiplying the reactive mass transfers by the system volume, but here for consistency we will use the density-based equations. A full derivation for conservation of mass and energy in an 0-D open system subject to inflow/outflow of mass and heat is provided in Appendix C.

We non-dimensionalize using the following scaling parameters:

$$\begin{aligned} t = \frac{t'}{r^*}, \quad T = T_0 T', \quad P = P_0 P', \quad \rho_i = \rho_0 \rho_i', \quad \Gamma_i = \rho_0 r^* \Gamma_i', \\ C_{Pi} = C_{P0} C_{Pi}', \quad \alpha_i = \alpha_0 \alpha_i', \quad s_i = C_{P0} s_i', \quad \mu_i^k = C_{P0} T_0 \mu_i^{k\prime} \end{aligned} \tag{4.14}$$

Where r^* is a a measure of the the reaction rate given by

$$r^* = \frac{r_0 S_0}{\rho_0} \tag{4.15}$$

Rewriting the reduced governing equations in terms of non-dimensional variables, and

dropping the primes, gives us

$$\frac{\mathrm{d}}{\mathrm{d}t}\rho_i\phi_i = \Gamma_i \quad i = ol,\ opx,\ qz,\ f \tag{4.16}$$

$$\rho_f\phi_f\frac{\mathrm{d}}{\mathrm{d}t}c_f^q = \Gamma_f^q - c_f^q\Gamma_f \tag{4.17}$$

$$\sum_{i=1}^{N}\left[\rho_i\phi_i C_{Pi}\frac{\mathrm{d}T}{\mathrm{d}t} - \phi_i\alpha_i T\frac{\alpha_0 P_0}{\rho_0 C_{P0}}\frac{\mathrm{d}P}{\mathrm{d}t} + Ts_i\Gamma_i\right] = \frac{1}{Da_Q} - \sum_{k=1}^{K_i}\sum_{i=1}^{N}\mu_i^k\Gamma_i^k \tag{4.18}$$

Da_Q is a dimensionless Damkohler number describing the relative rates of external heating and reaction

$$Da_Q = \frac{\rho_0 C_{P0} T_0 r^*}{Q_{ext}}. \tag{4.19}$$

In the following examples, we solve the initial value problem for $\boldsymbol{\phi}$, c_f^q and T in python using a numerical ODE solver that allows flexibility in the choice of integration method.

4.3.1 Adiabatic reaction paths

To explore the reaction paths taken by the system as it converges to equilibrium, let us first consider the simplest case of an isobaric adiabatic system. For this system, equations (4.16)-(4.18) are further simplified as $\left(\frac{\mathrm{d}P}{\mathrm{d}t}, Da_Q^{-1}\right) = \mathbf{0}$. As this is a perfectly isolated system, the only way to get reaction is if the system is initiated with a disequilibrium assemblage. It serves as a useful test to ensure the reactive framework we have chosen actually converges to equilibrium under closed-system conditions, and to demonstrate the coupling between temperature and reaction. Such a set-up could also have some practical applications for understanding how systems behave when suddenly displaced from equilibrium. For example, it could serve as a model for understanding reaction paths during experiments when the experimental apparatus is suddenly heated and left to anneal. Or in natural crustal magmatic systems when intrusion of a new batch of mafic magma, or eruption cause sudden changes in composition and pressure.

For now we consider the simple question of what happens when olivine and quartz are

put together at high temperature. Olivine and quartz are never stable together and we would expect them to react spontaneously. However without a model that couples the thermodynamics, kinetics and energetics it is not possible to predict the macroscopic reaction path. To model this we fix the pressure at 1 bar and use an initial temperature of 1720 °C and an initial assemblage comprising 50 vol% ol and 50 vol% qz. Although there is initially no melt present we still need to set an initial melt composition. Expanding equation (4.16) and substituting (4.17) in the limit $\phi \to 0$ shows that the first instantaneous melt composition satisfies

$$c_f^q = \frac{\Gamma_f^q}{\Gamma_f}. \tag{4.20}$$

This can be solved numerically.

The scaling parameters ρ_0, C_{P0}, T_0, and r^* are given in Table 1. We choose a value of $S_0 = 6000\text{m}^2\text{m}^{-3}$ by considering the total surface area for an aggregate of cubic crystals with grain diameters of 1 mm. The pre-exponential factor for the melting reactions are set to $r_0^+ = 10^{-8}\text{kg m}^{-2}\text{s}^{-1}$ in line with estimates for olivine dissolution from Brearley and Scarfe (1986). To explore the effect of different kinetic models on the reaction paths we use three different crystallization rates: $r_0^- = r_0^+$, $r_0^- = 5r_0^+$, and $r_0^- = 20r_0^+$.

The resulting disequilibrium reaction paths are shown in Figure 4.3. In all cases the system spontaneously reacts by melting out ol and qz, and crystallizing opx to converge to equilibrium. While the amount of transient melt produced in the $r_0^- = r_0^+$ path seems large, the amount of melt decreases as the relative crystallization rate is increased. For the $r_0- = 20r_0^+$ reaction paths, the transient melt produced is very small and could be likened to an amorphous grain-boundary material. Temperature is strongly coupled to reaction, such that it decreases during melting, and increases during crystallization. As the system is operating far from equilibrium, disequilibrium melting actually drives the system below the solidus temperature, with the degree of under-cooling depending on the kinetics and the amount of transient melt present at any one time. The system eventually buffers itself to the temperature of the opx-qz eutectic. At equilibrium all reactions cease and the reaction

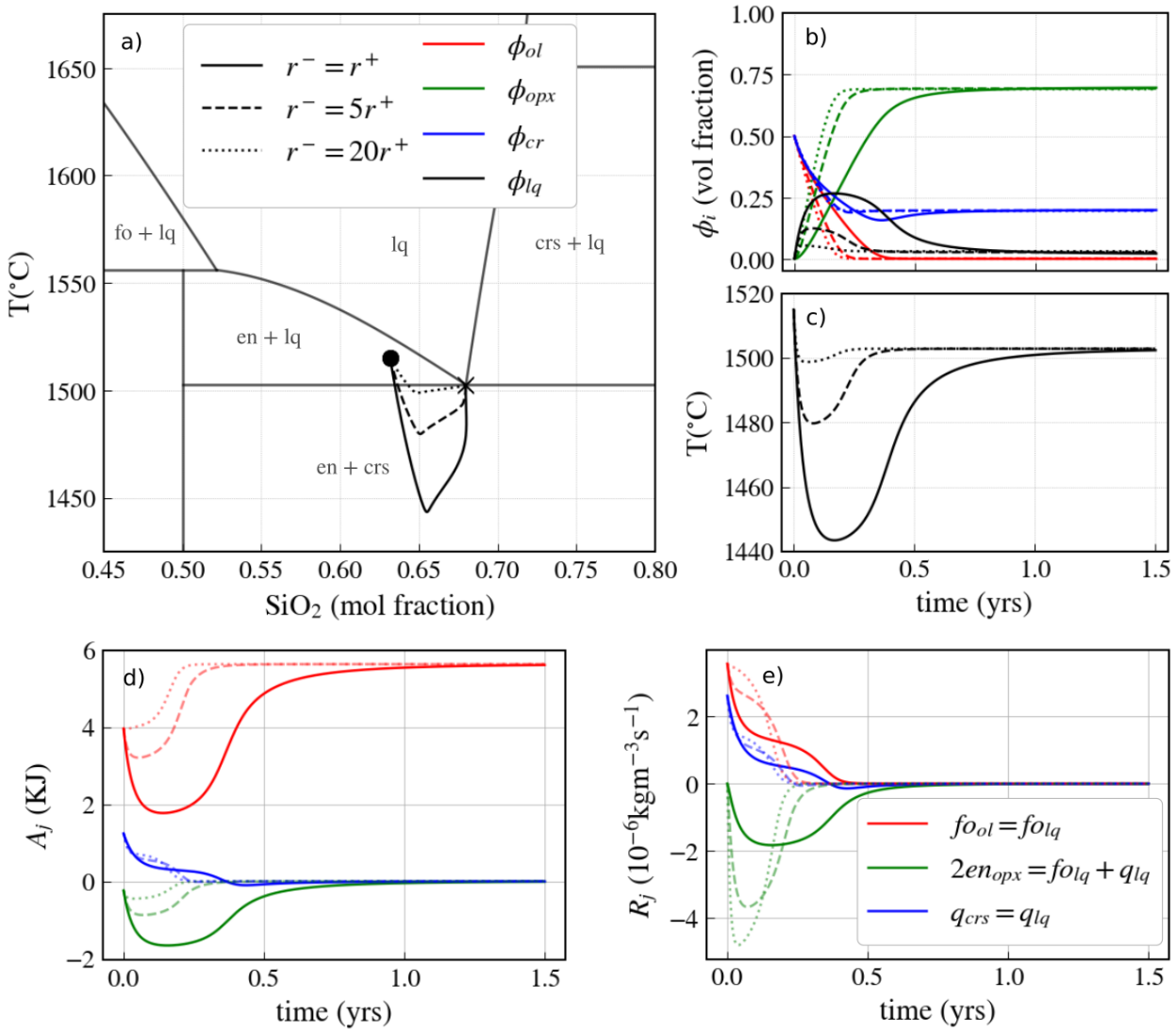

Figure 4.3: Isobaric adiabatic reaction paths for a system initially comprising a disequilibrium assemblage of ol and qz. Three different kinetic rate laws are shown: crystallization rate equal to melting rate (solid line); crystallization rate 5× faster than melting (dashed line); crystallization 20× faster than melting (dotted line). (a) Melt composition versus temperature compared to equilibrium phase diagram. (b) Phase volume fraction evolution. (c) Temperature evolution. (d) Chemical affinities of the three reactions. (e) Reaction rates of the three reactions: The rates converge to zero at equilibrium.

rates converge to zero. It is important to note that this is not equivalent to all affinities converging to zero, as only the affinities of reactions involving stable phases must converge to zero at equilibrium. In this case, ol is not stable in the final assemblage, the affinity of the ol melting reaction therefore does not tend to zero.

When we use a set of melt-mediated reactions along with an appropriate reaction rate law, the system is guaranteed to evolve to equilibrium under closed-system conditions at super-solidus temperatures. Starting from a disequilibrium assemblage, if a mineral endmember is undersaturated relative to the melt, it will melt out (i.e. the reaction will proceed in the forward direction) until $A_j = 0$, or until the phase is exhausted. Likewise, if an endmember is oversaturated in the original assemblage it will crystallize from the melt until either it reaches saturation, or the melt is exhausted. One obvious implication of this is that once the melt is exhausted—that is once the melt becomes undersaturated relative to the rest of the assemblage—all reactions cease. This puts a limit on the ability to use melt-mediated reactions at subsolidus conditions.

However, in most systems there is a region close to the solidus for which it is possible to model melt-mediated subsolidus reactions. This is shown for the Mg_2SiO_4-SiO_2 system in Figure 4.4 in which we have initiated the same initial assemblage of qz and ol at three different temperatures: one above the solidus (T_0 = 1550°C), one just below the solidus (T_0 = 1450°C), and one far below the solidus (T_0 = 1350°C). At 1550 °C the system is above the saturation surfaces of both ol and qz, meaning that both ol and qz will initially melt to allow the system to converge to the opx-qz cotectic. At 1450 °C the system is below the solidus, but is still above the metastable extensions of the ol and qz saturation surfaces (shown in Fig 4.4 as dashed lines) meaning that ol and qz will still initially melt. In this case, as the system is subsolidus, equilibrium is only attained when all of the transient melt has crystallized completely to leave a subsolidus assemblage of qz and opx. Here we have initiated the system with a melt composition that falls above the metastable extensions of both saturation surfaces (the dark purple shaded triangle in Figure 4.4), however if an initial

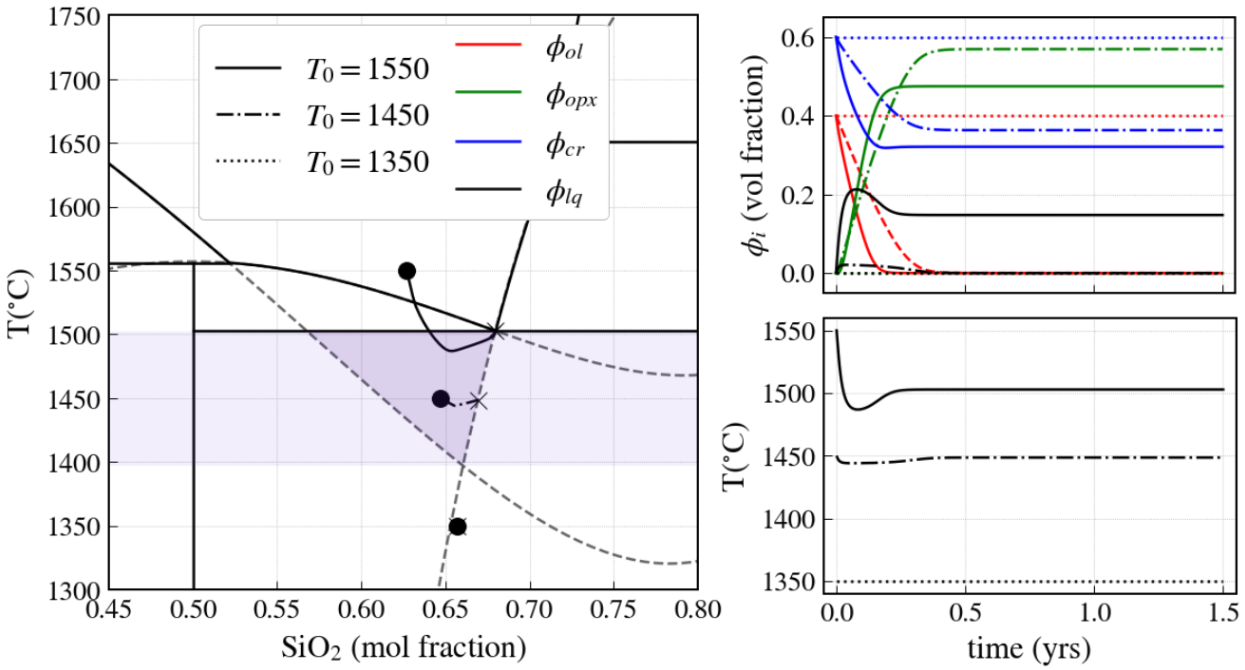

Figure 4.4: Isobaric adiabatic reaction paths for three different initial temperatures. (a) Melt composition versus temperature compared to the equilibrium phase diagram. The metastable extensions of the the saturation surfaces of ol, opx and qz are shown in dashed lines. The dark purple shaded region indicates the region in which melt is more stable than ol and qz. The light purple shading shows the temperature range over which subsolidus melt-mediated reactions are possible. (b) Phase volume fraction evolution. Note that no reaction occurs for $T_0 = 1350$°C (c) Temperature evolution.

melt composition outside this region were used the reaction would still go to completion, as long as the temperature is above the metastable intersection of the ol and qz melting curves. 1350 °C falls below this intersection. Despite being metastable, the assemblage of ol and qz is more stable than the melt, meaning that no melt-mediated reaction is possible.

More generally, for any given system, this can be summarized as follows: If there exists a metastable melt that is more stable than the original assemblage, then the melt can effectively act as a metastable reactive intermediate. Melt-mediated subsolidus reaction may not be the most realistic reaction pathway, but as long as the amount of transient melt is small, then it can be likened to an amorphous grain-boundary phase.

This problem demonstrates the importance of choosing appropriate reaction sets and kinetic rate laws in disequilibrium calculations. As the actual kinetics of these reactions

are not known, proper validation requires experiments. However this framework provides a means of guiding the design of such experiments, and for understanding experimental results.

4.3.2 Heated reaction paths

Next, we can explore how the system responds to an external driving force by considering a heated isobaric system. In this case we have $\frac{\mathrm{d}P}{\mathrm{d}t} = 0$ and $Da_Q^{-1} \geq 0$. By varying Da_Q we are able to model both quasi-equilibrium and disequilibrium batch melting and crystallization and to explore the effect of varying degrees of disequilibrium. Although rarely modeled, disequilibrium melting may be a relatively common phenomenon. For example in experimental phase equilibrium experiments, rapid heating is likely to cause initial superheating of the assemblage. Furthermore, in natural systems rapid decompression of a magma chamber due to eruption, or heating from a new batch of magma could also cause superheating.

As an example we simulate melting of an ol-opx assemblage, comprising 50 vol% ol and 50 vol% opx, at 1 bar. Unlike the previous model, we start in equilibrium at the ol-opx peritectic. The initial temperature and melt composition can be found by solving for the point of intersection of the ol and opx saturation surfaces, at which the affinities of melting of both ol and opx are equal to zero. That is

$$(A_1, A_2)\left(T_{eq}, c^q_{feq}\right) = \mathbf{0} \tag{4.21}$$

This can be solved numerically for T_{eq} and c^q_{feq}.

We use the same reaction rate parameters as previously, but this time assume equal crystallization and melting rates: $S_0 = 6000\mathrm{m}^2\mathrm{m}^{-3}$ and $r_0^- = r_0^+ = 10^8$. We vary the heating rate using three different values of Da_Q: $Da_Q = 10^5$, $Da_Q = 10^3$, and $Da_Q = 10^2$. We stop timestepping for each reaction path when the temperature reaches 1950 °C. The results are shown in Fig. 4.5. The total reaction duration differs vastly for the different heating rates. So that the reaction paths can be easily compared, we have plotted the phase fraction and

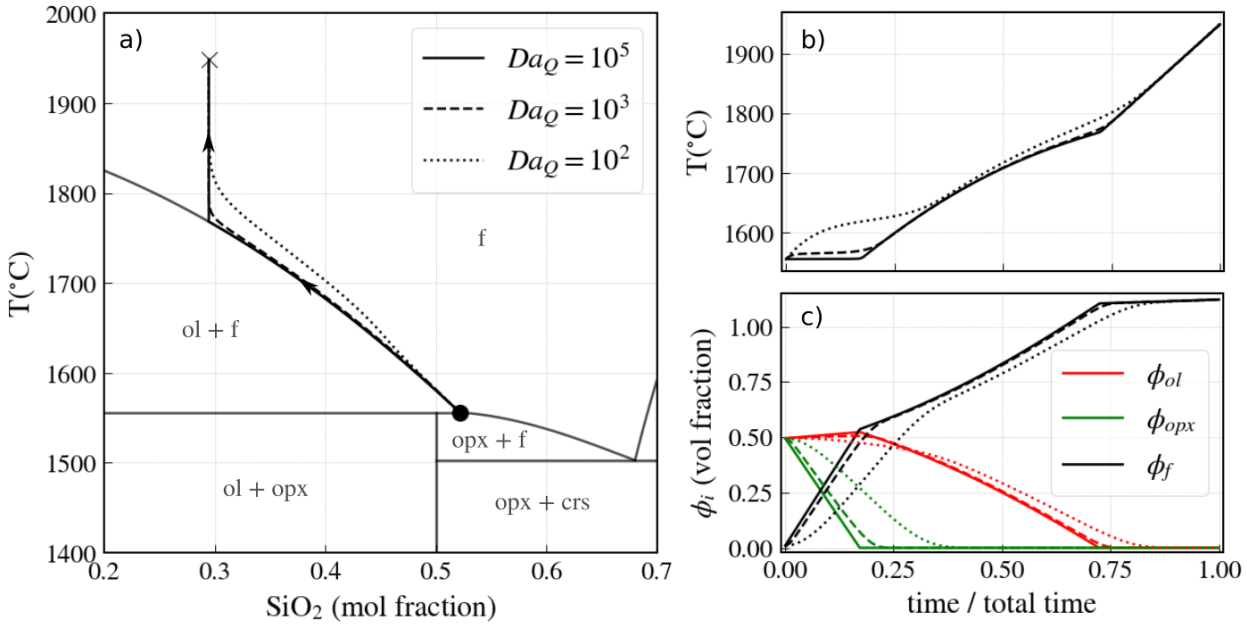

Figure 4.5: Isobaric heated reaction paths for $Da_Q = 10^5$ (solid), $Da_Q = 10^3$ (dashed), $Da_Q = 10^2$ (dotted). $Da_Q = 10^6$ approximates equilibrium batch melting. (a) Melt composition versus temperature compared to the equilibrium phase diagram. Circle shows the initial melt composition (at the ol-opx peritectic), and the cross shows the final condition. (b) Temperature evolution, and (c) normalized phase fraction evolution plotted versus relative reaction time. Note that for $Da_Q = 10^2$ the fraction of ol decreases slightly during initial melting contrary to what would be expected for the equilibrium peritectic melting reaction.

temperature evolution as a function of time/total time.

The $Da_Q = 10^5$ heating path effectively follows the reversible batch melting path ($Da_Q = \infty$) in which ol and opx melt incongruently (opx $\rightarrow$ lq + ol) at a constant temperature until opx is exhausted. The system then ascends along the ol liquidus until the remaining ol has melted, at which point the system leaves the liquidus and heats at a constant rate. For $Da_Q = 10^3$ and $Da_Q = 10^2$, heating is too fast for the system to remain in equilibrium. This results in overstepping of both the peritectic reaction and the ol liquidus. Perhaps less intuitively, disequilibrium also changes the stoichiometry of the ol-opx melting reaction to the point that for the $Da_Q = 10^2$ heating path, the melting reaction is eutectic (ol + opx $\rightarrow$ lq) rather than peritectic.

These calculations explicitly take account of the dissipative terms in the energy balance. For this system the only contribution to the internal entropy production is from disequilib-

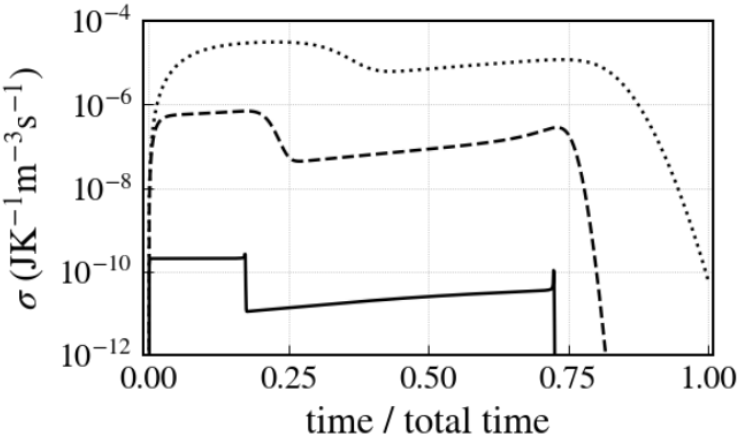

Figure 4.6: Internal entropy production σ for reaction paths shown in Fig 6: $Da_Q = 10^5$ (solid), $Da_Q = 10^3$ (dashed), $Da_Q = 10^2$ (dotted).

rium reaction.

$$\sigma = \frac{1}{T}\sum_{j=1}^{J} A_j R_j \tag{4.22}$$

Figure 4.6 shows how σ varies for the three reaction paths calculated in Figure 4.5. As σ scales as $\sum_j A_j^2$, it increases with decreasing Da_Q. This means that while σ has a negligible effect on the temperature evolution for the close-to-equilibrium reaction path, its effect on temperature for disequilibrium reaction paths can be significant: For $Da_Q = 10^2$ the reactive dissipation accounts for an additional 6°C of heating.

4.3.3 Adiabatic decompression reaction paths

Melting in Earth's interior is most commonly caused by adiabatic decompression beneath spreading centers, or within mantle plumes. In this scenario we have $Da_Q^{-1} = 0$ and $\frac{\mathrm{d}P}{\mathrm{d}t} < 0$. The decompression rate is set by the mantle upwelling velocity

$$\frac{\mathrm{d}P}{\mathrm{d}t} = -\rho_0 g W_0, \tag{4.23}$$

Where ρ_0 is the reference solid density, and W_0 is the upwelling velocity. Beneath a mid-ocean ridge, W_0 is roughly equal to the half-spreading rate.

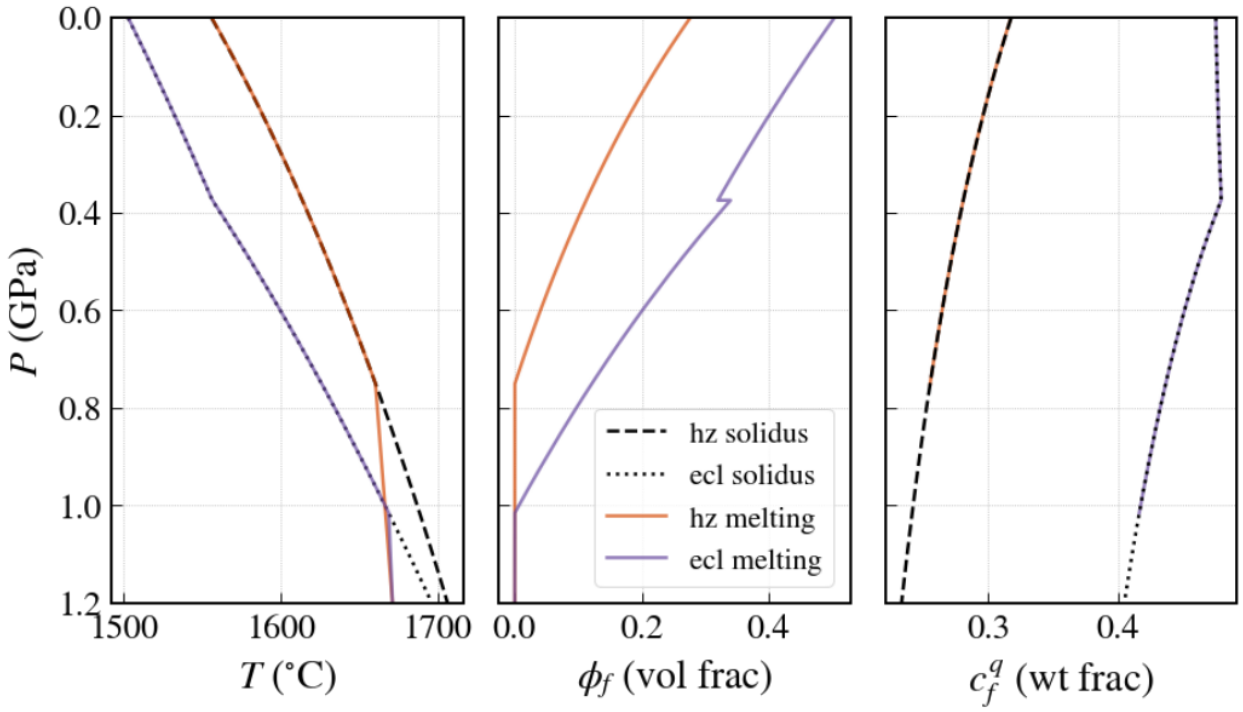

Figure 4.7: Calculated 0-D adiabatic decompression reaction paths for a 'harzburgite' (ol + opx) and 'eclogite' (opx + qz) assemblage. The reaction paths follow equilibrium batch melting trends. The discontinuity in the eclogite melting path is due to the qz-crs transition.

The Mg_2SiO_4–SiO_2 system contains two cotectic solid assemblages: opx + ol, and opx + qz, which serve as simplified models of harzburgite and eclogite which occur in the convecting mantle. To compare the different melting behaviour we model adiabatic decompression melting of a harzburgite assemblage comprising 50 vol% ol and 50 vol% opx, and an eclogite assemblage comprising 50 vol% opx and 50 vol% qz. We start both assemblages at 1.2 GPa and 1672 °C, which is below both the eclogite and harzburgite solidi, and allow them to decompress at a velocity of 10 cm/yr. The reaction rate parameters are the same as those used above for the heated reaction paths. The calculated adiabatic decompression reaction paths are shown for each assemblage in Figure 4.7.

The decompression rate is very slow compared to the rate of reaction. This creates a very stiff set of equations, and allows equilibrium to be maintained throughout. Eclogite is more fusible than harzburgite, it therefore starts to melt at a higher pressure and produces more silica-rich melt. The discontinuity in the eclogite melting path at 0.4 GPa is due to the qz-crs transition.

A useful feature of this approach is that the reactive mass transfer rates Γ_i give the stoichiometry of the net melting reaction. Eutectic harzburgite melting is therefore occurs when $\Gamma_{opx} < 0$ and $\Gamma_{ol} < 0$. Peritectic melting on the other hand occurs when $\Gamma_{opx} < 0$ and $\Gamma_{ol} > 0$. Interestingly, for the steady state batch harzburgitic melting column shown here, the net melting reaction transitions from eutectic to peritectic at a higher pressure (0.5 GPa) than the transition to peritectic melting in the equilibrium phase diagram (0.2 GPa), despite the fact that it maintains an equilibrium composition during ascent. As shown in Figure 4.8, the transition to peritectic melting in the batch upwelling column is independent of upwelling rate. In a dynamic system, the melting reaction at any point in time is the reaction required to bring the system back into chemical equilibrium. As such the deeper transition to eutectic melting can be understood in terms of the different pressure dependencies of the en and fo liquidi.

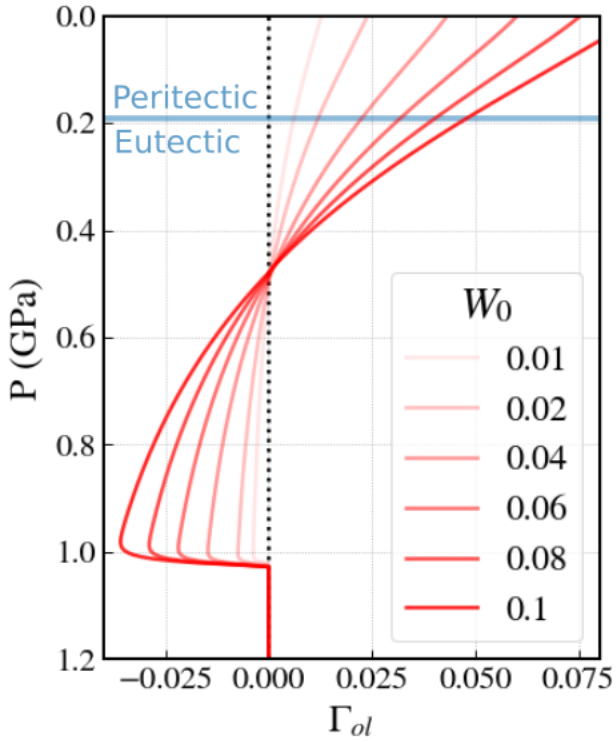

Figure 4.8: Olivine reactive mass transfer rate Γ_{ol} for 0-D adiabatic decompression with a range in upwelling rates. W_0 is in m yr^{-1}. $\Gamma_{ol} < 0$=eutectic melting, and $\Gamma_{ol} > 0$=peritectic melting. The blue line shows the transition to peritectic melting in the equilibrium phase diagram.

4.4 Reaction-diffusion dynamics

We can now add slightly more complexity by considering a system with diffusion of heat and mass, but no advection of melt relative to solid. Conservation of mass and energy in such a system is governed by

$$\frac{\partial}{\partial t}\rho_i\phi_i = \Gamma_i \quad i = ol,\ opx,\ qz,\ f \tag{4.24}$$

$$\phi_f \frac{\partial c_f^q}{\partial t} = \frac{1}{\rho_f}\left(\Gamma_f^q - c_f^q\Gamma_f\right) + \rho_f D_f^q \boldsymbol{\nabla}\cdot\left(\phi_f + \varepsilon_D\right)\boldsymbol{\nabla} c_f^q \tag{4.25}$$

$$\sum_{i=1}^{N}\left[\rho_i\phi_i C_{Pi}\frac{\partial T}{\partial t} - \phi_i\alpha_i T\frac{\mathrm{d}P}{\mathrm{d}t} + Ts_i\Gamma_i\right] = k\nabla^2 T \tag{4.26}$$

Where k is the thermal conductivity, and D_f^q is the diffusivity of silica in the melt in units of $\mathrm{m^2 s^{-1}}$. Here we have assumed effective diffusivity of silica through the porous medium takes the form

$$D_{eff}^q = D_f^q(\phi_f + \varepsilon_D) \tag{4.27}$$

The regularization parameter ε_D accounts for the fact that there is still diffusion of silica along grain boundaries at subsolidus conditions. As such, it is fit so that

$$\varepsilon_D = \frac{D_s^q}{D_f^q} \tag{4.28}$$

Where D_s^q is macroscopic diffusivity of silica in the aggregate solid.

We use the same scalings as listed in (4.14), with the addition of a length scale

$$x = Lx', \tag{4.29}$$

where L is the width of the system. As before, we assume that the whole system is being advected up through the melting region at a rate W_0 to give a decompression rate of $\frac{\mathrm{d}P}{\mathrm{d}t} =$

Table 4.2: Parameters, definitions, and reference values for reaction-diffusion models

Width	L	10 m
Melt silica diffusivity	D_f^q	(1e-11, 1e-9) m^2s^{-1}
Thermal diffusivity	κ	1e-6 m^2s^{-1}
Damköhler number	$Da_C = \frac{r^* L^2}{D_f^q}$	
Damköhler number	$Da_T = \frac{r^* L^2}{\kappa}$	
Decompression rate	$\frac{\mathrm{d}P}{\mathrm{d}t} = -\rho_0 g W_0$	

$-\rho_0 g W_0$.

The scaled governing equations in a frame moving with the solid become

$$\frac{\partial}{\partial t}\rho_i \phi_i = \Gamma_i \quad i = ol,\ opx,\ qz,\ f \tag{4.30}$$

$$\phi_f \frac{\partial c_f^q}{\partial t} = \frac{1}{\rho_f}\left(\Gamma_f^q - c_f^q \Gamma_f\right) + \frac{1}{Da_C}\boldsymbol{\nabla}\cdot\left(\phi_f + \varepsilon_D\right)\boldsymbol{\nabla} c_f^q \tag{4.31}$$

$$\sum_{i=1}^{N}\left[\rho_i \phi_i C_{Pi}\frac{\partial T}{\partial t} - \phi_i \alpha_i T \frac{\alpha_0 P_0}{\rho_0 C_{P0}}\frac{\mathrm{d}P}{\mathrm{d}t} + T s_i \Gamma_i\right] = \frac{1}{Da_T}\nabla^2 T \tag{4.32}$$

Where $\frac{\mathrm{d}P}{\mathrm{d}t}$ is the scaled decompression rate, and Da_T and Da_C are dimensionless Damkohler numbers describing the rates of heat conduction and diffusion, relative to reaction.

$$Da_T = \frac{r^* L^2}{\kappa} \tag{4.33}$$

$$Da_C = \frac{r^* L^2}{D_f^q} \tag{4.34}$$

where κ is the thermal diffusivity.

In the temperature equation (4.32) we have neglected the chemical dissipation terms due to reaction and diffusion. As demonstrated above, when the system is reacting close to equilibrium, dissipation due to reaction is negligible; likewise, the internal entropy production from chemical diffusion can be regarded as negligible (Asimow, 2002).

4.4.1 Decompression melting of an eclogite inclusion

An interesting application of this model is the melting of a fusible eclogite inclusion in a peridotite matrix during passive decompression. As shown for the 0-D system above, the simple analogue eclogite is more fusible than peridotite and starts melting at a greater depth. The silica-rich eclogite melts react with surrounding peridotite in the convecting mantle to produce secondary pyroxenites. Such reactions are considered an important process in the generation of mantle heterogeneity (Yaxley and Green, 1998), and contribute to the diversity of primary melt compositions erupted at the surface (Sobolev et al., 2007; Shorttle et al., 2014). The reactivity of silica-rich pyroxenite melts means that it is impossible to determine the fate of melts as they ascend without considering coupling between reaction and melt transport.

We consider a 10 m wide 1-D system that upwells at a constant rate of 10 cm yr^{-1} from 1.2 GPa to the surface. As demonstrated for the adiabatic decompression reaction path above, this ascent rate is sufficiently slow for the rocks to remain close to chemical equilibrium. The harzburgite is made up of 60 vol% ol and 40 vol% opx. In the centre of the domain is a 3 m wide eclogite inclusion comprising 40 vol% qz and 60 vol% opx. The edges of the inclusion are smoothed out over a width of 0.8 m. As before we set the initial temperature of the system at 1.2 GPa to 1672 °C, which is below both the eclogite and harzburgite solidus. The values of the dimensional and non-dimensional parameters used in the model are given in Tables 4.1 and 4.2.

The small relative proportion of recycled eclogite in the convecting mantle means that during partial melting, the system is buffered along the peridotite adiabat (Phipps Morgan, 2001). As we are only considering a small region around an eclogite inclusion, our model has an unrealistically high eclogite:harzburgite ratio and therefore does not properly account for the relative proportions of the two assemblages. As a result, to model the additional background heat from the surrounding harzburgite reservoir, we impose a Robin condition

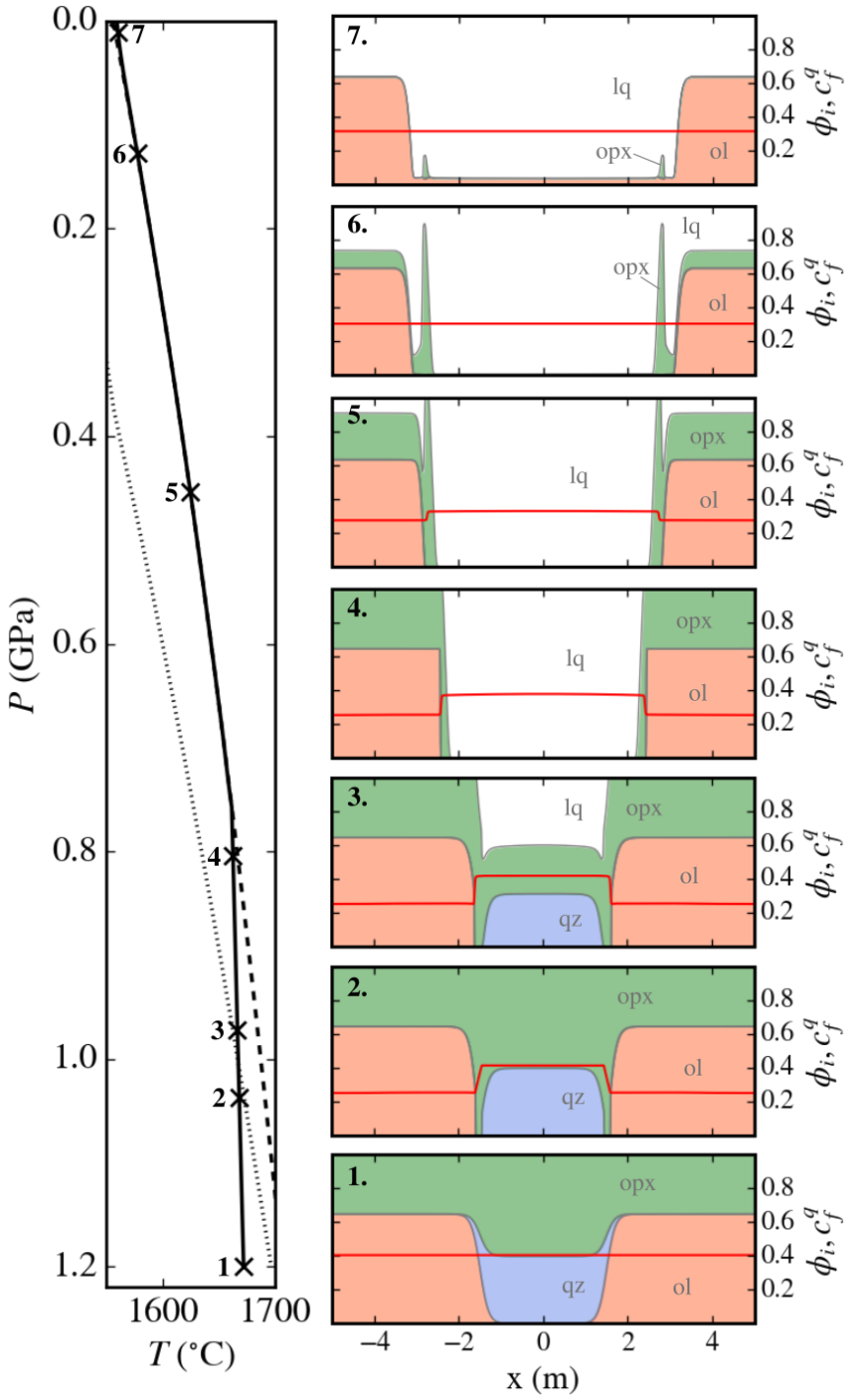

Figure 4.9: Isothermal decompression melting of a fusible eclogite (opx + qz) inclusion in a harzburgitic (ol + opx) matrix for a system that is open to diffusion of both heat and SiO_2. On the left is the P-T path of the system. The eclogite solidus (dotted line) and harzburgite solidus (dashed line) are shown. On the right are numbered snapshots of the system at different pressures. The phase assemblage is shown as a cumulative phase volume fraction and the melt composition in wt fraction SiO_2 is shown in red.

at the boundaries.

$$\frac{1}{Da_T}\boldsymbol{\nabla} T = \beta(T_{bc} - T) \quad \text{on } \partial\Omega \tag{4.35}$$

where T_{bc} is set to the solid harzburgite adiabat. This serves as a stand-in for the large pool of surrounding harzburgite outside the domain. We turn off this background heating once the harzburgite begins to melt by setting $\beta = 1$ below the harzburgite solidus, and $\beta = 0$ above. In the absence of this background heat supply, melting of the eclogite cools the domain resulting in an adiabat that is intermediate between the eclogite and harzburgite solidi.

Equations (4.30)-(4.32) with the initial and boundary conditions described above are solved numerically using finite elements in TerraFERMA (Wilson et al., 2017). This involves solving the weak form of the equations over a discretization of the domain. We use a semi-implicit time-stepping scheme with adaptive time-stepping to adjust the timesteps according to the melting rate and magnitude of the diffusive flux. We solve the equations at each timestep using Newton's method with a sparse direct solver. The results are shown in Figure 4.9.

As ol and qz are unstable together, the edges of the inclusion quickly undergo subsolidus reaction to form pure opx pyroxenite rims. At the eclogite solidus the eclogite melts rapidly, but with no advection, the melt remains trapped in the inclusion behind the pyroxenite walls. Melting is slightly amplified at the edges due to diffusion of heat and mass in from the surrounding harzburgite. As the inclusion continues to ascend, the pyroxenite rims become sharper and the melt composition tends towards a step function on either side. These self-sharpening reactions fronts, or shocks, are due to the porosity dependence of silica diffusion. Sharp reaction zones are a common feature metamorphic systems where there is an interplay between reaction and diffusion. Only at the harzburgite solidus, when the harzburgite matrix also starts to melt, do these compositional fronts relax. In the simplified binary system, the pure opx rims actually take the longest to melt due to their higher melting temperature; this would not be the case for natural pyroxenites. Eventually the system melts to such a degree

that only residual ol is left across the domain. The high degree of melting is a local effect, resulting from the large volume of silica-rich eclogite melt which must be mass-balanced by silica-poor harzburgite melt to maintain equilibrium.

4.5 1-D reactive porous flow

We now consider the full set of magma dynamics equations described in chapter 2, with advection of the solid and liquid phases and diffusion of heat and components. We will neglect deviatoric stresses and deviatoric components of the strain-rate tensor. The governing equations for a partially molten poro-viscous system undergoing isotropic compaction are then

$$\frac{\partial}{\partial t}\rho_i\phi_i c_i^k + \boldsymbol{\nabla}\cdot\rho_i\phi_i c_i^k\boldsymbol{v}_i = -\boldsymbol{\nabla}\cdot\boldsymbol{J}_i^k + \Gamma_i^k \quad (i=1,2,...,N; k=1,2,...,K_i-1) \tag{4.36}$$

$$\frac{\partial}{\partial t}\rho_i\phi_i + \boldsymbol{\nabla}\cdot\rho_i\phi_i\boldsymbol{v}_i = \Gamma_i \quad (i=1,2,...,N) \tag{4.37}$$

$$\phi_f(\boldsymbol{v}_f - \boldsymbol{v}_s) = -\frac{K}{\mu}\left(\boldsymbol{\nabla}P - \rho_f\boldsymbol{g}\right) \tag{4.38}$$

$$\boldsymbol{\nabla}P = \boldsymbol{\nabla}\cdot\zeta\boldsymbol{\nabla}\cdot\boldsymbol{v}_s\boldsymbol{I} + \bar{\rho}\boldsymbol{g} \tag{4.39}$$

$$\sum_{i=1}^{N}\left[\rho_i\phi_i C_{Pi}\frac{\mathrm{D}_i T}{\mathrm{D}t} - \phi_i\alpha_i T\frac{\mathrm{D}_i P}{\mathrm{D}t} + Ts_i\Gamma_i\right] = -\boldsymbol{\nabla}\cdot\boldsymbol{q} \tag{4.40}$$

where $\boldsymbol{v}_{s,f}$ are the solid and melt velocities, $\boldsymbol{J}_i^k$ is the diffusive flux, $\boldsymbol{q}$ is the heat flux, K is the permeability, μ is the melt viscosity and ζ is the solid bulk viscosity. We have neglected the dissipation terms in the energy balance as these terms are negligible for high temperature viscous systems close to chemical equilibrium (Asimow, 2002).

The magma dynamics equations can be more conveniently solved by linearly decomposing the fluid pressure into lithostatic $P_l = \bar{\rho}_s g z$, compaction $\mathcal{P}$ and dynamic P^* pressure components.

$$P = P_l + \mathcal{P} + P^* \tag{4.41}$$

where

$$\mathcal{P} = \zeta \boldsymbol{\nabla} \cdot \boldsymbol{v}_s \tag{4.42}$$

The P-split formulation is described in Appendix D. We non-dimensionalize the equations by introducing the following scalings

$$\begin{array}{llll} z = hz' & t = \frac{h}{q_0} t' & (\boldsymbol{v}_f, \boldsymbol{v}_s) = q_0(\boldsymbol{v}'_f, \boldsymbol{v}'_s) & \boldsymbol{g} = g\hat{\boldsymbol{g}} \\ T = T_0 T' & \rho_i = \Delta\rho_0 \rho'_i & P = \Delta\rho_0 g h P' & \Gamma_i = \Delta\rho_0 r^* \Gamma'_i \\ \zeta = \zeta(\phi_0)\xi' & K = K(\phi_0)K' & \mu = \mu_0 \mu' & \\ C_{Pi} = C_{P0} C'_{Pi} & s_i = C_{P0} s'_i & \alpha_i = \alpha_0 \alpha'_i & \end{array}$$

Where h is the height of the system; $\Delta\rho_0$ is the reference density difference between solid and melt; $K(\phi_0)$ and $\zeta(\phi_0)$ are the permeability and bulk viscosity at the reference porosity; and q_0 is the reference melt flux, given by

$$q_0 = \frac{K(\phi_0)\Delta\rho_0 g}{\mu_0} \tag{4.43}$$

For the Mg_2SiO_4-SiO_2 system, this gives the following set of equations for $\boldsymbol{\phi}$, c_f^q, v_f, v_s, P and T, in terms of non-dimensional variables.

$$\frac{\mathrm{D}_s \phi_i}{\mathrm{D}t} = -\frac{h^2}{\delta^2}\phi_i \frac{\mathcal{P}}{\zeta} + Da \frac{\Gamma_i}{\rho_i} \quad i = [ol, opx, qz] \tag{4.44}$$

$$\frac{\mathrm{D}_s \phi_f}{\mathrm{D}t} = \frac{h^2}{\delta^2}(1 - \phi_f)\frac{\mathcal{P}}{\zeta} - Da \sum_{i=2}^{N} \frac{\Gamma_i}{\rho_i} \tag{4.45}$$

$$\frac{h^2}{\delta^2}\frac{\mathcal{P}}{\zeta} = \frac{\partial}{\partial z} K \left(\frac{\partial \mathcal{P}}{\partial z} + \Delta\rho g \right) + Da \sum_{i=1}^{N} \frac{\Gamma_i}{\rho_i} \tag{4.46}$$

$$\frac{\partial v_s}{\partial z} = \frac{h^2}{\delta^2}\frac{\mathcal{P}}{\zeta} \tag{4.47}$$

$$\frac{\partial P}{\partial z} = \frac{\partial \mathcal{P}}{\partial z} + \bar{\rho} g \tag{4.48}$$

Table 4.3: Dimensional parameters, definitions, and reference values

Temperature	T_0	1925 K
Pressure	P_0	1.2 GPa
Density	ρ_0	3000 kgm^{-3}
Density difference	$\Delta\rho_0 = \bar{\rho}_s - \rho_f$	300 kgm^{-3}
Heat capacity	C_{P0}	1 $\text{Jkg}^{-1}\text{K}^{-1}$
Expansivity	α_0	5e-5 $\text{K}^{-}1$
Gravity	g	9.81 ms^{-2}
Solid velocity	W_0	4 cmyr^{-1}
Rate constant	r_0	1e-8 $\text{kgm}^{-2}\text{s}^{-1}$
Reactive surface area	S_0	6000 m^2m^{-3}
Reaction rate	$r^* = \frac{r_0 S_0}{\rho_0}$	2e-8 s^{-1}
Melt silica diffusivity	D_f^q	1e-9 m^2s^{-1}
Thermal diffusivity	κ	1e-6 m^2s^{-1}
Porosity	ϕ_0	0.05
Melt viscosity	μ_0	1 Pas
Bulk viscosity coefficient	ζ_0	1e19 Pas
Solid viscosity exponent	m	-1
Bulk viscosity	$\zeta(\phi_0) = \zeta_0\phi_0^m$	2e20 Pas
Permeability coefficient	K_0	1e-7 m^2
Permeability exponent	n	3
Permeability	$K(\phi_0) = K_0\phi_0^n$	1.25e-11 m^2
Melt flux	$q_0 = \frac{K(\phi_0)\Delta\rho_0 g}{\mu_0}$	3.68e-7 ms^{-1}

Table 4.4: Scaling parameters and non-dimensional numbers, definitions, and values

System depth	$h = \frac{P_0}{\rho_0 g}$	40775 m
Compaction length	$\delta = \sqrt{\frac{K(\phi_0)\zeta(\phi_0)}{\mu}}$	5e4 m
Damköhler number	$Da = \frac{r^* h}{q_0}$	2217
Peclet number	$Pe_C = \frac{D_f^q}{q_0 h}$	1.5e7
Peclet number	$Pe_T = \frac{\kappa}{q_0 h}$	1.5e4
Adiabatic parameter	$Ad = \frac{\alpha_0 g h}{C_{P0}}$	

$$\phi_f v_f = \phi_f v_s - \frac{K}{\mu}\left(\frac{\partial \mathcal{P}}{\partial z} - \Delta\rho g\right) \tag{4.49}$$

$$\phi_f \frac{\mathrm{D}_f c_f^k}{\mathrm{D}t} = \frac{Da}{\rho_f}\left(\Gamma_f^q - c_f^q \Gamma_f\right) + \frac{1}{Pe_c}\frac{\partial}{\partial z}\left((\phi_f + \varepsilon_D)\frac{\partial c_f^q}{\partial z}\right) \tag{4.50}$$

$$\sum_{i=1}^{N}\left[\rho_i\phi_i C_{Pi}\frac{\mathrm{D}_i T}{\mathrm{D}t} - Ad\phi_i\alpha_i T\frac{\mathrm{D}_i P}{\mathrm{D}t} + DaTs_i\Gamma_i\right] = \frac{1}{Pe_T}\frac{\partial^2 T}{\partial z^2} \tag{4.51}$$

Where $\Delta\rho = \bar{\rho}_s - \rho_f$. δ is the compaction length describing the length scale over which compaction pressure decays

$$\delta = \sqrt{\frac{K(\phi_0)\zeta(\phi_0)}{\mu_0}} \tag{4.52}$$

Da is the Damkohler number, and Pe_c and Pe_T are the compositional and thermal Peclet numbers

$$Da = \frac{r^* h}{q_0} \tag{4.53}$$

$$Pe_T = \frac{q_0 h}{\kappa} \tag{4.54}$$

$$Pe_C = \frac{q_0 h}{D_f^q} \tag{4.55}$$

The adiabatic term Ad describes the change in temperature due to adiabatic decompression over the height of the system.

$$Ad = \frac{\alpha_0 g h}{C_{P0}} \tag{4.56}$$

We assume that the constitutive laws for viscosities and permeabilities are given by simple power-law expressions

$$K = K_0(\phi_f + \varepsilon_K)^n, \quad n = 3 \tag{4.57}$$

$$\zeta = \zeta_0(\phi_f + \varepsilon_\zeta)^m, \quad m = -1 \tag{4.58}$$

Where ε_K and ε_ζ are regularization parameters that ensure the compaction pressure does not become singular, and varies smoothly, as $\phi_f \to 0$.

4.5.1 Batch melting column

To explore coupled flow and reaction, we consider a 1-D mantle column that is slowly ascending beneath a ridge axis by passive upwelling. This is a standard benchmark problem in magma dynamics that has been studied by many authors in the past using both equilibrium

and disequilibrium formulations (Ribe, 1985; Spiegelman and Elliott, 1993; Asimow and Stolper, 1999; Hewitt and Fowler, 2008; Katz, 2008; Rudge et al., 2011). In the absence of transient perturbations the solution for the 1-D melting column evolves to steady state. Here, we build on past formulations by incorporating disequilibrium, and also integrating a real thermodynamic model for eutectic/peritectic style melting in a multiphase assemblage, which fully couples the dynamics to the evolving phase assemblage.

We consider a harzburgitic mantle column, comprising 60 vol% ol and 40 vol% opx that ascends from 1.2 GPa to the surface. The solid phase fractions are fixed on the lower boundary. We fix the solid upwelling velocity at the upper boundary to $W_0 = 4$ cm/yr, with passive inflow across the lower boundary. We start the calculation with a solid adiabatic temperature gradient calculated for the initial harzburgitic assemblage.

$$T = T_0 \exp\left(\frac{\bar{\alpha} P}{\overline{\rho C}_P}\right) \tag{4.59}$$

Where T_0 is the potential temperature at the surface, and $\bar{\alpha}$ and $\overline{\rho C}_P$ are the average thermal expansivity and density and heat capacity for the initial solid assemblage. The temperature of the lower boundary is fixed to a temperature corresponding to the potential temperature of T_0 according to equation (4.59), such that the solidus occurs at 1 GPa. As the lower boundary is subsolidus, the compaction pressure is set to zero at the lower boundary, with free-flux on the upper boundary. The values of all scaling, dimensional, and non-dimensional parameters used in the calculation are given in Tables 4.3 and 4.4. The thermodynamic variables are calculated directly from the thermodynamic models. The remaining parameters have been chosen from the literature to best match those predicted for the partially molten upper mantle.

The non-dimensional system of equations with the initial and boundary conditions described above is solved using finite elements in TerraFERMA (Wilson et al., 2017). This involves solving the weak form of the equations over a discretization of the domain. We use

a semi-implicit time-stepping scheme with adaptive time-stepping to adjust the timesteps according to the melting rate. We solve the equations at each timestep using Newton's method with a sparse direct solver. The calculated steady state melting columns are shown in Fig.4.10.

The melt fraction F, that is the mass of melt extracted from the initial solid assemblage, is not directly calculated from equations (4.44)-(4.51), but is a useful property for understanding the degree of depletion of the solid residue. It can be calculated by tracking the concentration of a hypothetical perfectly compatible tracer in the solid c_s^{tr}, whose evolution is described by

$$\rho_s(1-\phi_f)\left(\frac{\partial c_s^{tr}}{\partial t} + v_s\frac{\partial c_s^{tr}}{\partial z}\right) = c_s^{tr}\Gamma_f \tag{4.60}$$

The melt fraction is then calculated by mass balance

$$F = 1 - \frac{c_{s0}^{tr}}{c_s^{tr}} \tag{4.61}$$

where c_{s0}^{tr} is the initial concentration in the solid, which we set to unity.

The column initially melts rapidly until a quasi-equilibrium steady state is reached after approximately 100 Kyr. In steady state, the permeability is sufficiently high that the porosity is low throughout the column at 1-2 vol%. The melt fraction on the other hand reaches 27 wt%, which is reflected in the depletion of opx in the residue. As for the batch adiabatic decompression model shown above, the system transitions from eutectic to peritectic melting around 0.5 GPa. This appears to be unaffected by transport. This shows up in Fig 4.10 as Γ_{ol} transitions from negative (melting), to positive (crystallizing).

The benefit of the thermodynamic approach is that the dynamics are directly coupled to the evolving petrology and thermodynamic properties of the phase assemblage. Fig. 4.11 shows the variation in the density and entropy of ol, opx and lq for the reference steady state melting column. All lq properties vary more extensively than those of the solid phases due to the variation in melt composition with depth. ρ_f, $C_{P,f}$, s_f, and α_f vary inversely with

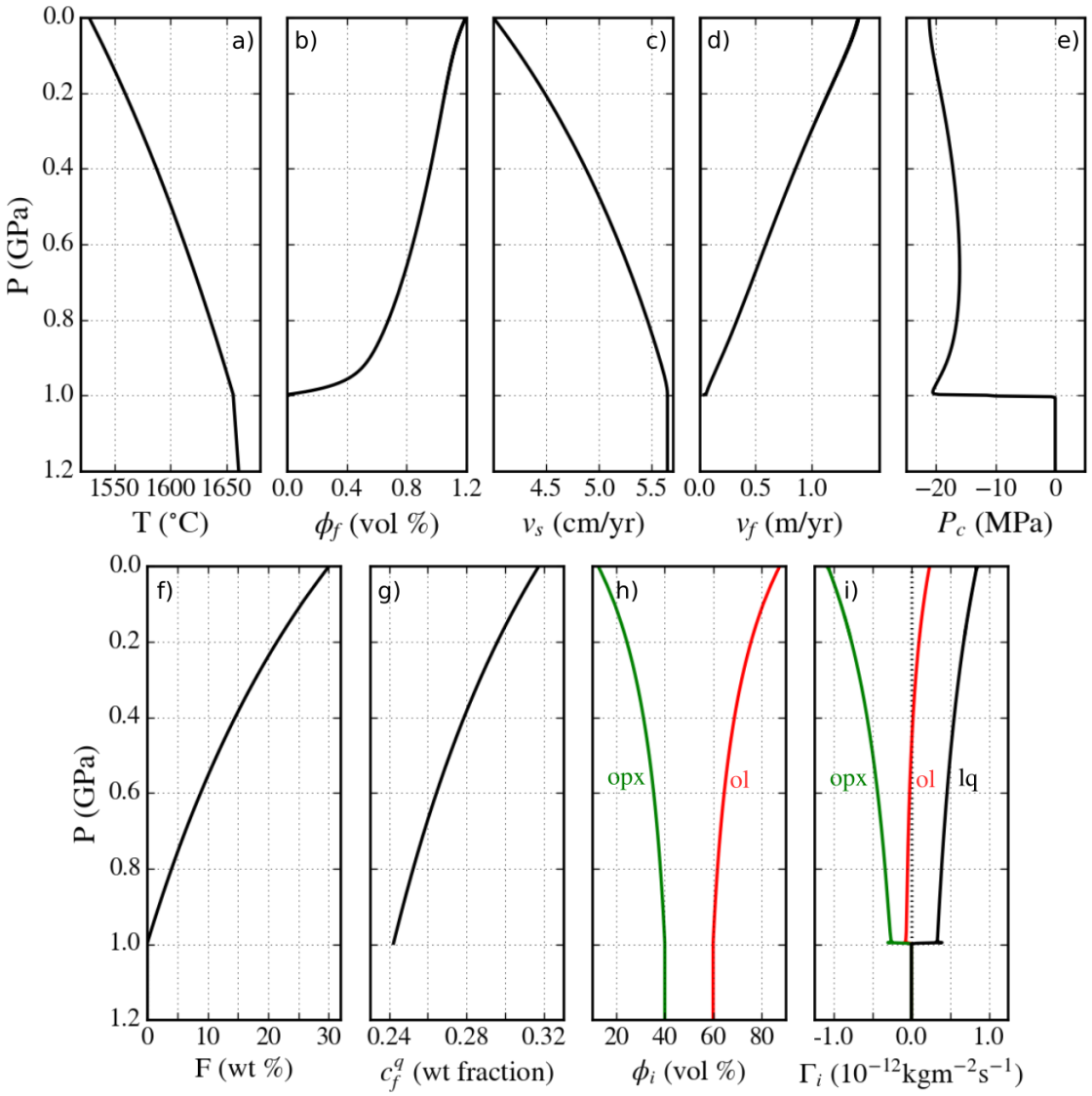

Figure 4.10: Calculated steady-state 1-D melting profiles in the Mg_2SiO_4-SiO_2 system. This is a near-equilibrium model with $Da \approx 10^4$. The solid phase fractions in plot (h) are normalized to 100% for the solid assemblage. The transition from eutectic to peritectic melting can be seen in subplot (i) in which Γ_{ol} becomes positive at 0.5 GPa, resulting in melting reaction opx=ol +f.

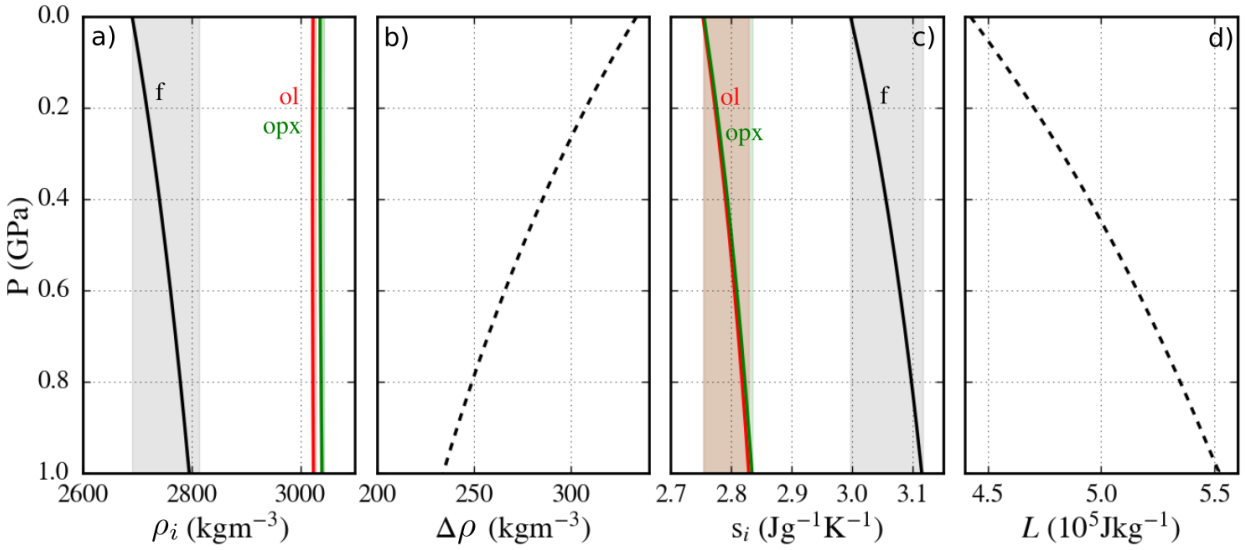

Figure 4.11: Thermodynamic phase properties for the steady-state profiles shown in Figure 4.10 from the solidus to the surface. (a) Phase densities; (b) $\Delta\rho = \rho_s - \rho_f$ is the density difference between the aggregate solid and melt. The observed variation in the ρ_f and $\Delta\rho$ is due to the variation in melt composition with pressure. (c) Phase entropies; (d) Latent heat of melting. The entropies of all phases are temperature-dependent, but s_f varies more extensively due to variation in melt composition.

melt silica content, and therefore decrease with decreasing pressure. The thermodynamic variables that are likely to have the most significant effect on melting profile are the density difference between the melt and solid residue $\Delta\rho$, and the latent heat L, which is defined as

$$L = T \sum_{i=1}^{N} s_i \frac{\Gamma_i}{\Gamma_f} \tag{4.62}$$

In most past formulations these are simply set as constants. However, as melting is non-modal, the latent heat depends on the stoichiometry of the net melting reaction which is dependent on pressure and extent of depletion of the solid residue. As shown in Figure 4.11, in this system, both $\Delta\rho$ and L show quite significant variation with pressure.

Parameter variation: *Da*

Of the four dimensionless parameters (Da, Pe_T, Pe_C, $\frac{h^2}{\delta^2}$, Ad), Da is particularly poorly constrained due to uncertainty in the macroscopic reaction kinetics. Fig. 4.12 shows the

behavior of the steady state column for a range of Da. Previous authors (Ribe, 1985; Spiegelman and Elliott, 1993; Asimow and Stolper, 1999) have demonstrated the equivalence of 1-D steady state equilibrium melting and batch melting, in terms of melt and solid composition, temperature, and extent of melting F. This provides us with a useful independent test of the model in the limit of high Da. The calculations for batch melting are shown for comparison in Fig. 4.12, and are in agreement with the pseudo-equilibrium runs. As the extent of disequilibrium increases, the profiles show lower F, higher T, lower c_f^q, and higher modal abundances of residual opx than expected for batch melting. The deviation does not increase linearly with decreasing Da due to the non-linear coupling, but increases markedly for $Da > 10$.

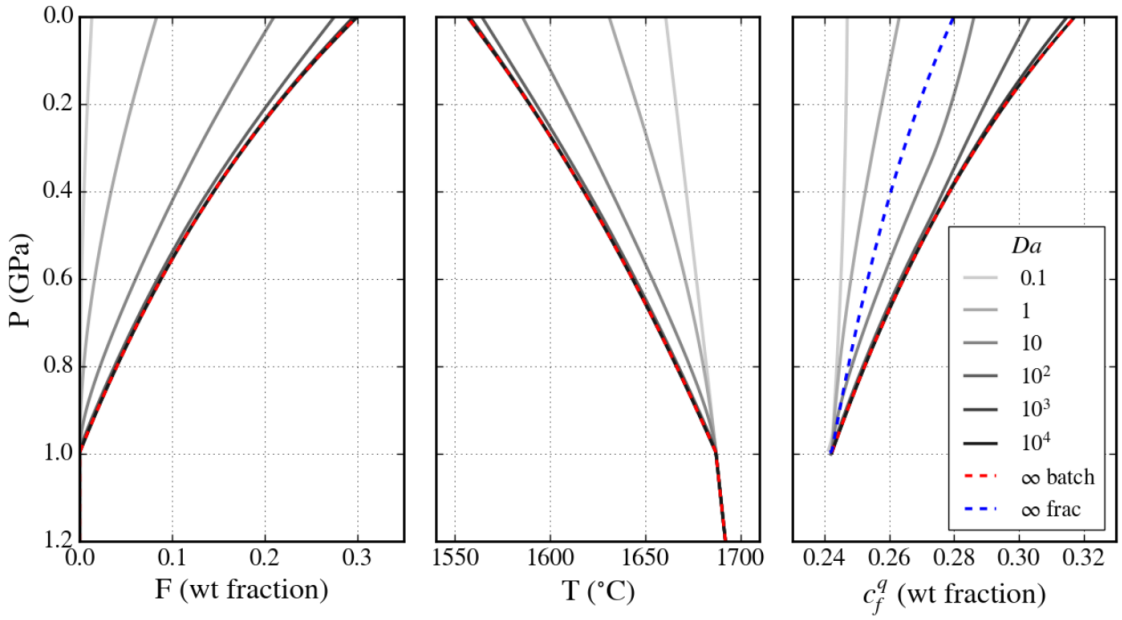

Figure 4.12: Calculated 1-D steady state melting columns for a range of Da compared to the calculated profile for equilibrium ($Da = \infty$) batch and fractional melting. All other model parameters in the disequilibrium melting columns are set to the reference values. F and T are the same for fractional and batch melting and are represented by the red dashed line. The fractional melt composition is the accumulated fractional melt composition that we would expect for melt transported in chemically-isolated channels.

One interesting observation is that for disequilibrium runs, the melt at the surface is undersaturated in opx, and compositionally preserves a deeper melting signature (Fig. 4.13).

This reflects one of the primary observations of MORB which is usually attributed to the transport of melt in high-porosity channels (Kelemen et al., 1997). This allows melts, that are locally produced in equilibrium, to be rapidly transported to the surface without chemically equilibrating with the overlying mantle, resulting in near-fractional melting. Although we would expect some degree of interaction between channelized melts and the surrounding mantle, simple scaling analysis can be used to show that a channel spacing of just 10 cm is sufficient to maintain significant disequilibrium (Spiegelman and Kenyon, 1992).

The endmember scenario of perfectly fractional melting is calculated and plotted in figure 4.12. As melting locally occurs in equilibrium, the T and F profiles match those for equilibrium batch melting. However as the accumulated fractional melt does not re-equilibrate with the overlying mantle, its composition preserves a weighted average of the deep melting signature. The calculated disequilibrium reactive flow profiles we calculate here do not capture this behaviour as they assume that the local melting reaction and the subsequent transport both involve the same degree of disequilibrium. This means that silica under-saturation in the melt is also accompanied by lower melt productivity and a higher adiabatic temperature. Recognition of these different modes of disequilibrium is important.

4.6 Discussion

These simplified problems provide a clear set of examples for illustrating how the coupled thermochemical-geodynamic formulation is applied to a real system of geological interest. The goal more generally was to develop a flexible, tractable and self-consistent approach to integrating general thermodynamic systems into magma dynamics calculations. The example models have been developed from the base up: from a thermodynamic description of the phases and the equilibrium phase diagrams; to describing the system of reactions and reaction kinetics; to integration of the reactive system into sets of conservation equations for problems of varying complexity. These examples extend previous magma dynamics models by including multiple solid phases, and eutectic and peritectic melting reactions. The

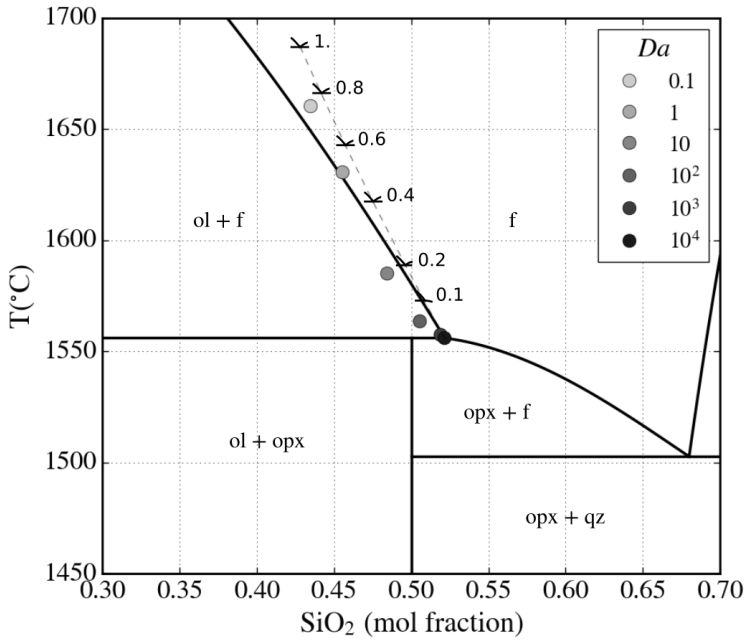

Figure 4.13: Surface melt compositions and temperatures from steady state melting columns shown in Fig. 4.12 for different Da, plotted on the 1 bar phase diagram. For low Da the melts are silica-deficient as they have not maintained equilibrium with the solid during ascent. The ol-opx cotectic for different pressures in GPa are plotted for comparison.

calculations are also fully coupled, in that the physical properties such as density and heat capacity, that feed into the dynamics and energetics of the system, are calculated directly from the same thermodynamic models governing reaction. This ensures full self-consistency between the chemistry and physics.

The behaviour of systems reacting far from equilibrium can be non-intuitive. By developing a hierarchy of models we were able to test how the kinetic model impacted the transient and steady-state behaviour of the system, and to fine-tune it as necessary. Building up the problems from simple 0-D models to more complex 1-D diffusive, and then 1-D reactive flow models also allowed us to separate out the response to different diving forces (i.e. heating, decompression, chemical diffusion, melt infiltration). The inclusion of disequilibrium reaction kinetics provides a more natural description of reaction as a time-dependent irreversible process. However by opening up the potential for disequilibrium, it also increases the parameter space of the model through the choice of reaction set and the kinetic rate

laws. In high-temperature geological systems, the kinetics of heterogeneous reaction are poorly constrained and there is additional ambiguity when considering averaged kinetics at a macroscale. The choices in the kinetic model therefore require careful consideration of the system and problem being modeled. Here we used melt-mediated reactions, and simple linear kinetics which are suitable for modelling interface-controlled kinetics within a homogeneous partially molten system close to equilibrium (Dohmen and Chakraborty, 2004).

The relative importance of the kinetic model, including the choice of reactions and the rate laws, depends on extent of disequilibrium. Close to equilibrium reaction is fast relative to other processes, and the impact of kinetics is negligible. As long as the reactions have been chosen to be consistent with equilibrium considerations discussed in Section 2.5.4, the system will follow, or closely approximate, the equilibrium reaction path. The potential difficulty in the equilibrium limit is rather that the system of governing equations becomes stiff. Thankfully modern computational libraries such as SciPy, PETSc, FEniCS, and TerraFERMA give considerable flexibility in constructing efficient solvers that are suitable for such problems. As models are extended to higher dimensions further development of efficient solvers will become paramount.

Further from equilibrium, the choice of reactions and rate laws have a significant impact on the time-dependence of the the system. This is demonstrated in the batch reactor models in Fig. 4.3 whereby a small change in the relative rates of the melting and crystallization reactions resulted in very different transient behaviour. At the high temperatures of the convecting mantle, we expect the mantle assemblages to be locally in, or very close to, equilibrium. However as discussed above, this is only true at the very local scale. Heterogeneities, such as melt channels, at scales smaller than the scale of discretization result in macroscale rates that are systematically slower than mineral dissolution and precipitation rates measured in the laboratory for single grains in well stirred liquids. Despite this, grain scale reaction rates used here provide a useful upper bound.

As noted above, a 1-D disequilibrium batch melting column with a single melt phase is

not able to capture the type of macroscopic disequilibrium that arises due to channelized flow. To capture the effect of sub-grid melt localisation requires a modelling approach that decouples the local melting reaction from the chemical exchange between the ascending melts and the solid residue. Rudge et al. (2011) do this for a simple binary phase loop by separating out the mass flux associated with phase change from the fluxes of components that occur without phase change. This is not readily extended to the more complex phase diagrams as the stoichiometry of the melting reaction varies with depth. Oliveira et al. (2020) model disequilibrium melting for more complex systems by introducing different thermodynamic subsystems that interact with each other to varying degrees; representing unmetasomatised regions far from melt channels, reactive regions at the rims of channels, and chemically isolated channel interiors. A similar approach could readily be taken using our disequilibrium formulation by introducing a second melt phase, representing the channelized melt that only reacts very slowly with the surrounding rock (i.e. at a rate governed by the background diffusion rate).

Further modelling in the Mg_2SiO_4-SiO_2 system would help further our understanding of feedbacks between melting and crystallization and transport. Of particular interest are models in 2- or 3-D that explore the formation of reaction infiltration instabilities. Dunite channels are thought to be formed through the incongruent dissolution reaction opx $\rightarrow$ ol + melt, but previous models have only considered congruent melting reactions. As this process has not been explored with real phase diagrams of incongruent melting, it is unresolved whether the gradient in silica activity with decreasing pressure of olivine-orthopyroxene saturated melts is sufficient to initiate channelisation. Stronger chemical gradients, such as that due the infiltration of deep hydrous melts may be required (Keller and Katz, 2016; Keller et al., 2017). Understanding this is critical for determining at what depth channelisation occurs in the mantle.

Extension of this approach to more complex thermodynamic systems would allow more direct comparison between models and field observations. For example applying this to a five

phase peridotite with solid solution would allow us to simulate the formation of the diverse reaction zones observed in orogenic peridotites. Furthermore, inclusion of aqueous fluids and hydrous phases such as amphibole and phlogopite would allow us to model important subduction zone processes. Application to such systems follows exactly the same workflow as outlined above, but would require an expanded set of reactions in the reactive system, and a greater number of fields to be solved for.

When extending the problem to higher dimensions, or to more complex petrological systems, it is important to consider the additional computational cost associated with greater model dimensions. To tackle such problems going forwards, the availability of efficient solvers will be paramount. One way to improve efficiency of more complex problems is to fix relatively invariable phase properties as constants where appropriate, so as to reduce the computational cost of calculating the Jacobian. For example, in the models above the densities, heat capacities, and expansivities of olivine and orthopyroxene could be approximated as constants over the melting region with very little loss of accuracy. Nonetheless, this framework provides a way to quantitatively assess what assumptions are suitable for a given problem, before scaling it up.

4.7 Summary

In this chapter I have implemented the general theory for disequilibrium reaction and open-system reactive transport described in chapter 2. The Mg_2SiO_4-SiO_2 binary system is the simplest model system for understanding silicate melting. We have extended previous thermodynamic modeling approaches by integrating thermodynamic models of the minerals and melt, with kinetic formulations of reaction. The simple 0-D batch reactor models presented here demonstrate consistency with the phase equilibrium models in the equilibrium limit, and also allow us to explore how choices in the kinetic models affect macroscopic reaction pathways. Reaction-diffusion models further serve to explore open-system reaction which is particularly useful for modeling the formation of reaction zones. Integration of more

complex thermodynamic systems into these simple batch and/or diffusive systems could be very useful in the interpretation and analysis of petrological experiments in which metastability and compositional and thermal gradients are often observed. Finally, we have modeled open-system reactive melt transport in the Mg_2SiO_4-SiO_2 in 1-D. This significantly extends the capabilities of previous magma dynamics models, which were previously restricted to modeling simple parameterized divariant melting reactions. Here we have directly incorporated a calibrated phase diagram with a variety of reaction morphologies, including eutectic and peritectic melting involving multiple solid phases. The goal in the future is to extend this to approach to higher dimensional models and to more complex petrological systems.

Chapter 5

Formation of High-Porosity Dunite Channels by Reactive Melt Transport

5.1 Introduction

Melt transport in high porosity dunite channels is thought to be an important mechanism during melt extraction beneath mid-ocean ridges. The major and trace element compositions of mid-ocean ridge basalts (MORBs) are not in equilibrium with the uppermost mantle (Stolper, 1980; Johnson et al., 1990; Elthon and Scarfe, 1984). In particular MORB is undersaturated in orthopyroxene (opx). This implies fractional or near-fractional melting and requires melts to be extracted rapidly from their source in high-flux channels (Spiegelman and Kenyon, 1992). Rapid melt extraction is corroborated by observations of uranium-series disequilibrium (McKenzie, 2000), and pulses of magmatism following deglaciation (Jull and McKenzie, 1996; Slater et al., 1998; Maclennan et al., 2002). Dunite channels observed in the mantle section of ophiolites are generally thought to represent the high-porosity conduits through which partial melts were transported (Kelemen et al., 1995a, 1997). Unlike the surrounding harzburgite, the dunites are in equilibrium with MORB. However, there remain significant questions concerning the mechanism driving melt channelization during partial melting.

In this chapter I develop numerical models to simulate the formation of dunite channels by reactive infiltration. The reactive infiltration instability is a chemo-dynamic instability that arises during porous flow through a solubility gradient (Chadam et al., 1986; Ortoleva et al., 1987). As melt ascends it dissolves, or melts, the surrounding solid matrix increasing

the local porosity. This locally increases the permeability and melt flux driving further dissolution: setting off a positive feedback. The reaction infiltration instability was first suggested as a mechanism for dunite channel formation by Aharonov et al. (1995) and Aharonov et al. (1997). Since then there have been numerous modeling efforts exploring channelization by coupled reactive melt transport in a deformable solid matrix. Early models only considered the mechanical and chemical couplings (Spiegelman et al., 2001; Spiegelman and Kelemen, 2003). Later models integrated thermal models by self-consistently conserving energy and accounting for latent heat of melting (Šrámek et al., 2007; Katz, 2008; Hewitt, 2010; Katz and Weatherley, 2012; Weatherley and Katz, 2012; Rudge et al., 2011; Keller and Katz, 2016; Keller et al., 2017). These studies have yielded important insights into the reaction-permeability-flux feedbacks, and have demonstrated the potential for background adiabatic decompression melting to suppress channelization. However, recent models have been restricted to simple parameterized phase diagrams. In particular they assume that both the melt and solid are homogeneous phases which vary smoothly in composition between compositional endmembers. In reality the mantle is a multimineralic medium in which melting occurs via eutectic or peritectic melting reactions. The formation of dunite channels themselves involves the open-system incongruent melting reaction

$$\text{melt}_1 + \text{opx} \rightarrow \text{melt}_2 + \text{ol} \tag{5.1}$$

Accurately modeling the melting process and the formation of replacive dunite reaction zones therefore requires an approach that explicitly accounts for the solid assemblage.

Here we build on previous modeling efforts by modeling reactive two-phase flow within a multimineralic solid residue. We use the disequilibrium reactive framework described in chapter 2, which consistently couples the dynamics and thermodynamics. We apply this to melting and reactive transport in the Mg_2SiO_4-SiO_2 binary system described in the previous chapters, which represents the simplest subsystem for modeling harzburgite (ol +

opx) melting. This chapter is organized as follows: Section 5.2 sets up the thermodynamic and kinetic models; Section 5.3 lays out the governing equations for reactive transport in a viscously compactible solid matrix; Section 5.4 describes the set-up for a series of 1-D and 2-D models; Section 5.5 presents the model results — the 1-D models provide a framework for understanding open-system melting in the Mg_2SiO_4-SiO_2 binary system, while the 2-D models explore the conditions for reactive channelization; finally Section 5.6 discusses the broader implications of these results.

5.2 Thermodynamic and reactive system

We model reaction between olivine (ol), orthopyroxene (opx) and melt (f) in the Mg_2SiO_4-SiO_2 binary system. In this system olivine is pure forsterite ($fo(ol)$, Mg_2SiO_4), orthopyroxene is pure enstatite ($en(opx)$, $Mg_2Si_2O_6$), and the melt is a binary solution between silica ($q(f)$, Si_2O_4) and forsterite ($fo(f)$, Mg_2SiO_4) endmembers. The details of the Gibbs free energy models of the pure endmembers and phases are described in chapter 3. Because we are considering reaction in a harzburgitic mantle, we do not include quartz in the reactive system. The phase assemblage is then described in terms of four variables: the volume fractions of the three phases ϕ_{ol}, ϕ_{opx}, and ϕ_f; and the concentration of silica in the melt c_f^q. We only need one compositional variable as the minerals are pure phases, and the melt forsterite concentration is simply $c_f^{fo} = 1 - c_f^q$.

The equilibrium phase diagrams at 1 bar and 1 GPa for mafic compositions in the Mg_2SiO_4-SiO_2 system are shown in Figure 5.1 (a) and (b). As shown, the *fo*-*en* cotectic melting reaction shifts from eutectic to peritectic at low pressure due to the relative expansion of the olivine phase field. This is responsible for the gradient in equilibrium melt silica concentration with pressure shown in Figure 5.1 (c). In this chapter we will be exploring reactive channelization as a result of melt transport up this silica gradient. While the binary subsystem reasonably approximates the gradient in silica content of natural peridotite melts, we do not capture the effects of incompatible components in the melt, ranging from

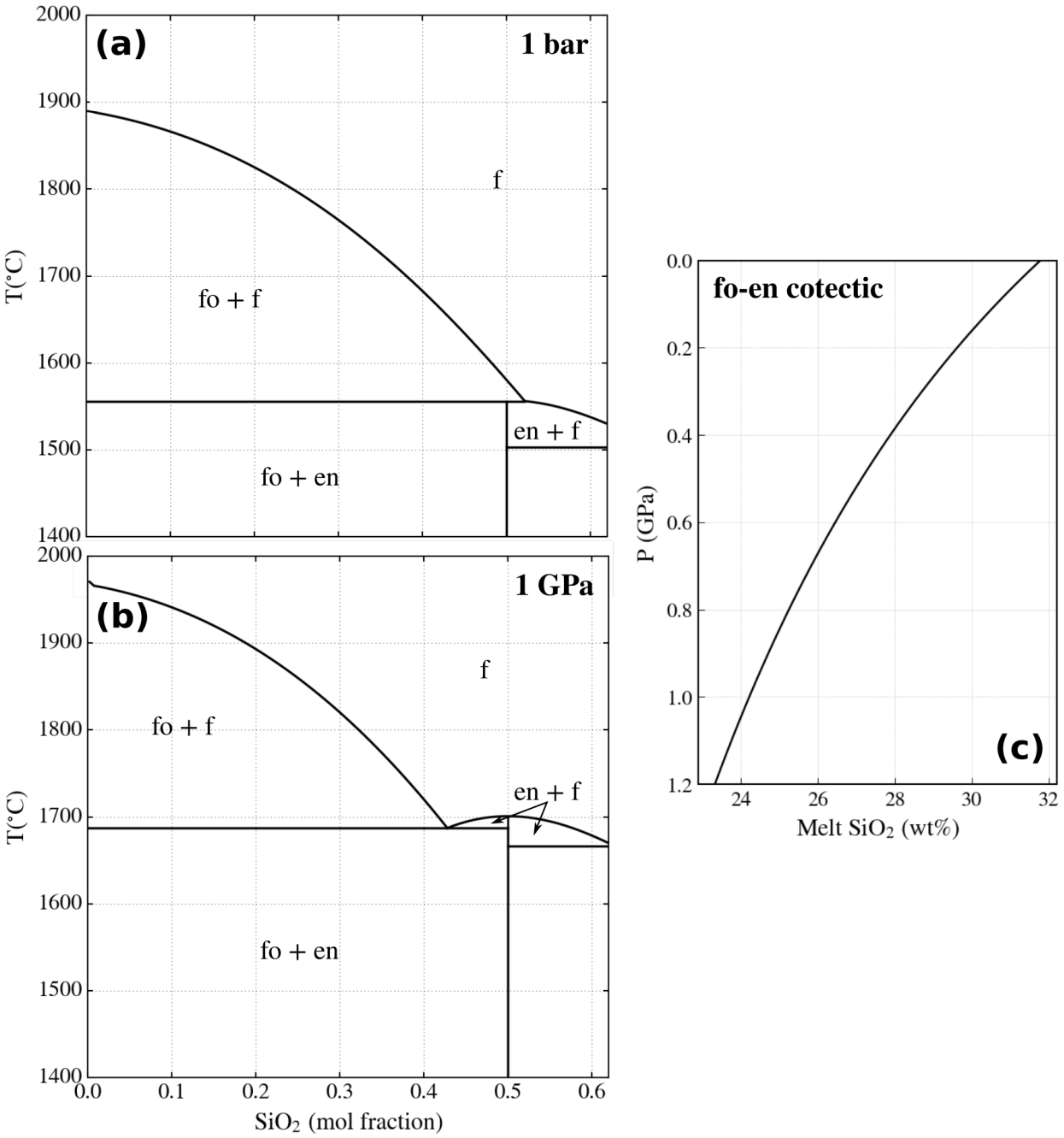

Figure 5.1: Calculated equilibrium phase diagrams for mafic compositions in the Mg_2SiO_4-SiO_2 binary system at (a) 1 bar, and (b) 1 GPa. (c) Variation fo-en cotectic melt composition as a function of pressure

Fe to H_2O, which further contribute to flux melting. The role of volatiles in reactive melt transport is explored by Keller and Katz (2016) and Keller et al. (2017). Furthermore, *fo-en* cotectic melting in the binary is a univariant reaction. This differs from natural systems in which melting is multivariate, occurring over a region in P-T space. Despite these shortcomings, this contribution is the first to include peritectic and eutectic melting reactions, involving multiple solid phases, in a coupled two-phase flow model. By explicitly describing the mineralogy of the solid residue we are able to model the formation of replacive dunites by incongruent open-system melting.

In this two-component thermodynamic system there are four phase endmembers in total meaning that there are two independent stoichiometric reactions. We use the following melt-mediated reactions

$$\begin{aligned} &1.\ fo(ol) \rightleftharpoons fo(f) \\ &2.\ en(opx) \rightleftharpoons \frac{1}{2}q(f) + fo(f) \end{aligned} \tag{5.2}$$

Weighting by the molar masses, the mass-based stoichiometric coefficients are

$$\boldsymbol{\nu} = \begin{bmatrix} \nu^{q}_{f,1} & \nu^{q}_{f,2} \\ \nu^{fo}_{f,1} & \nu^{fo}_{f,2} \\ \nu^{fo}_{ol,1} & \nu^{fo}_{ol,2} \\ \nu^{en}_{opx,1} & \nu^{en}_{opx,2} \end{bmatrix} = \begin{bmatrix} 0 & \frac{M^{q}_{f}}{M^{en}_{opx}} \\ 1 & \frac{M^{fo}_{f}}{M^{en}_{opx}} \\ -1 & 0 \\ 0 & -1 \end{bmatrix} \tag{5.3}$$

Where M^{k}_{i} is the molar mass of endmember k in phase i. These reactions are assumed to proceed at independent rates R_1 and R_2 as a function of their respective chemical affinities. At high temperature within the mantle we assume the system is close to chemical equilibrium We therefore use linear rate laws. The reaction rates in units of $\mathrm{kgm^{-3}s^{-1}}$ are

$$R_1 \begin{cases} = r_0 \exp\left(\frac{T}{T_r}\right) S_0 \phi_{ol} \frac{M_0}{M^{fo}_{ol}} \frac{A_1}{RT}, \ A_1 \geq 0 \\ = r_0 \exp\left(\frac{T}{T_r}\right) S_0 \phi_{f} \frac{M_0}{M^{fo}_{ol}} \frac{A_1}{RT}, \ A_1 < 0 \end{cases} \tag{5.4}$$

$$R_2 \begin{cases} = r_0 \text{exp}\left(\frac{T}{T_r}\right) S_0 \phi_{opx} \frac{M_0}{M^{en}_{opx}} \frac{A_2}{RT}, \ A_2 \geq 0 \\ = r_0 \text{exp}\left(\frac{T}{T_r}\right) S_0 \phi_f \frac{M_0}{M^{en}_{opx}} \frac{A_2}{RT}, \ A_2 < 0 \end{cases} \tag{5.5}$$

Where r_0 is the rate constant prefactor with units $\text{kgm}^{-2}\text{s}^{-1}$; T_r is a reference reaction temperature; and M_0 is a reference mass of reaction; S_0 is the reference mineral-melt surface area with units m^2m^{-3}; and R is the gas constant. A_j is the molar chemical affinity of reaction defined as before as

$$A_j = -\sum_{i=1}^{N} \sum_{k=1}^{K_i} \tilde{\nu}^k_{i,j} \tilde{\mu}^k_i \tag{5.6}$$

where $\tilde{\nu}^k_{i,j}$ are the molar stoichiometric coefficients, and $\tilde{\mu}^k_i$ are the molar chemical potentials.

The piecewise rate laws account for the different reactants in the forward and reverse direction. Here we have made the simplifying assumption that the surface area is a linear function of the reactant phase fraction: i.e. in the forward direction $S_j \propto [\phi_{ol}, \phi_{opx}]$, and in the reverse direction $S_j \propto \phi_f$. In reality the reactive surface area depends on the rock microstructure and therefore likely has a more complex functional form. Close to equilibrium, however, this does not have a significant impact on the melting reactions. Most importantly these reactive surface areas satisfy the condition that $S \to 0$ as the reactant phase is exhausted, ensuring positivity of phase fraction.

We describe the rate constants with an Arrhenius temperature dependence. However, we have made the simplifying assumption that they have the same values for both reactions in both the forward and reverse directions. The kinetics of dissolution and precipitation in igneous systems are poorly constrained, and there is not sufficient evidence to differentiate between the melting and crystallization rates during reactive porous flow. This assumption could easily be relaxed in light of further constraints.

Taking these reaction rates along with the reaction stoichiometries, the net reactive mass

transfers of the endmembers and phases are given by

$$\begin{aligned}
&\Gamma_{ol}^{fo} = -R_1 \quad \Gamma_{ol} = \Gamma_{ol}^{fo} = -R_1 \\
&\Gamma_{opx}^{en} = -R_2 \quad \Gamma_{opx} = \Gamma_{opx}^{en} = -R_2 \\
&\Gamma_f^q = \frac{M_f^q}{2M_{opx}^{en}} R_2 \quad \Gamma_f^{fo} = R_1 + \frac{M_f^{fo}}{M_{opx}^{en}} R_2 \quad \Gamma_f = \Gamma_f^q + \Gamma_f^{fo} = R_1 + R_2
\end{aligned} \tag{5.7}$$

As described in the previous chapters, the thermodynamic and kinetic models are implemented in custom C++ libraries generated using the thermocodegen and thermoengine packages of the ENKI project. The software has a hierarchical structure, and all of the relevant thermodynamic and reactive properties, along with their derivatives where appropriate, are accessible through the kinetics library. This library can be imported directly into the dynamics code. Thermocodegen also provides python bindings so that the system can be explored in a python environment. This is very useful when setting up the problem and doing simple batch calculations with which to compare the results of the dynamic models.

The properties of the pure endmembers are functions of P and T; those of the phases are functions of P, T, and the phase compositions $\boldsymbol{c} = \left[[c_f^q, 1 - c_f^q][1][1]\right]$. The reaction rates and reactive mass transfers are functions of P, T, $\boldsymbol{c}$, and the phase fractions $\boldsymbol{\phi} = [\phi_{ol}, \phi_{opx}, \phi_f]$. We assume here that the thermodynamic pressure is equivalent to the fluid pressure. The correct thermodynamic pressure to use is subject to debate. For a further discussion of this see Rudge et al. (2011).

5.3 Governing equations

The conservation equations for mass momentum and energy for porous multiphase reactive flow in a deformable solid matrix are described in chapter 2. These are based on the two-phase flow formulations of McKenzie (1984) and Rudge et al. (2011), but generalized for a multiphase solid. In the high temperature convecting mantle the solid deforms viscously on the timescale of melt extraction. Here, we ignore deviatoric strain and decompose the

fluid pressure P into the compaction pressure $\mathcal{P}$ and the lithostatic pressure $\rho_{s0}\boldsymbol{g}\cdot\boldsymbol{z}$. The governing equations for c_f^q, $\boldsymbol{\phi}$, $\mathcal{P}$, $\boldsymbol{v}_s$ and T are then as follows

$$\rho_f\phi_f\frac{\mathrm{D}_f c_f^k}{\mathrm{D}t} = \Gamma_f^k - c_f^k\Gamma_f + D_f^k\boldsymbol{\nabla}\cdot(\phi_f+\varepsilon_D)\boldsymbol{\nabla}c_f^k \tag{5.8}$$

$$\frac{\mathrm{D}_s\phi_i}{\mathrm{D}t} = -\phi_i\frac{\mathcal{P}}{\zeta} + \frac{\Gamma_i}{\rho_i} \quad \text{for } i = ol, opx \tag{5.9}$$

$$\frac{\mathrm{D}_s\phi_f}{\mathrm{D}t} = (1-\phi_f)\frac{\mathcal{P}}{\zeta} - \sum_{i=2}^{N}\frac{\Gamma_i}{\rho_i} \tag{5.10}$$

$$\frac{\mathcal{P}}{\zeta} = \boldsymbol{\nabla}\cdot\frac{K}{\mu}\left(\boldsymbol{\nabla}\mathcal{P} + \Delta\rho\boldsymbol{g}\right) + \sum_{i=1}^{N}\frac{\Gamma_i}{\rho_i} \tag{5.11}$$

$$\boldsymbol{\nabla}\cdot\boldsymbol{v}_s = \frac{\mathcal{P}}{\zeta} \tag{5.12}$$

$$\sum_{i=1}^{N}\left[\rho_i\phi_i C_{Pi}\frac{\mathrm{D}_i T}{\mathrm{D}t} - \phi_i\alpha_i T\frac{\mathrm{D}_i P}{\mathrm{D}t} + Ts_i\Gamma_i\right] = k\boldsymbol{\nabla}^2 T \tag{5.13}$$

Here we have used the convention $i = 1$ for the melt, and $i = 2$ for ol and $i = 3$ for opx. ρ_i, C_{Pi}, α_i, and s_i are the density, heat capacity, thermal expansivity, and entropy of phase i respectively. $\bar{\rho} = \sum_i \phi_i\rho_i$ is the average density of the multiphase assemblage. $\boldsymbol{v}_i$ is the velocity field of phase i: we assume that the aggregate solid (ol + opx) behaves as a single mechanical phase with velocity $\boldsymbol{v}_s$, and that the melt has velocity $\boldsymbol{v}_f$. $\frac{\mathrm{D}_i}{\mathrm{D}t}$ is the Lagrangian derivative following phase i $\frac{\mathrm{D}_i}{\mathrm{D}t} = \frac{\partial}{\partial t} + \boldsymbol{v}_i\cdot\boldsymbol{\nabla}$. μ is the melt viscosity, k is the thermal conductivity, D_f^q is the diffusivity of of silica in the melt, and ε_D is a regularization parameter to account for subsolidus diffusion along grain boundaries. As the phase densities are relatively constant, we have neglected the density derivative terms $\frac{\mathrm{D}_i\rho_i}{\mathrm{D}t}$. We have also neglected dissipative heating terms in the temperature equation.

Given ϕ_f, $\mathcal{P}$, and $\boldsymbol{v}_s$, the melt flux is reconstructed as

$$\phi_f\boldsymbol{v}_f = \phi_f\boldsymbol{v}_s - \frac{K}{\mu}\left(\boldsymbol{\nabla}\mathcal{P} + \Delta\rho\boldsymbol{g}\right) \tag{5.14}$$

The mechanical equations are closed with constitutive relations for the permeability K and bulk viscosity ζ. Following previous authors we will use the following ϕ_f-dependent expression for the bulk viscosity

$$\zeta = \zeta_0 \phi_f^m, \quad m = -1 \tag{5.15}$$

We use a simple power law relationship for the permeability

$$K = K_0 \phi_f^n, \quad n = 3 \tag{5.16}$$

5.3.1 Scaling

We non-dimensionalize the equations by introducing the following scalings

$$\begin{array}{llll} z = hz' & t = \frac{h}{q_0} t' & (\boldsymbol{v}_f, \boldsymbol{v}_s) = q_0(\boldsymbol{v}'_f, \boldsymbol{v}'_s) & \boldsymbol{g} = g\hat{\boldsymbol{g}} \\ T = T_0 T' & \rho_i = \Delta\rho_0 \rho'_i & P = \Delta\rho_0 g h P' & \Gamma_i = r_0 S_0 \Gamma'_i \\ \zeta = \zeta(\phi_0)\zeta' & K = K(\phi_0)K' & \mu = \mu_0 \mu' & \\ C_{Pi} = C_{P0} C'_{Pi} & s_i = C_{P0} s'_i & \alpha_i = \alpha_0 \alpha'_i & \end{array}$$

Where the primed terms indicate dimensionless variables. The scaling parameters are as follows: h is the height of the system; $\Delta\rho_0$ is the reference density difference between solid and melt; and $K(\phi_0)$ and $\zeta(\phi_0)$ are the permeability and bulk viscosity at the reference porosity. q_0 is the reference separation flux, given by

$$q_0 = \frac{K(\phi_0)\Delta\rho_0 g}{\mu_0} \tag{5.17}$$

and δ is the compaction length defined as

$$\delta = \sqrt{\frac{K(\phi_0)\zeta(\phi_0)}{\mu_0}} \tag{5.18}$$

Removing the primes the governing equations in terms of nondimensional variables are then

$$\rho_f \phi_f \frac{\mathrm{D}_f c_f^q}{\mathrm{D}t} = Da\left(\Gamma_f^q - c_f^q \Gamma_f\right) + \frac{1}{Pe_C}\boldsymbol{\nabla}\cdot\phi_f\boldsymbol{\nabla}c_f^q \tag{5.19}$$

$$\frac{\mathrm{D}_s\phi_i}{\mathrm{D}t} = -\frac{h^2}{\delta^2}\phi_i\frac{\mathcal{P}}{\zeta} + Da\frac{\Gamma_i}{\rho_i} \quad \text{for } i = ol, opx \tag{5.20}$$

$$\frac{\mathrm{D}_s\phi_f}{\mathrm{D}t} = \frac{h^2}{\delta^2}(1-\phi_f)\frac{\mathcal{P}}{\zeta} - Da\sum_{i=2}^{N}\frac{\Gamma_i}{\rho_i} \tag{5.21}$$

$$\frac{h^2}{\delta^2}\frac{\mathcal{P}}{\zeta} = \boldsymbol{\nabla}\cdot\frac{K}{\mu}\left(\boldsymbol{\nabla}\mathcal{P} + \hat{\boldsymbol{g}}\right) + Da\sum_{i=1}^{N}\frac{\Gamma_i}{\rho_i} \tag{5.22}$$

$$\boldsymbol{\nabla}\cdot\boldsymbol{v}_s = \frac{h^2}{\delta^2}\frac{\mathcal{P}}{\zeta} \tag{5.23}$$

$$\phi_f\boldsymbol{v}_f = \phi_f\boldsymbol{v}_s - \frac{K}{\mu}\left(\boldsymbol{\nabla}\mathcal{P} + \hat{\boldsymbol{g}}\right) \tag{5.24}$$

$$\sum_{i=1}^{N}\left[\rho_i\phi_i C_{Pi}\frac{\mathrm{D}_i T}{\mathrm{D}t} - Ad\phi_i\alpha_i T\frac{\mathrm{D}_i P}{\mathrm{D}t} + DaTs_i\Gamma_i\right] = \frac{1}{Pe_T}\boldsymbol{\nabla}^2 T \tag{5.25}$$

Where Da is the Damköhler number, Pe_C is the compositional Peclet number, and Pe_T is the thermal Peclet number

$$Da = \frac{r_0 S_0 h}{\Delta\rho_0 q_0} \tag{5.26}$$

$$Pe_C = \frac{\Delta\rho_0 q_0 h}{D_f^q \rho_0} \tag{5.27}$$

$$Pe_T = \frac{\Delta\rho_0 q_0 h}{\kappa\rho_0} \tag{5.28}$$

The dimensionless parameter Ad describes the adiabatic cooling due to decompression

$$Ad = \frac{\alpha_0 g h}{C_{P0}} \tag{5.29}$$

5.4 Model setup

We consider mantle melting and reactive melt transport within a decompressing region beneath the axis of a mid-ocean ridge. We will model both 1-D profiles, and melting within a simple 0.8:1 rectangular 2-D region. The 1-D column models allow us to establish the steady state vertical melting profiles and to explore the open-system melting systematics. The 2-D models the allow us to explore the coupling between reaction and fluid flow and to determine the regime under which reactive channelization occurs.

5.4.1 Initial and boundary conditions

The model domains of both the 1-D and 2-D models extend from 1.2 GPa and the surface. The geometry and setup of the 2-D models are shown in Figure 5.2. The 1-D models represent vertical sections through the 2-D domain. To simulate the effects of passive decompression we impose a constant solid upwelling velocity at the upper boundary $\boldsymbol{v}_s \cdot \hat{\boldsymbol{z}} = W_0$, and allow free flow across the lower boundary. The upwelling velocity is varied in the models between $0 \geq W_0 \geq 10$ cm yr^{-1}. Compaction within the melting region means that $\boldsymbol{v}_s \cdot \hat{\boldsymbol{z}} > W_0$ at the lower boundary. On the lower boundary we impose zero compaction pressure, and fix the temperature $T = T_0$ such that the mantle crosses the solidus around 1 GPa. Melting occurs at a much higher temperature in the Mg_2SiO_4–SiO_2 system than for natural peridotite compositions. As a result the model temperatures are higher than the natural mantle geotherm.

We consider two melting scenarios. The first is simple decompression melting in which solid rock upwells from below its solidus and begins to partially melt on crossing the solidus. In this case the inflowing mantle at the lower boundary has zero porosity and fixed solid phase proportions. For similarity to upper mantle harzburgites we use $\phi_{ol} = 0.6$ and $\phi_{opx} = 0.4$. Although there is no melt physically present at the lower boundary, we still have to specify a melt composition. Given the underlying thermo-kinetic model, reaction spontaneously oc-

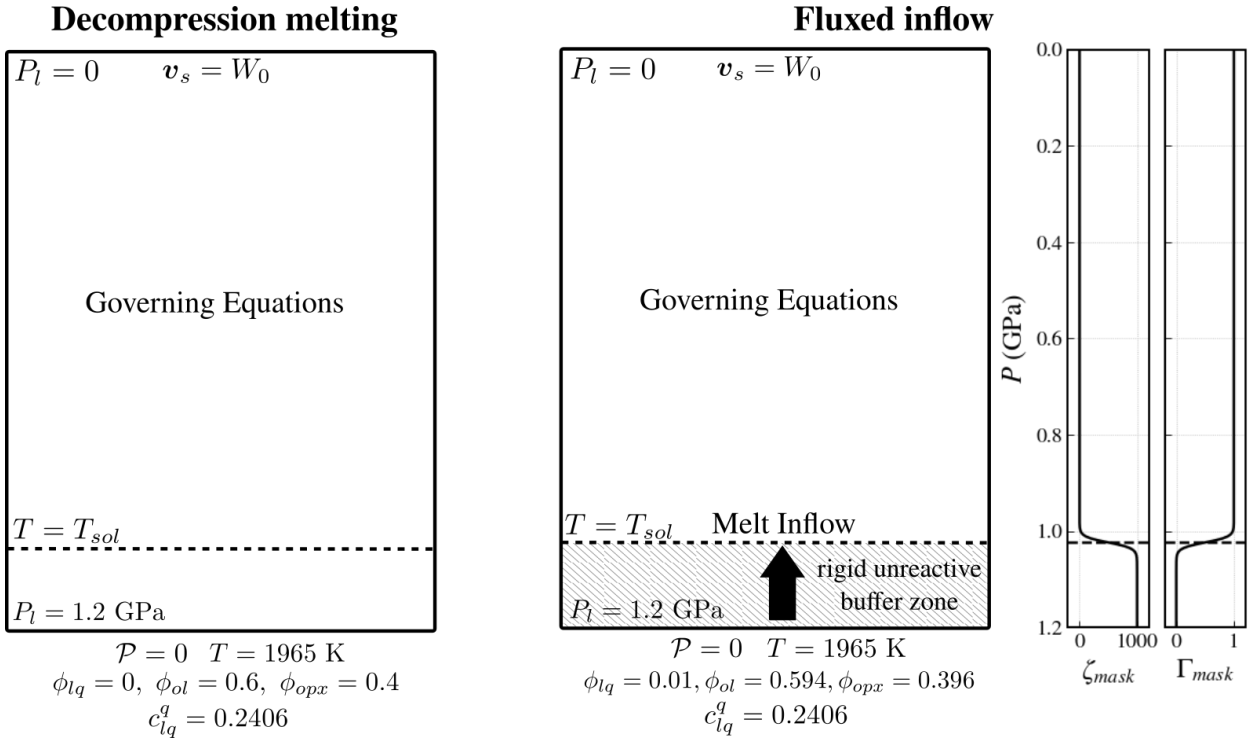

Figure 5.2: Model setup for 2-D upwelling column models. On the right is the setup for the decompression melting models with no melt flux across the lower boundary ($\phi_f = 0$). On the left is the setup for decompression melting with an influx of melt across the lower boundary ($\phi_=0.01$). For these models we apply 'masks' to ζ and Γ_i to impose a rigid unreactive buffer zone below the solidus. These are given by $\zeta_{mask} = 1000 + \frac{1-1000}{2}\left(\tanh\left(\frac{P_{sol}-P}{\lambda}\right) + 1.\right)$ and $\Gamma_{mask} = \frac{1}{2}\left(\tanh\left(\frac{P_{sol}-P}{\lambda}\right) + 1\right)$. The boundary conditions are the same for the 1-D models.

curs as a result of the relative stability of the melt and solid phases. To avoid disequilibrium melting beneath the solidus, the melt composition must be carefully chosen so that it falls below the metastable extensions of the fo and en liquidus surfaces. We use a melt composition of $c^q_f = 0.2406$ which is slightly more forsteritic than the equilibrium melt composition at the 1 GPa solidus.

In the second scenario we consider decompression melting with an influx of melt across the lower boundary. We refer to these models are 'fluxed inflow' melting scenarios. We impose 1% porosity at the lower boundary $\phi_f = 0.01$, while using the same relative proportions of ol and opx as before ($\phi_{ol} = 0.594, \ \phi_{opx} = 0.396$), and the same melt composition. In these models compaction and reactive crystallization of melt beneath the solidus are prohibited by imposing a rigid unreactive buffer zone. This is achieved by applying 'masks' to the bulk

viscosity and reactive mass transfer terms such that

$$\zeta' = \zeta_{\text{mask}}\zeta \tag{5.30}$$

$$\left(\Gamma_i,\ \Gamma_i^k\right)' = \Gamma_{\text{mask}}\left(\Gamma_i,\ \Gamma_i^k\right) \tag{5.31}$$

Where ζ_{mask} and Γ_{mask} are tanh transfer functions as shown in Figure 5.2.

The 1-D models are initialized with constant porosity, phase proportions, melt composition and temperature across the domain. As the system is initially far out of equilibrium there is a large transient melting pulse before it evolves to steady state. To avoid this transient, the 2-D models are instead initialized with the steady state 1-D melting profiles for pure decompression melting. On top of the steady state depletion gradient in the solid phase fractions we introduce some uniformly distributed random noise as shown in Figure 5.3. Because melting in the binary is univariant, the melting temperature is independent of ol and opx phase proportions. However, these heterogeneities in modal proportions produce variations in melting rate via the reactive surface area terms in the reaction rates. As opx is the main contributor to the net melting reaction, regions with high opx have locally increased melting rate.

5.4.2 Parameters

Apart from varying the solid upwelling velocity, the parameter values are the same for all model runs shown here. Parameters are selected based on estimates for partial melting in the mantle. To avoid numerical instabilities at the solidus, however, we use a factor of 10 lower reaction rates and higher diffusivities than might be expected. All reference and scaling parameters are reported in table 5.1. The thermodynamic properties, including ρ_i, C_{Pi}, α_i, and s_i, of all phases are calculated on the fly from the underlying thermodynamic models. Using the thermodynamic rate laws in Eq (5.5), the reaction rates and net melting stoichiometry also vary as a function of the chemical affinities. This ensures complete self-

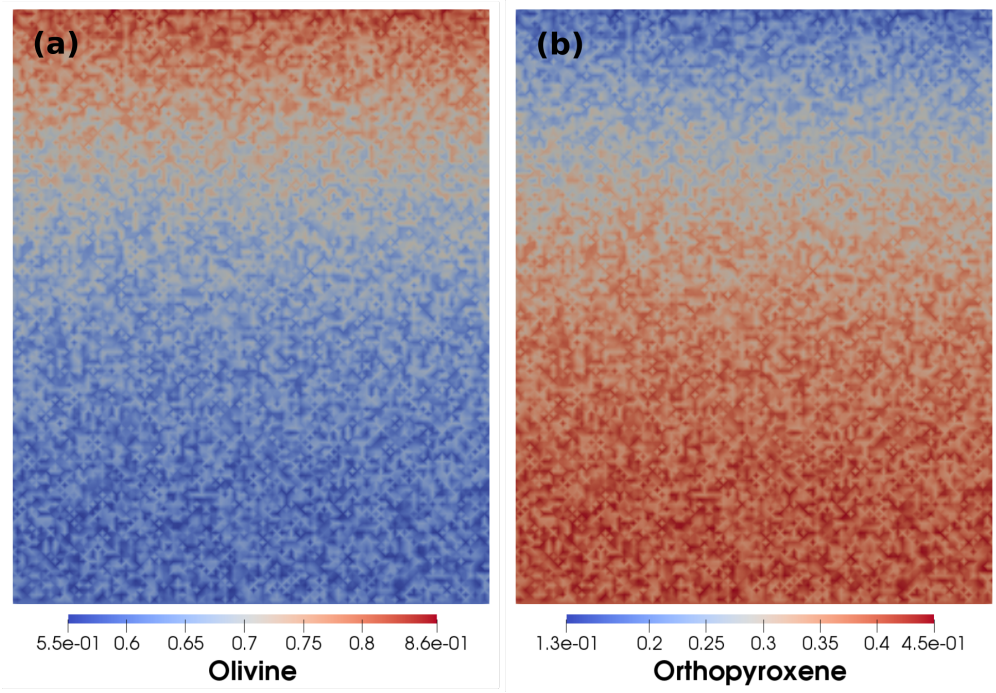

Figure 5.3: The initial fields for the modal proportions of olivine and opx in the solid residue ($\frac{\phi_{ol}}{1-\phi_f}$ and $\frac{\phi_{opx}}{1-\phi_f}$) used in the 2-D models. These are obtained from the steady state 1-D decompression melting profiles, with uniform random noise imposed over the top. The maximum amplitude of the random fluctuations is $\varepsilon_\phi = 0.05$.

consistency between the thermodynamics and dynamics.

5.4.3 Numerical implementation

We discretize the system of equations (5.19)-(5.25) using finite elements in space and finite difference in time. They are solved numerically using TerraFERMA (Wilson et al., 2017), which is an open-source software package for reproducible assembly and solution of finite element models that leverages the FEniCS (Alnæs et al., 2015), PETSc (Balay et al., 2012), and SPuD (Ham et al., 2009) libraries. The finite element method involves solution, within a finite element space, to the weak forms of the equations, which are provided in Appendix E. Solution to the system at each timestep is obtained using an iterative Newton solver. We improve convergence by solving over two steps: in the first we estimate solutions for $\boldsymbol{\phi}$, c_f^q, and T; before solving the full system of equations.

The domain for the 1-D models is discretized using a uniform grid with 320 nodes, giving

Table 5.1: Parameters, definitions, and reference values

Temperature	T_0	1965 K
Pressure	P_0	1.2 GPa
System depth	$h = \frac{P_0}{\rho_0 g}$	38226 m
Density	ρ_0	3200 kgm^{-3}
Density difference	$\Delta\rho_0 = \bar{\rho}_s - \rho_f$	300 kgm^{-3}
Heat capacity	C_{P0}	1.36 $\text{Jkg}^{-1}\text{K}^{-1}$
Expansivity	α_0	5e-5 K$^-$1
Gravity	g	9.81 ms^{-2}
Solid velocity	W_0	0-10 cm yr^{-1}
Rate constant	r_0	1e-9 $\text{kgm}^{-2}\text{s}^{-1}$
Reactive surface area	S_0	6000 m^2m^{-3}
Melt silica diffusivity	D_f^q	1e-7 m^2s^{-1}
Thermal diffusivity	κ	1e-6 m^2s^{-1}
Porosity	ϕ_0	0.05
Melt viscosity	μ_0	1 Pas
Bulk viscosity coefficient	ζ_0	1e19 Pas
Bulk viscosity	$\zeta(\phi_0) = \zeta_0\phi_0^{-1}$	2e20 Pas
Permeability coefficient	K_0	1e-7 m^2
Permeability	$K(\phi_0) = K_0\phi_0^3$	1.25e-11 m^2
Melt flux	$q_0 = \frac{K(\phi_0)\Delta\rho_0 g}{\mu_0}$	3.68e-7 ms^{-1}
Compaction length	$\delta = \sqrt{\frac{K(\phi_0)\zeta(\phi_0)}{\mu}}$	5e4 m
Damköhler number	$Da = \frac{r^* h}{q_0}$	2217
Peclet number	$Pe_C = \frac{D_f^q}{q_0 h}$	1.5e7
Peclet number	$Pe_T = \frac{\kappa}{q_0 h}$	1.5e4
Adiabatic parameter	$Ad = \frac{\alpha_0 g h}{C_{P0}}$	13.8

a resolution of 120 m. For the 2-D models we use a uniform triangular mesh with 100×125 cells; this gives a mesh resolution of 300 m.

5.5 Results

5.5.1 1-D models

The decompression melting model evolves to steady state after 100 kyrs. The steady state melting columns for a solid upwelling rate of $W_0 = 4$ cm yr^{-1} are shown in Figure

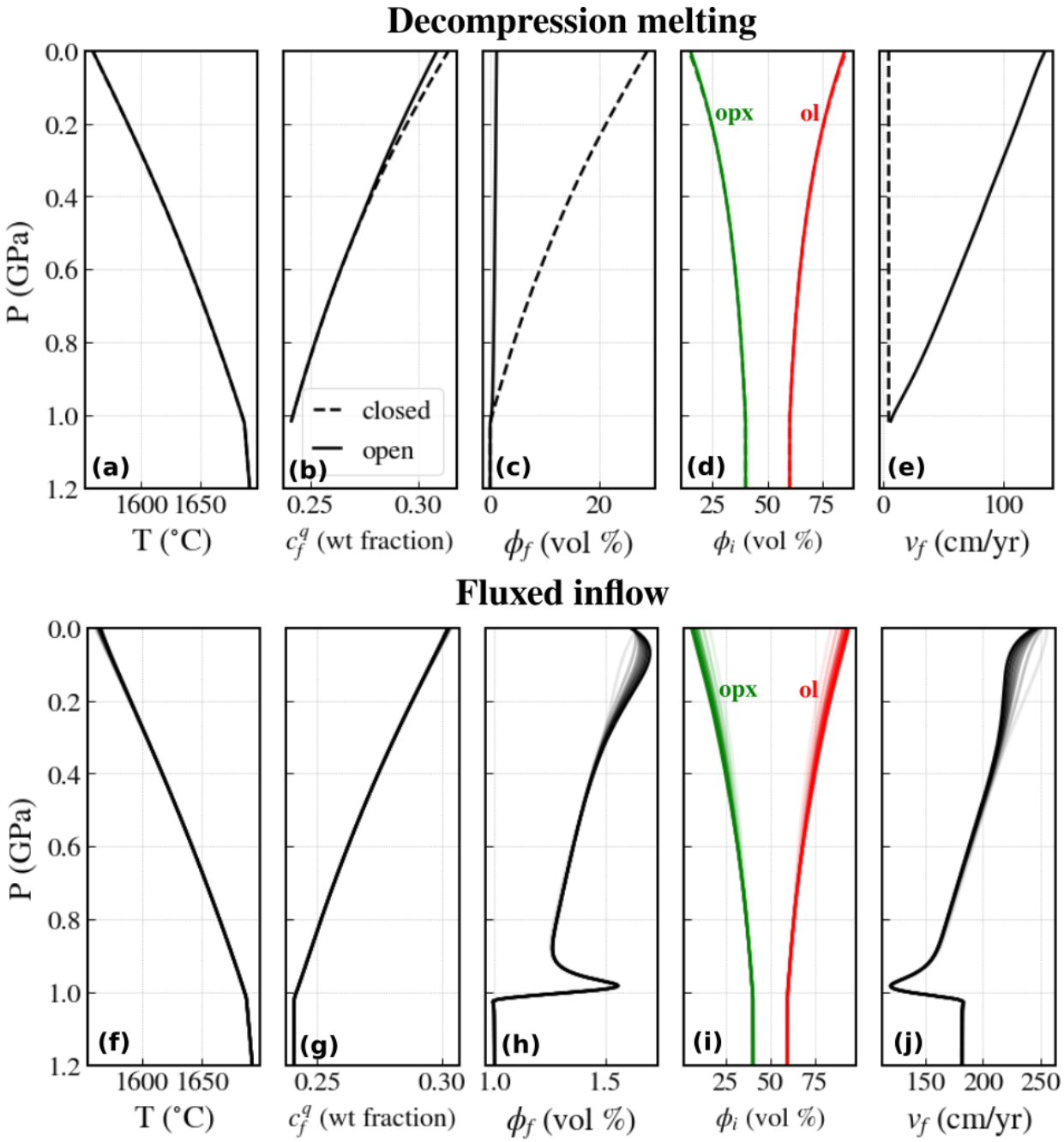

Figure 5.4: 1-D column models shown for $t = 10$ in model time. (a)-(e) show results for decompression melt models. The dashed lines correspond to 'closed-system' batch melting where we have set $K = 0$. (f)-(j) show results for the fluxed inflow models. These do not reach steady state due to the sustained flux of melt on the bottom boundary. Profiles at $t = 2, 4, 6, 7, 8, 9, 10$.

5.4 (a)-(e). In the equilibrium limit, steady state 1-D reactive porous flow is constrained to be equivalent to batch melting (Asimow and Stolper, 1999). In the models here some disequilibrium arises due to solid and melt advection. To separate out the disequilibrium effects of open-system melt transport versus solid upwelling, we have run a suite of models with the permeability set to zero. All the other parameters are the same, but now the melt does not separate from the solid residue. As such the melt velocity is equal to the solid velocity (i.e. $\boldsymbol{v}_f = \boldsymbol{v}_s = W_0$), and the porosity remains high. There is little appreciable difference between T and $\phi_{ol,opx}$ for the closed and open melting scenarios. However a more substantial difference is observed in c_f^q at the top of the column where the open-system melt velocity is greatest. This difference is caused by the additional component of disequilibrium due to melt transport relative to the solid.

Figure 5.4 (f)-(j) shows 1-D melting profiles with fluxed inflow of melt, again for an upwelling rate of $W_0 = 4$ cm yr^{-1}. The inflow of melt means that these models do not evolve to steady state, but rather become progressively more depleted in opx, eventually forming a dunite layer at the top of the column. The ledges in ϕ_f and v_f above the solidus are a result of the rigid buffer zone imposed at the base of the domain.

Analysis of open system reaction rates

Reactive channelization arises during open-system melting when local fluctuations in the melt flux produce variations in the melting rate in excess of those due to background decompression melting. This occurs during flow up a solubility gradient. channelization is favored when there are strong gradients in the equilibrium melt composition, and when melt velocities are high relative to the solid. This second condition requires implies high rock permeability. This is shown schematically in Figure 5.5.

In our reactive formulation, the melting rate Γ_f is a function of the disequilibrium due to both solid and melt advection, making it difficult to deconvolve the two. However, by comparing Γ_f for the open-system ($K = K_0(\phi_f)$) and closed-system ($K = 0$) models shown

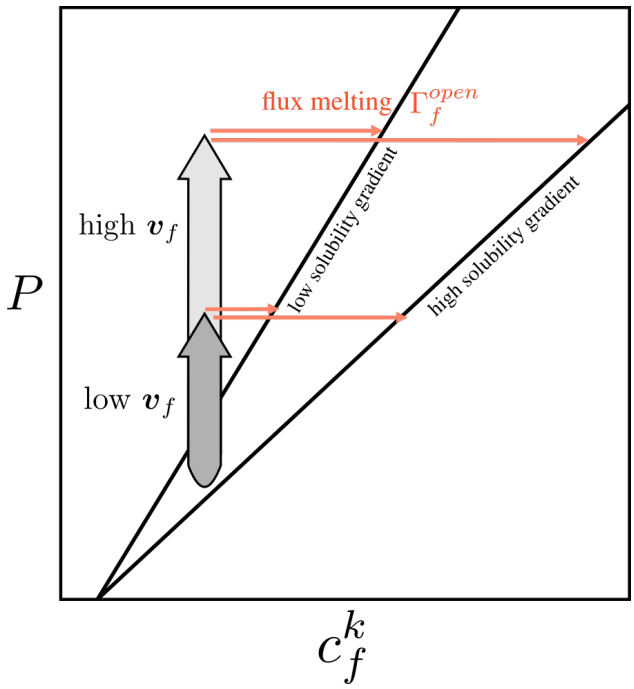

Figure 5.5: Schematic illustration of the additional component of flux melting driven by transport of melt relative to the solid matrix (i.e. open-system melting). Pressure decreases vertically on the y-axis and the x-axis is the concentration of a component k in the melt. The black lines show two examples of the equilibrium concentration of component k in the melt. Melt must react with the surrounding solid to maintain equilibrium as it ascends, with the additional component of flux melting given by Γ_f^{open}. The degree of flux melting therefore increases with solubility gradient and melt velocity.

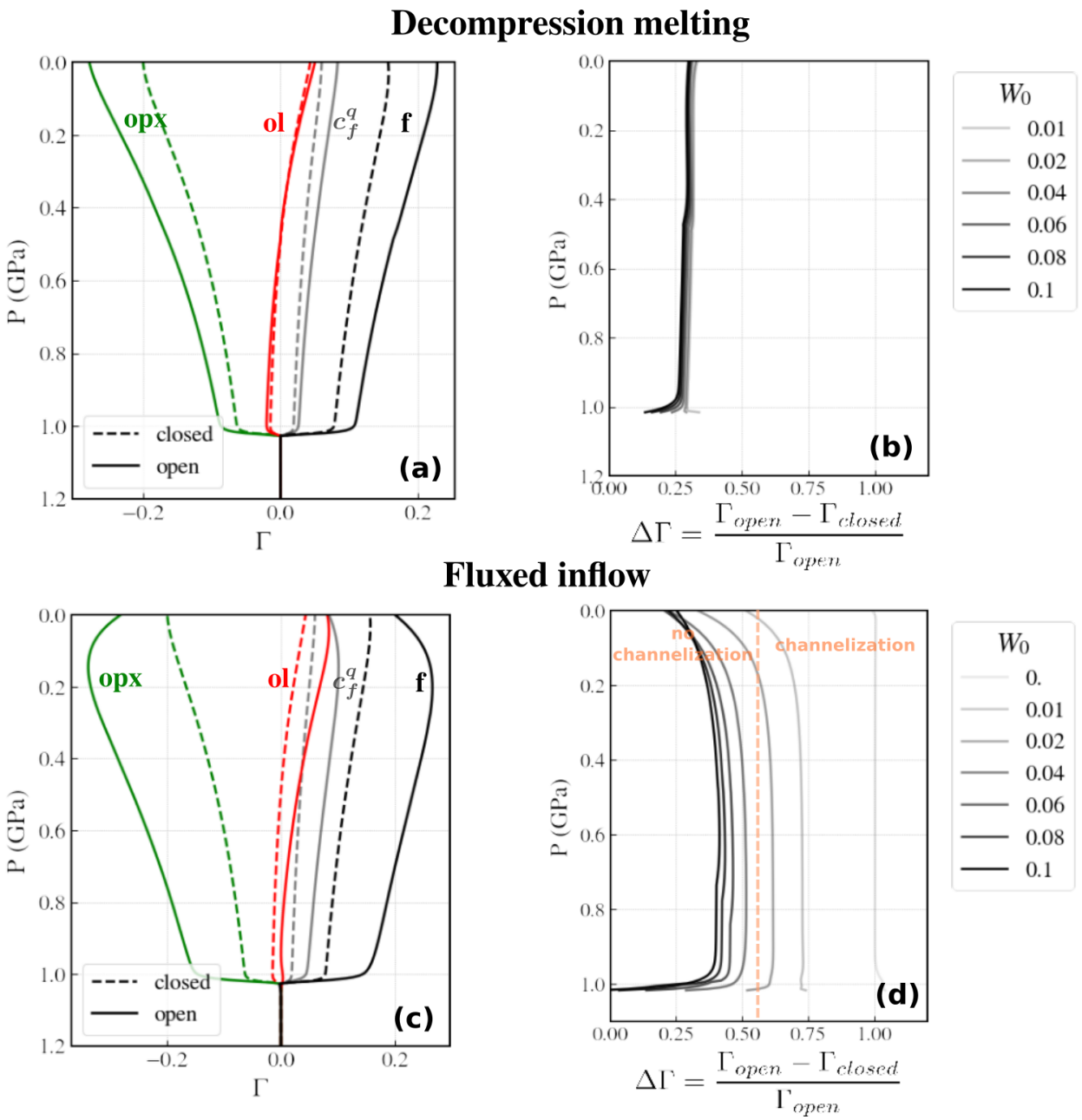

Figure 5.6: Analysis of reaction rates for 1-D melting columns. Plots (a) and (c) show the net reactive mass transfer into/out of each phase Γ_i and the reactive mass transfer of silica into/out o the melt Γ_f^q for melting columns with an upwelling rate of 4 cm yr^{-1}. Peritectic reaction corresponds to $\Gamma_{ol} > 0$. The dashed lines are for closed system batch melting ($K = 0$) and the solid lines are for open system melting. (b) and (d) show the relative contribution of flux melting to the total melting rate for different W_0. For decompression melting this is independent of W_0, but for the fluxed inflow models it increases as W_0 decreases.

in Figure 5.4, we can explicitly separate out these two components. All other things being equal, the excess melting due to flux melting is given by

$$\Delta\Gamma_f = \frac{\Gamma_{f,open} - \Gamma_{f,closed}}{\Gamma_{f,open}} \tag{5.32}$$

We have run open- and closed-system melting models for a range of upwelling velocities and plotted the reaction rates in Figure 5.6. For the adiabatic decompression models flux melting is responsible for increasing the melting rate by 25%. This excess melting is insensitive to changes in upwelling velocity, implying that changes in upwelling velocity will not affect the channelization potential for a region undergoing decompression melting. For the fluxed inflow models, there is an additional component of flux melting due to the inflow of deep melt. In this scenario, as the melt flux in the bottom of the domain is relatively independent of upwelling rate, the relative contribution of flux melting increases as W_0 decreases. In the limit of zero upwelling, when there is no background decompression melting, flux melting accounts for 100% of the melting rate. Where there is a sustained deeper source of melt, we would therefore expect channelization to be promoted for slow background upwelling rates.

Flux melting not only changes the melting rate, but also impacts the net melting reaction. This is demonstrated most clearly for the fluxed inflow model in Figure 5.6 (c) where we have plotted the Γ_i terms. Whereas for closed-system melting the net reaction transitions from eutectic to peritectic around 0.4 GPa, during flux melting, the net melting reaction is peritectic at all depths. This is because the flux of silica-poor deeper melts drives the incongruent melting reaction

$$opx + f_1 \rightarrow ol + f_2 \tag{5.33}$$

This incongruent melting reaction is responsible for the continued depletion of opx in the residue, which over time can result in dunite formation.

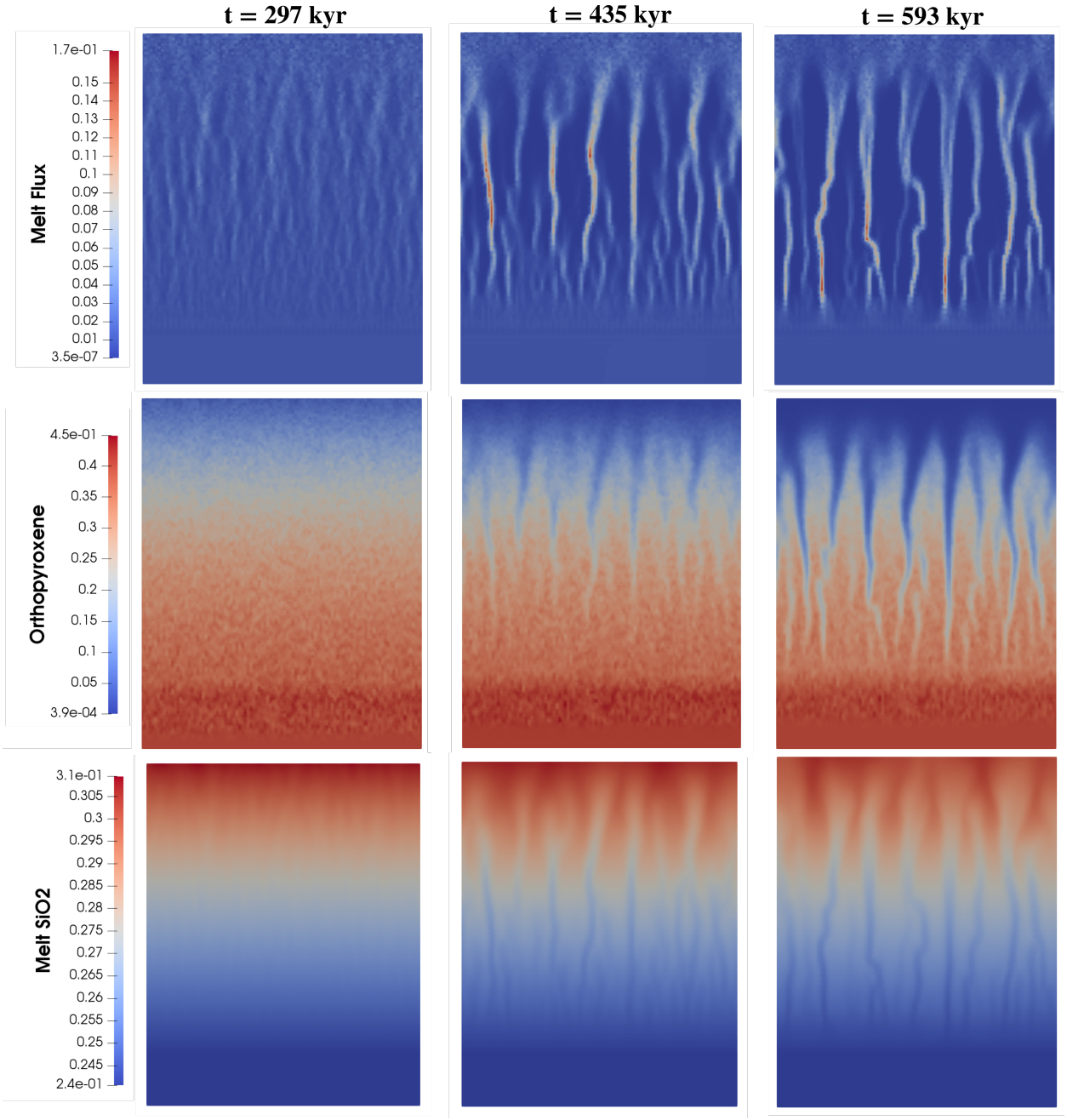

Figure 5.7: Time evolution of static ($W_0 = 0$) fluxed inflow model. The orthopyroxene field is the modal opx in the solid residue. Channels emerge pervasively through the melting region. Melt influx produces a thick dunite layer at the top of the domain.

5.5.2 2-D models

Here we explore the coupling between open-system melting and melt transport in 2-D to determine the condition under which the silica gradient of the binary melt composition drives reactive channelization.

Static fluxed inflow

The analysis of open-system melting rates above implies that channelization is most likely for a static system (i.e. $W_0 = 0$) subject to a flux of melt from below. In the 2-D model simulations we find that this setup is strongly unstable to reactive channelization. The time-series progression of channelization is shown in Figure 5.7. Because the silica gradient is relatively constant with pressure (as shown in Figure 5.1), The instability first emerges throughout the domain as periodic variations in ϕ_f, $\boldsymbol{q}$, and Γ_i. It takes slightly longer for the channels to show up appreciably in the solid assemblage, and thus for the high-flux regions to be preserved as dunite channels. At the beginning of the simulation ($\phi_f,\ \boldsymbol{q},\ \Gamma_i$) are positively correlated with the random fluctuations in ϕ_{opx}. This reflects the dependence of the melting rate on ϕ_{opx} through the reactive surface area terms in the rate law. However, as the channels become established, ($\phi_f,\ \boldsymbol{q},\ \Gamma_i$) become anti-correlated with ϕ_{opx}. This is shown in the horizontal profile in Figure 5.8.

In the absence of background solid advection, the system does not establish a steady state. Rather, the sustained flux of deep silica-poor melt progressively depletes the melting region of opx, eventually producing a thick dunite layer at the top of the domain. Once all of the opx has been exhausted, the incongruent melting reaction driving channelization shuts down, and the melt transport regime transitions to pervasive porous flow.

Decompression melting

Simulations for decompression melting with no melt flux on the lower boundary do not show any melt channelization. The melt is instead transported by pervasive porous flow.

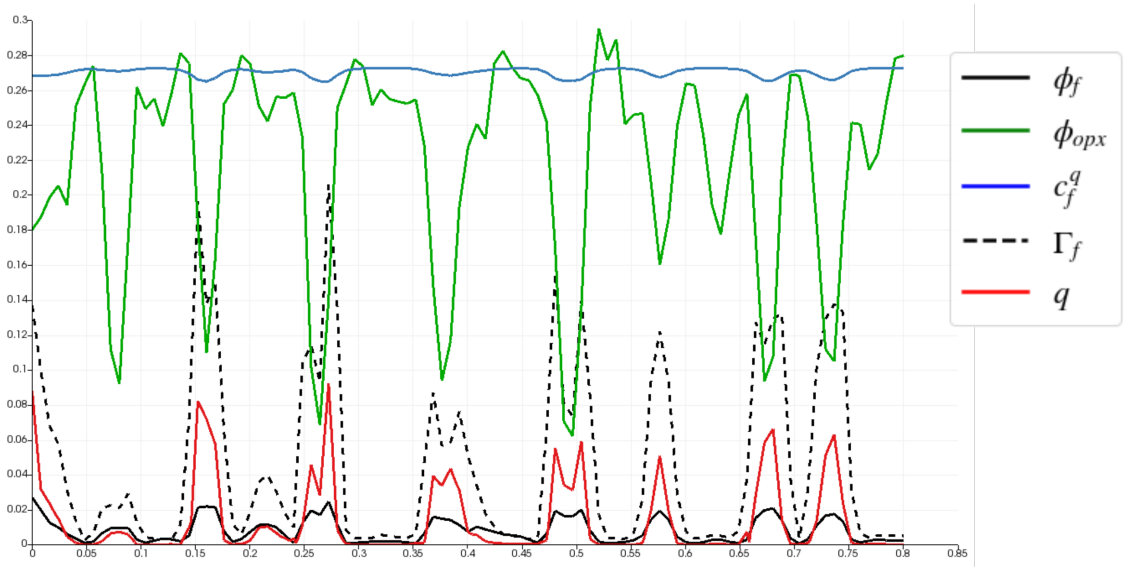

Figure 5.8: Cross section of the 2-D fluxed inflow model at $P = 0.4$ GPa and for $t = 593$ kyr. Plotted are ϕ_{opx}, ϕ_f, c_f^q and nondimensional melt flux magnitude $\boldsymbol{q}$ and melting rate Γ_f.

Figure 5.9 shows the porosity field and a horozontal profile across the melting region at t=310 kyr, for a simulation with an upwelling rate of 4 cm yr^{-1}. Unlike in the channelized model above, there is no wavelength selection and the random variations in (ϕ_f, $\boldsymbol{q}$, Γ_i) are positively correlated with the imposed fluctuations in ϕ_{opx}. The lower contribution of flux melting to the net melting rate in this model means that pervasive porous flow is stabilized by the background adiabatic decompression melting.

Decompression melting with fluxed inflow

Intermediate between the two endmember setups shown above are scenarios where there is both background melting ($W_0 > 0$) and an additional influx of melt across the lower boundary. Running models for a range of W_0 we find that, for the parameter space used here, channels only emerge for low upwelling rates $W_0 < 2$ cm yr^{-1}. Results for a simulation with $W_0 = 1$ cm yr^{-1} are shown in Figure 5.10. The stabilizing effect of background melting means that channels are less pronounced (i.e. have lower ϕ_f, $\boldsymbol{q}$ etc.) than for the static flux melting scenario. From examination of the open-system melting rate systematics shown in

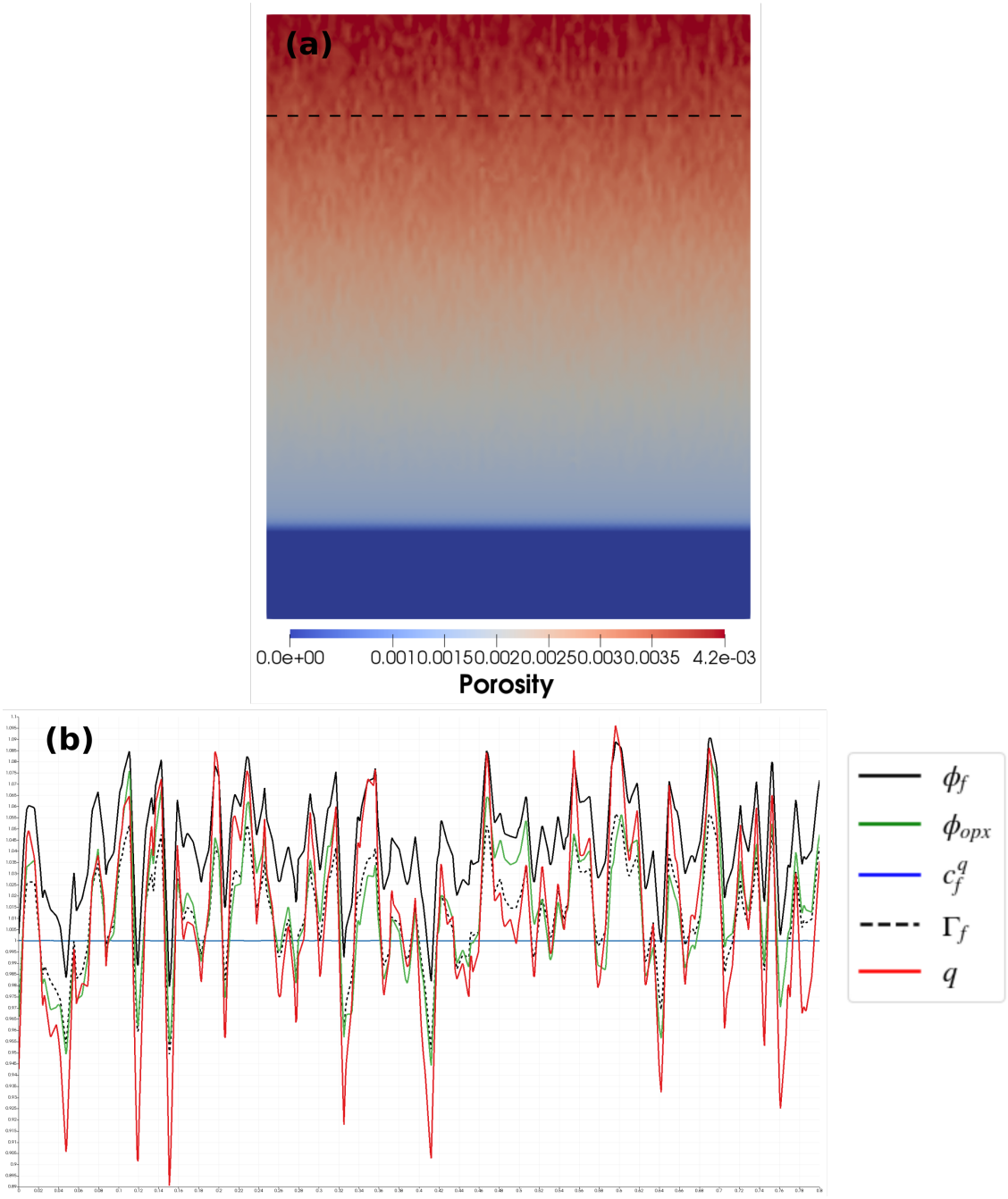

Figure 5.9: (a) Porosity field and (b) cross section of 2-D decompression melting model for $W_0 = 4$ cm yr^{-1}. For the reference parameters no channelization is observed.

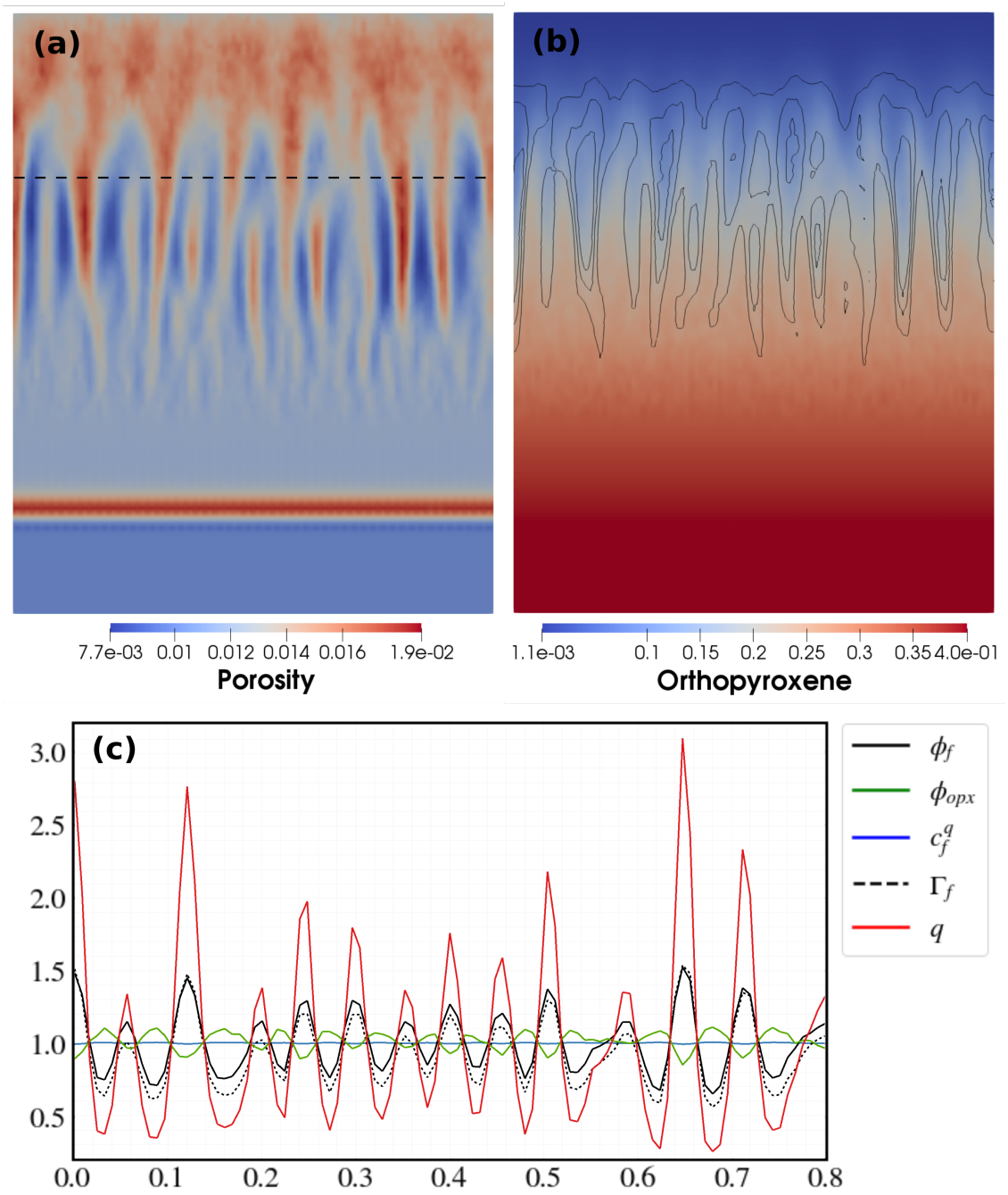

Figure 5.10: (a) Porosity field, (b) modal opx, and (c) cross section with renormalized fields for the fluxed inflow model with $W_0 = 1$ cm yr^{-1}. The position of the cross section is shown by the dashed line in (a).

Figure 5.6, these results imply that channelization only emerges when flux melting accounts for more than 50% of the net melting rate.

5.6 Discussion

5.6.1 Channel geometry and evolution

The channelized model runs show strong wavelength selection during channel growth. Linear analysis of the reactive infiltration instability during melting shows that the minimum wavelength is set by chemical diffusion, while the maximum wavelength is controlled by compaction (Aharonov et al., 1995; Spiegelman et al., 2001; Rees Jones and Katz, 2018). The interaction of compaction pressure with porous channels for the static inflow model is shown in Figure 5.11. Compaction occurs across the whole melting region, but is particularly strong within the high-porosity channels. Decompaction is restricted to regions above pockets of high porosity, or above jogs in the channel paths.

The channels evolve over time, with melt being progressively focused toward channel edges as opx is exhausted in the interior. This appears as a bifurcation in the porosity and melt flux as shown in Figure 5.12. Under the influence of compaction, some channels are also abandoned. As the mineralogy of the solid residue records the time-integrated melt flux, channels that have been abandoned are still preserved as replacive dunites. Likewise, as channels bifurcate, the residual dunite zones expand laterally. This highlights the fact that dunite channels preserved in ophiolite sections do not necessarily represent a porous melt network that was all active at the same time, and even within individual channels melt flux at any one time may be focused within a particular zone. However, the channelization process in natural peridotites is more complex than the simplified setup modeled here, with shear deformation (Holtzman et al., 2003; Spiegelman, 2003; Katz et al., 2006) and hydrofracture and channel decompaction (Connolly and Podladchikov, 1998) potentially playing a role. As such the interpretation of the channel geometries can only go so far.

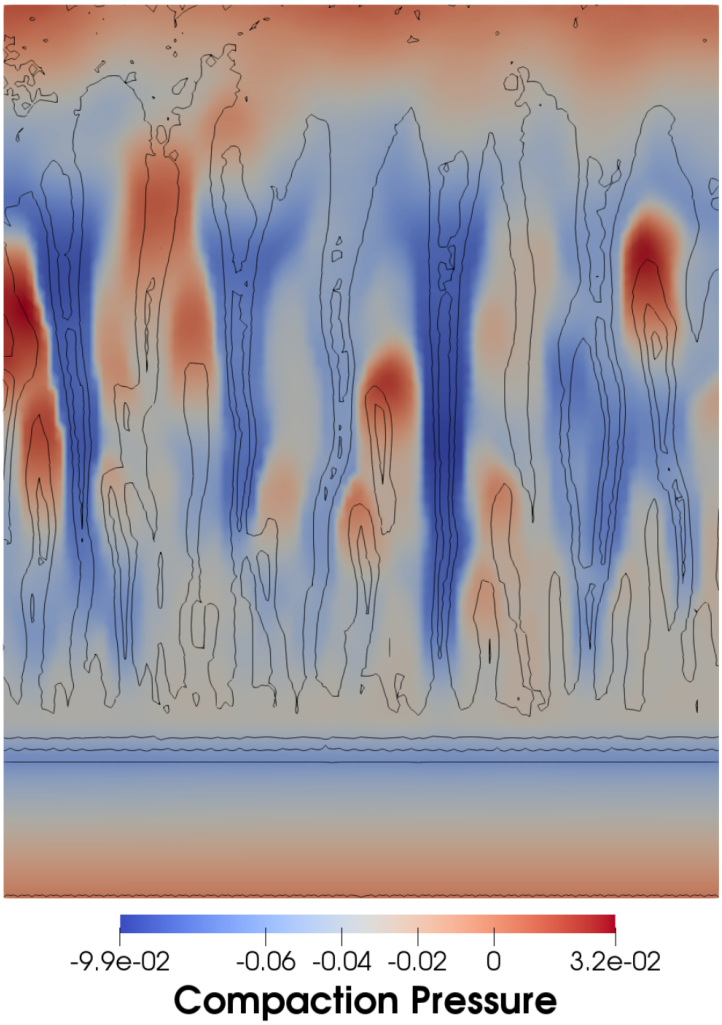

Figure 5.11: Dimensionless compaction pressure $\mathcal{P}$ field for the static fluxed inflow model at $t = 512$ kyr. blue and beige colors show compacting regions and dark red colors show decompacting regions. Porosity contours are plotted over the top.

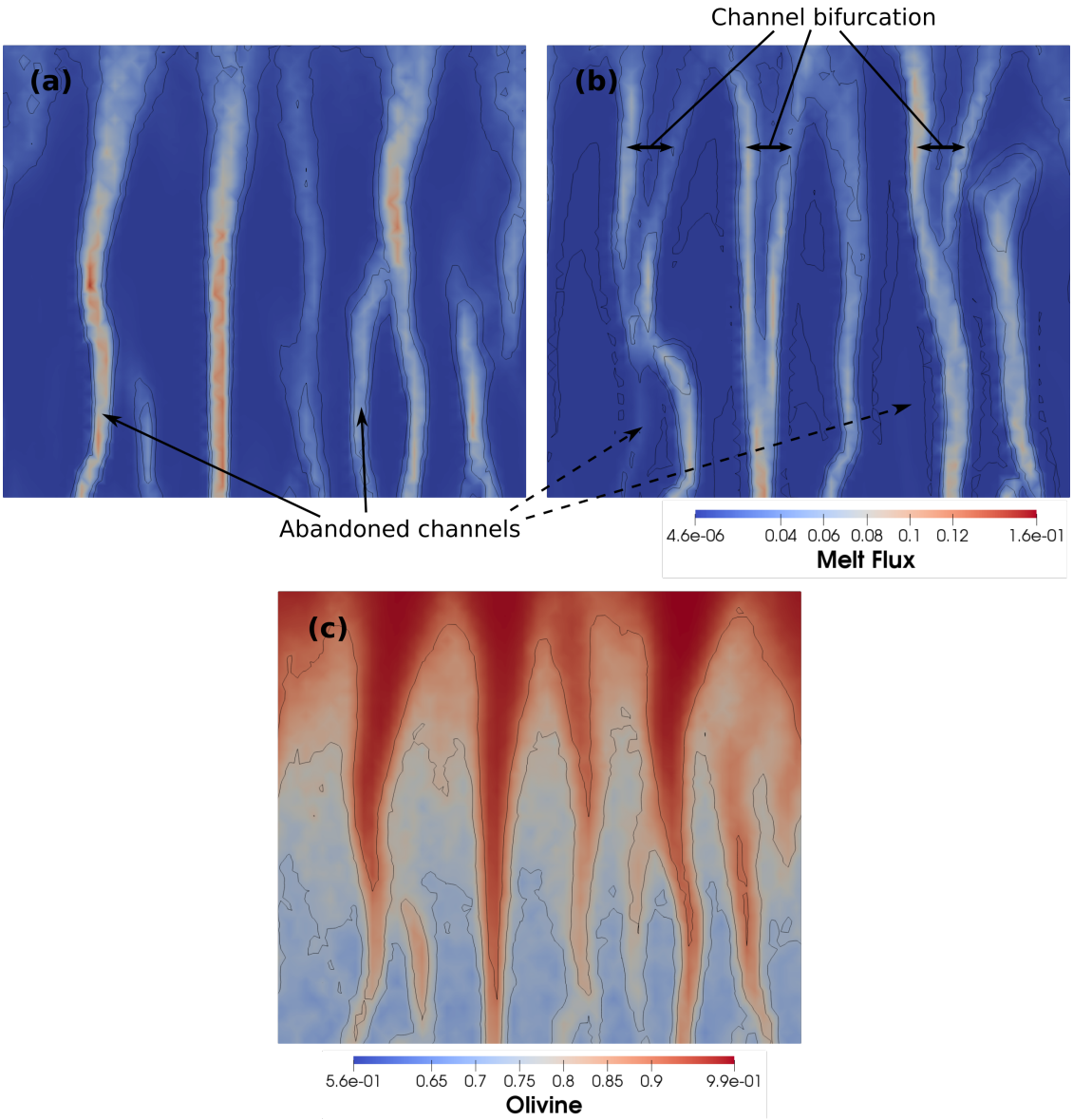

Figure 5.12: Snapshots of melt flux at (a) 512 kyr and (b) 638 kyr for the 2-D static fluxed infow model showing evolution in channel morphology over time. (c) Modal proportion of olivine in the solid residue at 638 kyr preserves a time-integrated record of melt transport.

5.6.2 Melt inflow as a driver of channelization

The results here demonstrate that in the absence of other solubility gradients, channelization of melt due to the reactive dissolution of opx during adiabatic decompression melting only occurs when there is an additional flux of deep silica-poor melt. The stabilizing impact of background decompression melting has been observed in previous model studies (Hewitt, 2010; Katz, 2008). We can consider three potential sources of deep melt flux. The first is from melting of fusible pyroxenitic heterogeneities. The role of mantle heterogeneity in seeding channels was examined for a simplified reactive model by Weatherley and Katz (2012) and Katz and Weatherley (2012). The second is from deep volatile-rich melting. However, as any volatile-rich melts produced at depth in the mantle are very low-degree, the role of volatile melting is more likely related to the chemical corrosivity of these melts. A perhaps more voluminous source of basal melt flux could be related to the focusing of melt towards the ridge axis. Recent models have demonstrated strong melt focusing at depth beneath the ridge axis through the combined effects of melt pressure focusing and ridge suction (Turner et al., 2017; Sim et al., 2020). Beneath the ridge axis, this focusing provides an additional flux of deep melt in excess of that for purely vertical flow. The role of melt focusing in reactive channelization has yet to be examined.

Here we have modeled the impact of the gradient in equilibrium melt silica concentration in the binary system. The silica gradient is responsible for dunite formation in regions of high flux relative to the solid upwelling rate, via the incongruent open-system melting reaction: opx + f_1 $\rightarrow$ ol + f_2. As demonstrated with the thick layers of replacive dunite at the top of the domain of the fluxed inflow models, dunites are expected to form wherever there is a sustained flux of deep melt. Here, we have shown that the gradient in silica content could also initiate an instability driving melt channelization. However, this does not mean that channelization in natural systems arises from the gradient in silica content alone. While silica is the main chemical component in the mantle, the presence of other chemical gradients in natural systems is expected to further contribute to flux melting and reactive channelization.

The conditions for channelization in the binary system should therefore be viewed as the most conservative scenario. Fluxing of highly incompatible components, including H_2O, CO_2, K_2O, and Na_2O in deep low fraction melts, could have a particularly strong channeling effect. This is in part due to the impact of these components on the equilibrium melt silica content (Kushiro, 1975; Ryerson, 1985), as discussed in chapter 3. The role of volatiles was considered for a simple system by Keller and Katz (2016) and Keller et al. (2017), who demonstrated the strong channelization potential during adiabatic decompression melting at the anhydrous solidus due to fluxing of H_2O and CO_2 rich melts.

5.6.3 Model limitations

The models presented here represent the first examples of eutectic and peritectic melting being included in two-phase magma dynamics. As discussed, they provide a framework for understanding the conditions under which reactive channels emerge, while directly accounting for the solid phase assemblage. We have also demonstrated the full self-consistent coupling between thermodynamics and melt transport dynamics. As discussed above, the role of other melt components in driving channelization is yet to be explored. We also have not explored the role of other mantle phases. These impact both the melting reaction, and the melt productivity. Clinopyroxene (cpx) in particular is a major contributor to deep partial melting. The greater solubility of cpx relative to opx was shown to promote reactive channelization in the experiments of Pec et al. (2020).

The role of shear deformation and the resulting mechanical feedbacks (Stevenson, 1989; Holtzman et al., 2003; Spiegelman and Kelemen, 2003; Katz et al., 2006; Butler, 2009, 2012) are beyond the scope of this study. The interaction between reactive channeling and shear-driven instabilities was subject to a recent analysis by Rees Jones et al. (2021). Field evidence in some ophiolites show that shear could play a role in melt focusing under some dynamical regimes (Kelemen and Dick, 1995). The simple viscous rheology used here also does not allow for failure of the solid residue. On the basis of field evidence and simple scaling analysis,

fracture-driven melt transport in the mantle cannot be ruled out Kelemen et al. (1997). Hydrofracture at the core of high-flux dunites would provide a channelization mechanism independent of the reactive focusing mechanism explored here.

Finally, the models presented here have relatively coarse spatial resolution of 100-300 m, limiting the lengthscales of features that can be modeled. This contrasts with field exposures in ophiolites, where dunite channels are observed down to the scale of a few cm. Furthermore, the requirement to have a smooth solution at the model resolution used means that we have been restricted to running models at lower Da and Pe_C than would be expected in natural systems. The high diffusivity suppresses high frequency channels.

5.6.4 Future work

Further analysis of these initial model simulations is required. In particular I aim to compare these numerical results with the linear stability analysis of Rees Jones and Katz (2018). I also aim to explore how variations in the model parameters affect the melt transport regime. A particular target is to run a series of high resolution simulations with higher Da and Pe_C.

The models here pave the way for integrating more complex chemistry in the future, in order to more closely approximate melting systematics of natural peridotites. One way of approaching this would be to use a reduced thermodynamic subsystem, as done here, but adding additional components. The Mg_2SiO_4–SiO_2–H_2O or Mg_2SiO_4–SiO_2–$CaMgSi_2O_6$ ternary systems would be suitable candidates. Alternatively, parameterized phase relations could be used, such as those implemented by previous authors (e.g. Keller and Katz, 2016), but with the inclusion of eutectic and peritectic melting reactions.

5.7 Conclusions

This work is the first demonstration of reactive channelization via incongruent flux melting. This is a significant extension over previous theories and opens up the potential to directly relate reactive melt transport to the mineralogical evolution of the solid residue. We have found that in the Mg_2SiO_4–SiO_2 binary system the gradient in melt silica content is able to drive channelization, but only when there is an additional flux of deep silica-poor melt. During natural peridotite melting, however, fluxing by other components including volatiles and alkali elements, may further promote channelization. We have further demonstrated the full coupling between a self-consistent thermodynamic model and melt transport dynamics.

Bibliography

Aagaard, P. and Helgeson, H. C. Thermodynamic and kinetic constraints on reaction rates among minerals and aqueous solutions. I. Theoretical considerations. *American Journal of Science*, 282(3):237–285, mar 1982. doi: 10.2475/ajs.282.3.237.

Accardo, N. J., Gaherty, J. B., Shillington, D. J., Hopper, E., Nyblade, A. A., Ebinger, C. J., Scholz, C. A., Chindandali, P. R. N., Wambura-Ferdinand, R., Mbogoni, G., Russell, J. B., Holtzman, B. K., Havlin, C., and Class, C. Thermochemical Modification of the Upper Mantle Beneath the Northern Malawi Rift Constrained From Shear Velocity Imaging. *Geochemistry, Geophysics, Geosystems*, 21(6):e2019GC008843, jun 2020. doi: 10.1029/2019GC008843.

Afonso, J. C., Zlotnik, S., and Fernàndez, M. Effects of compositional and rheological stratifications on small-scale convection under the oceans: Implications for the thickness of oceanic lithosphere and seafloor flattening. *Geophysical Research Letters*, 35(20):L20308, oct 2008. doi: 10.1029/2008GL035419.

Aharonov, E., Whitehead, J. A., Kelemen, P. B., and Spiegelman, M. Channeling instability of upwelling melt in the mantle. *Journal of Geophysical Research: Solid Earth*, 100(B10):20433–20450, oct 1995. doi: 10.1029/95JB01307.

Aharonov, E., Spiegelman, M., and Kelemen, P. Three-dimensional flow and reaction in porous media: Implications for the Earth's mantle and sedimentary basins. *Journal of Geophysical Research: Solid Earth*, 102(B7):14821–14833, jul 1997. doi: 10.1029/97JB00996.

Allègre, C. J., Provost, A., and Jaupart, C. Oscillatory zoning: A pathological case of crystal growth. *Nature*, 294(5838):223–228, 1981. doi: 10.1038/294223a0.

Alnæs, M. S., Blechta, J., Hake, J., Johansson, A., Kehlet, B., Logg, A., Richardson, C., Ring, J., Rognes, E., and Wells, G. N. The FEniCS project version 1.5. *Archive of Numerical Software*, 3(100):9–23, 2015.

Annen, C. and Sparks, R. Effects of repetitive emplacement of basaltic intrusions on thermal evolution and melt generation in the crust. *Earth and Planetary Science Letters*, 203(3):937–955, 2002. doi: 10.1016/S0012-821X(02)00929-9.

Annen, C., Blundy, J. D., and Sparks, R. S. J. The Genesis of Intermediate and Silicic Magmas in Deep Crustal Hot Zones. *Journal of Petrology*, 47(3):505–539, dec 2005. doi: 10.1093/petrology/egi084.

Arzilli, F., La Spina, G., Burton, M. R., Polacci, M., Le Gall, N., Hartley, M. E., Di Genova, D., Cai, B., Vo, N. T., Bamber, E. C., Nonni, S., Atwood, R., Llewellin, E. W., Brooker, R. A., Mader, H. M., and Lee, P. D. Magma fragmentation in highly explosive basaltic eruptions induced by rapid crystallization. *Nature Geoscience*, 12(12):1023–1028, dec 2019. doi: 10.1038/s41561-019-0468-6.

Asimow, P., Hirschmann, M., Ghiorso, M., O'Hara, M., and Stolper, E. The effect of pressure-induced solid-solid phase transitions on decompression melting of the mantle. *Geochimica et Cosmochimica Acta*, 59(21):4489–4506, 1995.

Asimow, P. D. Steady-state Mantle-Melt Interactions in One Dimension: II. Thermal Interactions and Irreversible Terms. *Journal of Petrology*, 43(9):1707–1724, sep 2002. doi: 10.1093/petrology/43.9.1707.

Asimow, P. D. and Ghiorso, M. S. Algorithmic modifications extending MELTS to calculate subsolidus phase relations. *American Mineralogist*, 83(9-10):1127–1132, 1998.

Asimow, P. D. and Stolper, E. M. Steady-state Mantle-Melt Interactions in One Dimension: I. Equilibrium Transport and Melt Focusing. *Journal of Petrology*, 40(3):475–494, mar 1999. doi: 10.1093/petroj/40.3.475.

Babeykoa, A. and Sobolev, S. High-resolution numerical modeling of stress distribution in visco-elasto-plastic subducting slabs. *Lithos*, 103(1-2):205–216, jun 2008. doi: 10.1016/J.LITHOS.2007.09.015.

Bachmann, O. and Huber, C. Silicic magma reservoirs in the Earth's crust. *American Mineralogist*, 101(11):2377–2404, nov 2016. doi: 10.2138/am-2016-5675.

Balay, S., Brown, J., Buschelman, K., Gropp, W., Kaushik, D., Knepley, M., McInnes, L., Smith, B., and Zhang, H. PETSc web page http://www.mcs.anl. gov/petsc, 2012.

Bercovici, D. and Ricard, Y. Energetics of a two-phase model of lithospheric damage, shear localization and plate-boundary formation. *Geophysical Journal International*, 152(3):581–596, mar 2003. doi: 10.1046/j.1365-246X.2003.01854.x.

Bercovici, D., Ricard, Y., and Schubert, G. A two-phase model for compaction and damage: 1. General Theory. *Journal of Geophysical Research: Solid Earth*, 106(B5):8887–8906, may 2001. doi: 10.1029/2000JB900430.

Berman, R. G. Internally-Consistent Thermodynamic Data for Minerals in the System Na2O-K2O-CaO-MgO-FeO-Fe2O3-Al2O3-SiO2-TiO2-H2O-CO2. *Journal of Petrology*, 29(2):445–522, apr 1988. doi: 10.1093/petrology/29.2.445.

Berman, R. G. and Brown, T. H. A thermodynamic model for multicomponent melts, with application to the system CaO-Al2O3-SiO2. *Geochimica et Cosmochimica Acta*, 48(4):661–678, apr 1984. doi: 10.1016/0016-7037(84)90094-2.

Biot, M. A. General theory of three-dimensional consolidation. *Journal of Applied Physics*, 12(2):155–164, 1941. doi: 10.1063/1.1712886.

Boudier, F. and Coleman, R. G. Cross section through the peridotite in the Samail ophiolite, southeastern Oman Mountains. *Journal of Geophysical Research*, 86(B4):2573–2592, apr 1981. doi: 10.1029/JB086iB04p02573.

Boudier, F. and Nicolas, A. Nature of the Moho Transition Zone in the Oman Ophiolite. *Journal of Petrology*, 36(3):777–796, jun 1995. doi: 10.1093/petrology/36.3.777.

Bowen, N. L. and Anderson, O. The Binary MgO-SiO2. *American Journal of Science*, 37 (222), 1914.

Boyd, F. R., England, J. L., and Davis, B. T. C. Effects of pressure on the melting and polymorphism of enstatite, MgSiO 3. *Journal of Geophysical Research*, 69(10):2101–2109, may 1964. doi: 10.1029/JZ069i010p02101.

Brearley, M. and Scarfe, C. M. Dissolution Rates of Upper Mantle Minerals in an Alkali Basalt Melt at High Pressure: An Experimental Study and Implications for Ultramafic Xenolith Survival. *Journal of Petrology*, 27(5):1157–1182, oct 1986. doi: 10.1093/petrology/27.5.1157.

Burke, K., Steinberger, B., Torsvik, T. H., and Smethurst, M. A. Plume Generation Zones at the margins of Large Low Shear Velocity Provinces on the core-mantle boundary. *Earth and Planetary Science Letters*, 265(1-2):49–60, jan 2008. doi: 10.1016/j.epsl.2007.09.042.

Butler, S. L. The effects of buoyancy on shear-induced melt bands in a compacting porous medium. *Physics of the Earth and Planetary Interiors*, 173(1-2):51–59, mar 2009. doi: 10.1016/J.PEPI.2008.10.022.

Butler, S. L. Numerical models of shear-induced melt band formation with anisotropic matrix viscosity. *Physics of the Earth and Planetary Interiors*, 200-201:28–36, jun 2012. doi: 10.1016/J.PEPI.2012.03.011.

Carlson, W. D., Pattison, D. R., and Caddick, M. J. Beyond the equilibrium paradigm: How consideration of kinetics enhances metamorphic interpretation. *American Mineralogist*, 100(8-9):1659–1667, aug 2015. doi: 10.2138/am-2015-5097.

Cashman, V., Sparks, R. S. J., and Blundy, J. D. Vertically extensive and unstable magmatic systems: A unified viewof igneous processes. *Science*, 355(6331):eaag3055, 2017. doi: 10.1126/science.aag3055.

Chadam, J., Hoff, D., Merino, E., Ortleva, P., and Sen, A. Reactive Infiltration Instabilities. *IMA Journal of Applied Mathematics*, 36(3):207–221, 1986. doi: 10.1093/imamat/36.3.207.

Chen, C. and Presnall, D. The system Mg2SiO4-SiO2 at pressure up to 25 kilobars. *American Mineralogist*, (160):398–406, 1975.

Chen, L. and Gerya, T. V. The role of lateral lithospheric strength heterogeneities in orogenic plateau growth: Insights from 3-D thermo-mechanical modeling. *Journal of Geophysical Research: Solid Earth*, 121(4):3118–3138, apr 2016. doi: 10.1002/2016JB012872.

Connolly, J. Computation of phase equilibria by linear programming: A tool for geodynamic modeling and its application to subduction zone decarbonation. 2005.

Connolly, J. A. D. and Podladchikov, Y. Y. Compaction-driven fluid flow in viscoelastic rock. *Geodinamica Acta*, 11(2-3):55–84, mar 1998. doi: 10.1080/09853111.1998.11105311.

Cooper, K. M. and Kent, A. J. Rapid remobilization of magmatic crystals kept in cold storage. *Nature*, 506(7489):480–483, feb 2014. doi: 10.1038/nature12991.

Dasgupta, R. and Hirschmann, M. M. The deep carbon cycle and melting in Earth's interior. *Earth and Planetary Science Letters*, 298(1-2):1–13, sep 2010. doi: 10.1016/j.epsl.2010.06.039.

Davidson, J., Morgan, D., Charlier, B., Harlou, R., and Hora, J. Microsampling and Isotopic Analysis of Igneous Rocks: Implications for the Study of Magmatic Systems. *Annual Review of Earth and Planetary Sciences*, 35(1):273–311, may 2007. doi: 10.1146/annurev.earth.35.031306.140211.

Davies, G. F. and Richards, M. A. Mantle convection. *Journal of Geology*, 100(2):151–206, sep 1992. doi: 10.1086/629582.

Davies, J. H. The role of hydraulic fractures and intermediate-depth earthquakes in generating subduction-zone magmatism. *Nature*, 398(6723):142–145, mar 1999. doi: doi:10.1038/18202.

De Capitani, C. and Petrakakis, K. The computation of equilibrium assemblage diagrams with Theriak/Domino software. *American Mineralogist*, 95(7):1006–1016, jul 2010. doi: 10.2138/am.2010.3354.

de Groot, S. and Mazur, P. *Non-equilibrium Themodynamics*. Dover, Mineola, NY, 1984. ISBN 978-0486647418.

Dick, H. J. Abyssal peridotites, very slow spreading ridges and ocean ridge magmatism. *Geological Society Special Publication*, 42(42):71–105, jan 1989. doi: 10.1144/GSL.SP.1989.042.01.06.

Dijkstra, A. H., Barth, M. G., Drury, M. R., Mason, P. R., and Vissers, R. L. Diffuse porous melt flow and melt-rock reaction in the mantle lithosphere at a slow-spreading ridge: A structural petrology and LA-ICP-MS study of the Othris Peridotite Massif (Greece). *Geochemistry, Geophysics, Geosystems*, 4(8), aug 2003. doi: 10.1029/2001GC000278.

Dohmen, R. and Chakraborty, S. Mechanism and kinetics of element and isotopic exchange mediated by a fluid phase. *American Mineralogist*, 88(8-9):1251–1270, aug 2004. doi: 10.2138/am-2003-8-908.

Dohmen, R. and Milke, R. Diffusion in Polycrystalline Materials: Grain Boundaries, Mathematical Models, and Experimental Data. *Reviews in Mineralogy and Geochemistry*, 72 (1):921–970, jan 2010. doi: 10.2138/rmg.2010.72.21.

Drew, D. A. Averaged Field Equations for Two-Phase Media. *Studies in Applied Mathematics*, 50(2):133–166, jun 1971. doi: 10.1002/sapm1971502133.

Dufek, J. and Bachmann, O. Quantum magmatism: Magmatic compositional gaps generated by melt-crystal dynamics. *Geology*, 38(8):687–690, jul 2010. doi: 10.1130/G30831.1.

Edwards, B. and Russell, J. A review and analysis of silicate mineral dissolution experiments in natural silicate melts. *Chemical Geology*, 130(3):233–245, 1996. doi: 10.1016/0009-2541(96)00025-3.

Elthon, D. Chemical trends in abyssal peridotites: refertilization of depleted suboceanic mantle. *Journal of Geophysical Research*, 97(B6):9015–9025, jun 1992. doi: 10.1029/92JB00723.

Elthon, D. and Scarfe, C. M. High-pressure phase equilibria of a high-magnesia basalt and the genesis of primary oceanic basalts. *American Mineralogist*, 69(1-2):1–15, 1984.

England, P. C. and Katz, R. F. Melting above the anhydrous solidus controls the location of volcanic arcs. *Nature*, 467(7316):700–3, oct 2010. doi: 10.1038/nature09417.

Evans, O., Spiegelman, M., and Kelemen, P. B. A Poroelastic Model of Serpentinization: Exploring the Interplay Between Rheology, Surface Energy, Reaction, and Fluid Flow. *Journal of Geophysical Research: Solid Earth*, 123(10):8653–8675, oct 2018. doi: 10.1029/2017JB015214.

Evans, O., Spiegelman, M., and Kelemen, P. B. Phase-Field Modeling of Reaction-Driven Cracking: Determining Conditions for Extensive Olivine Serpentinization. *Journal of Geophysical Research: Solid Earth*, 125(1), jan 2020. doi: 10.1029/2019JB018614.

Ferguson, D. J., Maclennan, J., Bastow, I. D., Pyle, D. M., Jones, S. M., Keir, D., Blundy, J. D., Plank, T., and Yirgu, G. Melting during late-stage rifting in Afar is hot and deep. *Nature*, 499(7456):70–3, jul 2013. doi: 10.1038/nature12292.

Ferry, J. M. and Gerdes, M. L. Chemically reactive fluid flow during metamorphism. *Annual Review of Earth and Planetary Sciences*, 26.1:255–287, 1998.

Fisher, G. W. Nonequilibrium thermodynamics as a model for diffusion-controlled metamorphic processes, 1973.

Forsyth, D. and Uyeda, S. On the Relative Importance of the Driving Forces of Plate Motion. *Geophysical Journal of the Royal Astronomical Society*, 43(1):163–200, oct 1975. doi: 10.1111/j.1365-246X.1975.tb00631.x.

Fowler, A. C. A mathematical model of magma transport in the asthenosphere. *Geophysical & Astrophysical Fluid Dynamics*, 33(1-4):63–96, sep 1985. doi: 10.1080/03091928508245423.

Ganne, J., Bachmann, O., and Feng, X. Deep into magma plumbing systems: Interrogating the crystal cargo of volcanic deposits. *Geology*, 46(5):415–418, may 2018. doi: 10.1130/G39857.1.

Gerya, T. V. and Meilick, F. I. Geodynamic regimes of subduction under an active margin: Effects of rheological weakening by fluids and melts. *Journal of Metamorphic Geology*, 29 (1):7–31, jan 2011. doi: 10.1111/j.1525-1314.2010.00904.x.

Ghiorso, M. Chemical mass transfer in magmatic processes I. Thermodynamic relations and numerical algorithms. *Contributions to Mineralogy and Petrology*, 90:107–120, 1985.

Ghiorso, M. S. A globally convergent saturation state algorithm applicable to thermodynamic systems with a stable or metastable omni-component phase. *Geochimica et Cosmochimica Acta*, 103:295–300, feb 2013. doi: 10.1016/J.GCA.2012.11.013.

Ghiorso, M. S. and Sack, R. O. Chemical mass transfer in magmatic systems: IV. A revised and internally consistent thermodynamic model for the interpolation and extrapolation of liquid-solid equilibria in magmatic systems at elevated temperatures and pressures. *Contributions to Mineralogy and Petrology*, 119:197–212, 1995.

Ghiorso, M. S., Hirschmann, M. M., and Grove, T. L. xMELTS: A thermodynamic model for the estimation of magmatic phase relations over the pressure range 0-30 GPa and at temperatures up to 2500 C, 2007.

Goes, S., Agrusta, R., van Hunen, J., and Garel, F. Subduction-transition zone interaction: A review. Geosphere. *Geosphere*, 13(3):644–664, 2017.

Green, E. C. R., Holland, T. J. B., and Powell, R. A thermodynamic model for silicate melt in CaO-MgO-Al2O3-SiO2 to 50 kbar and 1800 °C. *Journal of Metamorphic Geology*, 30 (6):579–597, aug 2012. doi: 10.1111/j.1525-1314.2012.00982.x.

Green, H. W. and Houston, H. The mechanics of deep earthquakes. *Annu. Rev. Earth Planet. Sci*, 23:169–213, 1995.

Grove, T., Chatterjee, N., Parman, S., and Medard, E. The influence of H2O on mantle wedge melting. *Earth and Planetary Science Letters*, 249(1-2):74–89, sep 2006. doi: 10.1016/j.epsl.2006.06.043.

Hageman, V. B. M. and Oonk, H. A. J. Liquid immiscibility in the SiO2+ MgO, SiO2+ SnO, SiO2+ La2O3, and SiO2+ Y2O3 systems. *Physics and chemistry of glasses*, 27(5): 194–198, 1986.

Hager, B. H. and O'Connell, R. J. A simple global model of plate dynamics and mantle convection. *Journal of Geophysical Research*, 86(B6):4843–4867, jun 1981. doi: 10.1029/JB086iB06p04843.

Ham, D. A., Farrell, P. E., Gorman, G. J., Maddison, J. R., Wilson, C. R., Kramer, S. C., Shipton, J., Collins, G. S., Cotter, C. J., and Piggott, M. D. Spud 1.0: Generalising and automating the user interfaces of scientific computer models. *Geoscientific Model Development*, 2(1):33–42, mar 2009. doi: 10.5194/gmd-2-33-2009.

Hart, S. R. Equilibration during mantle melting: a fractal tree model. *Proceedings of the National Academy of Sciences of the United States of America*, 90(24):11914–8, 1993. doi: 10.1073/pnas.90.24.11914.

Harvey, J.-P., Gheribi, A. E., and Asimow, P. D. A self-consistent optimization of multicomponent solution properties: Ab initio molecular dynamic simulations and the MgO–SiO2 miscibility gap under pressure. *Geochimica et Cosmochimica Acta*, 161:146–165, 2015. doi: 10.1016/j.gca.2015.04.004.

Havlin, C., Parmentier, E., and Hirth, G. Dike propagation driven by melt accumulation at the lithosphere–asthenosphere boundary. 2013.

Hebert, L. B., Antoshechkina, P., Asimow, P., and Gurnis, M. Emergence of a low-viscosity channel in subduction zones through the coupling of mantle flow and thermodynamics. *Earth and Planetary Science Letters*, 278(3-4):243–256, feb 2009. doi: 10.1016/J.EPSL.2008.12.013.

Helgeson, H. *A chemical and thermodynamic model of ore deposition in hydrothermal systems*. 1970.

Helgeson, H. C. Evaluation of irreversible reactions in geochemical processes involving minerals and aqueous solutions—I. Thermodynamic relations. *Geochimica et Cosmochimica Acta*, 32(8):853–877, aug 1968. doi: 10.1016/0016-7037(68)90100-2.

Helgeson, H. C., Garrels, R. M., and MacKenzie, F. T. Evaluation of irreversible reactions in geochemical processes involving minerals and aqueous solutions—II. Applications. *Geochimica et Cosmochimica Acta*, 33(4):455–481, apr 1969. doi: 10.1016/0016-7037(69)90127-6.

Herzberg, C. and Zhang, J. Melting experiments in the systems CaO-MgO-Al ₂ O ₃ -SiO ₂ and MgO-SiO ₂ at 3 to 15 GPa. *American Mineralogist*, 83(5-6):491–500, jun 1998. doi: 10.2138/am-1998-5-609.

Hewitt, I. and Fowler, A. Partial melting in an upwelling mantle column. *Proceedings of the Royal Society of London A: Mathematical, Physical and Engineering Sciences*, 464(2097), 2008.

Hewitt, I. J. Modelling melting rates in upwelling mantle. *Earth and Planetary Science Letters*, 300(3-4):264–274, dec 2010. doi: 10.1016/j.epsl.2010.10.010.

Hildreth, W. and Moorbath, S. Crustal contributions to arc magmatism in the Andes of Central Chile. *Contributions to Mineralogy and Petrology*, 98(4):455–489, apr 1988. doi: 10.1007/BF00372365.

Hirose, K., Morard, G., Sinmyo, R., Umemoto, K., Hernlund, J., Helffrich, G., and Labrosse, S. Crystallization of silicon dioxide and compositional evolution of the Earth's core. *Nature*, 543(7643):99–102, mar 2017. doi: 10.1038/nature21367.

Hirschmann, M., Baker, M., and Stolper, E. The Effect of Alkalis on the Silica Content of Mantle-Derived Melts. *Geochimica et Cosmochimica Acta*, 62(5):883–902, mar 1998. doi: 10.1016/S0016-7037(98)00028-3.

Hirschmann, M. M. Water, melting, and the deep Earth H2O cycle. *Annual Review of Earth and Planetary Sciences*, 34:629–653, apr 2006. doi: 10.1146/annurev.earth.34.031405.125211.

Hirschmann, M. M., Asimow, P. D., Ghiorso, M. S., and Stolper, E. M. Calculation of Peridotite Partial Melting from Thermodynamic Models of Minerals and Melts. III. Controls on Isobaric Melt Production and the Effect of Water on Melt Production. *Journal of Petrology*, 40(5):831–851, may 1999. doi: 10.1093/petroj/40.5.831.

Hirth, G. and Kohlstedt, D. L. Experimental constraints on the dynamics of the partially molten upper mantle: Deformation in the diffusion creep regime. *Journal of Geophysical Research*, 100(B2):1981, 1995a. doi: 10.1029/94JB02128.

Hirth, G. and Kohlstedt, D. L. Experimental constraints on the dynamics of the partially molten upper mantle: 2. Deformation in the dislocation creep regime. *Journal of Geophysical Research*, 100(B8):15441, 1995b. doi: 10.1029/95JB01292.

Hofmann, A. W. and Hart, S. R. An assessment of local and regional isotopic equilibrium in the mantle. *Earth and Planetary Science Letters*, 38(1):44–62, feb 1978. doi: 10.1016/0012-821X(78)90125-5.

Hogrefe, A., Rubie, D. C., Sharp, T. G., and Seifert, F. Metastability of enstatite in deep subducting lithosphere. *Nature*, 372(6504):351–353, 1994. doi: 10.1038/372351a0.

Holland, T. and Powell, R. Activity-composition relations for phases in petrological calculations: an asymmetric multicomponent formulation. *Contributions to Mineralogy and Petrology*, 145(4):492–501, jul 2003. doi: 10.1007/s00410-003-0464-z.

Holland, T. J. B. and Powell, R. An internally consistent thermodynamic data set for phases of petrological interest. *Journal of Metamorphic Geology*, 16(3):309–343, oct 1998.

Holland, T. J. B. and Powell, R. An improved and extended internally consistent thermodynamic dataset for phases of petrological interest, involving a new equation of state for solids. *Journal of Metamorphic Geology*, 29(3):333–383, apr 2011. doi: 10.1111/j.1525-1314.2010.00923.x.

Holness, M. B. Melt–Solid Dihedral Angles of Common Minerals in Natural Rocks. *Journal of Petrology*, 47(4):791–800, apr 2006. doi: 10.1093/petrology/egi094.

Holtzman, B. K., Groebner, N. J., Zimmerman, M. E., Ginsberg, S. B., and Kohlstedt, D. L. Stress-driven melt segregation in partially molten rocks. *Geochemistry, Geophysics, Geosystems*, 4(5):n/a–n/a, may 2003. doi: 10.1029/2001GC000258.

Hopper, E., Gaherty, J. B., Shillington, D. J., Accardo, N. J., Nyblade, A. A., Holtzman, B. K., Havlin, C., Scholz, C. A., Chindandali, P. R. N., Ferdinand, R. W., Mulibo, G. D., and Mbogoni, G. Preferential localized thinning of lithospheric mantle in the melt-poor Malawi Rift. *Nature Geoscience 2020 13:8*, 13(8):584–589, jul 2020. doi: 10.1038/S41561-020-0609-Y.

Hudon, P., Jung, I.-H., and Baker, D. R. Melting of β-quartz up to 2.0 GPa and thermodynamic optimization of the silica liquidus up to 6.0 GPa. *Physics of the Earth and Planetary Interiors*, 130(3-4):159–174, apr 2002. doi: 10.1016/S0031-9201(02)00005-5.

Hudon, P., Jung, I.-H., and Baker, D. R. Experimental Investigation and Optimization of Thermodynamic Properties and Phase Diagrams in the Systems CaO-SiO2, MgO-SiO2, CaMgSi2O6-SiO2 and CaMgSi2O6-Mg2SiO4 to 1{middle dot}0 GPa. *Journal of Petrology*, 46(9):1859–1880, apr 2005. doi: 10.1093/petrology/egi037.

Iidaka, T. and Suetsugu, D. Seismological evidence for metastable olivine inside a subducting slab. *Nature*, 356(6370):593–595, 1992. doi: 10.1038/356593a0.

Jackson, M. and Cheadle, M. A continuum model for the transport of heat, mass and momentum in a deformable, multicomponent mush, undergoing solid-liquid phase change. *International Journal of Heat and Mass Transfer*, 41(8-9):1035–1048, apr 1998. doi: 10.1016/S0017-9310(97)00197-X.

Jackson, M. D., Cheadle, M. J., and Atherton, M. P. Quantitative modeling of granitic melt generation and segregation in the continental crust. *Journal of Geophysical Research: Solid Earth*, 108(B7), jul 2003. doi: 10.1029/2001JB001050.

Jackson, M. D., Blundy, J., and Sparks, R. S. Chemical differentiation, cold storage and remobilization of magma in the Earth's crust. *Nature*, 564(7736):405–409, dec 2018. doi: 10.1038/s41586-018-0746-2.

Jha, K., Parmentier, E. M., and Phipps Morgan, J. The role of mantle-depletion and melt-retention buoyancy in spreading-center segmentation. *Earth and Planetary Science Letters*, 125(1-4):221–234, jul 1994. doi: 10.1016/0012-821X(94)90217-8.

Joesten, R. Evolution of mineral assemblage zoning in diffusion metasomatism. *Geochimica et Cosmochimica Acta*, 41(5):649–670, may 1977. doi: 10.1016/0016-7037(77)90303-9.

Johnson, K. T. M., Dick, H. J. B., and Shimizu, N. Melting in the oceanic upper mantle: An ion microprobe study of diopsides in abyssal peridotites. *Journal of Geophysical Research*, 95(B3):2661–2678, 1990.

Jordan, J. S. and Hesse, M. A. Reactive transport in a partially molten system with binary solid solution. *Geochemistry, Geophysics, Geosystems*, 16(12):4153–4177, dec 2015. doi: 10.1002/2015GC005956.

Jordan, J. S., Hesse, M. A., and Rudge, J. F. On mass transport in porosity waves. *Earth and Planetary Science Letters*, 485:65–78, mar 2018. doi: 10.1016/j.epsl.2017.12.024.

Jull, M. and McKenzie, D. The effect of deglaciation on mantle melting beneath Iceland. *Journal of Geophysical Research B: Solid Earth*, 101(B10):21815, 1996.

Jung, H., II, H. W. G., and Dobrzhinetskaya, L. F. Intermediate-depth earthquake faulting by dehydration embrittlement with negative volume change. *Nature*, 428(6982):545–549, apr 2004. doi: 10.1038/NATURE02412.

Karakas, O. and Dufek, J. Melt evolution and residence in extending crust: Thermal modeling of the crust and crustal magmas. *Earth and Planetary Science Letters*, 425:131–144, sep 2015. doi: 10.1016/J.EPSL.2015.06.001.

Kato, T. and Kumazawa, M. Incongruent melting of Mg2SiO4 at 20 GPa. *Physics of the Earth and Planetary Interiors*, 41(1):1–5, dec 1985. doi: 10.1016/0031-9201(85)90097-4.

Katz, R., Knepley, M., Smith, B., Spiegelman, M., and Coon, E. Numerical simulation of geodynamic processes with the Portable Extensible Toolkit for Scientific Computation. *Physics of the Earth and Planetary Interiors*, 163(1):52–68, 2007. doi: 10.1016/j.pepi.2007.04.016.

Katz, R. F. Magma Dynamics with the Enthalpy Method: Benchmark Solutions and Magmatic Focusing at Mid-ocean Ridges. *Journal of Petrology*, 49(12):2099–2121, dec 2008. doi: 10.1093/petrology/egn058.

Katz, R. F. and Weatherley, S. M. Consequences of mantle heterogeneity for melt extraction at mid-ocean ridges. *Earth and Planetary Science Letters*, 335-336:226–237, jun 2012.

Katz, R. F., Spiegelman, M., and Langmuir, C. H. A new parametrization of hydrous mantle melting. *Geochemistry, Geophysics and Geosystems*, 4(9), 2003.

Katz, R. F., Spiegelman, M., and Holtzman, B. The dynamics of melt and shear localization in partially molten aggregates. *Nature*, 442(7103):676–679, aug 2006. doi: 10.1038/nature05039.

Kay, R. W. Elemental abundances relevant to identification of magma sources. *Philosophical Transactions of the Royal Society of London*, 310(A310(1514)):535–547, apr 1984. doi: 10.1098/rsta.1984.0007.

Kelemen, P. B. Reaction Between Ultramafic Rock and Fractionating Basaltic Magma I. Phase Relations, the Origin of Calc-alkaline Magma Series, and the Formation of Discordant Dunite. *Journal of Petrology*, 31(1):51–98, feb 1990. doi: 10.1093/petrology/31.1.51.

Kelemen, P. B. and Dick, H. J. B. Focused melt flow and localized deformation in the upper mantle: Juxtaposition of replacive dunite and ductile shear zones in the Josephine peridotite, SW Oregon. *Journal of Geophysical Research: Solid Earth*, 100(B1):423–438, jan 1995. doi: 10.1029/94JB02063.

Kelemen, P. B., Shimizu, N., and Salters, V. J. M. Extraction of mid-ocean-ridge basalt from the upwelling mantle by focused flow of melt in dunite channels. *Nature*, 375(6534):747–753, jun 1995a. doi: 10.1038/375747a0.

Kelemen, P. B., Whitehead, J. A., Aharonov, E., and Jordahl, K. A. Experiments on flow focusing in soluble porous media, with applications to melt extraction from the mantle. *Journal of Geophysical Research: Solid Earth*, 100(B1):475–496, jan 1995b. doi: 10.1029/94JB02544.

Kelemen, P. B., Hirth, G., Shimizu, N., Spiegelman, M., and Dick, H. J. A review of melt migration processes in the adiabatically upwelling mantle beneath oceanic spreading ridges. *Philosophical Transactions of the Royal Society A: Mathematical, Physical and Engineering Sciences*, 355(1723):283–318, feb 1997. doi: 10.1098/rsta.1997.0010.

Keller, T. and Katz, R. F. The Role of Volatiles in Reactive Melt Transport in the Asthenosphere. *Journal of Petrology*, 57(6):1073–1108, jun 2016. doi: 10.1093/petrology/egw030.

Keller, T. and Suckale, J. A continuum model of multi-phase reactive transport in igneous systems. *Geophysical Journal International*, 219(1):185–222, oct 2019. doi: 10.1093/gji/ggz287.

Keller, T., May, D. A., and Kaus, B. J. P. Numerical modelling of magma dynamics coupled to tectonic deformation of lithosphere and crust. *Geophysical Journal International*, 195 (3):1406–1442, dec 2013. doi: 10.1093/gji/ggt306.

Keller, T., Katz, R. F., and Hirschmann, M. M. Volatiles beneath mid-ocean ridges: Deep melting, channelised transport, focusing, and metasomatism. 2017.

Kim, D.-G., Konar, B., and Jung, I.-H. Coupled Experimental Study and Thermodynamic Optimization of the K2O-MgO and K2O-MgO-SiO2 Systems. *Metallurgical and Materials Transactions B*, 48(5):2788–2803, oct 2017. doi: 10.1007/s11663-017-1038-1.

King, S., Frost, D., and Rubie, D. Why cold slabs stagnate in the transition zone. *Geology*, 43(3):231–234, 2015.

Kirby, S. H., Stein, S., Okal, E. A., and Rubie, D. C. Metastable mantle phase transformations and deep earthquakes in subducting oceanic lithosphere. *Reviews of Geophysics*, 34 (2):261–306, 1996. doi: 10.1029/96RG01050.

Kohlstedt, D. L. and Holtzman, B. K. Shearing Melt Out of the Earth: An Experimentalist's Perspective on the Influence of Deformation on Melt Extraction. *Annual Review of Earth and Planetary Sciences*, 37(1):561–593, may 2009. doi: 10.1146/annurev.earth.031208.100104.

Kohlstedt, D. L. and Zimmerman, M. E. Rheology of partially molten mantle rocks. *Annual Review of Earth and Planetary Sciences*, 24(1):41–62, may 1996. doi: 10.1146/annurev.earth.24.1.41.

Kohlstedt, D. L., Bai, Q., Wang, Z.-C., and Mei, S. Rheology of Partially Molten Rocks. pages 3–28. Springer, Dordrecht, 2000. doi: 10.1007/978-94-011-4016-4_1.

Konrad-Schmolke, M., Halama, R., Wirth, R., Thomen, A., Klitscher, N., Morales, L., Schreiber, A., and Wilke, F. D. H. Mineral dissolution and reprecipitation mediated by an amorphous phase. *Nature Communications*, 9(1):1637, dec 2018. doi: 10.1038/s41467-018-03944-z.

Korenaga, J. and Kelemen, P. B. Origin of gabbro sills in the Moho transition zone of the Oman ophiolite: Implications for magma transport in the oceanic lower crust. *Journal of Geophysical Research: Solid Earth*, 102(B12):27729–27749, dec 1997. doi: 10.1029/97JB02604.

Kushiro, I. On the nature of silicate melt and its significance in magma genesis: Reglarities in the shift of the liquidus boundaries involving olivine, pyroxene and silica materials. *American Journal of Science*, 275:411–431, 1975.

La Spina, G., Burton, M., de' Michieli Vitturi, M., and Arzilli, F. Role of syn-eruptive plagioclase disequilibrium crystallization in basaltic magma ascent dynamics. *Nature Communications*, 7(1):13402, dec 2016. doi: 10.1038/ncomms13402.

Labrosse, S., Hernlund, J. W., and Coltice, N. A crystallizing dense magma ocean at the base of the Earth's mantle. *Nature*, 450(7171):866–869, dec 2007. doi: 10.1038/nature06355.

Lambart, S., Laporte, D., Provost, A., and Schiano, P. Fate of pyroxenite-derived melts in the peridotitic mantle: thermodynamic and experimental constraints. *Journal of Petrology*, 53(3):451–476, jan 2012.

Lasaga, A. Rate Laws of Chemical Reactions. In *Kinetics of geochemical processes.*, pages 1–68. Mineral. Sot. Amer. Rev. in Mineral. 8, Washington D.C., 1981.

Lasaga, A. *Kinetic theory in the earth sciences.* Princeton university press, 1998. ISBN 0691037485.

Lasaga, A. C. Metamorphic reaction rate laws and development of isograds. *Mineralogical Magazine*, 50:359–373, 1986.

Lay, T., Garnero, E. J., and Williams, Q. Partial melting in a thermo-chemical boundary layer at the base of the mantle. *Physics of the Earth and Planetary Interiors*, 146(3-4):441–467, sep 2004. doi: 10.1016/j.pepi.2004.04.004.

Lesher, C. E. and Walker, D. Thermal Diffusion in Petrology. In J., G., editor, *Diffusion, Atomic Ordering, and Mass Transport. Advances in Physical Geochemistry, vol 8*, pages 396–451. Springer, New York, NY, 1991. doi: 10.1007/978-1-4613-9019-0_12.

Li, L., Peters, C. A., and Celia, M. A. Upscaling geochemical reaction rates using pore-scale network modeling. *Advances in Water Resources*, 29(9):1351–1370, sep 2006. doi: 10.1016/J.ADVWATRES.2005.10.011.

Liang, Y. Kinetics of crystal-melt reaction in partially molten silicates: 1. Grain scale processes. *Geochemistry, Geophysics, Geosystems*, 4(5):n/a–n/a, may 2003. doi: 10.1029/2002GC000375.

Liang, Y., Schiemenz, A., Hesse, M. A., Parmentier, E. M., and Hesthaven, J. S. High-porosity channels for melt migration in the mantle: Top is the dunite and bottom is the harzburgite and lherzolite. *Geophysical Research Letters*, 37(15):n/a–n/a, aug 2010. doi: 10.1029/2010GL044162.

Lichtner, P. C. Continuum model for simultaneous chemical reactions and mass transport in hydrothermal systems. *Geochimica et Cosmochimica Acta*, 49(3):779–800, mar 1985. doi: 10.1016/0016-7037(85)90172-3.

Liu, T.-C. and Presnall, D. C. Liquidus phase relationships on the join anorthite-forsterite-quartz at 20 kbar with applications to basalt petrogenesis and igneous sapphirine. *Contributions to Mineralogy and Petrology*, 104(6):735–742, nov 1990. doi: 10.1007/BF01167290.

Lo Cascio, M., Liang, Y., and Hess, P. C. Grain-scale processes during isothermal-isobaric melting of lherzolite. *Geophysical Research Letters*, 31(16):16605, aug 2004. doi: 10.1029/2004GL020602.

Maclennan, J., Jull, M., McKenzie, D., Slater, L., and Grönvold, K. The link between volcanism and deglaciation in Iceland. *Geochemistry, Geophysics and Geosystems*, 3, 2002.

Malaspina, N., Hermann, J., Scambelluri, M., and Compagnoni, R. Polyphase inclusions in garnet–orthopyroxenite (Dabie Shan, China) as monitors for metasomatism and fluid-related trace element transfer in subduction zone peridotite. *Earth and Planetary Science Letters*, 249(3-4):173–187, sep 2006. doi: 10.1016/j.epsl.2006.07.017.

Malvoisin, B., Podladchikov, Y. Y., and Vrijmoed, J. C. Coupling changes in densities and porosity to fluid pressure variations in reactive porous fluid flow: Local thermodynamic equilibrium. *Geochemistry, Geophysics, Geosystems*, 16(12):4362–4387, dec 2015. doi: 10.1002/2015GC006019.

Mangan, M. and Sisson, T. Delayed, disequilibrium degassing in rhyolite magma: decompression experiments and implications for explosive volcanism. *Earth and Planetary Science Letters*, 183(3-4):441–455, dec 2000. doi: 10.1016/S0012-821X(00)00299-5.

Manning, C. The chemistry of subduction-zone fluids. *Earth and Planetary Science Letters*, 223(1-2):1–16, jun 2004. doi: 10.1016/j.epsl.2004.04.030.

McCulloch, M. T. and Gamble, J. A. Geochemical and geodynamical constraints on subduction zone magmatism. *Earth and Planetary Science Letters*, 102(3-4):358–374, mar 1991. doi: 10.1016/0012-821X(91)90029-H.

McKenzie, D. The Generation and Compaction of Partially Molten Rock. *Journal of Petrology*, 25(3):713–765, aug 1984. doi: 10.1093/petrology/25.3.713.

McKenzie, D. Constraints on melt generation and transport from U-series activity ratios. *Chemical Geology*, 162(2):81–94, jan 2000. doi: 10.1016/S0009-2541(99)00126-6.

McKenzie, D. and Bickle, M. J. The volume and Composition of Melt Generated by Extension of the Lithosphere. *Journal of Petrology*, 29:625–679, 1988.

Miller, K. J., Zhu, W.-l., Montési, L. G., and Gaetani, G. A. Experimental quantification of permeability of partially molten mantle rock. 2014.

Miller, S. A., van der Zee, W., Olgaard, D. L., and Connolly, J. A. A fluid-pressure feedback model of dehydration reactions: Experiments, modelling, and application to subduction zones. *Tectonophysics*, 370(1-4):241–251, jul 2003. doi: 10.1016/S0040-1951(03)00189-6.

Monteux, J., Andrault, D., and Samuel, H. On the cooling of a deep terrestrial magma ocean. *Earth and Planetary Science Letters*, 448:140–149, aug 2016. doi: 10.1016/j.epsl.2016.05.010.

Morgan, W. J. Convection plumes in the lower mantle. *Nature*, 230(5288):42–43, 1971. doi: 10.1038/230042a0.

Morgan, Z. and Liang, Y. An experimental and numerical study of the kinetics of harzburgite reactive dissolution with applications to dunite dike formation. *Earth and Planetary Science Letters*, 214(1-2):59–74, sep 2003. doi: 10.1016/S0012-821X(03)00375-3.

Mosenfelder, J. L., Rubie, D. C., Marton, F. C., Ross, C. R., and Kerschhofer, L. Experimental constraints on the depth of olivine metastability in subducting lithosphere. *Physics of the Earth and Planetary Interiors*, 127(1-4):165–180, dec 2001. doi: 10.1016/S0031-9201(01)00226-6.

Murphy, W. M. and Helgeson, H. C. Thermodynamic and kinetic constraints on reaction rates among minerals and aqueous solutions. III. Activated complexes and the pH-dependence of the rates of feldspar, pyroxene, wollastonite, and olivine hydrolysis. *Geochimica et Cosmochimica Acta*, 51(12):3137–3153, dec 1987. doi: 10.1016/0016-7037(87)90124-4.

Murrell, S. A. and Ismail, I. A. The effect of decomposition of hydrous minerals on the mechanical properties of rocks at high pressures and temperatures. *Tectonophysics*, 31 (3-4):207–258, apr 1976. doi: 10.1016/0040-1951(76)90120-7.

Oliveira, B., Afonso, J. C., Zlotnik, S., and Diez, P. Numerical modelling of multiphase multicomponent reactive transport in the Earth's interior. *Geophysical Journal International*, 212(1):345–388, 2018. doi: 10.1093/gji/ggx399.

Oliveira, B., Afonso, J. C., and Tilhac, R. A disequilibrium reactive transport model for mantle magmatism. *Journal of Petrology*, 2020. doi: 10.1093/PETROLOGY/EGAA067.

Ol'shanskii, Y. Equilibrium of two immiscible liquids in silicate systems of alkali-earth metals. *In Dokl Akad Nauk SSSR*, 76:93–96, 1951.

Omlin, S., Räss, L., and Podladchikov, Y. Y. Simulation of three-dimensional viscoelastic deformation coupled to porous fluid flow. *Tectonophysics*, 746:695–701, oct 2018. doi: 10.1016/j.tecto.2017.08.012.

Onsager, L. Reciprocal Relations in Irreversible Processes. I. *Physical Review*, 37(4):405–426, feb 1931a. doi: 10.1103/PhysRev.37.405.

Onsager, L. Reciprocal Relations in Irreversible Processes. II. *Physical Review*, 38(12): 2265–2279, dec 1931b. doi: 10.1103/PhysRev.38.2265.

Ortoleva, P., Chadam, J., Merino, E., and Sen, a. Geochemical self-organization II; the reactive-infiltration instability, 1987.

Parsons, R. A., Nimmo, F., Hustoft, J. W., Holtzman, B. K., and Kohlstedt, D. L. An experimental and numerical study of surface tension-driven melt flow. *Earth and Planetary Science Letters*, 267(3-4):548–557, mar 2008. doi: 10.1016/J.EPSL.2007.11.064.

Pec, M., Holtzman, B. K., Zimmerman, M. E., and Kohlstedt, D. L. Influence of Lithology on Reactive Melt Flow Channelization. *Geochemistry, Geophysics, Geosystems*, 21(8), aug 2020. doi: 10.1029/2020GC008937.

Phipps Morgan, J. Thermodynamics of pressure release melting of a veined plum pudding mantle. *Geochemistry Geophysics Geosystems*, 2(4), apr 2001.

Pirard, C. and Hermann, J. Focused fluid transfer through the mantle above subduction zones. *Geology*, 43(10):915–918, oct 2015. doi: 10.1130/G37026.1.

Plank, T. and Forsyth, D. W. Thermal structure and melting conditions in the mantle beneath the Basin and Range province from seismology and petrology. *Geochemistry, Geophysics, Geosystems*, 17(4):1312–1338, apr 2016. doi: 10.1002/2015GC006205.

Plank, T. and Langmuir, C. H. Tracing trace elements from sediment input to volcanic output at subduction zones. *Nature*, 362(6422):739–743, apr 1993. doi: 10.1038/362739a0.

Plümper, O., John, T., Podladchikov, Y. Y., Vrijmoed, J. C., and Scambelluri, M. Fluid escape from subduction zones controlled by channel-forming reactive porosity. *Nature Geoscience*, 10(2):150–156, dec 2016. doi: 10.1038/ngeo2865.

Poulet, T., Regenauer-Lieb, K., and Karrech, A. A unified multi-scale thermodynamical framework for coupling geomechanical and chemical simulations. *Tectonophysics*, 483(1-2):178–189, mar 2010. doi: 10.1016/J.TECTO.2009.10.018.

Powell, R., Holland, T., and Worley, B. Calculating phase diagrams involving solid solutions via non-linear equations, with examples using THERMOCALC. *Journal of Metamorphic Geology*, 16(4):577–588, jul 1998. doi: 10.1111/j.1525-1314.1998.00157.x.

Presnall, D. C., Weng, Y.-H., Milholland, C. S., and Walter, M. J. Liquidus phase relations in the system MgO–MgSiO3 at pressures up to 25 GPa—constraints on crystallization of a molten Hadean mantle. *Physics of the Earth and Planetary Interiors*, 107(1):83–95, 1998. doi: 10.1016/S0031-9201(97)00126-X.

Prigogine, I. On the kinetics of the approach to equilibrium. *Physica*, 27(7):629–646, jul 1961. doi: 10.1016/0031-8914(61)90008-8.

Prigogine, I. *Introduction to thermodynamics of irreversible processes*. 3rd ed edition, 1967.

Prigogine, I. and Glansdorff, P. L'écart à l'équilibre interprété comme une source d'ordre. Structures dissipatives. *Bulletins de l'Académie Royale de Belgique*, 59(1):672–702, 1973. doi: 10.3406/BARB.1973.60756.

Prigogine, I. and Lefever, R. Symmetry Breaking Instabilities in Dissipative Systems. II. *The Journal of Chemical Physics*, 48(4):1695, sep 1968. doi: 10.1063/1.1668896.

Prigogine, I. and Nicolis, G. On Symmetry-Breaking Instabilities in Dissipative Systems. *The Journal of Chemical Physics*, 46(9):3542, may 1967. doi: 10.1063/1.1841255.

Proussevitch, A. and Sahagian, D. Bubbledrive-1: A numerical model of volcanic eruption mechanisms driven by disequilibrium magma degassing. *Journal of Volcanology and Geothermal Research*, 143(1-3):89–111, may 2005. doi: 10.1016/J.JVOLGEORES.2004.09.012.

Putnis, A. Mineral replacement reactions: from macroscopic observations to microscopic mechanisms. *Mineralogical Magazine*, 66(5):689–708, oct 2002. doi: 10.1180/0026461026650056.

Quick, J. E. Petrology and petrogenesis of the Trinity peridotite, An upper mantle diapir in the eastern Klamath Mountains, northern California. *Journal of Geophysical Research*, 86(B12):11837, 1981. doi: 10.1029/JB086iB12p11837.

Raleigh, C. B. and Paterson, M. S. Experimental deformation of serpentinite and its tectonic implications. *Journal of Geophysical Research*, 70(16):3965–3985, aug 1965. doi: 10.1029/JZ070I016P03965.

Rees Jones, D. W. and Katz, R. F. Reaction-infiltration instability in a compacting porous medium. *Journal of Fluid Mechanics*, 852:5–36, oct 2018. doi: 10.1017/jfm.2018.524.

Rees Jones, D. W., Zhang, H., and Katz, R. F. Magmatic channelization by reactive and shear-driven instabilities at mid-ocean ridges: a combined analysis. *Geophysical Journal International*, 226(1):582–609, may 2021. doi: 10.1093/gji/ggab112.

Ribe, N. M. The generation and composition of partial melts in the earth's mantle. *Earth and Planetary Science Letters*, 73(2):361–376, 1985. doi: 10.1016/0012-821X(85)90084-6.

Rozhko, A. Y., Podladchikov, Y. Y., and Renard, F. Failure patterns caused by localized rise in pore-fluid overpressure and effective strength of rocks. *Geophysical Research Letters*, 34 (22), nov 2007. doi: 10.1029/2007GL031696.

Rudge, J. F. The Viscosities of Partially Molten Materials Undergoing Diffusion Creep. *Journal of Geophysical Research: Solid Earth*, 123(12):10,534–10,562, dec 2018. doi: 10.1029/2018JB016530.

Rudge, J. F., Bercovici, D., and Spiegelman, M. Disequilibrium melting of a two phase multicomponent mantle. *Geophysical Journal International*, 184(2):699–718, feb 2011. doi: 10.1111/j.1365-246X.2010.04870.x.

Ryerson, F. Oxide solution mechanisms in silicate melts: Systematic variations in the activity coefficient of SiO2. *Geochimica et Cosmochimica Acta*, 49(3):637–649, mar 1985. doi: 10.1016/0016-7037(85)90159-0.

Sack, R. O. and Ghiorso, M. S. Thermodynamics of multicomponent pyroxenes: I. Formulation of a general model. *Contributions to Mineralogy and Petrology*, 116(3):277–286, 1994.

Schiemenz, A., Liang, Y., and Parmentier, E. M. A high-order numerical study of reactive dissolution in an upwelling heterogeneous mantle - I. Channelization, channel lithology and channel geometry. *Geophysical Journal International*, 186(2):641–664, aug 2011.

Scott, D. R. and Stevenson, D. J. Magma solitons. *Geophysical Research Letters*, 11(11): 1161–1164, nov 1984. doi: 10.1029/GL011i011p01161.

Shervais, J. W. and Mukasa, S. B. The Balmuccia Orogenic Lherzolite Massif, Italy. *Journal of Petrology*, Special_Vo(2):155–174, jan 1991. doi: 10.1093/petrology/Special_Volume.2.155.

Shorttle, O., Maclennan, J., and Lambart, S. Quantifying lithological variability in the mantle. *Earth and Planetary Science Letters*, 395:24–40, jun 2014. doi: 10.1016/j.epsl.2014.03.040.

Siebert, J., Badro, J., Antonangeli, D., and Ryerson, F. J. Terrestrial accretion under oxidizing conditions. *Science*, 339(6124):1194–1197, mar 2013. doi: 10.1126/science.1227923.

Sim, S. J., Spiegelman, M., Stegman, D. R., and Wilson, C. The influence of spreading rate and permeability on melt focusing beneath mid-ocean ridges. *Physics of the Earth and Planetary Interiors*, 304:106486, jul 2020. doi: 10.1016/j.pepi.2020.106486.

Simpson, G., Spiegelman, M., and Weinstein, M. I. A multiscale model of partial melts: 2. Numerical results. *Journal of Geophysical Research: Solid Earth*, 115(4), apr 2010a. doi: 10.1029/2009JB006376.

Simpson, G., Spiegelman, M., and Weinstein, M. I. A multiscale model of partial melts: 1. Effective equations. *Journal of Geophysical Research: Solid Earth*, 115(4), apr 2010b. doi: 10.1029/2009JB006375.

Slater, L., Jull, M., McKenzie, D., and Gronvöld, K. Deglaciation effects on mantle melting under Iceland: results from the northern volcanic zone. *Earth and Planetary Science Letters*, 164(1-2):151–164, dec 1998. doi: 10.1016/S0012-821X(98)00200-3.

Sleep, N. H. Tapping of melt by veins and dikes. *Journal of Geophysical Research*, 93(B9): 10255–10272, sep 1988. doi: 10.1029/JB093iB09p10255.

Smith, W. *Chemical reaction equilibrium analysis. Theory and Algorithms*. 1982.

Sobolev, A., Hofmann, A. W., Kuzmin, D., Yaxley, G., Arndt, N. T., Chung, S., Danyushevsky, L., Elliott, T., Frey, F., Garcia, M., and Others. The amount of recycled crust in sources of mantle-derived melts. *Science*, 316(5823):412, 2007.

Solano, J. M., Jackson, M. D., J Sparks, R. S., Blundy, J. D., and Annen, C. Melt Segregation in Deep Crustal Hot Zones: a Mechanism for Chemical Differentiation, Crustal Assimilation and the Formation of Evolved Magmas. *Journal of Petrology*, 53(10):1999–2026, 2012. doi: 10.1093/petrology/egs041.

Solano, J. M. S., Jackson, M. D., Sparks, R. S. J., and Blundy, J. Evolution of major and trace element composition during melt migration through crystalline mush: Implications for chemical differentiation in the crust. *American Journal of Science*, 314(5):895–939, may 2014. doi: 10.2475/05.2014.01.

Spence, D. A. and Turcotte, D. L. Magma-driven propagation of cracks. *Journal of Geophysical Research*, 90(B1):575–580, jan 1985. doi: 10.1029/JB090iB01p00575.

Spiegelman, M. Physics of Melt Extraction: Theory, Implications and Applications. *Philosophical Transactions of the Royal Society A: Mathematical, Physical and Engineering Sciences*, 342(1663):23–41, jan 1993a. doi: 10.1098/rsta.1993.0002.

Spiegelman, M. Flow in deformable porous media. Part 1 Simple analysis. *Journal of Fluid Mechanics*, 247(-1):17, feb 1993b. doi: 10.1017/S0022112093000369.

Spiegelman, M. Flow in deformable porous media. Part 2 Numerical analysis – the relationship between shock waves and solitary waves. *Journal of Fluid Mechanics*, 247(-1):39, feb 1993c. doi: 10.1017/S0022112093000370.

Spiegelman, M. Linear analysis of melt band formation by simple shear. *Geochemistry, Geophysics, Geosystems*, 4(9):8615, sep 2003. doi: 10.1029/2002GC000499.

Spiegelman, M. and Elliott, T. Consequences of melt transport for uranium series disequilibrium in young lavas. *Earth and Planetary Science Letters*, 118(1-4):1–20, jul 1993. doi: 10.1016/0012-821X(93)90155-3.

Spiegelman, M. and Kelemen, P. B. Extreme chemical variability as a consequence of channelized melt transport. *Geochemistry, Geophysics, Geosystems*, 4(7):n/a–n/a, jul 2003. doi: 10.1029/2002GC000336.

Spiegelman, M. and Kenyon, P. The requirements for chemical disequilibrium during magma migration. *Earth and Planetary Science Letters*, 109(3):611–620, 1992. doi: 10.1016/0012-821X(92)90119-G.

Spiegelman, M. and McKenzie, D. Simple 2D models of melt extraction at mid-ocean ridges and island arcs. *Earth and Planetary Science Letters*, 83:137–152, 1987.

Spiegelman, M., Kelemen, P. B., and Aharonov, E. Causes and consequences of flow organization during melt transport: The reaction infiltration instability in compactible media. *Journal of Geophysical Research: Solid Earth*, 106(B2):2061–2077, feb 2001. doi: 10.1029/2000JB900240.

Šrámek, O., Ricard, Y., and Bercovici, D. Simultaneous melting and compaction in deformable two-phase media. *Geophysical Journal International*, 168(3):964–982, mar 2007. doi: 10.1111/j.1365-246X.2006.03269.x.

Steefel, C. I. and Lasaga, A. C. A coupled model for transport of multiple chemical species and kinetic precipitation/dissolution reactions with application to reactive flow in single phase hydrothermal systems. *American Journal of Science*, 294(5):529–592, may 1994. doi: 10.2475/ajs.294.5.529.

Steefel, C. I. and MacQuarrie, K. T. B. Approaches to modeling of reactive transport in porous media. pages 83–130. De Gruyter, 1996.

Stevenson, D. J. Spontaneous small-scale melt segregation in partial melts undergoing deformation. *Geophysical Research Letters*, 16(9):1067–1070, sep 1989. doi: 10.1029/GL016i009p01067.

Stixrude, L. and Lithgow-Bertelloni, C. Thermodynamics of mantle minerals - I. Physical properties. *Geophysical Journal International*, 162(2):610–632, aug 2005. doi: 10.1111/j.1365-246X.2005.02642.x.

Stixrude, L., Lithgow-Bertelloni, C., T.J., S., D.J., W., J.Z., Z., Y.B., W., T., G., and Y., O. Thermodynamics of mantle minerals - II. Phase equilibria. *Geophysical Journal International*, 184(3):1180–1213, mar 2011. doi: 10.1111/j.1365-246X.2010.04890.x.

Stolper, E. A phase diagram for mid-ocean ridge basalts: Preliminary results and implications for petrogenesis. *Contributions to Mineralogy and Petrology*, 74(1):13–27, sep 1980. doi: 10.1007/BF00375485.

Takei, Y. Phase-Field Modeling of Grain Boundary Premelting. *Journal of Geophysical Research: Solid Earth*, 124(8):8057–8076, aug 2019. doi: 10.1029/2019JB017632.

Takei, Y. and Holtzman, B. K. Viscous constitutive relations of solid-liquid composites in terms of grain boundary contiguity: 1. Grain boundary diffusion control model. *Journal of Geophysical Research: Solid Earth*, 114(6):B06205, jun 2009. doi: 10.1029/2008JB005850.

Tatsumi, Y., Hamilton, D., and Nesbitt, R. Chemical characteristics of fluid phase released from a subducted lithosphere and origin of arc magmas: Evidence from high-pressure experiments and natural rocks. *Journal of Volcanology and Geothermal Research*, 29(1-4):293–309, sep 1986. doi: 10.1016/0377-0273(86)90049-1.

Taylor, J. H. C. Melting Relations in the System MgO-Al2O3-SiO2 at 15 Kb. *Geological Society of America Bulletin*, 84(4):1335–1348, 1973. doi: 10.1130/0016-7606(1973)84<1335:MRITSM>2.0.CO;2.

Tetzlaff, M. and Schmeling, H. The influence of olivine metastability on deep subduction of oceanic lithosphere. *Physics of the Earth and Planetary Interiors*, 120(1):29–38, jun 2000. doi: 10.1016/S0031-9201(00)00139-4.

Thompson, B. J. Local equilibrium in metasomatic processes. *Researches in Geochemistry*, 1959.

Till, C. B., Grove, T. L., and Withers, A. C. The beginnings of hydrous mantle wedge melting. *Contributions to Mineralogy and Petrology*, 163(4):669–688, oct 2011. doi: 10.1007/s00410-011-0692-6.

Tirone, M. Petrological Geodynamics of Mantle Melting II. AlphaMELTS + Multiphase Flow: Dynamic Fractional Melting. *Frontiers in Earth Science*, 6:18, mar 2018. doi: 10.3389/feart.2018.00018.

Tirone, M. Petrological Geodynamics of Mantle Melting III. AlphaMELTS + Multiphase Flow: the Effect of Water (revision II). *Geoscience Frontiers*, 6, dec 2019. doi: 10.1016/j.gsf.2019.10.010.

Tirone, M. and Sessing, J. Petrological Geodynamics of Mantle Melting I. AlphaMELTS + Multiphase Flow: Dynamic Equilibrium Melting, Method and Results. *Frontiers in Earth Science*, 5:81, oct 2017. doi: 10.3389/feart.2017.00081.

Tirone, M., Ganguly, J., and Morgan, J. P. Modeling petrological geodynamics in the Earth's mantle. *Geochemistry, Geophysics, Geosystems*, 10(4):n/a–n/a, apr 2009. doi: 10.1029/2008GC002168.

Tolman, R. C. and Fine, P. C. On the Irreversible Production of Entropy. *Reviews of Modern Physics*, 20(1):51, jan 1948. doi: 10.1103/RevModPhys.20.51.

Turner, A. J., Katz, R. F., Behn, M. D., and Keller, T. Magmatic focusing to mid-ocean ridges: the role of grain size variability and non-Newtonian viscosity. jun 2017.

von Bargen, N. and Waff, H. S. Permeabilities, interfacial areas and curvatures of partially molten systems: Results of numerical computations of equilibrium microstructures. *Journal of Geophysical Research: Solid Earth*, 91(B9):9261–9276, aug 1986. doi: 10.1029/JB091IB09P09261.

Walker, D. and DeLong, S. E. Soret separation of mid-ocean ridge basalt magma. *Contributions to Mineralogy and Petrology*, 79(3):231–240, jul 1982. doi: 10.1007/BF00371514.

Walter, M. J. Melting of Garnet Peridotite and the Origin of Komatiite and Depleted Lithosphere. *Journal of Petrology*, 39(1):29–60, 1998.

Wasylenki, L. E., Baker, M. B., Kent, A. J. R., and Stolper, E. M. Near-solidus melting of the shallow upper mantle: Partial melting experiments on depleted peridotite. *Journal of Petrology*, 44(7):1163–1191, 2003.

Weatherley, S. M. and Katz, R. F. Melting and channelized magmatic flow in chemically heterogeneous, upwelling mantle. *Geochemistry Geophysics Geosystems*, 2012.

Wiggins, C. and Spiegelman, M. Magma migration and magmatic solitary waves in 3-D. *Geophysical Research Letters*, 22(10):1289–1292, may 1995. doi: 10.1029/95GL00269.

Williams, Q. and Garnero, E. J. Seismic evidence for partial melt at the base of earth's mantle. *Science*, 273(5281):1528–1530, sep 1996. doi: 10.1126/science.273.5281.1528.

Wilson, C. R., Spiegelman, M., van Keken, P. E., and Hacker, B. R. Fluid flow in subduction zones: The role of solid rheology and compaction pressure. *Earth and Planetary Science Letters*, 401:261–274, sep 2014. doi: 10.1016/j.epsl.2014.05.052.

Wilson, C. R., Spiegelman, M., and van Keken, P. E. TerraFERMA: The Transparent Finite Element Rapid Model Assembler for multiphysics problems in Earth sciences. *Geochemistry, Geophysics, Geosystems*, 18(2):769–810, feb 2017. doi: 10.1002/2016GC006702.

Yaxley, G. M. Experimental study of the phase and melting relations of homogeneous basalt + peridotite mixtures and implications for the petrogenesis of flood basalts. *Contributions to Mineralogy and Petrology*, 139:326–338, 2000.

Yaxley, G. M. and Green, D. H. Reactions between eclogite and peridotite: mantle refertilisation by subduction of oceanic crust. *Contributions to Mineralogy and Petrology*, 139: 326–338, 1998.

Yoshino, T., Takei, Y., Wark, D. A., and Watson, E. B. Grain boundary wetness of texturally equilibrated rocks, with implications for seismic properties of the upper mantle. *Journal of Geophysical Research: Solid Earth*, 110(B8):1–16, aug 2005. doi: 10.1029/2004JB003544.

Zhang, Y. *Geochemical Kinetics*. Princeton University Press, 2008. ISBN 9780691124322.

Zimmerman, M. E. and Kohlstedt, D. L. Rheological properties of partially molten lherzolite. *Journal of Petrology*, 45(2):275–298, feb 2004. doi: 10.1093/petrology/egg089.

Appendix A: Thermodynamic relations

The molar Gibbs energy of a general solution phase can be broken up into three components: $\tilde{G}_i^{\circ}$ describing the contributions from the pure endmebers, $\tilde{G}_i^{config}$ describing ideal mixing between endmembers, and $\tilde{G}_i^{excess}$ describing the additional energy due to non-ideality.

$$\tilde{G}_i(T,P,\boldsymbol{c}_i) = \sum_{k=1}^{K_i} \Big[\underbrace{x_i^k \tilde{\mu}_i^{k\circ}(T,P)}_{\tilde{G}_i^{\circ}} + \underbrace{RTx_i^k \ln x_i^k}_{\tilde{G}_i^{config}} + \underbrace{RTx_i^k \ln \tilde{\gamma}_i^k(T,P,\boldsymbol{x}_i)}_{\tilde{G}_i^{excess}} \Big] \tag{A.1}$$

Where the tildes refer to molar quantities. $\tilde{\mu}_i^{\circ,k}$ are the the molar chemical potentials of the pure endmembers: these include models of the molar enthalpies, entropies, volumes, heat capacities, and equations of state (e.g. Berman, 1988). x_i^k is the molar concentration of endmember k, and $\tilde{\gamma}_i^k$ is the activity coefficient. The functional form of $\tilde{G}_i^{excess}$ depends on the solution model used. As the independent variable for composition is mass concentration, we transform to molar concentration in the definition of $\tilde{G}_i$ according to

$$x_i^k = \frac{\frac{c_i^k}{M_i^k}}{\sum_{k=1}^{K_i} \frac{c_i^k}{M_i^k}} \tag{A.2}$$

Given expressions for the molar Gibbs free energy surfaces for the phases, the relevant thermodynamic properties are defined as follows

$$\begin{gathered} \tilde{s}_i = -\frac{\partial \tilde{G}_i}{\partial T}, \quad \tilde{V}_i = \frac{\partial \tilde{G}_i}{\partial P}, \quad \tilde{\mu}_i^k = \frac{\partial \tilde{G}_i}{\partial n_k}, \\ \tilde{C}_{Pi} = -T\frac{\partial^2 \tilde{G}_i}{\partial T^2}, \quad \tilde{\alpha}_i = \frac{1}{\tilde{V}_i}\frac{\partial^2 \tilde{G}_i}{\partial P \partial T} \end{gathered} \tag{A.3}$$

These are converted to specific quantities by dividing through by the relevant molar

masses

$$s_i = \frac{\tilde{s}_i}{\sum_{k=1}^{K_i} x_i^k M_i^k}, \quad \rho_i = \frac{\sum_{k=1}^{K_i} x_i^k M_i^k}{\tilde{V}_i^k}, \quad \mu_i^k = \frac{\tilde{\mu}_i^k}{\sum_{k=1}^{K_i} x_i^k M_i^k}$$
$$C_{Pi} = \frac{\tilde{C}_{Pi}}{\sum_{k=1}^{K_i} x_i^k M_i^k}, \quad \alpha_i = \frac{\tilde{\alpha}_i}{\sum_{k=1}^{K_i} x_i^k M_i^k} \tag{A.4}$$

Appendix B: Deriving independent reaction sets

By the rank-nullity theorem, for any reactive system, there is a set of $\mathcal{J} = N_{tot} - C$ linearly independent reactions. This is the minimum number of reactions required to describe the chemical state of the system. In simple systems such a set can be determined by inspection. But more generally a reaction set can be constructed by dividing the system into *mediating* endmembers, whose compositions span the column space of $\boldsymbol{F}$, and *non-independent*, or reacting, endmembers whose compositions can be expressed in terms of the mediating endmembers. Mathematically this is equivalent to putting $\boldsymbol{F}$ in reduced row echelon form, with possible rearrangement of columns such that the pivot columns occupy the leftmost columns

$$\text{RREF}(\boldsymbol{F}) = \begin{bmatrix} \boldsymbol{I}_C & \boldsymbol{Q} \end{bmatrix} \tag{B.1}$$

Where $\boldsymbol{I}_C$ is a $C \times C$ identity matrix, and $\boldsymbol{Q}$ is a $C \times \mathcal{J}$ matrix that maps the stoichiometry of the non-independent endmembers onto the mediating endmembers. This then allows us to derive the $N_{tot} \times \mathcal{J}$ stoichiometric matrix $\tilde{\boldsymbol{\nu}}$

$$\tilde{\boldsymbol{\nu}} = \begin{bmatrix} \boldsymbol{Q} \\ -\boldsymbol{I}_{\mathcal{J}} \end{bmatrix} \tag{B.2}$$

Where $\boldsymbol{I}_{\mathcal{J}}$ is a $\mathcal{J} \times \mathcal{J}$ identity matrix. The columns of $\tilde{\boldsymbol{\nu}}$ correspond to the stoichiometric vectors for the respective reactions $\tilde{\boldsymbol{\nu}}_j$ for a set of reactions of the form

$$[\text{non-independent phase endmember}]_j = \sum_{k=1}^{C} \nu_j^k [\text{mediating phase endmember}]_k \tag{B.3}$$

Appendix C: Evolution equations for an open system batch reactor

Here we will derive a set of conservation equations for mass and energy for disequilibrium multiphase reaction in an open batch system as shown in Figure C.1. As we are not considering spatial gradients and time is the only independent variable, we write the conservation equations in integral form in which we conserve the net mass and energy fluxes in the system volume.

The system exchanges heat with the surroundings via a boundary heat flux at a rate Q^E. Mass of a phase i is transferred into the system at a rate Ψ_i^{in} and with composition c_{ik}^{in}. This incoming material has a temperature T^{in} which may be different to that of the system. It is assumed that this material is instantaneously homogenized, both thermally and chemically, within the system. Mass then flows out at a rate Ψ_i^{out} with a composition and temperature identical to that of the system. The net boundary heat and mass transfer rates can be equated to integrals of the heat and mass fluxes according to

$$Q^E = -\oiint_{S(V)} \mathbf{q} \cdot \mathrm{d}\mathbf{S} = -\iiint_V \nabla \cdot \mathbf{q} \mathrm{d}V \tag{C.1}$$

$$\Psi_i^{in} - \Psi_i^{out} = -\oiint_{S(V)} \mathbf{J}_i^A \cdot \mathrm{d}\mathbf{S} = -\iiint_V \nabla \cdot \mathbf{J}_i^A \mathrm{d}V, \tag{C.2}$$

where $\mathbf{q}$ is the heat flux and $\mathbf{J}_i^A$ is the advective mass flux.

Reaction, mass flux and heating/cooling produce a mechanical response that depends on the assumptions made about the rheology of the system boundaries. As the system expands it does work on the surroundings at a rate given by

$$W = P\frac{\mathrm{d}V}{\mathrm{d}t}, \tag{C.3}$$

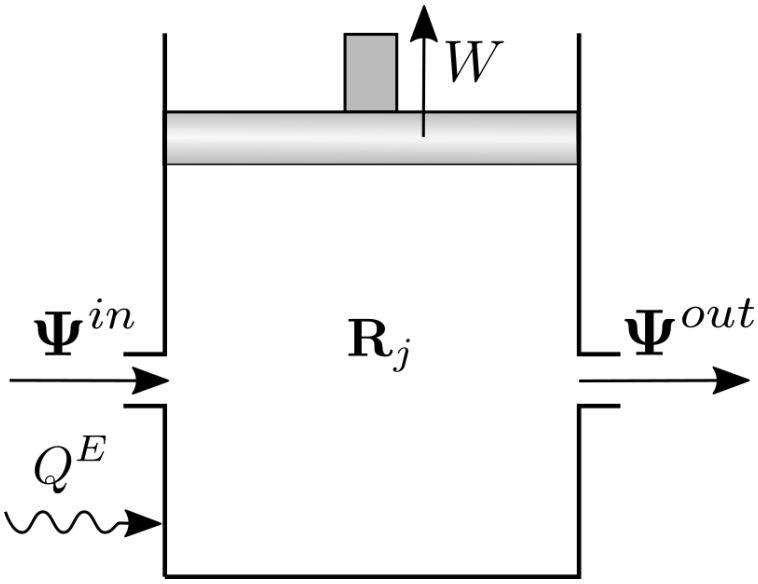

Figure C.1: Schematic sketch of the open batch reactor. Heterogeneous reaction R_j and heat production Q^I occur within the system, while boundary heat flux Q^E and the advective mass fluxes Ψ_i^{in} and Ψ_i^{out}, into and out of the system respectively, allow it to exchange heat and mass with the surroundings. As the system expands it does work on the environment at a rate W

where V is the system volume. We can consider two endmember scenarios. The first corresponds to an isobaric system. In this case, P is the independent variable and the system is free to expand or contract in response to any changes in assemblage, temperature or in-flux or out-flux of material (e.g. a deformable partially molten region in the mantle). We assume that the expansion and contraction are perfectly reversible such that no energy is dissipated as the volume changes. The second scenario is that of an isochoric system in which V is the independent variable. In this case the system volume remains constant and reaction, mass flux and heating produce changes in P instead (e.g. a magma chamber in the brittle upper crust).

C.0.1 Conservation of composition

We start by conserving the mass of endmember k in phase i

$$\frac{\mathrm{d}}{\mathrm{d}t} m_i c_{ik} = \Gamma_{ik} + \Psi_i^{in} c_{ik}^{in} - \Psi_i^{out} c_{ik} \tag{C.4}$$

where m_i is the mass of phase i, c_{ik} is the concentration as a mass fraction of k in i. Γ_{ik} is the net rate of production or consumption of endmember k by internal heterogeneous reaction

$$\Gamma_{ik} = \sum_{j=1}^{J} \hat{\nu}_{ikj} R_j \tag{C.5}$$

where $\hat{\nu}_{ikj}$ is the mass-normalized stoichiometric coefficient of k in reaction j, defined as

$$\hat{\nu}_{kij} = \frac{\frac{\nu_{kij}}{M_k}}{\sum_{i=1}^{M} \sum_{k=N_{i-1}}^{N_i} \frac{\nu_{kij}}{M_k}} \tag{C.6}$$

where M_k is the molar mass of endmember k. R_j is the reaction rate of reaction j in units of kgs^{-1}: $R_j > 0$ is a forward reaction and $R_j < 0$ is a reverse reaction. As the concentrations within each phase sum to 1, we need $K_i - 1$ equations to track the composition of a single phase; giving $K_{tot}-$ equations for all the endmembers in the system.

C.0.2 Conservation of phase mass

Summing over all the endmembers in each phase, we get equations for the conservation of phase mass

$$\frac{\mathrm{d}m_i}{\mathrm{d}t} = \sum_{k=1}^{N_i} \Gamma_{ik} + \Psi_i^{in} - \Psi_i^{out} \tag{C.7}$$

where we have used the fact that

$$\sum_{k=1}^{N_i} c_{ik} = 1. \tag{C.8}$$

Phase masses are dimensional quantities that are not constrained to sum to unity. They can be converted to equivalent mass fractions by normalizing by the total mass

$$\phi_i = \frac{m_i}{\sum_{i=1}^{N_i} m_i}. \tag{C.9}$$

C.0.3 Conservation of energy

For non-isothermal systems we must also conserve energy to track the temperature evolution of the system. Summing the internal energy of all phases gives

$$\sum_{i=1}^{M}\left(\frac{\mathrm{d}}{\mathrm{d}t}m_i u_i + \Psi_i^A u_i\right) = Q^E - W + \sum_{i=1}^{M}\left(\Psi_i^{in}u_i^{in} - \Psi_i^{out}u_i\right) \tag{C.10}$$

where u_i is the specific internal energy of phase i. Applying conservation of mass to this expression gives

$$\sum_{i=1}^{M}\left[m_i\frac{\mathrm{d}}{\mathrm{d}t}u_i + u_i\sum_{k=1}^{N_i}\Gamma_{ik} + \Psi_i^{in}\left(u_i - u_i^{in}\right)\right] = Q^E - W. \tag{C.11}$$

By substituting in the thermodynamic relations

$$u_i = \sum_{k=1}^{N_i}\mu_{ik}c_{ik} - \frac{P}{\rho_i} + Ts_i \tag{C.12}$$

$$\frac{\mathrm{d}u_i}{\mathrm{d}t} = T\frac{\mathrm{d}s_i}{\mathrm{d}t} + \frac{P}{\rho_i^2}\frac{\mathrm{d}\rho_i}{\mathrm{d}t} + \sum_{k=1}^{N_i}\mu_{ik}\frac{\mathrm{d}c_{ik}}{\mathrm{d}t}, \tag{C.13}$$

where s_i is the specific entropy of phase i and μ_{ik} is the specific chemical potential of end-member k in phase i, we can convert to an equation for conservation of entropy

$$\begin{aligned}\sum_{i=1}^{M}\Bigg[T\left(m_i\frac{\mathrm{d}s_i}{\mathrm{d}t} + s_i\sum_{k=1}^{N_i}\Gamma_{ik}\right) + \sum_{k=1}^{N_i}\mu_{ik}\left(m_i\frac{\mathrm{d}c_{ik}}{\mathrm{d}t} + \sum_{k=1}^{N_i}\Gamma_{ik}c_{ik}\right)\\ +\Psi_i^{in}\left(\sum_{k=1}^{N_i}\left(\mu_{ik}c_{ik} - \mu_{ik}^{in}c_{ik}^{in}\right) + Ts_i - T^{in}s_i^{in}\right)\\ +P\left(\frac{m_i}{\rho_i^2}\frac{\mathrm{d}\rho_i}{\mathrm{d}t} - \frac{1}{\rho_i}\sum_{k=1}^{N_i}\Gamma_{ik} - \Psi_i^{in}\left(\frac{1}{\rho_i} - \frac{1}{\rho_i^{in}}\right)\right)\Bigg] = Q^E - W.\end{aligned} \tag{C.14}$$

This can be simplified by noting that

$$P\sum_{i=1}^{M}\left[\frac{m_i}{\rho_i^2}\frac{\mathrm{d}\rho_i}{\mathrm{d}t}-\frac{1}{\rho_i}\sum_{k=1}^{N_i}\Gamma_{ik}-\Psi_i^{in}\left(\frac{1}{\rho_i}-\frac{1}{\rho_i^{in}}\right)\right]=-P\frac{\mathrm{d}V}{\mathrm{d}t}=-W. \tag{C.15}$$

This cancels with the work term on the right-hand side. If we also apply conservation of composition, we can put the entropy equation in the following more compact form

$$\begin{gathered}\sum_{i=1}^{M}\left[m_i\frac{\mathrm{d}s_i}{\mathrm{d}t}+\sum_{k=1}^{N_i}\left(s_i\Gamma_{ik}+\frac{1}{T}\mu_{ik}\Gamma_{ik}\right)\right]= \\ \frac{1}{T}\left[Q^E-\sum_{i=1}^{M}\Psi_i^{in}\left(Ts_i-T^{in}s_i^{in}+\sum_{k=1}^{N_i}c_{ik}^{in}\left(\mu_{ik}-\mu_{ik}^{in}\right)\right)\right]\end{gathered} \tag{C.16}$$

We can convert (C.16) into equation for the temperature evolution by substituting in

$$\frac{\mathrm{d}s_i}{\mathrm{d}t}=\frac{C_{Pi}}{T}\frac{\mathrm{d}T}{\mathrm{d}t}-\frac{\alpha_i}{\rho_i}\frac{\mathrm{d}P}{\mathrm{d}t} \tag{C.17}$$

where C_{Pi} is the heat capacity and α_i is the thermal expansivity. This gives

$$\begin{gathered}\sum_{i=1}^{M}\left[m_i\left(C_P\frac{\mathrm{d}T}{\mathrm{d}t}-\frac{\alpha_i T}{\rho_i}\frac{\mathrm{d}P}{\mathrm{d}t}\right)+Ts_i\sum_{k=1}^{N_i}\Gamma_{ik}+\sum_{k=1}^{N_i}\mu_{ik}\Gamma_{ik}\right]= \\ Q^E+\sum_{i=1}^{M}\Psi_i^{in}\left[Ts_i-T^{in}s_i^{in}+\sum_{k=1}^{N_i}c_{ik}^{in}\left(\mu_{ik}-\mu_{ik}^{in}\right)\right].\end{gathered} \tag{C.18}$$

Here we have written the temperature evolution with P as the independent variable. This is appropriate for the isobaric scenario discussed above where the system is free to expand in response to reaction, inflowing material, and thermal or adiabatic expansion, so that P is held constant. If we want to simulate the isochoric scenario in which V is the fixed independent variable we would simply need to substitute in

$$-\frac{\alpha_i}{\rho_i}\frac{\mathrm{d}P}{\mathrm{d}t}=-\frac{\mathrm{d}}{\mathrm{d}T}P(V_i,T)\frac{\mathrm{d}V_i}{\mathrm{d}t} \tag{C.19}$$

where V_i is the specific molar volume of phase i. P is no longer an independent variable, but is dependent on the V_i and T through the equations of state (EOS) of the constituent phases which are provided by the thermodynamic models.

Appendix D: Pressure-split formulation

To put the governing equations (2.23)-(2.27) into a more convenient form, following Spiegelman (1993b,c) and Katz et al. (2007) we use the pressure-split formulation to rewrite them as a function of phase fraction, solid velocity and pressure. The fluid pressure is decomposed into three components

$$P = \mathcal{P} + P^* + \rho_{s0}\boldsymbol{g}\cdot\boldsymbol{z} \tag{D.1}$$

where $\mathcal{P} = \zeta\boldsymbol{\nabla}\cdot\boldsymbol{v}_s$ is the compaction pressure, and P^* describes the remaining dynamic pressure components.

Following the same approach as Spiegelman (1993b), but here summing over the multiple solid phases, we get the following set of equations

$$\rho_f\phi_f\frac{\mathrm{D}_f c_f^k}{\mathrm{D}t} = \Gamma_f^k - c_f^k\Gamma_f + D_f^k\boldsymbol{\nabla}\cdot\phi_f\boldsymbol{\nabla}c_f^k \tag{D.2}$$

$$\frac{\mathrm{D}_s\phi_i}{\mathrm{D}t} = -\phi_i\frac{\mathcal{P}}{\zeta} + \frac{\Gamma_i}{\rho_i} \tag{D.3}$$

$$\frac{\mathrm{D}_s\phi_f}{\mathrm{D}t} = (1-\phi_f)\frac{\mathcal{P}}{\zeta} + \sum_{i=2}^{N}\left[\frac{\phi_i}{\rho_i}\frac{\mathrm{D}_s\rho_i}{\mathrm{D}t} - \frac{\Gamma_i}{\rho_i}\right] \tag{D.4}$$

$$\frac{\mathcal{P}}{\zeta} = \boldsymbol{\nabla}\cdot\frac{K}{\mu}\left(\boldsymbol{\nabla}P^* + \boldsymbol{\nabla}\mathcal{P} + \Delta\rho\boldsymbol{g}\right) + \sum_{i=1}^{N}\frac{\Gamma_i}{\rho_i} - \sum_{i=1}^{N}\left(\frac{\phi_i}{\rho_i}\frac{\mathrm{D}_i\rho_i}{\mathrm{D}t}\right) \tag{D.5}$$

$$\boldsymbol{\nabla}\cdot\boldsymbol{v}_s = \frac{\mathcal{P}}{\zeta} \tag{D.6}$$

$$\boldsymbol{\nabla}P^* = \boldsymbol{\nabla}\cdot\eta(\boldsymbol{\nabla}\boldsymbol{v}_s + \boldsymbol{\nabla}\boldsymbol{v}_s^T - \frac{2}{3}\boldsymbol{\nabla}\cdot\boldsymbol{v}_s\boldsymbol{I}) - \phi_f\Delta\rho\boldsymbol{g} \tag{D.7}$$

Where $\frac{\mathrm{D}_i}{\mathrm{D}t}$ is the Lagrangian derivative following phase i $\frac{\mathrm{D}_i}{\mathrm{D}t} = \frac{\partial}{\partial t} + \boldsymbol{v}_i\cdot\boldsymbol{\nabla}$. Here we have used

the convention $i = 1$ for the melt, and $i = 2 - N$ for the solid phases. As long as the phase densities are relatively constant, the density derivative terms $\frac{\mathrm{D}_i \rho_i}{\mathrm{D}t}$ may be neglected. Given ϕ_i, ϕ_f, $\mathcal{P}$, $\boldsymbol{v}_s$, and P^*, the melt flux is reconstructed as

$$\phi_f \boldsymbol{v}_f = \phi_f \boldsymbol{v}_s - \frac{K}{\mu} \left(\boldsymbol{\nabla} P^* + \boldsymbol{\nabla} \mathcal{P} + \Delta \rho \boldsymbol{g} \right) \tag{D.8}$$

The temperature is given as before by

$$\sum_{i=1}^{N} \left[\rho_i \phi_i C_{Pi} \frac{\mathrm{D}_i T}{\mathrm{D}t} - \phi_i \alpha_i T \frac{\mathrm{D}_i P}{\mathrm{D}t} + T s_i \Gamma_i \right] = k \boldsymbol{\nabla}^2 T \tag{D.9}$$

Appendix E: Numerical solution using finite elements

The weak forms of equations (5.19)-(5.25) are as follows

$$F_{\phi_f} = \int_\Omega \left[\phi_{ft} \left(\phi_{fn} - \phi_{fn-1} + \Delta t \left(\boldsymbol{v}_{sn-\frac{1}{2}} \cdot \boldsymbol{\nabla} \phi_{fn-\frac{1}{2}} - \frac{h^2}{\delta^2} (1-\phi_f) \frac{\mathcal{P}}{\zeta}_{n-\frac{1}{2}} - Da \frac{\Gamma_f}{\bar{\rho}_s}_n \right) \right) \right] \mathrm{d}V \tag{E.1}$$

$$F_{\boldsymbol{\phi}} = \int_\Omega \left[\boldsymbol{\phi}_t \cdot \left(\boldsymbol{\phi}_n - \boldsymbol{\phi}_{in-1} + \Delta t \left(\boldsymbol{v}_{sn-\frac{1}{2}} \boldsymbol{\nabla} \boldsymbol{\phi}_{n-\frac{1}{2}} + \frac{h^2}{\delta^2} \boldsymbol{\phi} \frac{\mathcal{P}}{\zeta}_{n-\frac{1}{2}} - Da (\boldsymbol{\Gamma} \oslash \boldsymbol{\rho})_n \right) \right) \right] \mathrm{d}V \tag{E.2}$$

$$\begin{aligned} F_{c_f^q} = & \int_\Omega \Big[c_{ft}^q \Big((\rho_f \phi_f)_{n-\frac{1}{2}} (c_{fn}^q - c_{fn-1}^q) \\ & + \Delta t \left((\rho_f \boldsymbol{q})_{n-\frac{1}{2}} \cdot \boldsymbol{\nabla} c_{fn-\frac{1}{2}}^q - Da \left(\Gamma_{fn}^q - c_{fn}^q \Gamma_{fn} \right) \right) + \Delta t \frac{1}{Pe_C} \boldsymbol{\nabla} c_{ft}^q \cdot \phi_{fn} \boldsymbol{\nabla} c_{fn}^q \Big] \mathrm{d}V \\ & - \int_{\partial\Omega} \Delta t \frac{1}{Pe_C} c_{ft}^q \phi_{fn} \boldsymbol{\nabla} c_{fn}^q \cdot \mathrm{d}\boldsymbol{S} \end{aligned} \tag{E.3}$$

$$\begin{aligned} F_{\mathcal{P}} = & \int_\Omega \left[\mathcal{P}_t \left(\frac{h^2}{\delta^2} \frac{\mathcal{P}_n}{\zeta_n} - Da \sum_{i=1}^{N} \frac{\Gamma_{in}}{\rho_{in}} \right) + \boldsymbol{\nabla} \mathcal{P}_t \cdot \frac{K_n}{\mu} \left(\boldsymbol{\nabla} \mathcal{P}_n + \hat{\boldsymbol{g}} \right) \right] \mathrm{d}V \\ & - \int_{\partial\Omega} \mathcal{P}_t \frac{K_n}{\mu} \left(\boldsymbol{\nabla} \mathcal{P}_n + \hat{\boldsymbol{g}} \right) \cdot \mathrm{d}\boldsymbol{S} \end{aligned} \tag{E.4}$$

$$F_U = \int_\Omega \left[\boldsymbol{v}_{ct} \cdot \boldsymbol{v}_{cn} + \boldsymbol{\nabla} \cdot \boldsymbol{v}_{ct} U_n \right] \mathrm{d}V - \int_{\partial\Omega} \boldsymbol{v}_{ct} U_n \cdot \mathrm{d}\boldsymbol{S} \tag{E.5}$$

$$F_{\boldsymbol{v}_c} = \int_\Omega U_t \left(\frac{h^2}{\delta^2} \frac{\mathcal{P}}{\zeta}_n - \boldsymbol{\nabla} \cdot \boldsymbol{v}_{cn} \right) \mathrm{d}V \tag{E.6}$$

$$F_{\boldsymbol{q}} = \int_\Omega \left[\boldsymbol{q}_t \left(\boldsymbol{q}_n - \phi_{fn} \boldsymbol{v}_{sn} + \frac{K_n}{\mu} \left(\boldsymbol{\nabla} \mathcal{P}_n + \hat{\boldsymbol{g}} \right) \right) \right] \mathrm{d}V \tag{E.7}$$

$$\begin{aligned} F_T = \int_\Omega \Bigg[& T_t \left(\sum_{i=1}^{N} \left(\rho_i \phi_i C_{Pi} \right)_{n-\frac{1}{2}} \left(T_n - T_{n-1} \right) + \Delta t \left(\sum_{i=2}^{N} \left(\rho_i \phi_i C_{Pi} \boldsymbol{v}_s \right)_{n-\frac{1}{2}} + \left(\rho_f C_{Pf} \boldsymbol{q} \right)_{n-\frac{1}{2}} \right) \boldsymbol{\nabla} T_{n-\frac{1}{2}} \right. \\ & - Ad \sum_{i=1}^{N} \left(\phi_i \alpha_i T \right)_{n-\frac{1}{2}} \left(P_n - P_{n-1} \right) - \Delta t Ad \left(\sum_{i=2}^{N} \left(\phi_i \alpha_i T \boldsymbol{v}_s \right)_{n-\frac{1}{2}} + \alpha_f T \boldsymbol{q}_{n-\frac{1}{2}} \right) \boldsymbol{\nabla} P_{n-\frac{1}{2}} \\ & \left. + \Delta t Da T_i \sum_{i=1}^{N} s_i \Gamma_i \right) + \Delta t \frac{1}{Pe_T} \boldsymbol{\nabla} T_t \cdot \boldsymbol{\nabla} T_i \Bigg] \mathrm{d}V \\ & - \int_{\partial\Omega} \Delta t \frac{1}{Pe_T} T_t \boldsymbol{\nabla} T_n \cdot \mathrm{d}\boldsymbol{S} \end{aligned} \tag{E.8}$$

Where $[\cdot]_t$ is the test function. $[\cdot]_n$ and $[\cdot]_{n-1}$ are the variable values at the current and previous timesteps, and $[\cdot]_{n-\frac{1}{2}} = 0.5([\cdot]_n + [\cdot]_{n-1})$.